STORAGE, ASCENT, AND RELEASE OF SILICIC MAGMA IN CALDERA-FORMING ERUPTIONS

by

MADISON LOGAN MYERS

A DISSERTATION

Presented to the Department of Earth Sciences
and the Graduate School of the University of Oregon
in partial fulfillment of the requirements
for the degree of
Doctor of Philosophy

June 2017

DISSERTATION APPROVAL PAGE

Student: Madison Logan Myers

Title: Storage, Ascent, and Release of Silicic Magma in Caldera-Forming Eruptions

This dissertation has been accepted and approved in partial fulfillment of the requirements for the Doctor of Philosophy degree in the Department of Earth Sciences by:

Paul J. Wallace	Chairperson
Colin J.N. Wilson	Core Member
James Watkins	Core Member
Ilya Bindeman	Core Member
Darren Johnson	Institutional Representative

and

Scott L. Pratt	Dean of the Graduate School

Original approval signatures are on file with the University of Oregon Graduate School.

Degree awarded June 2017

DISSERTATION ABSTRACT

Madison Logan Myers

Doctor of Philosophy

Department of Earth Sciences

June 2017

Title: Storage, Ascent, and Release of Silicic Magma in Caldera-Forming Eruptions

The mechanisms and timescales associated with the triggering of caldera-forming eruptions remain ambiguous and poorly constrained. Do such eruptions start vigorously, then escalate, or can there be episodicity? Are they triggered through internal processes (e.g. recharge, buoyancy), or can external modulations play an important role? Key to answering these questions is the ability to reconstruct the state of the magma body immediately prior to eruption. My dissertation research seeks to answer these questions through detailed investigation of four voluminous caldera-forming eruptions: (1) 650 km^3, 0.767 Ma Bishop Tuff, Long Valley, (2) 530 km^3, 25.4 ka Oruanui eruption, Taupo, (3) 2,500 km^3, 2.08 Ma Huckleberry Ridge Tuff, Yellowstone and (4) 250 km^3, 26.91 Ma Cebolla Creek Tuff, Colorado. The main techniques I applied integrated glass geochemistry (major, trace and volatile), diffusion modeling, and detailed field sampling.

In chapters two, three, and four these methods are applied to the initial fall deposits of three supereruptions (Bishop, Oruanui and Huckleberry Ridge) that preserve field-evidence for different opening behaviors. These behaviors range from continuous deposition of fall deposits and ignimbrite (Bishop), to repetitive start/stop behavior, with time breaks between eruptive episodes on the order of weeks to months (Oruanui,

Huckleberry Ridge). To reconstruct the timescales of opening activity and relate this to conduit processes, I used two methods that exploit diffusion of volatiles through minerals and melt, providing estimates for the rate at which magmas ascended to the surface. This knowledge is then integrated with the pre-eruptive configuration of the magma body, based on melt inclusion chemistry, to interpret what triggered these systems into unrest. Finally, in chapter five I take a different approach by integrating geochemical data for melt inclusions and phenocryst minerals to test whether the mechanism of heat and volatile recharge often called upon to trigger crystal-rich dacitic magmas (the so-called monotonous intermediates), is applicable to the Cebolla Creek Tuff.

Three supplemental excel files are associated with this dissertation. The first supplemental file contains 4 tables pertinent to Chapter II, including geochemical analyses and timescale information. The second supplemental file contains 3 tables associated with Chapter III, including major and trace elemental data, volatile profiles, and decompression rate comparisons. The third supplemental file contains 2 tables to Chapter IV, both geochemical datasets.

This dissertation includes both previously published and unpublished co-authored material.

CURRICULUM VITAE

NAME OF AUTHOR: Madison Logan Myers

GRADUATE AND UNDERGRADUATE SCHOOLS ATTENDED:

University of Oregon, Eugene
University of Idaho, Moscow
University of New Hampshire, Durham

DEGREES AWARDED:

Doctor of Philosophy, Geological Science, 2017, University of Oregon
Master of Science, Geology, 2012, University of Idaho
Bachelor of Science, Geology, 2010, University of New Hampshire
Minor of Science, Applied Mathematics, 2010, University of New Hampshire

AREAS OF SPECIAL INTEREST:

Field Geology
Geochemistry
Petrology
Volcanology

PROFESSIONAL EXPERIENCE:

Graduate Teaching and Research Fellowship, Department of Geological Sciences, University of Oregon, 2012-2017

Researcher, EAPSI, Earth Observatory of Singapore, 2015

Physical Science Student Teacher, NSF GK-12 Fellowship, 2011-2012

Research Assistant, Idaho Geological Survey, 2011

Graduate Teaching Assistant, University of Idaho, 2010-2011

Undergraduate Researcher, University of New Hampshire, 2007-2010

GRANTS, AWARDS, AND HONORS:

Travel Grant, Collapse Caldera Workshop, 2016

Research Excellence Award, University of Oregon, 2016

Women in Graduate Sciences Award, University of Oregon, 2016

Graduate Award, Mineralogy, Geochemistry, Petrology, and Volcanology, 2015

Graduate Student Research Grant, Geological Society of America, 2015

East Asian Pacific Summer Institute, National Science Foundation, 2015

Lipman Research Award, Geological Society of America, 2013

Jack Kleinman Memorial Fund for Volcano Research, USGS, 2013

Waters of the West, National Science Foundation, 2011

Summer Undergraduate Research Award, University of New Hampshire, 2008

PUBLICATIONS:

Swallow, E.J., Wilson, C.J.N., **Myers, M.L.**, Wallace, P.J. (under revision). Melt compositional diversities in early ignimbrite from the 2.08 Ma Huckleberry Ridge eruption, Yellowstone. *Earth and Planetary Science Letters.*

Miller, S.A., **Myers, M.L.**, Bryce, J.G., Blichert-Toft, J. (in review). Magma dynamics beneath ancient Mt. Etna inferred from isotopic and trace element systematics of clinopyroxene. *Geochemical Perspectives Letters*.

Regier, M., Hervig, R.L., **Myers, M.L.**, Roggensack, K., Wilson, C.J.N. (2016). Analyzing nitrogen in natural and synthetic silicate glasses by secondary ion mass spectrometry. *Chemical Geology*, 447, 27-39.

Myers, M.L., Wallace, P.J., Wilson, C.J.N., Morter, B.K., Swallow, E.J. (2016). Prolonged ascent and episodic venting of discrete magma batches at the onset of the Huckleberry Ridge supereruption, Yellowstone. *Earth and Planetary Science Letters*, 451, 285-297.

Myers, M.L., Geist, D.J., Rowe, M.C., Harpp, K.S., Wallace, P.J., Dufek, J. (2014). Replenishment of volatile-rich mafic magma into a degassed chamber drives mixing and eruption of Tungurahua volcano. *Bulletin of Volcanology*, 76 (11), 872.

ACKNOWLEDGMENTS

One of the most influential concepts I will take away from my time as a graduate student is one which I learned through being on the board of Women in Graduate Science: every decade of your life can bring a new and challenging pursuit. This past decade I have been fortunate to spend my time pursuing my passion for science, knowledge, melt inclusions, and most of all, volcanology. I am forever grateful to my main advisor, Paul Wallace, who has made the Ph.D. experience immensely rewarding. His extreme patience and subtle humor is only surpassed by his brilliance. I feel honored to have had such a Ph.D. advisor. I also owe a great deal to the mentorship I have received from my co-advisor, Colin J.N Wilson, who not only taught me the importance of the two middle initials, but has fostered my love for field volcanology. Thank you both so much. I have enjoyed every minute of intellectual debate, and all of the sassy retorts that accompanied them.

My mentorship reached throughout our extremely collegial department, making my dissertation committee a group of colleagues that I respect to the highest degree. Thanks to Jim Watkins for teaching me all I know about diffusion modeling, and always being a steady sounding board. Thank you Ilya Bindeman for your passion for all things isotopes, silicic magma chambers, and Yellowstone. Additionally I would like to thank my UO external committee member Darren Johnson for his guidance during my time with Women in Graduate Science, as well as on my dissertation committee. Of course, my experience at the University of Oregon would have been tremendously different if it wasn't for the mentorship of Mike Dungan, who provided constant advice, amusement, Nick Cave factoids, and opened both numerous figurative doors, and bottles of wine, for me. Thank you.

I owe so much to the friends and family that have provided me with stability, laughter and encouragement over the years. I feel so lucky to have such a wonderful foundation, and am sorry for all those times I worked during a dinner, vacation, outside adventures, at the beach, etc.

This research was supported through a Jack Kleinman Award for Volcano Research from the USGS awarded to Madison Myers, and grants to Madison Myers from the University of Oregon, the NSF East Asia Pacific Summer Institute, and two grants through the Geological Society of America. Additional support through NSF grant EAR-1524824 awarded to Paul Wallace.

For my mom

TABLE OF CONTENTS

Chapter Page

Chapter Page

LIST OF FIGURES

Figure Page

Figure Page

Figure Page

Chapter V

LIST OF TABLES

CHAPTER I

PREAMBLE

How exceedingly large, caldera-forming eruptions begin provides crucial information on the storage, ascent and release of silica-rich magma in catastrophic events, where clues to the onset and initial behavior lie in their volcanic deposits. However, we currently lack the ability to thoroughly assess the mechanisms that drive magmas from their long-term storage region into volcanic conduits, and what controls the residence time of magma ascending through conduit systems. This is largely due to a scarcity of geospeedometers that record the short timescales of magma ascent in explosive eruptions and lack of geochemical data on the deposits from the very opening stages of activity from large eruptions. This works seeks to answer the following questions:

1. How do we quantify and discern between the long-term storage characteristics and those that exist just prior to an eruption?
2. What do end-member field observations (continuous fall deposition vs. start/stop behaviors) tell us about the initiation of these eruptions?
3. Can we observe and quantify these processes through geochemical techniques?

To address these questions, I integrate glass geochemistry (major, trace and volatile elements) for melt inclusions (pockets of melt trapped in a growing phenocryst) and reentrants (melt pockets that were not fully sealed in the host mineral and thus are open to the surroundings) with two diffusion models, in the context of detailed field stratigraphy. Ascent timescales and magma decompression rates are reconstructed using two volatile-based diffusion techniques: (1) H_2O loss from fully enclosed melt inclusions through the crystal host, and (2) measurement and modeling of H_2O and CO_2 concentration gradients

in reentrants. Both of these processes are responses to magma decompression, and the results can be used to calculate the amount of time material spent in the conduit system, and ultimately to calculate an ascent rate.

Chapter II was coauthored with Paul Wallace (University of Oregon), Colin Wilson (Victoria University of Wellington), Beth Morter (University of Oregon), and Elliot Swallow (Victoria University of Wellington), and published in *Earth and Planetary Science Letters* in October 2016.

Chapter II focuses on the oldest caldera forming eruption from the Yellowstone Volcanic Field, the Huckleberry Ridge Tuff. Subtle evidence for reworking in the initial fall deposits suggests repeated start/stop behavior at eruption onset. Integrating geochemistry and diffusion modeling, I show that the opening phases of this eruption tapped multiple magma bodies, which were erupted sequentially and episodically from separate vents. The wide H_2O variations in MIs from individual fall horizons indicate as much as ~14 days of diffusive loss to a degassed external melt, reflecting highly variable and surprisingly slow decompression conditions. Water and CO_2 gradients in reentrants, however, are consistent with final ascent times of <1 to 4 hours, similar to those represented by MIs that are inferred to have experienced little to no diffusive H_2O loss. Chapter II highlights that supereruptions can start hesitatingly if the parental magma bodies are not strongly overpressured, with small-scale episodic activity that is modulated by external controls.

In Chapter III, co-authored with Paul Wallace, Colin Wilson (Victoria University of Wellington), James Watkins (University of Oregon), and Yang Liu (Jet Propulsion

Lab), and in preparation for submission to *American Mineralogist*, I expand upon the use of modeling gradients preserved in reentrants to determine magma ascent rates.

In this chapter, I measured and modeled reentrants from several stratigraphic levels in the opening phases of the Bishop and Oruanui eruptions to compare with those calculated in Chapter II for the Huckleberry Ridge Tuff. From there measurements I show that most reentrants from these systems have experienced an initial slow ascent phase prior to the faster final ascent conditions, indicating that modeling using a constant decompression rate is likely incorrect for most systems. However, in the upper portions of the Bishop eruption, the initial slow phase is absent, suggesting that reentrants afford insight into the 'maturing' of the conduit system. Finally, through integrating these ascent rates with field-based stratigraphy together with inferences on mass discharge rates and caldera-formation, ascent rates are shown to correlate favorably with higher discharge rates, and vent maturation (e.g. development of multiple vents, widening from a point source).

Chapter IV contains co-authored material with Paul Wallace (University of Oregon) and Colin Wilson (Victoria University of Wellington). This chapter investigates the diffusive losses of H_2O from melt inclusions in quartz from the very initial fall phases of the Bishop and Oruanui supereruptions.

Because a longer magma residence time within the conduit system is likely the result of lower degrees of overpressure in the underlying magma system, I use the degree of diffusive loss, integrated with field evidence, to investigate the triggering mechanisms for these two eruptions. I show that the majority of Bishop melt inclusions have experienced little to no diffusive losses from their storage conditions, representing limited

time in the conduit system, consistent with field evidence for a continuous short-lived eruption. However, melt inclusions from the Oruanui display significant scatter in their conduit residence times, consistent with field evidence that rifting (an external mechanism) was important for triggering initial eruptions.

Chapter V contains material coauthored with Chloe Elliot, Mike Dungan, Amy Krauss and Paul Wallace (all University of Oregon), and discusses the volatile and petrologic history of the magma that was erupted to form the Cebolla Creek Tuff, CO.

Combing melt inclusion volatile concentrations with phenocryst zoning (amphibole and plagioclase), I investigate the pre-eruptive state of the crystal-rich Cebolla Creek Tuff. The homogeneous whole-rock dacitic composition (SiO_2 61-64 wt.%) and high crystal content (35-40%) of the juvenile ejecta in Cebolla Creek Tuff qualify the deposit as a 'monotonous intermediate', thought to require volatile and heat fluxing in order to mobilize the parental magma to eruption. However, the lack of late-stage reverse zonation or strong dissolution textures on any rims of major phenocrysts (plagioclase, amphibole) precludes late-stage heating, volatile fluxing or mafic recharge, and requires an alternative eruption triggering mechanism for the Cebolla Creek eruption.

CHAPTER II

PROLONGED ASCENT AND EPISODIC VENTING OF DISCRETE MAGMA BATCHES AT THE ONSET OF THE HUCKLEBERRY RIDGE SUPERERUPTION, YELLOWSTONE

This chapter was published in *Earth and Planetary Science Letters* in October of 2016. I was lead author on the paper, which involved sample preparation, analysis, synthesis of all data, development of diffusion models, and writing the manuscript. Paul Wallace (University of Oregon) served as the main advisor, aiding in data interpretation and manuscript editing. Colin Wilson (Victoria University of Wellington) helped with field sampling, data interpretation and provided feedback on manuscript drafts. Beth Morter (University of Oregon) provided geochemical data, and Elliot Swallow (Victoria University of Wellington) aided in manuscript editing.

1. Introduction

Caldera-forming silicic eruptions are among the most devastating natural events on Earth, with the largest (supereruptions) disgorging vast quantities of material on geologically instantaneous timescales (Mason et al., 2004; Self, 2006). However, the mechanisms and timescales associated with eruption onset remain unclear. Do such eruptions start vigorously, then escalate (Wilson and Hildreth, 1997), or can there be episodicity (Wilson, 2001), and what might cause an explosive eruption to stop once initiated? Although most researchers agree that overpressure due to magma recharge or volatile exsolution is a common triggering mechanism in small-volume chambers (Roche and Druitt, 2001; Jellinek and DePaolo, 2003; Gregg et al., 2012), there remains

controversy about its role in larger, caldera-forming eruptions (see Gregg et al., 2015). In the latter case, there is also debate as to whether buoyancy is central to the initiation (Caricchi et al., 2014; Malfait et al., 2014) or if an external mechanism, such as roof destabilization or tectonic rifting, is a requirement for mobilization (Gregg et al., 2012; de Silva and Gregg, 2014; Gregg et al., 2015). This controversy is exacerbated by a scarcity of geochemical data on the very earliest deposits from supereruptions that could constrain how they start. However, discriminating between these mechanisms is possible (e.g. Allan et al., 2012) if the state and behavior of magma at eruption onset could be assessed. In particular, because magma ascent rates reflect the extent of overpressure in the magma chamber (e.g., Melnik and Sparks, 1999), determining ascent rates for the earliest erupted materials can reveal whether or not internal triggering by overpressure in the source magma body was important.

Here we address these issues by combining field evidence with evaluation of magma ascent timescales derived from diffusive H_2O losses from enclosed melt inclusions (MIs) and H_2O and CO_2 loss from reentrants (REs; unsealed melt inclusions), all preserved in quartz phenocrysts. We take advantage of the inferences that significant diffusive loss of H_2O species from MIs through their host phenocryst can occur on timescales of hours to days during magma rise (Severs et al., 2007), and from REs on even shorter timescales associated with the final stages of magma ascent (Liu et al., 2007; Humphreys et al., 2008; Lloyd et al., 2014). We couple our timescale information with micro-scale geochemistry to examine magma chamber conditions and conduit processes shortly before and during the opening stages of the Huckleberry Ridge supereruption.

2. Geological background

The Huckleberry Ridge Tuff (HRT) is the product of the oldest and largest (2.08 Ma; 2,500 km^3) of the three caldera-forming eruptions at the Yellowstone Plateau volcanic field (Christiansen, 2001; Fig. 2.1). The HRT consists of initial fall deposits overlain by three voluminous welded ignimbrite units [members A, B and C], with minor additional fall deposits beneath member C. Here we focus on the initial fall deposits beneath member A, which consist of multiple bedded layers, including several that are normally graded up to fine ash tops. This grading implies that the eruption plume stopped and restarted several times, reflecting episodicity during the opening explosive phases. In addition, there is evidence in these deposits for reworking in their lower parts at multiple stratigraphic levels, observed in widely-spaced stratigraphic sections (Fig. 2.1b,c and Appendix A, Fig. 1A). A lack of wholesale reworking or significant gullying of the fine-grained ash-rich beds, however, precludes time periods of months to years for any single hiatus, but rather requires pauses in deposition on the order of days (see also Appendix A, Fig. 1A).

3. Methods

Nine individual layers were sampled from the lowest 1.8 meters of the 2.5-m thick, largely unconsolidated fall deposits preserved beneath the welded base of ignimbrite member A on the western rim of Mt Everts near Mammoth, Wyoming, north of the inferred eruptive source (Fig. 2.1a). The nine sampled layers were chosen to bracket horizons of reworking and to be distributed over changes in grain size (Fig. 2.1b).

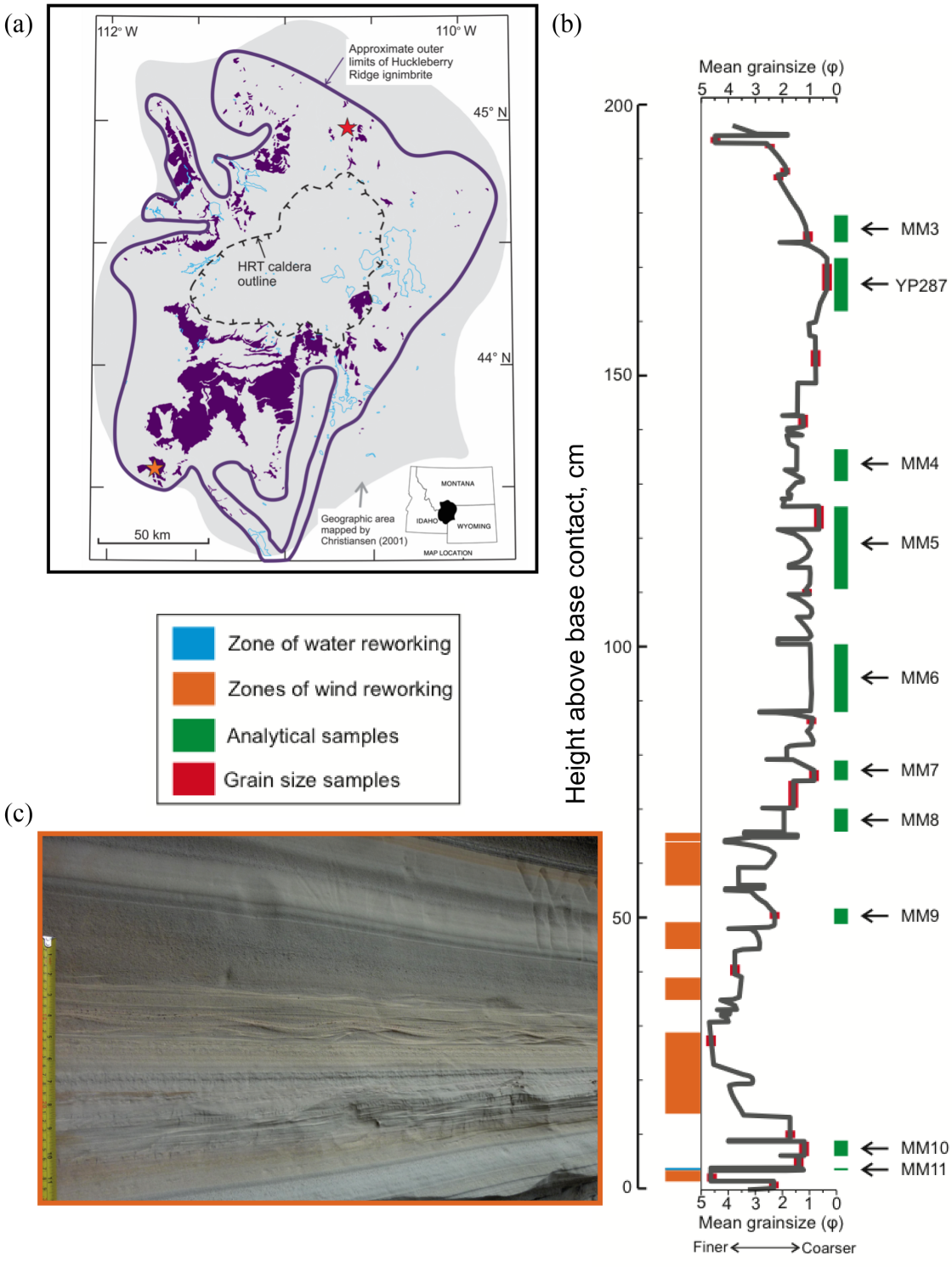
(a)
112° W
110° W
45° N
44° N
Approximate outer limits of Huckleberry Ridge ignimbrite
HRT caldera outline
Geographic area mapped by Christiansen (2001)
MONTANA
IDAHO
WYOMING
MAP LOCATION
50 km
Zone of water reworking
Zones of wind reworking
Analytical samples
Grain size samples
(b)
Mean grainsize (φ)
5 4 3 2 1 0
200
150
100
50
0
Height above base contact, cm
MM3
YP287
MM4
MM5
MM6
MM7
MM8
MM9
MM10
MM11
Mean grainsize (φ)
Finer ⟷ Coarser
(c)

At higher levels than those sampled, the fall deposits are baked or fused by the overlying welded ignimbrite, the matrix glasses are darkened and MIs devitrified; this material was not used in this study. Samples were sieved to 500 μm and picked for loose, but glass-coated, quartz crystals. Individual crystals were mounted and doubly polished to expose glassy, bubble-free MIs and REs (Fig. 2.2). Size, glass color, and distance from the nearest crystal rim were recorded for each MI (Supplement Chapter II Table 1) and cathodoluminescence images of the quartz hosts were acquired (Appendix A, Fig. 2A). We report data only from those samples with pristine and glassy MIs, which are thus inferred to have quenched rapidly on eruption, preserving information about their entrapment and ascent histories. Black obsidian shards to micro-pyroclasts (<1 mm across) from each layer were also sampled, and mounts prepared and analyzed in a similar manner to the MIs and REs.

←

Figure 2.1. (a) Outline map of the area covered by ignimbrite of the Huckleberry Ridge Tuff. The geographical area mapped by Christiansen (2001) is shown by gray shading, purple areas represent outcrops of the ignimbrite, and the purple line represents its approximate outer limits. The red star denotes the location at Mt. Everts of the fall deposit section (panel b), which shows evidence of reworking (panel c). The orange star marks a locality in Swan Valley, 180 km SSW of Mount Everts, where correlated reworking horizons have been identified (see Appendix A).

(b) Stratigraphic representation of the lower part of the 2.5 meter-thick HRT initial fall deposits on Mt. Everts. Green zones represent samples reported on here. The red fields indicate samples that were collected for sieve analysis and used to calibrate the grainsize variation curve shown. Zones of reworking (see Appendix A, Fig. 1A) are also shown as colored fields: zones of water reworking (one blue sliver affecting the layer sampled as MM11), and zones of wind reworking (in orange).

(c) View of the lower, fine-ash-dominated portion of the HRT fall deposits at Mount Everts. Note the two prominent zones of inferred wind reworking within the fine ash deposits, and the sharp break (horizon 'h': see Appendix A, Fig. 1A, Panel G for detail) into the coarser ash to fine lapilli middle parts of the fall deposits (at ~65 cm above base in the stratigraphic log).

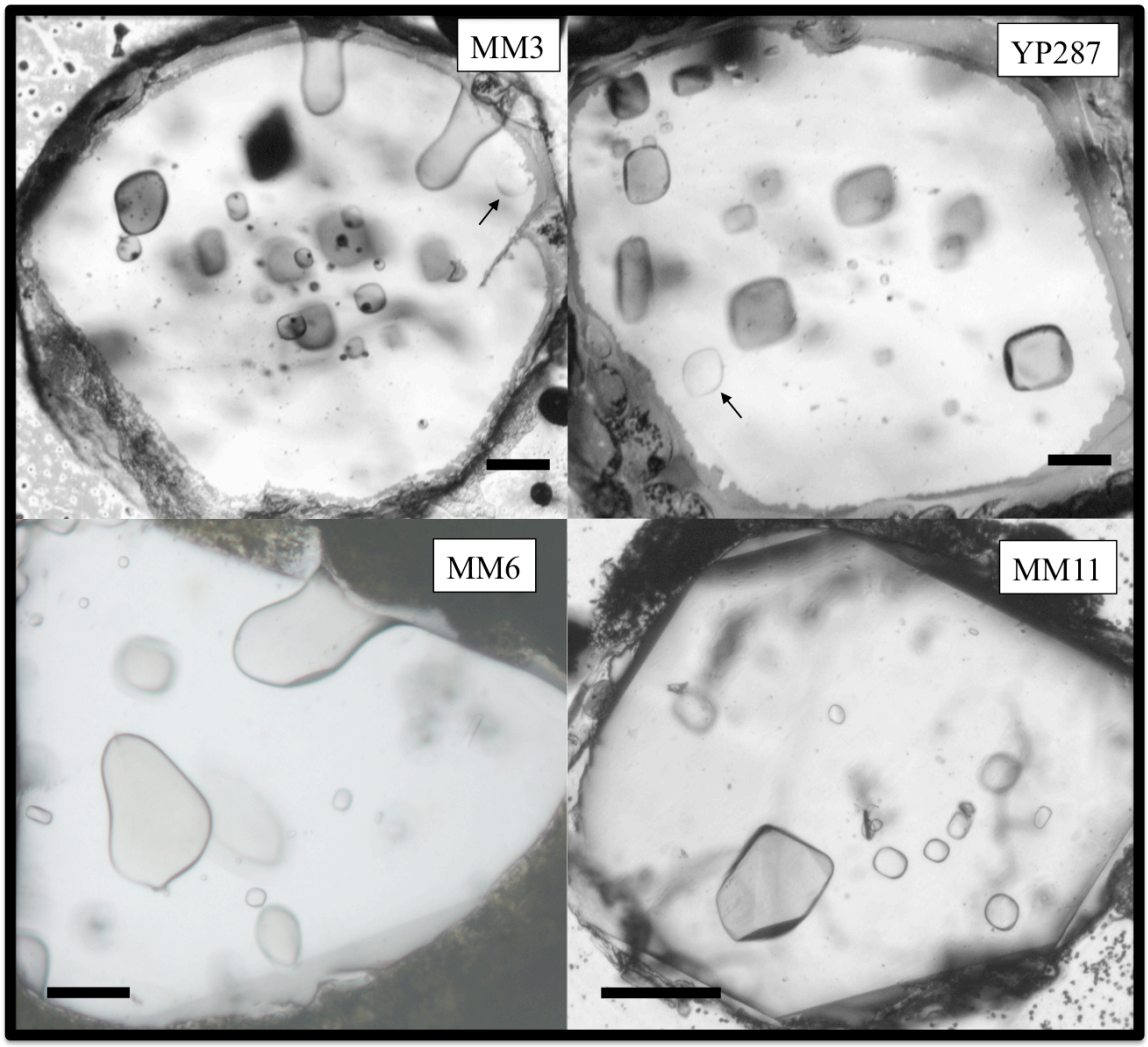

Figure 2.2. Photomicrographs of quartz-hosted MIs and REs typical of samples from the fall section. Samples MM3 and YP287 contain both colorless and brown MIs; arrows point to colorless MIs. A 100 μm scale bar is shown in each image.

Water and CO_2 concentrations were measured using a Thermo Nicolet Nexus 670 Fourier transform infrared (FTIR) spectrometer interfaced with a Continuum IR microscope at the University of Oregon. Absorbances measured were converted to H_2O and CO_2 concentrations using the Beer-Lambert law ($c_i = M_i \cdot A/\rho \cdot d \cdot \varepsilon$), where c_i is the concentration of the absorbing species, M_i is the molecular weight of the species (g/mol),

A is the absorbance (height) of the relevant vibration band, ρ is the glass density (g/L), d is the thickness of the wafer analyzed (cm) and ε is the molar absorption coefficient (L/mol·cm). In rhyolitic compositions, ρ and ε strongly depend on total H_2O concentration. This requires the use of an iterative process to converge on appropriate values [Eq. 1 (Skirius, 1990) and Eq. 2 (Leschik et al., 2004)]:

$$\rho = 2350 - 12.6\ C_{H_2O} \qquad \text{Eq. 1}$$

$$\varepsilon = 80 - 1.36\ C_{H_2O} \qquad \text{Eq. 2,}$$

where C_{H_2O} is the concentration of total dissolved H_2O in wt.%. Final densities using Eq. 1 range from 2295-2336 kg/m^3, and final ε values using Eq. 2 are between 73 and 79 L/mol·cm. Total H_2O concentration was calculated using the 3570 cm^{-1} peak, which required that thicknesses for the quartz wafers be between 30 and 70 μm. For thicker wafers, total H_2O was calculated using the near IR peaks (5230 cm^{-1} and 4520 cm^{-1}: Zhang et al., 1997). The absorption coefficient (ε) for molecular CO_2 (2350 cm^{-1}) in rhyolitic glass is 1214 L/mol·cm (Behrens et al., 2004). Peak heights were calculated using a straight-line background correction (Dixon et al., 1995). Thicknesses were measured using both a digital micrometer (±2 μm) and the reflectance interference fringe method (Wysoczanski and Tani, 2006). Agreement between the two methods is within 4 μm.

After FTIR analysis, the quartz and obsidian pyroclast wafers were set in a 1-inch epoxy mount for analysis of major elements using a Cameca SX-100 electron microprobe (EPMA) at University of Oregon. Operating conditions were 15 kV and 10 nA sample

current for Si, Ca, Na, Fe, Al, and K, and 50 nA current for Cl, F, Mg and Ti. A beam size of 5-10 μm was used for all analyses. Sodium, K, Si, and Al were measured first, and their concentrations were calculated using a time-dependent intensity correction in Probe for Windows (Donovan et al., 2007**)**. Glasses were then analyzed for trace elements by Laser-Ablation Inductively Coupled Plasma Mass Spectrometry (LA-ICP-MS) at Oregon State University using a 50-μm spot size, with five glass standards (GSD-1G, BHVO, ANTO, NIST-612, and BCR) for calibration, ^{29}Si as an internal standard, and GSD-1G as a check standard throughout the run. Major, trace, and volatile element concentrations, along with their associated errors, can be found in online Supplement Chapter II Table 1 and 2.

4. Results

All quartz-hosted MIs and REs from the nine stratigraphic levels sampled are high silica rhyolite (SiO_2 = 75-77 wt.%, volatile-free). The data show a negative correlation between SiO_2 and Al_2O_3, consistent with compositional control dominated by feldspar crystallization (Fig 2.3a). Concentrations of U (6-10 ppm), Cl (1200-2000 ppm), and B (9-20 ppm) produce continuous arrays when plotted against Rb (170-270 ppm), which is expected to be incompatible during crystallization (Fig. *2*.3b, e). Using appropriate partition coefficients and an equilibrium crystallization model (see Fig. 2.3 caption) the range of compositions is consistent with ~55% crystallization of the least-evolved MI compositions in the middle and upper sampled layers to yield the most-evolved MI compositions in the earliest layers sampled. Some trace elements (e.g. Ba, Sr), however,

Table 2.1. Average major (EPMA; in wt.%, Cl and F in ppm) and trace element data, with variability given as 1 SD (italics) for the six quartz populations determined using melt inclusions (see Section 5 for discussion), and the final three erupted cupolas based upon reentrant and obsidian pyroclast compositions (Fig. 2.7, Supplementary Fig. 8A)

	Quartz Poulation 1		Quartz Poulation 2		Quartz Poulation 3		Quartz Poulation 4		Quartz Poulation 5		Quartz Poulation 6		Eruptive Cupola 1		Eruptive Cupola 2		Eruptive Cupola 3	
SiO_2	76.23	*0.60*	76.28	*0.36*	76.66	*0.42*	76.28	*0.38*	76.15	*0.30*	76.56	*0.18*	76.86	*0.39*	76.80	*0.48*	76.65	*0.54*
TiO_2	0.08	*0.01*	0.09	*0.02*	0.09	*0.01*	0.11	*0.02*	0.12	*0.01*	0.10	*0.01*	0.08	*0.01*	0.08	*0.02*	0.10	*0.02*
Al_2O_3	12.39	*0.41*	12.11	*0.28*	12.05	*0.29*	12.26	*0.30*	12.15	*0.23*	12.27	*0.25*	12.27	*0.27*	12.13	*0.30*	12.10	*0.44*
FeO	1.28	*0.11*	1.40	*0.10*	1.41	*0.08*	1.46	*0.06*	1.53	*0.09*	1.41	*0.06*	1.21	*0.11*	1.38	*0.13*	1.43	*0.13*
MgO	0.01	*0.00*	0.02	*0.00*	0.02	*0.00*	0.02	*0.00*	0.03	*0.00*	0.02	*0.00*	0.01	*0.00*	0.02	*0.00*	0.02	*0.00*
CaO	0.55	*0.03*	0.55	*0.01*	0.55	*0.02*	0.57	*0.01*	0.47	*0.09*	0.44	*0.04*	0.55	*0.02*	0.54	*0.02*	0.55	*0.02*
Na_2O	3.98	*0.19*	3.68	*0.41*	3.59	*0.26*	3.73	*0.17*	4.12	*0.31*	3.99	*0.06*	4.05	*0.13*	3.66	*0.43*	3.55	*0.34*
K_2O	5.07	*0.23*	5.46	*0.47*	5.34	*0.27*	5.19	*0.21*	5.06	*0.15*	4.90	*0.08*	4.97	*0.14*	5.29	*0.23*	5.45	*0.34*
Total	94.44	*1.02*	96.14	*1.37*	95.72	*1.23*	95.57	*1.17*	95.66	*0.96*	96.74	*1.30*	97.28	*0.04*	95.41	*1.14*	95.66	*1.19*
Cl	1889	*86*	1688	*108*	1560	*99*	1527	*61*	1272	*36*	1434	*74*	1830	*129*	1687	*112*	1478	*101*
F	2698	*345*	2338	*443*	2188	*206*	2177	*448*	2557	*1185*	1579	*461*	3301	*1499*	3473	*1348*	3085	*1090*
Li	78.8	*7.8*	56.0	*22.4*	46.8	*23.5*	55.9	*10.5*	70.0	*20.8*	81.1	*23.7*	61.7	*9.7*	47.9	*11.8*	42.6	*14.8*
B	17.5	*3.3*	13.4	*1.4*	12.5	*1.1*	12.9	*1.4*	11.1	*1.6*	12.7	*0.8*	16.5	*1.9*	15.2	*1.8*	12.9	*1.7*
P	54.8	*10.5*	54.4	*9.0*	60.9	*8.5*	58.8	*11.1*	75.3	*8.1*	54.3	*7.3*	58.2	*4.1*	60.1	*8.3*	63.4	*12.9*
Ti	520	*55*	614	*67*	675	*29*	695	*32*	823	*64*	696	*37*	479	*22*	552	*28*	658	*32*
Rb	259	*12*	230	*8*	208	*14*	211	*10*	191	*14*	212	*16*	263	*9*	242	*11*	220	*12*
Sr	1.7	*0.6*	3.5	*1.4*	5.6	*0.6*	5.7	*0.9*	11.9	*1.6*	5.0	*1.3*	1.1	*0.2*	2.4	*0.2*	5.0	*0.4*
Y	82.1	*14.0*	82.9	*5.2*	78.6	*9.0*	75.3	*4.2*	66.8	*3.6*	74.6	*6.1*	80.6	*4.9*	82.4	*6.2*	74.0	*5.9*
Zr	173	*39.5*	204	*10.2*	211	*27.4*	210	*13.5*	227	*37.0*	206	*14.9*	148	*10.4*	200	*13.4*	199	*15.4*
Nb	71.8	*6.7*	70.0	*2.5*	63.7	*4.0*	64.1	*3.6*	56.9	*4.6*	65.6	*3.6*	71.0	*2.7*	69.5	*2.9*	62.7	*3.0*
Sn	6.9	*0.5*	6.0	*0.5*	5.4	*0.4*	5.4	*0.4*	4.8	*0.5*	5.6	*0.3*	7.2	*0.4*	6.6	*0.6*	5.7	*0.5*
Ba	20.9	*12.1*	56.4	*33.5*	107	*13.2*	112.6	*24.0*	318	*80.7*	60.0	*29.0*	12.7	*1.0*	36.2	*3.9*	101	*6.9*
La	45.7	*16.7*	65.6	*8.8*	72.0	*8.2*	71.8	*5.2*	86.6	*12.3*	71.3	*5.6*	33.0	*1.4*	62.1	*3.8*	66.7	*5.2*
Ce	101	*27.8*	134	*12.8*	142	*8.7*	145	*7.0*	172	*20.0*	144	*9.2*	79.0	*2.9*	132	*6.0*	137	*5.1*
Pr	10.4	*3.0*	13.8	*1.4*	14.6	*1.4*	14.6	*0.8*	16.7	*2.1*	14.5	*1.0*	8.4	*0.4*	13.5	*0.9*	13.8	*0.8*
Nd	40.9	*11.8*	53.7	*5.2*	56.5	*5.3*	56.2	*3.6*	64.7	*9.2*	56.3	*5.0*	33.4	*1.6*	52.7	*4.0*	53.1	*3.5*
Sm	10.4	*2.2*	12.4	*1.5*	12.4	*1.9*	12.1	*1.0*	12.6	*1.9*	12.0	*1.3*	9.2	*0.9*	12.3	*1.2*	11.9	*1.1*
Eu	0.2	*0.1*	0.3	*0.1*	0.4	*0.1*	0.4	*0.1*	0.8	*0.2*	0.4	*0.1*	0.2	*0.0*	0.3	*0.0*	0.4	*0.1*
Gd	11.8	*2.0*	13.4	*1.2*	13.1	*1.7*	12.8	*1.2*	12.3	*1.7*	12.6	*1.3*	11.1	*0.5*	13.3	*1.5*	12.4	*1.0*
Dy	14.1	*2.5*	14.5	*0.9*	13.8	*1.5*	13.5	*1.2*	12.3	*0.9*	13.3	*1.1*	13.9	*1.3*	14.6	*1.3*	13.0	*1.2*
Er	9.1	*1.9*	9.3	*0.8*	8.8	*1.0*	8.5	*0.3*	7.1	*0.6*	8.4	*0.5*	9.0	*1.0*	9.3	*0.8*	8.3	*0.8*
Yb	8.2	*1.1*	7.9	*0.8*	7.6	*0.8*	7.5	*0.5*	6.5	*0.4*	7.3	*0.5*	8.0	*0.7*	8.1	*0.7*	7.2	*0.7*
Hf	7.8	*1.7*	8.6	*0.9*	8.6	*1.0*	8.4	*0.8*	8.4	*1.1*	8.5	*0.9*	6.9	*0.6*	8.5	*0.9*	8.2	*0.9*
Ta	4.7	*0.8*	4.7	*0.3*	4.1	*0.3*	4.2	*0.3*	3.5	*0.2*	4.2	*0.3*	4.7	*0.4*	4.6	*0.3*	4.0	*0.3*
Pb	45.6	*3.4*	39.9	*3.7*	37.8	*4.1*	37.6	*2.2*	32.0	*2.6*	34.6	*2.5*	45.1	*3.4*	43.1	*2.7*	38.3	*2.6*
Th	28.1	*5.6*	30.0	*2.1*	29.3	*2.3*	28.9	*1.9*	28.6	*1.3*	28.6	*2.3*	26.3	*1.6*	30.2	*1.9*	27.1	*2.0*
U	9.0	*0.6*	8.1	*0.6*	7.4	*0.5*	7.7	*0.5*	6.6	*0.4*	7.5	*0.5*	9.3	*0.5*	8.8	*0.7*	7.4	*0.4*

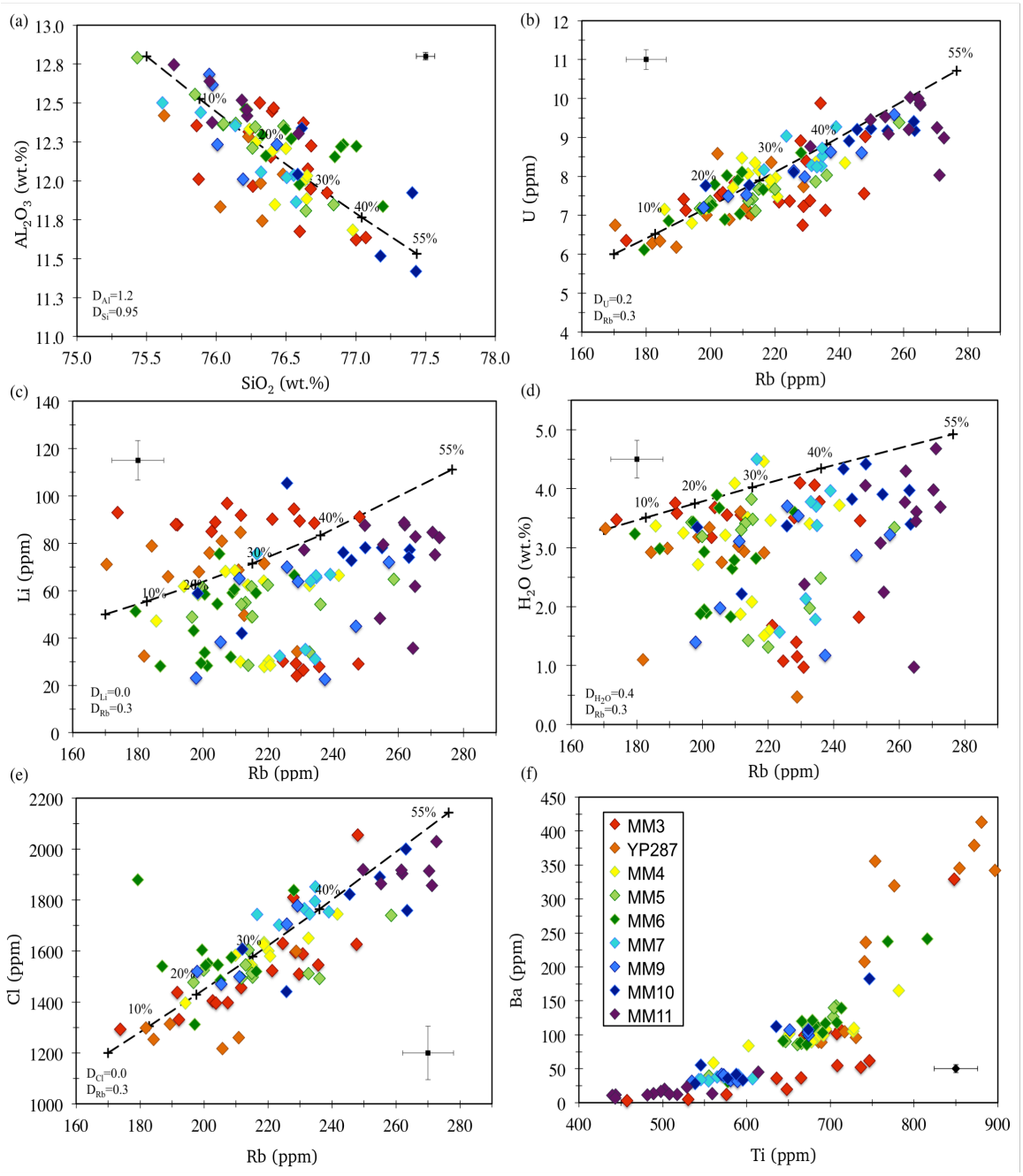
(a)
AL_2O_3 (wt.%)
SiO_2 (wt.%)
10%
20%
30%
40%
55%
D_{Al}=1.2
D_{Si}=0.95
(b)
U (ppm)
Rb (ppm)
D_U=0.2
D_{Rb}=0.3
(c)
Li (ppm)
Rb (ppm)
D_{Li}=0.0
D_{Rb}=0.3
(d)
H_2O (wt.%)
Rb (ppm)
D_{H_2O}=0.4
D_{Rb}=0.3
(e)
Cl (ppm)
Rb (ppm)
D_{Cl}=0.0
D_{Rb}=0.3
(f)
Ba (ppm)
Ti (ppm)
MM3
YP287
MM4
MM5
MM6
MM7
MM9
MM10
MM11

tend to cluster the MI data into distinct groups rather than produce continuous arrays (e.g. Fig. 2.3f). Although REs and obsidian pyroclasts largely overlap in composition with the MIs from their equivalent layer (Appendix A, Fig. 3A), they are more closely clustered than the MIs (see discussion in Section 6).

In each fall horizon sampled, including the lowermost (<2-3 cm above the basal contact, likely the first ≤0.1 km^3 of erupted magma), there is a wide range of H_2O contents (~1.0 to 4.5 wt.%) in sealed MIs (Fig. 2.4, Appendix A, Fig. 4A). This is in contrast to the factor of two variation preserved by other incompatible elements (e.g. Rb: Fig. 2.3, Appendix A, Fig. 4A). Although the majority of inclusions analyzed are colorless, higher up in the fall deposit samples YP287 and MM3 contain both colorless and brown inclusions, sometimes in the same crystal. The colorless inclusions in MM3 and YP287 contain much lower H_2O and higher CO_2 concentrations than the brown inclusions, and overall are smaller in volume and/or closer to the crystal edge. In all other sampled horizons, the lowest-H_2O MIs are in grains that do not contain high-H_2O MIs. Additionally, cathodoluminescence (CL) images of the quartz hosts show no evidence that any of the lower-H_2O MIs were trapped by late-stage growth of crystal rims (cf. Peppard et al., 2001; Appendix A, Fig. 2A).

←

Figure 2.3. Volatiles and trace elements vs. Rb for MIs from the nine layers sampled from the HRT fall deposit (see Fig. 2.1). Legend is shown in lower right panel. Curves show equilibrium crystallization (in wt.%) calculated using bulk partition coefficients as follows: D = 0 for Cl and Li, D = 0.3 for Rb, and D = 0.2 for U (Roberge et al., 2013), appropriate for a high-silica rhyolite crystallizing quartz and two feldspars, with biotite and amphibole absent. For H_2O, D = 0.4 was used to simulate crystallization of vapor-saturated rhyolitic melt (see discussion in text). Error bars show average 1 SE analytical uncertainties. Uncertainties for individual MI analyses can be found in online Supplement Chapter II Table 1.

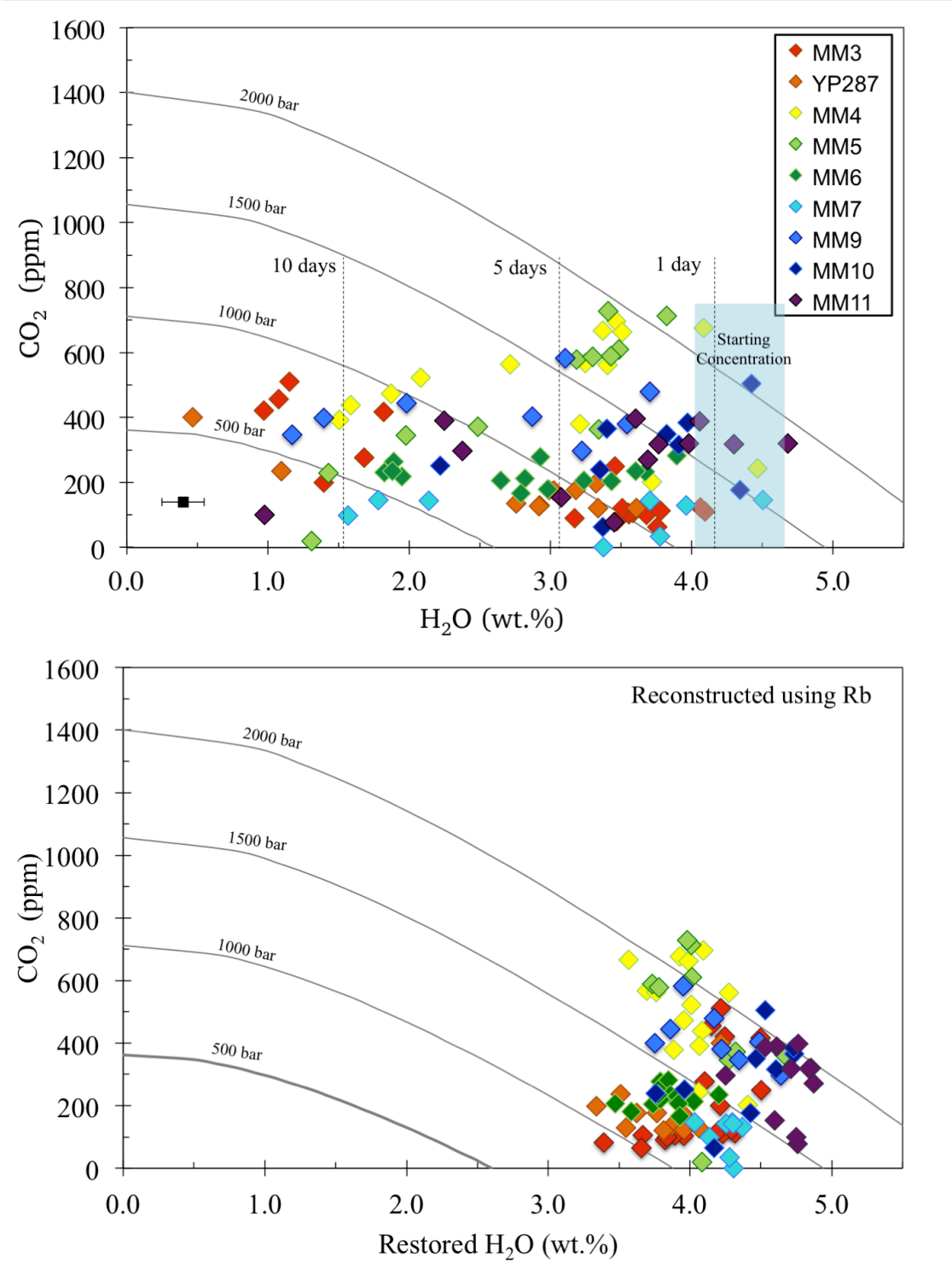

Figure 2.4. (a) H_2O vs. CO_2 for MIs from the HRT fall deposit. Curves show vapor saturation isobars calculated at 800°C using VolatileCalc (Newman and Lowenstern, 2002). Error bar in lower left of top panel shows mean SE analytical uncertainties, where SE for CO_2 is less than symbol size. (b) Restored H_2O values, calculated as described in the text, vs. CO_2 for all MIs.

5. Causes of volatile variations and modeling of magma ascent timescales

5.1. H_2O concentrations from quartz-hosted MIs

The wide range of H_2O values in MIs from each sampled layer compared to the more limited variation in Rb concentration is best explained by diffusive loss of H species through the quartz host crystal during ascent (Severs et al., 2007). Consistent with this interpretation, Li, which also has a relatively rapid diffusivity in quartz (Charlier et al., 2012), is also highly scattered when plotted against Rb (Fig. 2.3c). This scatter contrasts strongly with the consistency shown by all other major and trace elements, which diffuse through quartz at much slower rates. Thus we interpret the MIs with the highest H_2O values to reflect magmatic concentrations at the storage depth prior to eruption, and the lower values to reflect variable diffusive losses, suggesting that at a given stratigraphic horizon, co-deposited crystals experienced different ascent histories and decompression rates (Appendix A, Fig. 4A). The variable H_2O concentrations can be used to calculate a decompression timescale for each MI and host crystal if initial and external melt concentrations of H_2O can be constrained. However, timescales cannot be estimated using the Li variations because of complexity in Li solubility and diffusivity (Charlier et al., 2012).

Alternative explanations for the wide range of MI H_2O values in co-deposited quartz crystals include reheating of the fall deposit by the thick overlying ignimbrite, and recycling (after ~1 day to a week) of crystals from hot, surficial deposits. If reheating by overlying ignimbrite was important, the crystals in any layer would have all experienced the same temperature-time history. As a result, there would be a more uniform distribution of H_2O values within a given layer (with H_2O values more strongly

correlating with inclusion volume), and there should be systematic trends through the section (i.e., more diffusive loss at the top, in closer proximity to ignimbrite). None of these features are observed. Recycling of quartz from hot, near-vent surficial deposits could create the variable H_2O values, but there is no evidence for dome-derived material (obsidian pyroclasts contain detectable concentrations of CO_2) or for thermal oxidation of, or microlite growth in, the selvedge glasses. In addition, none of the inclusions are devitrified, nor are there fragments of recycled tuff found as lithic material. Based on these observations, we interpret the range of H_2O values in MI in co-deposited crystals to be the result of highly variable ascent histories and decompression rates of magma within the conduit system.

5.2. Temperature estimates

To calculate timescales associated with diffusive losses of H_2O through the quartz hosts, we need to constrain the pre-eruptive temperature of the HRT fall deposit magma because diffusivity of H-species in minerals is strongly temperature dependent (e.g., Johnson and Rossman, 2013). Experimental phase equilibria on compositionally similar rhyolites from the Bruneau-Jarbidge eruptive center of the Yellowstone hotspot track have been determined at pressures of 2 and 5 kbar, with H_2O concentrations up to 4 wt.% (Almeev et al., 2012). In the more applicable 2 kbar experiments (see Fig. 2.4), the mineral assemblage present in the HRT A fall deposit (quartz, plagioclase, sanidine) occurs in equilibrium with melt containing 4 wt.% H_2O at 800 ºC. Glass compositions from the experiments at these conditions are similar to our average MI composition (Supplement Chapter II Table 3), with the largest discrepancy found in Na_2O (Almeev et

al., 2012: 2.85 wt. %; HRT MI: 3.78 wt. %). In agreement with the Almeev et al. (2012) experimental phase equilibria and H_2O concentrations from MIs, application of the plagioclase-melt hygrometer of Waters and Lange (2015) using plagioclase and matrix glass compositions from our samples (Swallow et al., in review) yield melt H_2O concentrations of 4.0-4.5 wt.% at 800 °C.

For comparison, we also calculated zircon saturation temperatures. Using the Watson and Harrison (1983) calibration, the average temperature for all MI and RE is 800 ± 24 °C (2 s.d.; online Supplement Chapter II Table 1). The Boehnke et al. (2013) calibration, however, yields lower values of 753 ± 28 °C. The magnitude of the offset between the two methods in these compositions was noted by Boehnke et al. (2013). Given the agreement between the phase equilibrium, plagioclase-melt hygrometer results, and Watson and Harrison (1983) temperatures, and the observation that the Boehnke et al. (2013) calibration gives temperatures that are consistently lower than other geothermometers in rhyolitic systems (e.g. Barker et al., 2014; Loewen and Bindeman, 2015), we use 800 ºC as the pre-eruption magmatic temperature. However, because of the implications surrounding the temperature estimate, the diffusion calculations presented in the next section were also calculated at 775 and 825 ºC for one sample (Appendix A, Fig. 5A). We find that the uncertainty in our temperature estimate has a minor effect on our calculated timescales (factor of ±1.6) and does not affect our overall conclusions.

5.3. Ascent timescales based on diffusive H loss from MIs

Calculating a timescale of diffusive H loss from each MI through the quartz host requires an estimate of (1) the diffusion coefficient of H in quartz, (2) the H_2O partition

coefficient between quartz and melt (0.0001: Qin et al., 1992), (3) the initial MI H_2O concentration, and (4) the external H_2O concentration. We calculate a diffusion coefficient of 10^{-11} m^2/s using the diffusion model of Cottrell et al. (2002) and the experimental data of Severs et al. (2007) on H diffusive losses from MI in quartz at 800 ºC.

To approximate the initial H_2O contents (before diffusive loss) we applied two methods. In the first, we assumed that H_2O behaved moderately incompatibly through partial loss to a vapor phase during vapor-saturated crystallization (Roberge et al., 2013; Fig. 2.3). During crystallization, the fact that H_2O is much more soluble than CO_2 causes dissolved H_2O to increase in the melt, but to a lesser extent than it would if the system were not vapor saturated. A vapor–melt partition coefficient of 0.4 can explain the variations observed for least-degassed melt inclusions from all samples (Fig. 2.3), and represents a similar value to model results for vapor-saturated crystallization using rhyolite-MELTS with included H_2O and CO_2 solubility relations (Ghiorso and Gualda, 2015). Using the calculated fractionation curve in Fig. 2.3d, we estimate the initial (restored) H_2O content of each MI based on its composition (Fig. 2.4b).

The second method is based on an assumption that the MIs were trapped with variable Rb and H_2O and then held in a magma chamber such that all MIs re-equilibrated to the surrounding H_2O concentration, regardless of their variable Rb (Fig. 2.3, Appendix A, Fig. 3A). In such a scenario, the highest H_2O concentration of MIs from each sample would best estimate the initial H_2O concentration at that stratigraphic level. This method yields starting values of 3.7-4.5 wt. % H_2O (Fig. 2.4a, Appendix A, Fig. 4bA), whereas the first method using Rb gives 3.3-4.5 wt.% (Figs. 2.3 and 2.4b). Given the overlap of

these values, the choice of method has a minimal effect on calculated decompression timescales, and we adopt the first approach here.

The external H_2O concentration was estimated specifically for each unit using the lowest H_2O value measured in the interiors of REs from that sample (online Supplement Chapter II Table 4). These concentrations are similar to the lowest MI H_2O concentration measured in that same horizon. REs were used for this purpose because they rapidly re-equilibrate with the surrounding depressurized melt (within hours). Decompression timescales for each MI were modeled assuming an instantaneous pressure drop (step function), yielding the fastest decompression timescale and giving us the minimum possible ascent time. A more realistic scenario would be that each MI responded to a constantly decreasing external H_2O concentration throughout its ascent until it reached the depth at which the interiors of REs last equilibrated. This method, however, would yield longer timescales and requires a greater number of model assumptions that are not easily constrained, so we have adopted the first, simpler approach.

Minimum timescales for H_2O loss from each MI (using inclusion size and distance from crystal rim as input conditions) were calculated using the diffusion model of Cottrell et al. (2002). This model assumes a spherical MI in the center of a spherical phenocryst. In our model calculations, we chose the radius of the quartz phenocryst to be the minimum distance (rather than the average) between the actual MI and the crystal rim (measured in 2D section, online Supplement Chapter II Table 1). Thus our model-derived times are again minima.

Most MIs (~78%, n = 93) yield decompression times from <12 hours to 5 days, whereas the lowest measured H_2O concentrations (~1 wt.%) imply as long as two weeks

(Fig. 2.4a; Appendix A, Fig. 4bA). This variability reveals that HRT magma ascent was complex: single fall layers contain crystals from both faster ascending magma (<12 hours) and magma that had decompressed to varying degrees for varying times within the conduit system (days to weeks). The MI evidence for ascent times of hours to weeks for co-erupted crystals in single layers requires that magma rose and was released episodically over corresponding periods of days to weeks to generate the fall deposits studied (see Fig. 2.1, Appendix A, Fig. 1A). This interpretation finds qualitative support in the episodic deposition and periodic reworking of individual beds within the fall deposits.

To translate these diffusive loss times into ascent rates, an initial storage depth before diffusive loss began is required. An entrapment pressure for each MI can be calculated using the restored H_2O and measured CO_2 concentration (Fig. 2.4b). These pressures, which should represent the crystallization pressures of the quartz hosts, are converted into depths using a crustal density of 2600 kg/m^3. For the inclusions that experienced <12 hours of diffusive loss, ascent rates are >0.1 m/s, whereas inclusions that underwent days of diffusive loss ascended much more slowly, at apparent rates of ~0.01-0.005 m/s. These slow rates could be the result of either slow, continuous magma ascent, as occurs in dome forming eruptions (Melnik and Sparks, 1999), or more rapid ascent, with periodic stalling at shallower depths in the conduit (e.g. Cashman and McConnell, 2005, Riker et al., 2015).

It is possible that our estimated entrapment pressures overestimate the starting depth before ascent, because the CL zoning patterns of the quartz reveal a complex history for each crystal between the original time of trapping and final eruption

(Appendix A, Fig. 2A). The minimum starting depth for melt containing these quartz crystals is constrained using the pressure at which H_2O solubility is ~4 wt.%, consistent with the highest concentrations found in inclusions from each sample (Fig. 2.4). Storage at lower pressure for a week or longer would cause reequilibration to lower values (Fig. 2.4, Appendix A, Fig. 3A). The 4 wt.% H_2O solubility value corresponds to depths closer to 4 km (1000 bars; Fig. 2.4), which would (at most) reduce our estimated ascent rates by a factor of two.

The variable range of ascent rates for co-erupted quartz in the HRT fall deposits has an intriguing parallel with the activity at Mount St. Helens from May 25 to October 1980. Eruptions during this period involved lava dome formation (from June to August) punctuated by explosive episodes (Rutherford and Hill, 1993; Blundy et al., 2010). Pumices from the explosive episodes contain amphiboles with breakdown-rim thicknesses that imply residence in magma for varying durations outside the amphibole stability field during ascent. Experimental data link the range in breakdown-rim thicknesses to timescales of up to 16 days (Rutherford and Hill, 1993), equivalent to ascent rates of 0.004-0.007 m/s for effusive magma, to >0.018 m/s for magma feeding the explosive episodes (i.e., no breakdown rims present). The diversity within single clasts was interpreted to result from mixing in the conduit of slowly ascending magma (feeding dome extrusion in the MSH case) with more rapidly ascending magma (feeding explosive activity). Subsequent work using plagioclase and pumice textures reached similar conclusions for the summer 1980 explosive eruptions, whereby deeper, volatile-rich magma co-erupted with shallower degassed magma that had been stored within the conduit (Cashman and McConnell, 2005; Riker et al., 2015). Diverse H_2O contents of

plagioclase-hosted MIs from the summer 1980 explosive eruptions (Blundy et al., 2010) could also be interpreted to reflect variable amounts of diffusive loss, reflecting slow ascent and mixing processes. These ascent models can be applied to explain our HRT dataset, where in any individual layer, co-erupted quartz crystals have experienced varied decompression histories.

5.4. Final ascent rates from modeling of volatile gradients in reentrants

Melt-filled reentrants (REs) are not sealed off by crystal growth and therefore record late-stage changes in the melt surrounding the host crystal. In contrast to MIs, which experience loss of H_2O but not CO_2, REs lose both H_2O and CO_2 by diffusion to the surrounding degassing melt during ascent. As decompression causes volatile exsolution from the host melt, it creates H_2O and CO_2 gradients in the REs that can be modeled to estimate ascent timescales (Liu et al., 2007; Humphreys et al., 2008; Lloyd et al., 2014). Importantly, the HRT REs show total H_2O (molecular + hydroxyl) values that decrease outwards towards the exterior melt with relatively constant $OH^-/H_2O_{molecular}$ ratios. Secondary hydration is thus inferred to be absent as it would result in increasing $H_2O_{molecular}$ towards the mouth of the RE (Liu et al., 2007).

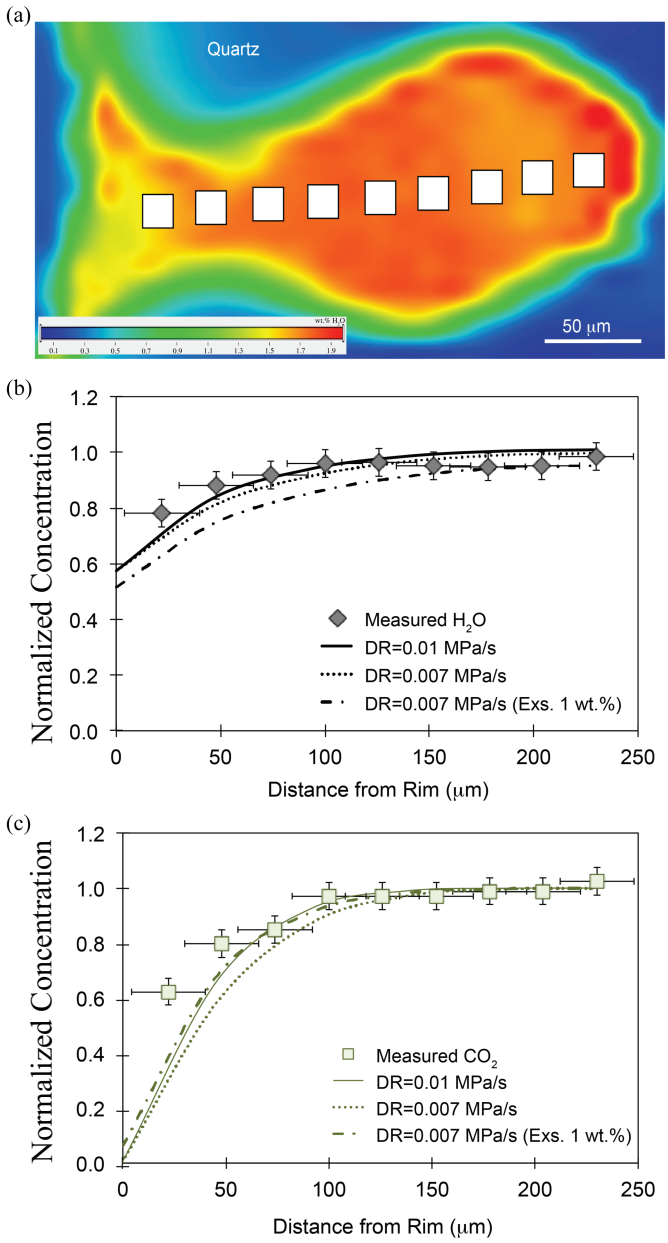

Figure 2.5. (a) H_2O concentration map for a 200-μm-long reentrant from sample MM7 (blue = 0.1 wt.% H_2O; red = 1.9 wt.%). The nine white boxes represent the FTIR aperture locations (20 x 20 μm) used for measurement of H_2O (b) and CO_2 (c) concentration profiles. Concentration profiles for ten reentrants from six units were modeled using the diffusion code of Liu et al. (2007) to constrain decompression rates (panels b and c). The first two curves in each best-fit model (solid and dotted lines) are for open-system degassing, whereas the third curve (dashed line) represents a closed-system model with 1 wt.% exsolved gas (Liu et al., 2007). Additional assumptions and boundary conditions are discussed in the text and Appendix A.

Concentration maps were measured by FTIR for 10 REs (100-280 μm in length), providing H_2O and CO_2 profiles with a spatial resolution of ~20 μm (Fig. 2.5a). Because CO_2 diffuses at a slower rate than H_2O, modeling both gradients simultaneously provides more robust constraints on ascent timescales. We compared our measured H_2O and CO_2 profiles to simulated profiles for various ascent rates calculated with a one dimensional diffusion code (modified from Liu et al., 2007), and constrained our dataset with those ascent rates that most closely reconstructed our measured profiles. REs with simple rectilinear geometries were favored for modeling. An overall homogeneity in the concentration maps for H_2O and CO_2 in the direction orthogonal to the main diffusional direction implies that a 1-D model does not introduce significant error to the calculated timescales (Fig. 2.5a).

For our model, the innermost concentrations were used as starting conditions because this assumption gave the best agreement between simulated and measured H_2O and CO_2 profiles. Using the average H_2O and CO_2 concentrations for MIs from a given sample as a starting condition or using a specific MI in the same crystal as the modeled RE both yielded poorer fits to the data. Lloyd et al. (2014) emphasized the importance of the RE having an observable bubble at its mouth in order to ensure accurate placement of the external boundary in the model calculations. The majority of our REs, however, lack such a bubble, but the glass in the REs is continuous with glass adhering to the quartz rim. We simulated profiles for which the external boundary of the RE was assumed to be coincident with the crystal rim, and another set of profiles for which the external boundary was extended 50 μm outward from the quartz rim (a realistic distance to the nearest bubble in a exsolving rhyolitic magma). Best-fit profiles were achieved using the

rim as the boundary condition. To simulate changes in the external melt H_2O and CO_2 concentrations during decompression, which are time-dependent, we used models for open-system degassing and for closed-system degassing with 1 wt.% initial exsolved gas (Fig. 2.5b,c; Appendix A, Fig. 6A).

In the model calculations, diffusion is assumed to cease at the fragmentation depth, because the timescale between fragmentation and quenching of pyroclasts in the plume is likely to be very short (see discussion in Liu et al., 2007). Estimates of fragmentation pressure for hydrous rhyolitic magmas are mostly in the range of 10-30 MPa based on H_2O contents preserved in matrix glasses (Thomas et al., 1994) and critical bubble volume fraction (Sparks, 1978; Thomas et al., 1994). Following Liu et al. (2007), we chose a single value of 10 MPa. Based on calculations for REs with a range of sizes, the uncertainty associated with the choice of fragmentation pressure introduces a factor of 1.4-1.6 variability in ascent rates (Liu et al., 2007).

Decompression rates determined from the H_2O and CO_2 profiles (Figs. 2.5b,c; Appendix A, Fig. 6A) result in estimated ascent times of <1 to 4 hours and ascent rates of ~0.3-1.5 m/s. These rates are similar to those of MIs that we infer to have experienced little to no H_2O loss (Fig. 2.4a, Appendix A, Fig. 4bA). This is consistent with our model of slowly ascending magma in the conduit being mixed with more rapidly ascending magma during punctuated, explosive eruptions. The final ascent rates for HRT magmas are notably slower than those inferred using the RE technique for moderate-sized explosive eruptions, for example, May 18, 1980 Mount St. Helens (Humphreys et al., 2008) and Fuego (Lloyd et al., 2014). The ascent rates are, however, similar to those for

of the Oruanui supereruption (Liu et al., 2007), which also shows time breaks between units in its fall deposits (Wilson, 2001).

6. Trace-element evidence for sequential tapping of discrete magma bodies

Trace element concentrations in MIs (n = 105), REs (n = 81), and obsidian pyroclasts (n = 23) measured using LA-ICP-MS techniques provide further information on onset conditions for the HRT eruption.

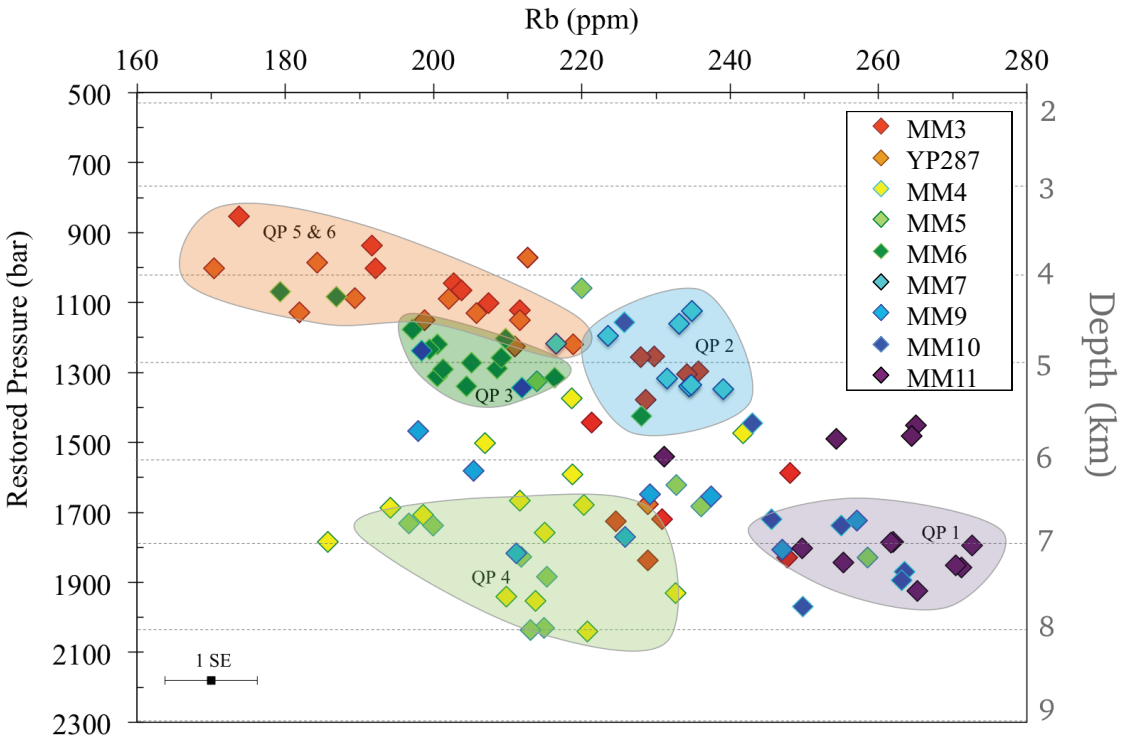

Figure 2.6. Restored pressures (from Fig. 2.4) vs. Rb for all MIs. Pressures were converted to depths using a crustal density of 2600 kg/m^3. The range in crystallization pressures is strongly controlled by the concentration of CO_2 in the MIs (Fig. 2.4). Colored fields delineate MI groups that correspond to five of the six quartz populations deduced from cluster analysis of MI compositions (see section 6.1 for details). The color of each quartz population is based on the sample that contains the majority of that quartz population. For example, sample MM11 is represented completely by quartz population 1 and therefore is noted on the figures using the same color as MM11. Although quartz populations 5 and 6 have similar storage regions and Rb concentrations in this figure, they are distinguished on the basis of their Ba and Sr concentrations (see Fig. 2.7 and Appendix A, Figs. 5A, 6A).

6.1. Trace elements in melt inclusions

Concentrations of Ba, Rb, Sr, Cl, Nb and CO_2 (among other elements) cluster the MI data into distinct groups. For example, Rb values and restored entrapment pressures group the MIs into two main storage depths and five compositional populations (Fig. 2.6). Entrapment pressures indicate that although earlier erupted samples MM10 and MM11 have the most evolved compositions and H_2O-rich MIs (Figs. 2.3, 2.4) they crystallized at greater depths (6-8 km) than MIs in the least evolved, later erupted units (samples MM3 and YP287: 4-5 km; Fig. 2.6). In addition, another MI population in sample MM3 is revealed by Rb/Zr and Ba/Sr ratios that plot along a separate evolutionary trend (Appendix A, Fig. 2.7A). These relationships demonstrate that the MI compositions cannot reflect a single zoned magma chamber. We thus infer that the unique clusters, and separate trends, represent distinct crystallizing magma domains that evolved from chemically similar parent magma(s) but were spatially separated during crystallization.

To test the robustness of multiple MI groups based on trace element data (Fig. 2.6, Fig. 2.7a, Appendix A, Fig. 7A), we used the statistical program JMP® (Version 10: SAS Institute Inc., Cary, North Carolina, 1989-2007). Variables that most clearly distinguished compositional groups (CaO, Cl, CO_2, Sr, B, Nb, Eu, Ba, Ta, and Rb) were selected for a multi-component cluster analysis. The results indicated six clusters based on MI composition. After identifying the clusters, we used discriminant function analysis to assess the significance of the results. This showed that there is only a 4% probability that a given MI would be assigned to the wrong cluster based on the ten variables that were used. We interpret the six clusters of MI composition to indicate six distinct populations of host quartz crystals (Fig. 2.7b). This evidence for six distinct quartz

populations (revealed by MI compositions) suggests that the quartz crystals in fall deposits from the onset of the HRT eruption originally formed in six chemically distinct crystallizing magma bodies.

Of the nine horizons sampled (Fig. 2.1b), some contain a mixture of the six quartz populations (samples MM3, MM4, MM5, MM9), whereas others contain crystals from only one population (samples YP287, MM6, MM7, MM10, MM11; see Fig. 2.7b). Of particular relevance is the relationship between quartz populations and stratigraphic position. Although later erupted units contain quartz crystals with similar MI compositions to the first eruptive units (e.g. quartz population 1 appears sporadically in

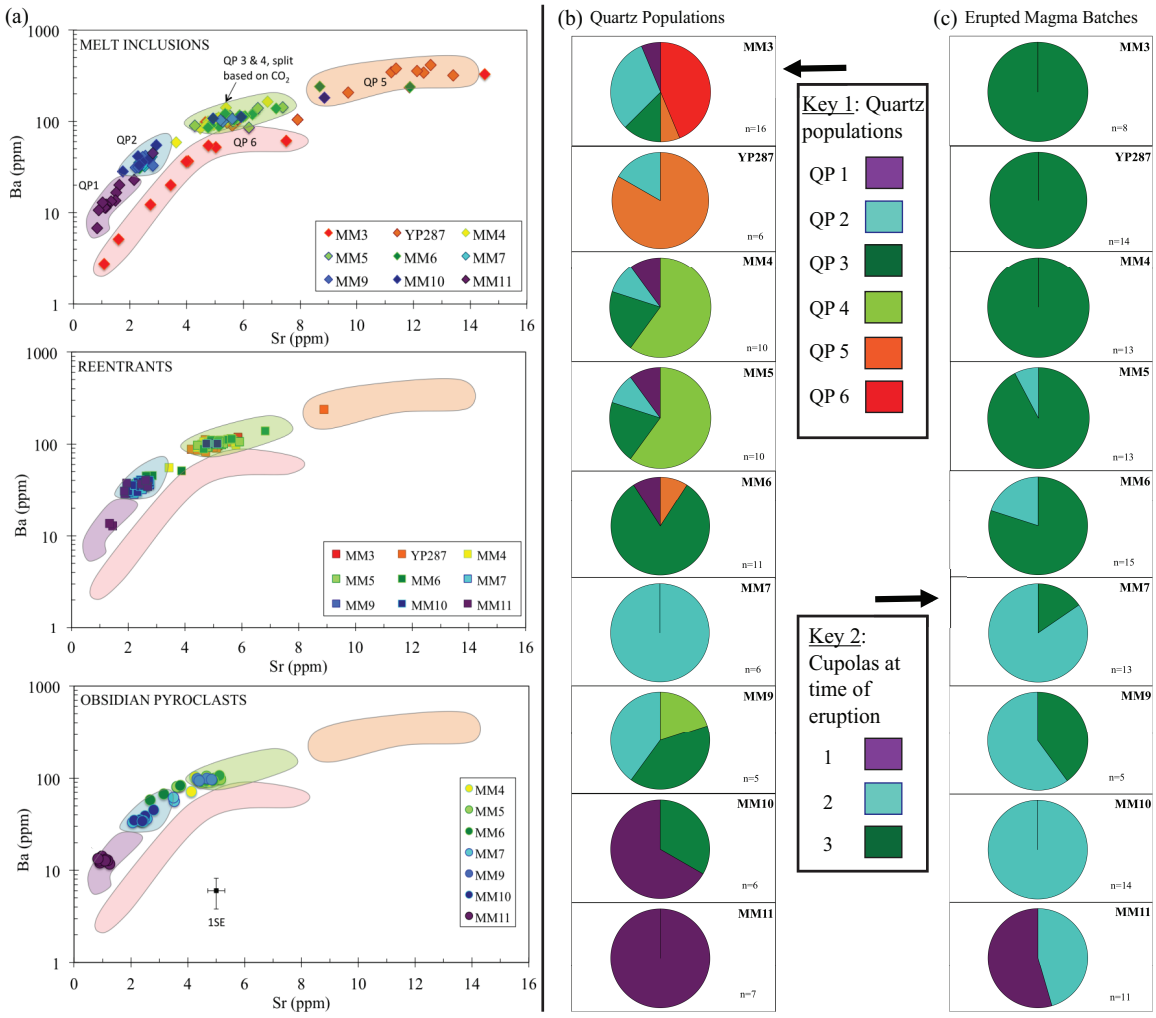

MM3-6), there is no evidence for the opposite (e.g. quartz populations 5 or 6 do not occur at levels below sample MM6; see Fig. 2.7b).

6.2. Trace elements in reentrants and obsidian pyroclasts

Here we evaluate the extent to which the six distinct magma bodies in which the quartz populations originally crystallized were still present at the time of eruption, using the compositions of REs and obsidian pyroclasts as a record of the host melts surrounding the quartz crystals on evacuation. The geochemical similarity of the obsidian pyroclasts to the RE populations in each fall deposit layer (Figs. 2.7a; and Appendix A, Fig. 8A) suggests that both pyroclasts and REs represent external, host melt compositions at the

←

Figure 2.7. (a) Concentrations of Sr vs. Ba for all melt inclusions (MIs: top panel, shown as diamonds), reentrants (REs: middle panel, shown as squares), and obsidian pyroclasts (bottom panel, shown as circles). The six quartz populations based on cluster analysis of MI compositions (as described in the text) are highlighted as colored fields in all panels. Reentrant and obsidian pyroclast compositions fall into three of the six quartz populations, suggesting that three distinct magma bodies were present at the time of eruption. Obsidian pyroclasts from MM3 and YP287 were not analyzed.

(b) Distribution of quartz populations based on cluster analysis of MI compositions (see section 6.1 for details). Each of the nine stratigraphic layers studied is shown by an individual pie diagram. The proportions of quartz in each sample that come from the six quartz populations (Key 1) are shown by colors within each pie.

(c) Distribution of compositions for REs and obsidian pyroclasts, both of which represent the host melts at the time of eruption (Key 2). The RE and obsidian compositions fall into the fields for three of the six quartz populations (see middle and lower panels in a). Each pie diagram shows the proportion of the three compositional types of REs and obsidians in a particular sampled layer. Colors for the three populations were chosen to match the colors for the quartz population whose MIs are compositionally similar to the REs and obsidians (see middle and lower panels in a). The limited overlap between the three clusters of RE and obsidian composition suggests that there were three compositionally distinct magma bodies or batches that were vented over the portion of the HRT eruption represented by our sampling (see text for discussion).

time of eruption. Of the ~81 REs analyzed, >90% fall into two distinct populations, one of which overlaps with quartz population 2, and the other appears to be a mixture of quartz populations 3 and 4 (Fig. 2.7a; Appendix A, Fig. 8A). This observation implies that much of the compositional diversity associated with the quartz populations was reduced between the time of MI entrapment and eruption, such that only two distinct magma bodies were present just before eruption. However, the obsidian pyroclasts from samples MM4-MM11 establish that a third melt, similar to quartz population 1, was also present as a distinct magma composition at the time of eruption (Fig. 2.7a). Together, the RE and obsidian pyroclast compositions establish that the six quartz populations based on MI compositions had been integrated into three distinct melt groups prior to eruption (Fig. 2.7; Appendix A, Figs. 8A and 9A). Although a collapse of melt diversity is observed in the fall deposit, more recent work has shown that diversity increases to at least 8 melt-dominate populations in the basal HRT ignimbrite A (Swallow et al., in review). Average (±1 s.d.) major and trace element compositions for melts in each of the six quartz populations and for the three melt groups present at the time of eruption are in Table 2.1.

We infer that these three melt groups represent three cupolas: chemically discrete, volumetrically minor bodies along the roof of the main magma volume that subsequently erupted to form the later ignimbrite members. However, whether the main magma volume was a unitary magma chamber or a distributed set of reservoirs of variable size (e.g., figure 15 in Cashman and Giordano, 2014) is currently under investigation (E.J.S. et al., unpublished data). As with the quartz populations (Fig. 2.7b), the proportion of material erupted from the three cupolas varies systematically with stratigraphy in the fall deposit, as follows (see Fig. 2.7c):

- Cupola 1 is represented in the first fraction of material erupted and is the most evolved and smallest in volume (dominant only in sample MM11), which was then followed by a reworking time break (Fig. 2.1). Material from Cupola 1 does not recur above the level of sample MM11 (Fig. 2.7c).
- Cupola 2 is represented in much of the material (samples MM9 and MM10) that makes up the sections between the reworked layers (Fig. 2.7c). Cupola 2 continued to be tapped up to the level sampled as MM5, but thereafter was absent. The presence of material from both cupolas 2 and 3 in samples MM9 through MM5 is inferred to represent co-deposition from two separate vents, with cupola 3 becoming dominant by the stage represented as sample MM6.
- Cupola 3 is represented in sample MM6 and above and was thus likely the largest in volume (Figs. 2.1 and 2.7; Appendix A, Figs. 8A and 9A). The vent for this cupola may have developed into a major structure as no time breaks, apart from those represented by deposition of normally graded fall layers, are inferred to have occurred before ignimbrite deposition commenced at the Mount Everts location.

7. Implications for the onset of the Huckleberry Ridge eruption

Our dataset highlights the complexity and fine-scale detail that can be associated with the initiation of a large supereruption. Six compositionally distinct magma bodies (based on quartz-hosted MI compositions) had amalgamated into three cupolas (based on RE and obsidian pyroclast compositions) by the time of eruption (Fig. 2.7, Appendix A, Figs. 8A and 9A). Melt inclusions in each stratigraphic layer sampled experienced highly variable extents of H_2O diffusive loss, requiring prolonged ascent conditions from all

eruptive vents (Appendix A, Fig. 4bA). The coherency of the RE and obsidian pyroclast glass compositions with stratigraphic position and the lack of geochemical evidence in pumice shards that the different compositions mixed or mingled within the conduit (Elliot Swallow, unpublished data) necessitates that the cupolas were erupted sequentially from separate vents, but with some degree of temporal overlap (Fig. 2.7c, Appendix A, Fig. 9A). The nature of the compositional variations and their systematic stratigraphic ordering preclude them as resulting from the chaotic mixing or tapping of a single chemically stratified, physically integrated magma body. Our results, along with the field evidence, show that the initial Huckleberry Ridge eruptive activity was episodic and prolonged, with magma slowly ascending to feed periodic explosive activity, and with time breaks manifested by contemporaneous reworking in the fall deposits.

A key question then arises: what would allow an eruption (especially one of such magnitude) to stop once started, repetitively, with similarly prolonged ascent behavior at three separate vents? The prolonged decompression with punctuated explosive events could potentially be explained by the progressive development of a fracture network that becomes increasingly connected over time to form a transport system feeding magma to the surface, as has been proposed for the 1980 Mount St. Helens and 1991 Pinatubo eruptions (Scandone et al., 2007). However, our evidence for sequential eruption of three distinct magma bodies from separate vents, along with the episodic shutting off of the plume, suggests an external control for the initiation of the Huckleberry Ridge eruption. Furthermore, the slow ascent rates inferred from the variable H_2O losses from melt inclusions require low degrees of overpressure in the feeding magma bodies (Melnik and Sparks, 1999), consistent with the start/stop nature of the initial eruptive activity. It is

important to note, though, that our data pertain only to the very initial eruption dynamics, and other factors may have become important in controlling the subsequent voluminous, caldera collapse-related parts of the eruption.

Parallels can be drawn with the 25.4 ka Oruanui eruption (Liu et al., 2007; Allan et al., 2012). The Oruanui fall deposits contain evidence for multiple eruption hiatuses (Wilson, 2001), and syn-eruptive lateral transport of a foreign magma type, which collectively are used to infer that the eruption was modulated in its early stages by tectonic mechanisms (Allan et al., 2012). Considering that several large regional faults intersect the HRT caldera area (Christiansen, 2001; Simakin and Ghassemi, 2010), we suggest that tectonic processes were the controlling factor on (and at) eruption onset. Movement along a fault-bound or dike-controlled structure would have permitted magma to ascend slowly from spatially separated locations, with intermittent eruptions controlled by changes in the stress regime (Fig. 2.8; Allan et al., 2012). The causes and effects between regional tectonic forces and those imposed by the presence of the magma body itself in causing any fault fracturing (Bursik et al., 2003; Hampel and Hetzel, 2008; Gregg et al., 2012) cannot, however, be resolved from our data. Despite this uncertainty, our combined field and geochemical approach provides some of the first time-resolved evidence for prolonged decompression at the onset of a major caldera-forming eruption, and suggests that external factors may have modulated the initial eruptive behavior.

8. Conclusions

Insights into the mechanisms and timescales associated with the initiation of caldera-forming eruptions can be revealed using geochemical data for the earliest deposits that

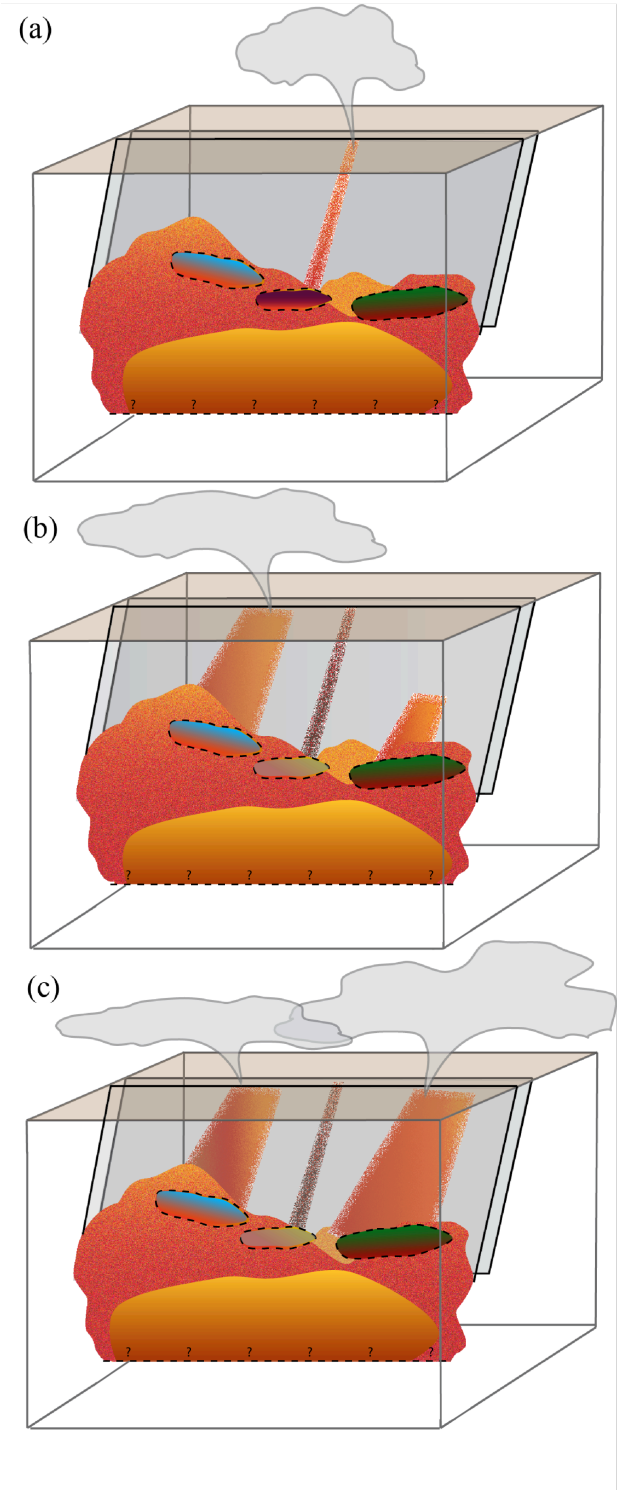

Figure 2.8. Schematic interpretation for the earliest stages of the Huckleberry Ridge eruption, with three compositionally distinct magma cupolas (colors correspond to individual cupolas, see Key 2 in Fig. 2.7c) located above a larger magma body. Each cupola was tapped sequentially (see section 6.2) in response to destabilization, likely due to tectonic processes. See section 7 for more details.

formed during eruption onset. Here we present geochemical data for the 2.5-m initial fall deposit of the Huckleberry Ridge eruption, which preserves evidence for multiple reworked layers that reflect short eruptive pauses (each on the order of days) prior to the emplacement of voluminous ignimbrite. Our results reveal evidence for three distinct magma bodies that were erupted episodically and sequentially during eruption onset, most likely from separate vents. In addition, highly variable extents of H_2O diffusive losses from melt inclusions through quartz phenocrysts provide evidence for prolonged ascent times, suggesting that the magma bodies were not strongly overpressured at eruption onset. Our evidence for sequential eruption of three distinct magma bodies, together with the start-stop nature of the eruption inferred from the deposits and comparisons with the Oruanui supereruption, suggest an external (likely tectonic) control modulated the initiation of the Huckleberry Ridge eruption. Our results reveal the complexity that can be resolved for the initiation of a large eruption, and raises the question as to whether similar evidence is present in other cases but has not been looked for. Furthermore, our work highlights a new geochemical approach for obtaining information about the immediate pre-eruptive state of magma bodies that could be applied to other systems to shed light on eruption triggering mechanisms.

9. Bridge

In Chapter II, I analyzed major and trace elements and volatiles in quartz-hosted melt inclusions and reentrants to establish quartz crystallization and storage depths and melt compositional groupings from multiple horizons in the 2.5 meter initial fall deposit beneath the Huckleberry Ridge Tuff ignimbrite member A. The wide H_2O variations

(1.0-4.7 wt.%) in melt inclusion from individual fall horizons imply as much as ~14 days of diffusive loss, reflecting highly variable and surprisingly slow decompression conditions. Water and CO_2 gradients in reentrants, however, are consistent with final ascent times of <1 to 4 hours (ascent rates of ~0.3-1.5 m/s), similar to those represented by MIs that we infer to have experienced little to no diffusive H_2O loss. To be able to test our hypothesis that start/stop behavior in the initial fall deposits prior to caldera-formation equate to low-overpressure systems, I next apply these methods to the Bishop Tuff and Oruanui eruptions. These systems were chosen because of their end member behavior (inferred through field evidence). On one end, the Bishop eruption was continuous, where fall integrated directly into flow, with no time breaks (longer than a few hours). In contrast, in the Oruanui eruption there are ten separate phases, where time breaks are inferred between the deposition of five of these phases. In Chapter III, I calculate the ascent rates from reentrants sampled through the opening stratigraphy for both the Bishop and Oruanui eruptions, and compare these results to Chapter II. These rates are then compared to those calculated using melt inclusions, taken from Chapters II and IV.

CHAPTER III

ASCENT RATES OF RHYOLITIC MAGMA AT THE ONSET OF THREE CALDERA-FORMING ERUPTIONS

This chapter is in preparation for *American Mineralogist*. I am the lead author on the paper, which involved sample preparation, analysis, synthesis of all data, development of diffusion models, and writing the manuscript. Paul Wallace (University of Oregon) served as the main advisor, aiding in data interpretation and manuscript editing. Colin Wilson (Victoria University of Wellington) helped with field sampling, data interpretation and provided feedback on manuscript drafts. James Watkins (University of Oregon) and Yang Liu (Jet Propulsion Lab) helped develop the diffusion model and aided in data interpretation.

1. Introduction to Magma Ascent Rates

The rate at which magma ascends has a strong influence on the manner in which it (eventually) erupts. Slower ascent allows degassing of volatiles from the magma, favoring a more effusive eruption, whereas fast decompression fosters volatile retention and consequently results in more explosive behavior (Eichelberger et al., 1986; Mangan and Sisson, 2000; Cashman, 2004; Castro and Gardner, 2008, Castro and Dingwell, 2009). Determining the rates at which magma ascends, and how those rates evolve over the course of an eruption, is thus important for understanding eruptive activity and improving monitoring and response for specific volcanoes (Dingwell, 1996). Furthermore, the ability to determine ascent rates through the use of erupted materials would permit reconstruction of the progression of activity associated with individual eruptions,

including historic events. Ascent rates have been estimated using experimentally determined rates of breakdown rim formation on hydrous phases, the growth of microlites in matrix melt, and bubble number densities (see review in Rutherford, 2008). However, many of these methods are more applicable to either slower ascent conditions or are heavily influenced by processes in specific regions of the conduit system (e.g. bubbles nucleating at the fragmentation front; Toramaru, 2006; Rotella et al., 2014). For large explosive rhyolitic eruptions, ascent timescales are often so short that they remain difficult to constrain with petrological tools. As a result, many studies have used theoretical and numerical conduit modeling to constrain values (5-30 m/s; see reviews by Rutherford, 2008 and Gonnermann and Manga, 2013), or used estimates based on the theoretical diffusion rates of H_2O into bubbles (0.7-5 m/s; Baker et al., 2006; Gardner, 2007). Thus our ability to determine rates for explosive rhyolitic eruptions requires the application of a speedometer that can respond quickly along the entire ascent path, until quenched on or shortly after fragmentation.

Several studies have exploited the rapid nature of volatile exsolution in response to decompression during magma ascent to estimate ascent rates (Liu et al., 2007; Humphreys et al., 2008; Lloyd et al., 2014; Myers et al., 2016; Ferguson et al., 2016). Melt-filled reentrants (REs) in phenocryst minerals are not sealed by crystal growth and therefore can record late-stage changes in the melt surrounding the host crystal, in particular those resulting in gradients in H_2O and CO_2 (and in more mafic examples, S) in the REs that can be modeled to estimate ascent timescales (Liu et al., 2007; Humphreys et al., 2008; Lloyd et al., 2014; Myers et al., 2016; Ferguson et al., 2016; Chapter II). Because pressure-dependent solubilities are well-known and precise measurements of

H_2O and CO_2 concentrations can be made, modeling of volatile profiles in REs provides opportunities for constraining ascent conditions for individual eruptions (Liu et al., 2007).

Here we present volatile data and best-fit diffusion profiles from 31 reentrants in quartz crystals from the fall deposits of three rhyolitic supereruptions for which extensive fieldwork has been previously conducted, providing a solid framework for integrating our calculated ascent rates. The main questions we investigate are: (1) do decompression rates increase with eruption intensity, as inferred from field studies?, (2) how do ascent rates evolve over the course of the eruption?, (3) are ascent rates related to inferred vent geometry, including the shift into the caldera-forming stages of the eruptions?

2. Geological background for three supereruptions

We investigated three voluminous, caldera-forming eruptions in this study (Fig. 3.1).

1. The Bishop Tuff, Long Valley, California (650 km^3 magma, 0.767 Ma), where early fall activity graded continuously into climactic eruption (Wilson and Hildreth, 1997).
2. The Oruanui eruption, Taupo, New Zealand (530 km^3 magma, 25.4 ka), which experienced a time break of months between the first outbreak and subsequent activity (Wilson, 2001)
3. The Huckleberry Ridge Tuff, Yellowstone (2,500 km^3 magma, 2.08 Ma) where the initial activity was prolonged and episodic over days to weeks (Myers et al., 2016; Wilson et al., in prep.).

Besides the variation in initial explosive behavior, both the Bishop and Oruanui eruptions exhibit a marked transition, inferred from field evidence, from a single-vent configuration

to multiple vents associated with caldera formation. Because the corresponding transition in the Huckleberry Ridge Tuff is associated with deposition of hot ignimbrite (Swallow et al., 2017, in review) and has no associated rapidly quenched fall material, no ascent rates could be constrained for the caldera-forming phase of this eruption.

In the iconic Bishop Tuff, the deposition of fall material and evolution into flow initiation is inferred to have been a continuous process, with the great bulk of the ignimbrite being emplaced coevally with continuing fall deposition. The transition from a single vent focus to multiple vents is documented from lithic evidence (Hildreth and Mahood, 1986). The changing lithic lithologies indicate shifting or multiplication of vents along the southern margin of what became Long Valley caldera, prior to a sharp onset of venting along the northern rim of the ring fracture (Fig. 3.1). This transition is manifested in the deposit by the incoming of the Glass Mountain obsidian lithics preserved towards the top of Fall Unit 8 (F8: Wilson and Hildreth, 1997). However partial collapse very likely began before F8, as roughly 2/3 of the erupted volume had already been discharged by this stage (Hildreth and Wilson, 2007). Importantly, there is no field evidence for significant (more than a few hours) depositional breaks inferred from any of the Bishop Tuff deposits.

In contrast, the Oruanui supereruption is subdivisible from the layering in its fall deposits into ten phases, where time breaks are inferred to have occurred between the deposition of five of these phases (Wilson, 2001). The most significant time break, of weeks to months, lies between the deposition of phases one and two, where significant

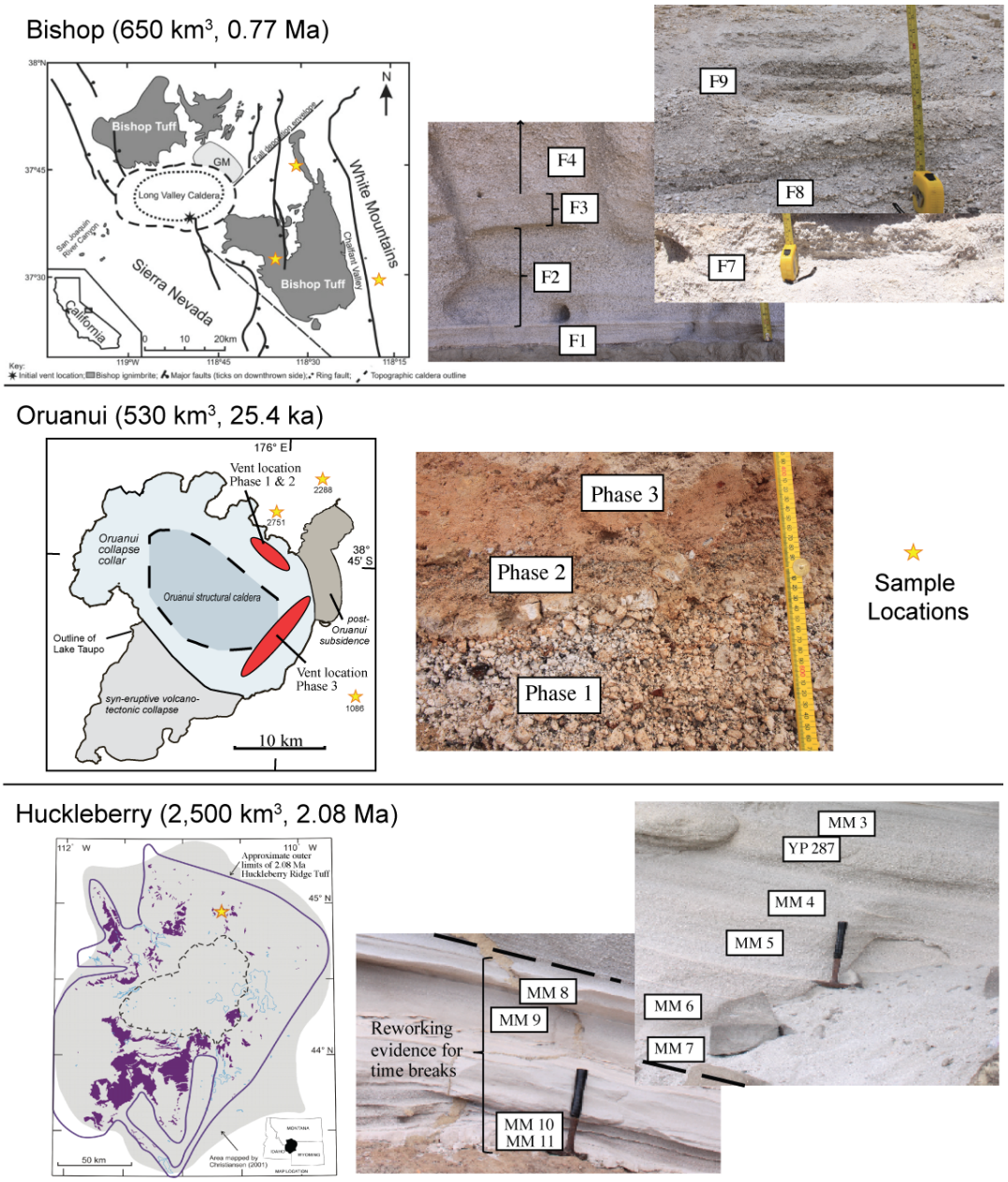

Figure 3.1. Generalized caldera outlines for the three rhyolitic supereruptions investigated in this study: Bishop (modified from Wilson and Hildreth, 1997), Oruanui (modified from Wilson, 2001), and Huckleberry Ridge (Myers et al., 2016). Stars on each map represent a sampling location, where in some cases the same fall layer was collected in multiple locations (Table 3.1). Samples were collected from several stratigraphic layers in the fall deposit of each eruption.

reworking and bioturbation of the earlier fall layer is observed (Wilson, 2001). These two phases are also associated with the co-deposition of 'foreign' biotite-bearing pumices (3%-16% of deposit) sourced from an independent magmatic system 10-15 km away (Allan et al., 2012). This laterally injected magma body suggests that the initiation of these phases was modulated through rifting along regional faults (Allan et al., 2012). The transition to caldera formation is piecemeal, however, probably starting in phase three, with a marked escalation in the volume, eruption rate and dispersal power of the eruption. Additionally, this transition is associated with a jump to an elongated vent geometry on the eastern margin of what became the caldera, perhaps reflecting an advancement of the rifting processes rather than simple caldera opening (Fig. 3.1; Wilson, 2001).

Deposits of the Huckleberry Ridge eruption are divided into three ignimbrite members (A, B and C), inferred to have originated from three separate foci within a single mapped caldera (Christiansen, 2001). Initial fall deposits erupted prior to ignimbrite member A preserve evidence in their lower parts for small-scale reworking and rain interaction, suggesting short breaks in deposition in the opening eruption stages (Myers et al., 2016, Wilson et al., in prep.). Support for this episodic eruption onset comes also from scatter in measured H_2O concentrations from enclosed melt inclusions, observed in multiple layers through the fall deposit, requiring slow ascent of initial material through the conduit system (Myers et al., 2016). In addition, the clustering of melt inclusion, obsidian and matrix glass compositions throughout the fall deposit suggests that multiple vent systems were simultaneously active and co-depositing tephra, tapping three distinct magma domains (Myers et al., 2016; Swallow et al., 2017, in review). The transition from fall to flow is marked by a striking further increase in the

diversity of matrix melt compositions appearing in the earliest member A ignimbrite, and this is inferred to represent the onset of caldera collapse in the Huckleberry Ridge eruption (Swallow et al., 2017, in review).

3. Analytical Methods

Whole pumice clasts were sampled where possible from individual layers (linked to the published stratigraphies for the Bishop and Oruanui examples) through each fall deposit. Where the grain size was too fine for individual pumices to be sampled (e.g., early Bishop Tuff, Huckleberry Ridge), loose glass-coated crystals were separated from samples of bulk fall material from distinct stratigraphic horizons (Fig. 3.1). Nine layers were sampled in the Huckleberry Ridge and Bishop fall deposits, and the first three phases of the Oruanui eruption, where some layers were thick enough to allow for multiple levels to be sampled (see details in Table 3.1). Samples were crushed (when necessary), sieved to 500-1000 μm and picked for whole, glass-coated quartz crystals. Quartz crystals were then immersed in isopropyl alcohol to aid in visual inspection under a binocular microscope. Crystals were chosen that contained a RE >100 μm in length that preserved a simple morphology, that is, a rectilinear shape with a wide mouth and lacking internal bends (Fig. 3.2, Appendix B, Fig. 1B). Selected crystals were individually mounted in crystal bond and carefully positioned to ensure intersection of the entire length of the RE (Fig. 3.2b,c). The crystals were then ground and polished to doubly expose the RE, with only those REs preserving inner and rim glass being used for analysis.

Table 3.1. Field description and locality for all samples used in this study.

Eruption	Sample Locality	Latitude/ Longtitude	Samples Collected	Outcrop Description
Bishop	Locality 25	0359400 m E, 4156400 m N	BTMM F2-5, F4-5	West side of Owens Gorge near Upper Power House penstocks. Thick section of F1 and F2, with the fall continuing to F6. Capped by ignimbrite.
Bishop	Locality 22	37°24'32.06"N, 118°29'36.75"W	BTMM F7-1 and F9-1	Chalk Bluffs. Full stratigraphy present from F1-F9, with thick ignimbrite on top.
Bishop	Locality 876	0366254 m E, 4184127 m N	BTMM F8-2	In the Blind Spring valley. Great exposure of F7 with interbedded IgE1b. F8 and F9 also sampled, with the introduction of Glass Mountain obsidian lithics.
Bishop	Locality 764	0383041 m E, 4152929 m N	BP138, BP141, BP147	On the western slopes of the White Mountains. Thick, 3 meter exposure of F9 with a thin layer of ignimbrite enclosed.
Oruanui	Locality 2288	2773700 m E 6278500 m N	Samples P1958-P1971	Punatekahi scoria quarry. Fall Phases 1-3 are found interbedded with phase flows F4 and capped by Phase 7 flows
Oruanui	Locality 2751	2770800 m E 6273900 m N	Additional sample of the P1970 and P1971 layers	Phases 1 and 2 present, with a thin ignimbrite interbedded with phase 2.
Oruanui	Locality 1086	2777000 m E 6253300 m N	P2305 whole pumices	Phase 3 present in a 100 cm thick exposed zone
HRT	Mt. Everts	44°58'19.17"N, 110°39'53.18"W	MM3-MM11	2.5 meter fine-grained fall deposit with all sampled layers present. Capped by thick, welded ignimbrite. In the first 0.5 meters there is evidence for hail impact, accretionary lapilli, low angle concentration offsets and ashy vs. crystal rich layers.

Water and CO_2 concentration maps and transects with a spatial resolution of ~20-25 μm were measured using a Thermo Nicolet Nexus 670 Fourier transform infrared (FTIR) spectrometer interfaced with a Continuum IR microscope at the University of Oregon using a computer-controlled stage. Measured absorbance peak heights were converted to H_2O and CO_2 concentrations using the Beer-Lambert law ($c_i = M_i \cdot A/\rho \cdot d \cdot \varepsilon$). In this equation, c_i is the concentration of the absorbing species, M_i is the molecular weight of the species (g/mol), A is the absorbance (height) of the relevant vibration band, ρ is the glass density (g/L), d is the thickness of the wafer analyzed (cm) and ε is the molar

absorption coefficient (L/mol·cm). Total H_2O concentration was calculated using the 3550 cm^{-1} peak. In rhyolitic compositions, ρ and ε strongly depend on total H_2O concentration. This requires the use of an iterative process to converge on appropriate values [Eq. 1 (Skirius, 1990) and Eq. 2 (Leschik et al., 2004)]:

$$\rho = 2350 - 12.6\, C_{H_2O} \quad \text{Eq. 1}$$

$$\varepsilon = 80 - 1.36\, C_{H_2O} \quad \text{Eq. 2,}$$

where C_{H_2O} is the concentration of total dissolved H_2O in wt% associated with each individual analytical spot. The absorption coefficient (ε) for molecular CO_2 (2350 cm^{-1}) in rhyolitic glass is 1214 L/mol·cm (Behrens et al., 2004). Thicknesses were measured using both a digital micrometer (±2 μm) and the reflectance interference fringe method, which allows for specific locations of the grain (e.g. interior vs. rim of each reentrant) to be measured (Wysoczanski and Tani, 2006). All H_2O and CO_2 profile concentrations and distances from rim can be found in online Supplement Chapter III Table 1.

After FTIR analysis, quartz wafers were set in a 1-inch epoxy mount for analysis of major elements using a Cameca SX-100 electron microprobe (EPMA) at the University of Oregon. Operating conditions were 15 kV and 10 nA sample current for Si, Ca, Na, Fe, Al, and K, and 50 nA current for Cl, F, Mg and Ti. A 10 μm-defocused beam was used for all analyses. Sodium, K, Si, and Al were measured first, and their concentrations were calculated using a time-dependent intensity correction in Probe for Windows (Donovan et al., 2007**)**. Glasses were then analyzed for trace elements by Laser-Ablation Inductively Coupled Plasma Mass Spectrometry (LA-ICP-MS) at Oregon State University using a 50-μm spot size, with four glass standards (GSE-1G, BHVO, ANTO, and BCR) for secondary calibration, ^{29}Si as an internal standard, and GSE-1G as

a check standard throughout the run. All major and trace element data for each reentrant can be found in online Supplement Chapter III Table 2.

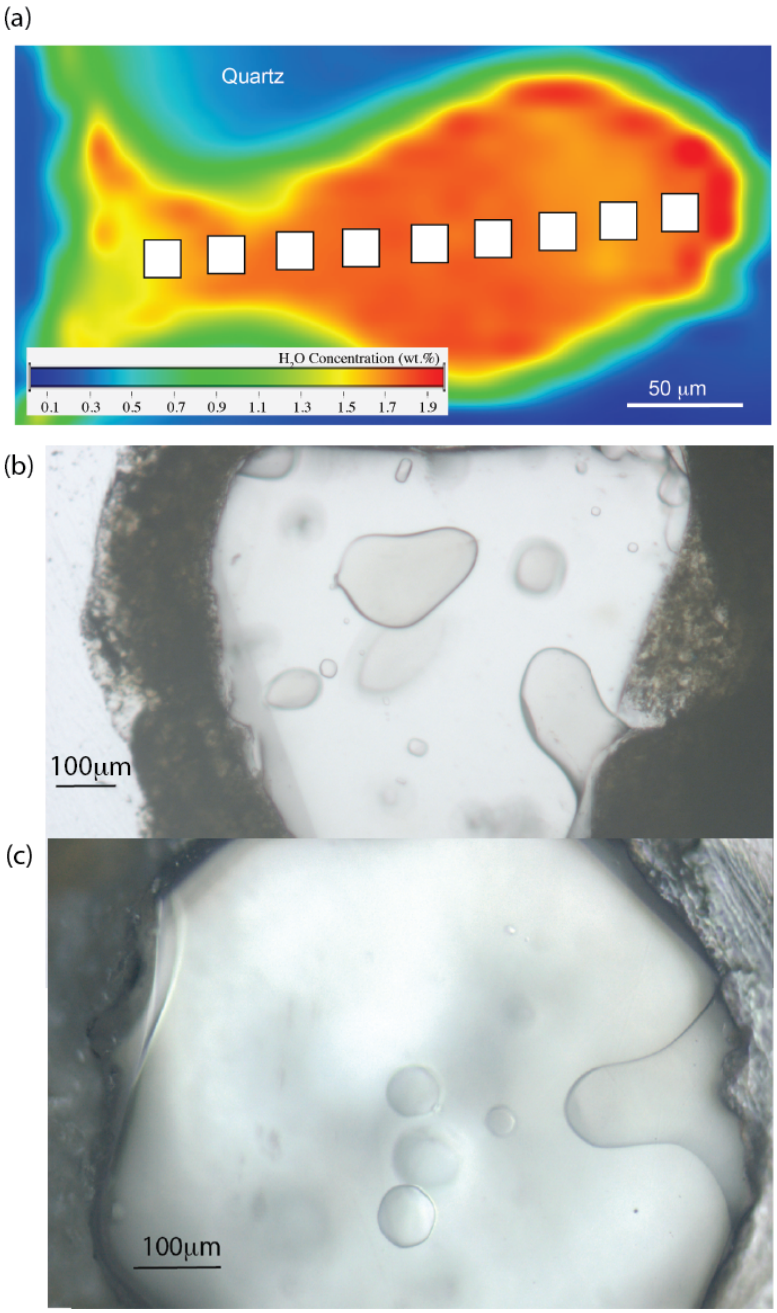

Figure 3.2. (a) A compositional map of H_2O concentration in a reentrant (open melt pocket), where white boxes (20 x 20 μm) represent the aperture size of the analyzed area. (b and c) Photomicrographs of quartz grains from the Huckleberry Ridge Tuff, where each grain contains several large melt inclusions and one large reentrant that extends out to adhering matrix glass.

4. Results

4.1 Reentrant major, trace and volatile (H_2O and CO_2) contents

All quartz-hosted reentrants (RE) from the Bishop and Oruanui deposits and Huckleberry Ridge (Myers et al., 2016) are high-silica rhyolite in composition (SiO_2 = 75-77 wt%, volatile-free). For the 31 REs analyzed for H_2O and CO_2, lengths ranged from 100-450 μm, providing 4-17 analyzed spots per RE to define profiles (Fig. 3.2, Table 3.2). The RE lengths differed by deposit, with the Bishop (100-400, median 240 μm) and Oruanui (140-450, median 255 μm) containing longer and more variable lengths compared to the Huckleberry Ridge (110-230 μm, median 170 μm). Interior volatile concentrations (H_2O and CO_2) of the REs range as follows: Bishop H_2O = 2.6-5.3 wt%, CO_2 = 18-240 ppm; Huckleberry Ridge H_2O = 1.8-3.4 wt%, CO_2 = 50-450 ppm; and Oruanui H_2O = 1.9-3.9 wt%, CO_2 = 40-100 ppm (Fig. 3.3).

Many REs from Bishop and Oruanui have interior H_2O and CO_2 concentrations that are lower than enclosed melt inclusions (MIs) in quartz from the same deposits, though there is some overlap (Fig. 3.3). In contrast, for Huckleberry Ridge, there is complete overlap between RE interior and MI values, but this is largely a reflection of the wide range of MI H_2O values (Myers et al., 2016). Enclosed MIs acquire a certain H_2O and CO_2 concentration at the time of trapping. However, the H_2O concentration can be modified by diffusion of H through the host quartz post entrapment (Qin et al., 1992; Severs et al., 2007), which can occur during long-term storage and/or slow ascent towards the surface (Myers et al., 2016). Thus, MIs with lower H_2O concentrations at a given CO_2 content could be the result of diffusive loss, and the highest H_2O values likely reflect the H_2O of the melt inclusion after prolonged storage at high temperature in a

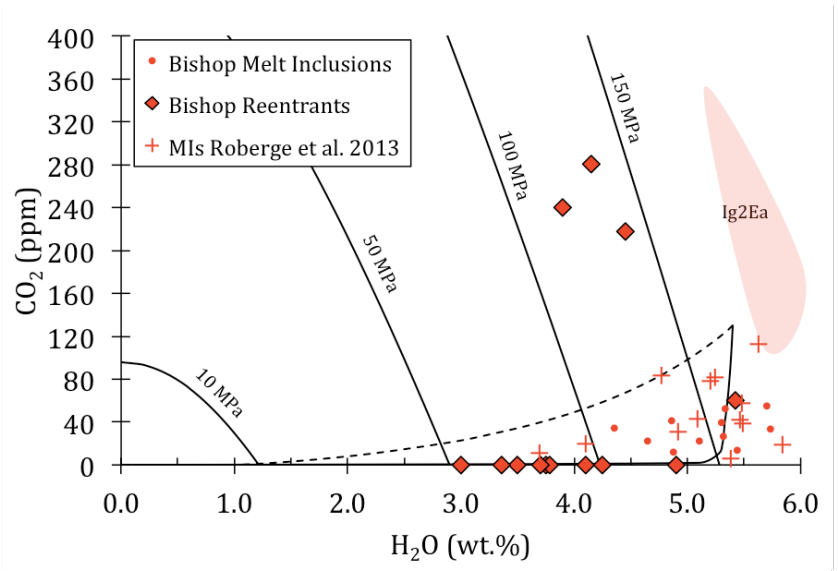
Bishop Melt Inclusions
Bishop Reentrants
MIs Roberge et al. 2013
10 MPa
50 MPa
100 MPa
150 MPa
Ig2Ea
CO2 (ppm)
H2O (wt.%)

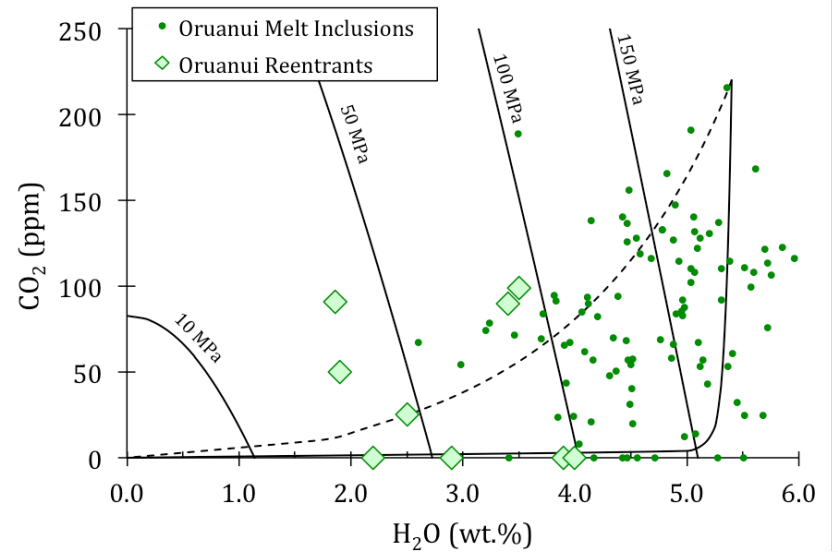
Oruanui Melt Inclusions
Oruanui Reentrants
10 MPa
50 MPa
100 MPa
150 MPa
CO2 (ppm)
H2O (wt.%)

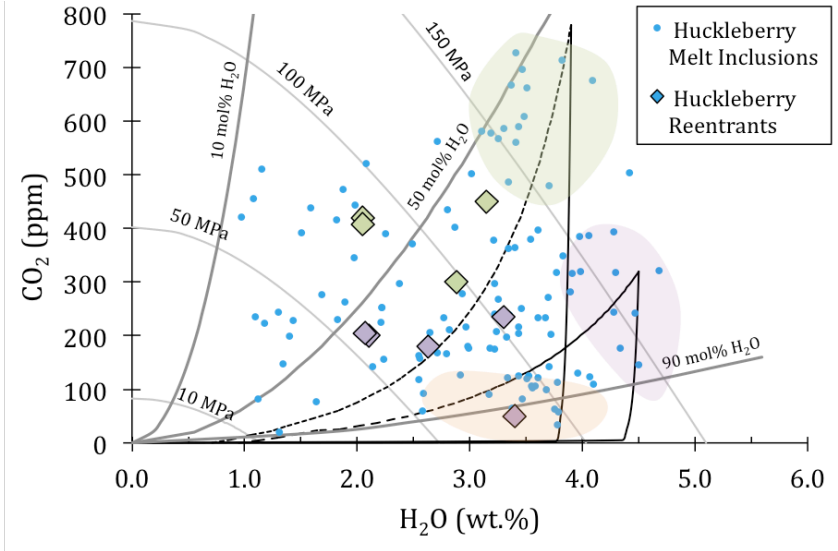
Huckleberry Melt Inclusions
Huckleberry Reentrants
10 mol% H2O
50 mol% H2O
90 mol% H2O
10 MPa
50 MPa
100 MPa
150 MPa
CO2 (ppm)
H2O (wt.%)

magma body but before ascent to the surface during eruption. Of the three eruptions studied, the Bishop MIs show the least effects of diffusive H_2O loss during ascent (i.e., the least variation in H_2O for a given CO_2 content), Huckleberry Ridge shows the most, and Oruanui is intermediate between the two (see Fig. 3.3; Chapter IV). Interestingly, only the Bishop fall deposits have interior RE concentrations that extend back to the MI H_2O and CO_2 concentrations that likely represent the storage conditions for MIs before ascent began (Fig. 3.3).

All measured profiles presented here preserve gradients of H_2O and CO_2 (when present) towards their mouths, with longer REs occasionally showing more variability in their interiors (online Supplement Chapter III Table 1, Appendix B, Figure 3B). There were four REs, sampled from the upper portions of the Huckleberry Ridge (sample MM3, RE=1) and Bishop (sample BTMMF9-1, RE=3) eruptions that have much flatter profiles of H_2O vs. distance. These REs were sampled from fall deposit layers directly beneath thick ignimbrite (Table 3.1). We interpret these flatter profiles to be the result of post-depositional heating of the fall deposit by ignimbrite (e.g., Wallace et al., 2003), which

←

Figure 3.3. H_2O vs. CO_2 concentrations for melt inclusions, shown as circles, and reentrants, shown as diamonds, from the Bishop (top panel), Oruanui (middle panel) and Huckleberry Ridge (bottom panel) tuffs. Additional melt inclusion data to compliment our F1 dataset is plotted for the Bishop Tuff fall layers F2-F9, shown as plus signs, from Roberge et al., (2013), and a red field for middle Bishop melt inclusions, sampled from Ig2Ea (Wallace et al., 1999). Light gray lines are isobars (bars of constant pressure), black solid lines are open-system degassing trends, and black dashed lines represent closed-system degassing with 3 wt.% exsolve vapor phase (Newman and Lowenstern, 2002). Vapor composition isopleths (in mol% H_2O) are shown as bold gray lines. For the Huckleberry Ridge tuff (bottom panel), colored regions represent distinct melt clusters, inferred to represent compositionally distinct starting regions (Myers et al., 2016) for associated reentrants (colored to match starting region).

allowed for continued H_2O diffusion to occur. Although the ascent rates calculated from these REs were not used in final figures, their profiles are displayed in italics in online Supplement Chapter III Table 1.

Three REs from the Bishop fall deposit (F9), sampled in a location where no overlying ignimbrite was deposited, have normal H_2O profiles and contain CO_2 contents between 220-280 ppm, higher than all MIs measured from the earlier parts of the fall deposit. These F9 CO_2 contents extend to slightly higher values than are found in F9 melt inclusions but overlap with the high end of the range for coeval Ig2Ea ignimbrite and the low end of the range for late Bishop Tuff (Wallace et al., 1999; Roberge et al., 2013). Fourteen of the 31 REs measured have no measureable CO_2. These are all from the early Bishop and Oruanui deposits, in which CO_2 concentrations in co-erupted, fully enclosed MIs are relatively low (maximum CO_2: early Bishop F1-F8 120 ppm, Oruanui 200 ppm, Fig. 3.3) compared to those of the Huckleberry Ridge (maximum CO_2 800 ppm, Fig. 3.3). The H_2O and CO_2 profiles from REs in the Huckleberry Ridge initial fall deposits were previously published and discussed (Myers et al., 2016). In this paper, we present refined ascent rates for these REs using the modified ascent code presented below so the results can be directly compared with values deduced for Bishop and Oruanui samples.

4.2 Modeling of diffusive loss of H_2O and CO_2 from reentrants

We used a 1-D forward diffusion numerical model modified from Liu et al. (2007) for fitting the measured H_2O and CO_2 profiles in each RE. In the Liu et al. (2007) model, H_2O and CO_2 diffuse through a melt-filled reentrant in response to changing external boundary conditions chosen to simulate magma decompression. Diffusion is

assumed to be negligible once the sample has reached the fragmentation level, because the timescale between fragmentation and quenching of pyroclasts in the plume is likely to be very short (Liu et al., 2007). Estimates of fragmentation pressure for hydrous rhyolitic magmas are in the range of 10-30 MPa based on the vesicularities of pumice clasts and H_2O contents preserved in matrix glasses (Thomas et al., 1994; Gardner et al., 1996; Klug and Cashman, 1996) as well as critical bubble volume fraction (Sparks, 1978). Although fragmentation pressure may fluctuate during the course of an eruption (Melnik and Sparks, 2002; Dufek and Bergantz, 2005), we chose a constant value of 10 MPa for all analyses.

The boundary condition at the contact between the host melt and the rim of the RE is based on the melt H_2O and CO_2 solubility at a given pressure, assumed to be in equilibrium with the gas bubbles present in the melt outside the crystal (Liu et al., 2007). Solubilities come from the temperature- and pressure- dependent H_2O and CO_2 solubility relationships developed in Liu et al., (2005). One requirement to ensure that equilibrium exchange of volatiles between the rim of the RE and external melt is maintained is visual confirmation of a bubble wall at the mouth of each RE (Lloyd et al., 2014). Although bubbles were noted at the mouths of Bishop and Oruanui REs (Appendix B, Fig. 1B), they are less frequent on those from the Huckleberry Ridge. However, we have shown (see Myers et al., 2016) that using the glass adhering to the quartz rim as the exterior boundary position for these REs provides the best fit to measured profiles.

We created a Matlab version of the 1-D decompression model of Liu et al., (2007). The diffusivity of CO_2 in rhyolitic melt as a function of temperature, pressure and water content was updated using Zhang et al., (2007). The updated CO_2 diffusivities result in

decompression rates that are up to 1.2 times faster than those calculated by Liu et al., (2007) (see Appendix B, Fig. 2B and online Supplement Chapter III Table 3B). For each model run the H_2O and CO_2 profiles produced from the specified starting concentrations, exsolved gas content and decompression rate are then compared with FTIR measured profiles. The most likely starting pressures are constrained either from co-genetic melt inclusion H_2O and CO_2 measurements or the volatile concentrations at the innermost part of the RE analyzed. The RE profiles tend to plateau in the RE interior, suggesting that the plateau values represent the starting H_2O and CO_2 conditions at the time of final ascent. However, to further evaluate the results from both starting conditions (MI or RE interior), we model both scenarios, discussed in further detail later in the paper.

By comparing our measured H_2O and CO_2 profiles to simulated profiles for various decompression rates we can constrain those ascent conditions that most closely reconstruct our measured profiles. Because CO_2 diffuses at a slower rate than H_2O, modeling both gradients simultaneously provides more robust constraints on ascent timescales. However, as previously noted, 14 out of the 31 REs measured, (all from Bishop and Oruanui deposits) have no measureable CO_2, and were thus modeled based solely on their H_2O profiles. The significance of the absence of CO_2 is discussed in greater detail later in the discussion section. All models were run assuming constant decompression rate and isothermal conditions, with temperature estimates as follows: Bishop 740 ºC, Oruanui 780 ºC, and Huckleberry Ridge 800 ºC (see Appendix B for discussion).

To ensure that a best-fit profile was achieved, we added an iterative grid-search function to optimize fitting of the measured profiles. This iterative function allows the

user to define a range of plausible decompression rates and initial exsolved gas concentrations, which the model cycles through. After each ascent simulation with one set of input parameters, the chi-squared error representing the goodness of fit between the modeled profile points and the measured concentrations is calculated using:

$$\chi^2=[((H_2O_{mod}-H_2O_{meas})/error_{H2O})^2+((CO_{2mod}-CO_{2meas})/error_{CO2})^2]/n \quad \text{Eq. 3}$$

in which H_2O and CO_2 species are weighted according to their analytical uncertainties and n is the number of measured data points. For all model runs presented in this paper, we used a standard deviation error for H_2O of ±0.2 or 0.3 wt% and for CO_2, ±20 or 30 ppm (specified in Table 3.3).

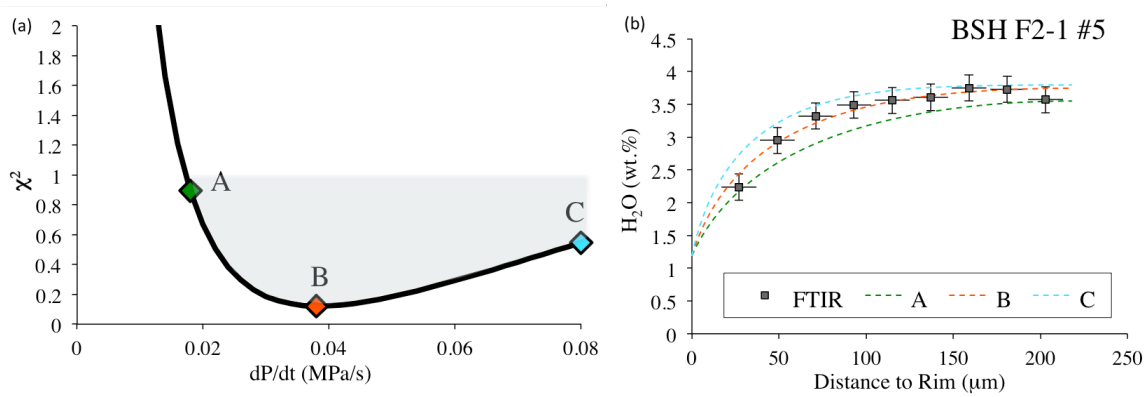

Figure 3.4. (a) Chi-squared misfit plot for a range of decompression rates. All decompression rates in the shade region, between 0.018-0.1 MPa/s produce a profile that is deemed acceptable valid χ^2 <1. (b) The three profiles produced from the decompression rate associated with misfit points A, B and C shown in (a). Profile 'B' represents the best-fit profile for the H_2O measurements, although A and C also represent acceptable fits, based on error bars.

A similar method was employed by Ferguson et al. (2016) for their analysis of fit to olivine-hosted basaltic REs from Kilauea volcano, Hawaii. After all simulations have been run, the decompression and exsolved gas concentration that produces the lowest misfit (χ^2) is taken as the best-fit profile. The model results are most sensitive to the decompression rate (*dP/dt*). Although in most model runs a range of decompression rates

yields χ^2 values that indicate acceptable fits (see *dP/dt* error bar values in Table 3.2), profiles from these decompression rates produce slopes that are visually poorer fits for the data than those produced by the best-fit decompression rate (Fig. 3.4). This is because the range of decompression rates that fit the data is strongly controlled by the analytical uncertainties of the H_2O and CO_2 measurements.

4.3 Best-fit ascent rates

Using the H_2O and CO_2 concentrations in the interiors of the REs as starting conditions, best-fit decompression rates for the 31 REs modeled range from 0.003-0.5 MPa/s (Table 3.3). These decompression rates were converted into ascent rates using the difference between the starting pressure, based on H_2O and CO_2 solubility relationships, and the fragmentation pressure, which was assumed to be 10 MPa. Starting and ending pressures were converted to depth using a mean crustal density of 2,600 kg/m^3. Best-fit profiles for all REs yield ascent rates between 0.13-16 m/s, ranging over two orders of magnitude (Fig. 3.5). However, the majority (75%) of ascent rates are between 0.7 and 10 m/s. Our ascent rates based on REs overlap with estimates based on the theoretical

→

Figure 3.5. Ascent rates modeled for individual reentrants, shown as diamonds, positioned according to their relative stratigraphic level within each eruption. The bottom of each diagram represents the earliest erupted material. Diamonds containing an X represent reentrants that lacked measurable CO_2, meaning ascent rates were constrained by modeling H_2O only. Shaded fields represent estimated ascent rates for rhyolitic magma based on alterative models. The blue field represents the ascent rate associated with the theoretical time it takes for H_2O to diffuse into a bubble, with estimates between 0.7 and 5 m/s (Baker et al. 2006; Gardner 2007). The yellow field is an analytical model for rhyolitic magma ascent, providing ascent rates of 5-8 m/s (Papale et al. 1998). The red region, with rhyolitic ascent rates estimated between 5-30 m/s, comes from conduit flow models (Mastin 2002, 2005).

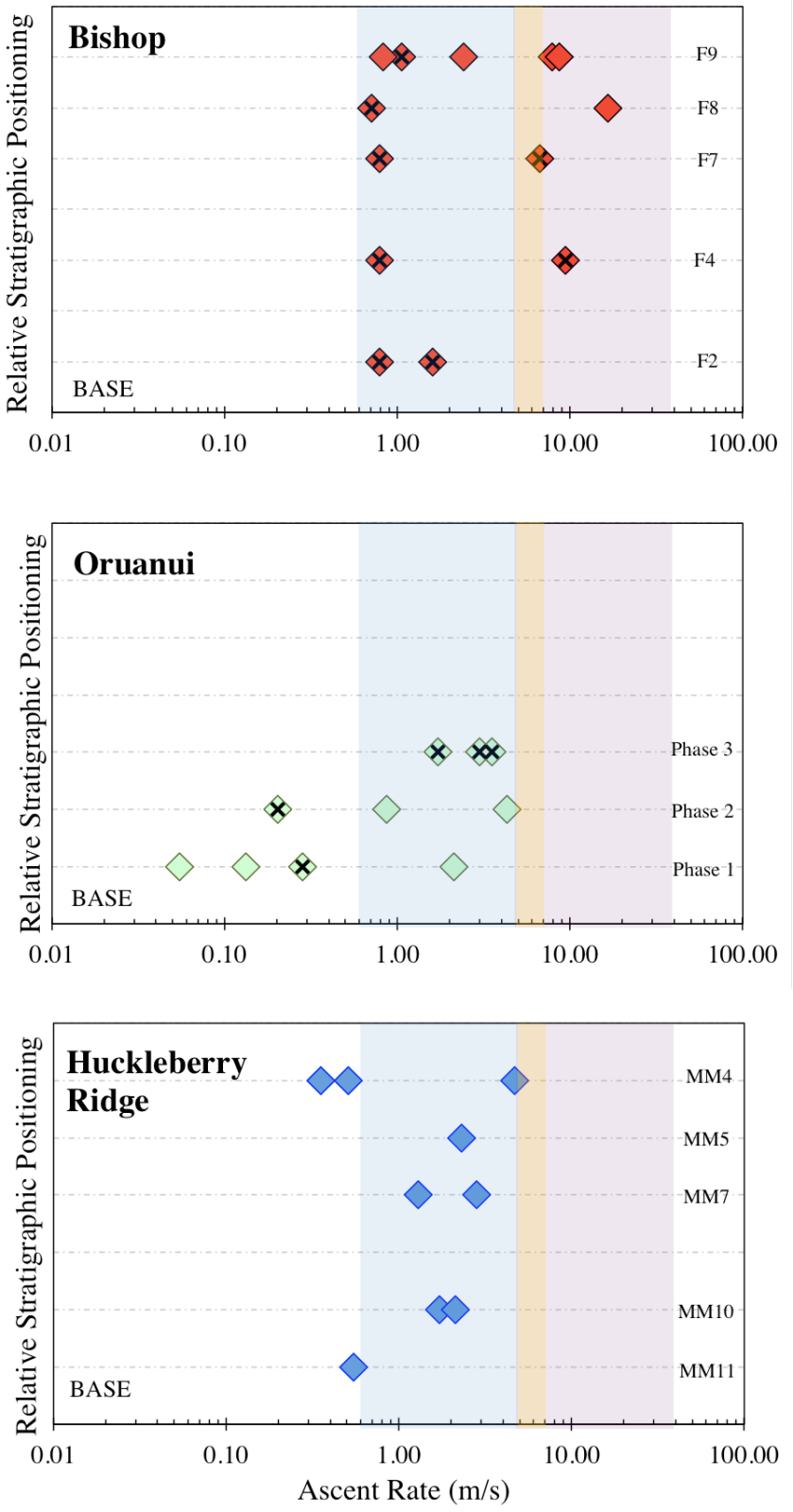
Bishop
F9
F8
F7
F4
F2
BASE
Relative Stratigraphic Positioning
0.01
0.10
1.00
10.00
100.00
Oruanui
Phase 3
Phase 2
Phase 1
BASE
Relative Stratigraphic Positioning
0.01
0.10
1.00
10.00
100.00
Huckleberry Ridge
MM4
MM5
MM7
MM10
MM11
BASE
Relative Stratigraphic Positioning
0.01
0.10
1.00
10.00
100.00
Ascent Rate (m/s)

diffusion rates of H_2O into bubbles (0.7-5.0 m/s; Baker et al., 2006; Gardner, 2007), and are similar, albeit on the lower end, to values based on analytical and numerical models of conduit flow (5-30 m/s; Papale et al., 1998; Mastin, 2002, 2005).

For the Oruanui eruption, average ascent rates increase upwards through the stratigraphy (Fig. 3.5). For the Bishop and Huckleberry Ridge eruptions, however, there is no strong up-section variation in ascent rate (Fig. 3.5), but for Bishop, there is an increased number of faster ascent rates higher in the stratigraphy. Our results show that faster ascent rates are associated with higher RE interior pressure and RE rim equilibration pressure (Fig. 3.6). The ascent rates yield magma ascent times as short as tens of minutes to as long as 2.5 hrs. The fastest ascent rates are found in the upper parts of the Bishop fall deposit, coming from depths as deep as 5.5 km (170 MPa), and the slowest rates (0.13-0.28 m/s) are from the earliest phases of the Oruanui. For the Oruanui eruption, notably slow ascent rates are associated with the initial two phases, but ascent rates are higher for phase three of the eruption (Fig. 3.5).

5. Discussion

5.1 Ascent rates and eruption characteristics

Similar ascent rates are observed in the initial fall deposits from all three systems (Fig. 3.5). This suggests that although the eruptions had differences in initial behavior, inferred from field evidence (start/stop vs. continuous activity), the differences do not correspond to systematic differences in magma ascent rates. However, as noted above, the third phase of the Oruanui eruption lacks the very slow ascent rates that are observed in the first two phases. These first two phases of this eruption had relatively weak

eruption styles, were separated by a break of weeks to months, and have been linked to an external rifting event (Wilson, 2001; Allan et al., 2012). Importantly, the transition from phases one and two to phase three was associated with a shift from a focused vent at the northeastern margin of what became the caldera to an elongate vent geometry on the eastern edge (Wilson, 2001). The association of faster ascent rates with a wider vent and inferred escalation in eruption intensity suggests that final ascent rates, in general, may be more closely related to the vent geometry and mass flux than the overpressure within the feeding magma body (see review by Jaupart, 1996). For the Bishop Tuff, the fastest ascent rates (~10 m/s) occur in several of the upper fall layers (F4, F7, F8 and F9). However, there are no strong changes at the onset of Glass-Mountain-derived obsidian lithics (F8), when there was significant migration of vents, likely associated with caldera ring fracture development. During this period of the Bishop eruption, fall and flow activity may have been from separate and evolving conduits (Wilson and Hildreth, 1997), which would complicate or obscure a record of any relationships between ascent rate and changes in conduit and vent configuration.

A key result of Figure 3.6 is that faster ascent rates are associated with deeper starting depths, as inferred from the interior H_2O and CO_2 concentrations of REs. Interestingly, the melt at the mouths of REs preserve a record of greater apparent quenching depths for REs that experienced higher ascent rates (Fig. 3.6). This suggests one of two things: (1) our assumption of a constant fragmentation pressure (10 MPa) is incorrect, and instead the fragmentation level became deeper as the eruption progressed, or (2) for REs that experienced faster ascent, there was a greater extent of disequilibrium between the melt outside the crystal and the melt at the mouth of the RE. These REs

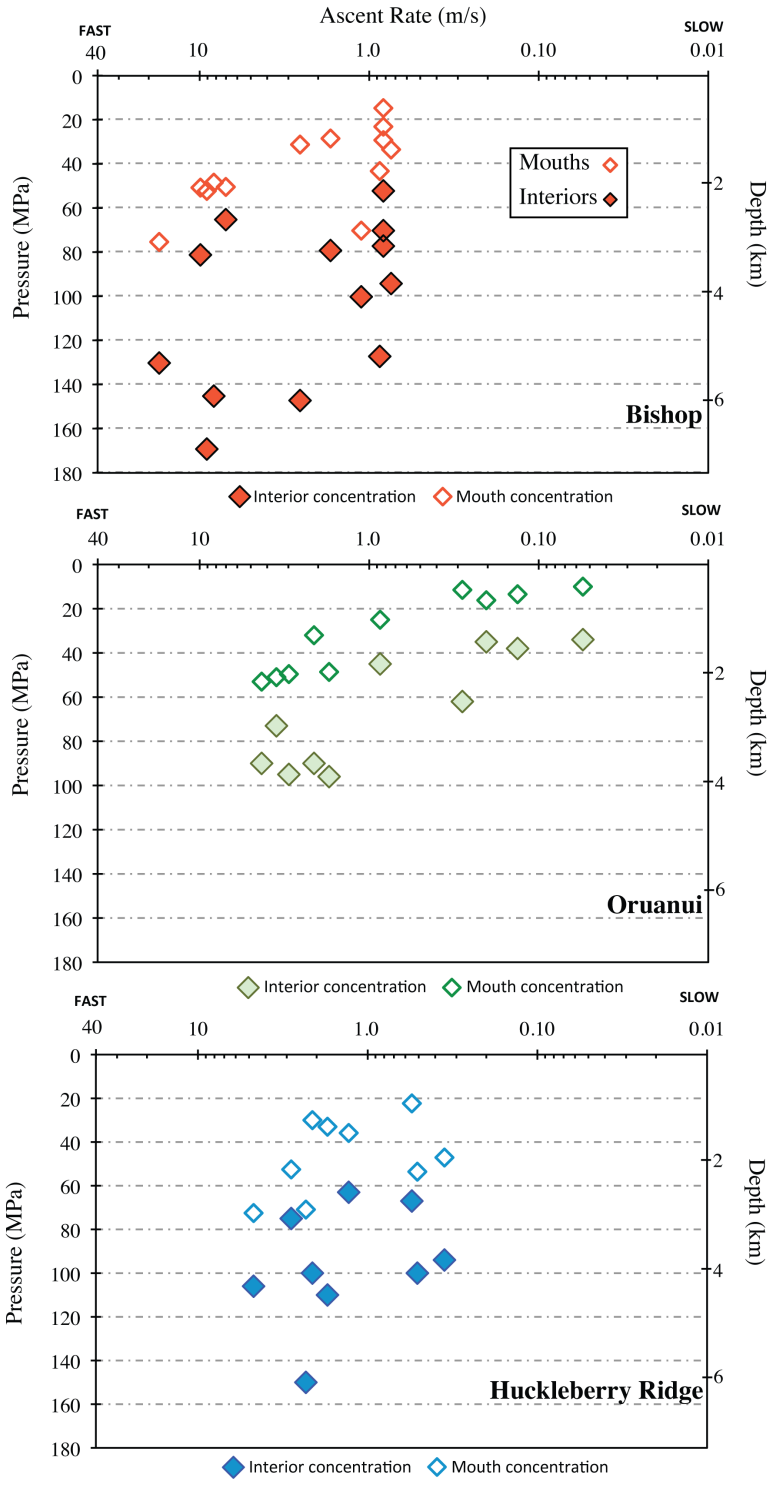

Figure 3.6. Ascent rate vs. pressure and depth for individual reentrants (diamonds). Pressures are based on the vapor saturation pressure associated with H_2O and CO_2 concentrations measured at the mouth of the reentrant (open diamond) and the interior of the reentrant (filled diamond). Pressures were converted to depths using a crustal density of 2600 kg/m^3.

likely are reflecting the development of the conduit system, perhaps due to vent enlargement due to conduit erosion (e.g. Oruanui: Wilson, 2001) or through additional vents activating (e.g. Bishop: Hildreth and Wilson, 2007 and Huckleberry Ridge: Myers et al., 2016), allowing for magma to ascend faster to the surface.

5.2 Evidence for a two-stage decompression history

One notable observation from our dataset is the significant offset between the starting pressures associated with the RE innermost H_2O and CO_2 concentration and the deeper pressures associated with the pre-eruptive storage depth of co-erupted MIs (Fig. 3.3; Fig. 3.6). We found that the best fits to the RE volatile concentration profiles were achieved when using the innermost RE concentrations, which tend to plateau to constant values as the starting condition (Appendix B, Fig. 3B). In contrast, when the initial H_2O and CO_2 concentrations of MIs were used as starting conditions, the chi-squared misfits were found to be 1.5-15x worse for all but four REs (Table 3.3). Although ascent rates associated with using MIs as starting conditions are consistently slower than those calculated using the RE interior concentrations, and provide poorer fits, all estimates fall within a factor of 6 (Fig. 3.7). The extent of this variation is significantly less than the 2 orders of magnitude represented by the entire RE ascent rate dataset (Fig. 3.5). This observation emphasizes that fitting of a volatile profile(s) is not particularly sensitive to the starting conditions but rather the concentration gradients.

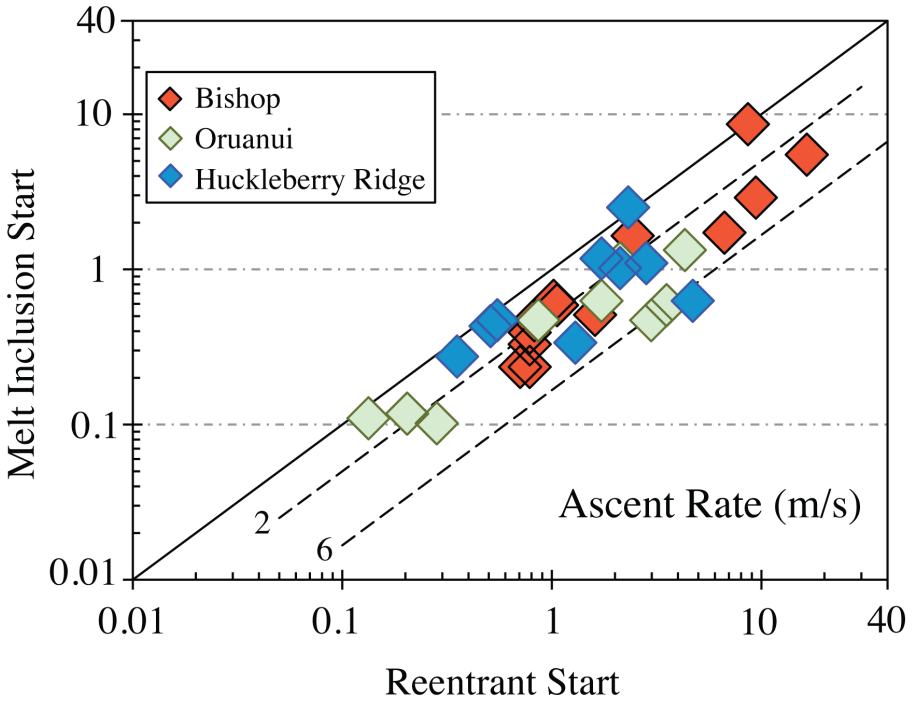

Figure 3.7. Comparison between the ascent rate (m/s) calculated using the melt inclusion concentration as the starting conditions, verses using the concentrations of H_2O and CO_2 measured at the interior. Solid black line represents a 1:1 comparison, with dashed lines representing the extent of offset between the two starting conditions as factors of 2 and 6.

In the 28 scenarios where the interior RE concentrations provide better starting conditions for the measured profiles (i.e. produce gradients that are better fits to the measured data points), a mechanism is then required to explain the shallower starting depths, and associated H_2O and CO_2 concentrations, compared to the values for MIs. We interpret this offset to suggest that there was a deeper, and initially slower, decompression period experienced by the REs, which allowed them to partially or fully reequilibrate with external melt prior to final, more rapid ascent (Fig. 3.8). A similar explanation was called upon to explain the large variation in H_2O concentrations measured in MIs from the initial fall deposit of the Huckleberry Ridge supereruption (Myers et al., 2016). In Myers et al. (2016), the wide H_2O variations (1.0-4.7 wt.%)

measured within individual fall horizons from Huckleberry Ridge was interpreted to represent variable loss of H by diffusion through the quartz host during slow decompression or shallow storage that led to degassed melt surrounding the quartz. We interpret the offset recorded by interior RE plateaus from those MIs that represent storage conditions to represent additional support for this process, where partial reequilibration occurred during extended time within the conduit system. In this interpretation, the measured RE volatile gradients near the outlets of REs are recorders of the faster, final ascent rate, but do not represent the entire ascent history of a given host crystal (Fig. 3.8).

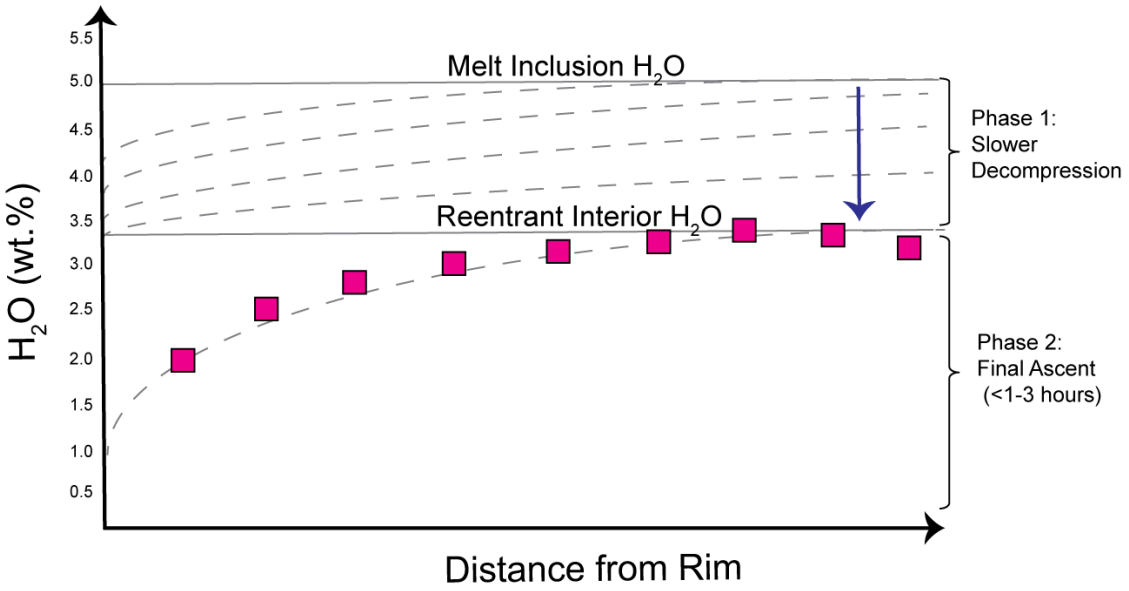

Figure 3.8. Simplified visualization of the offset between melt inclusion starting conditions and those preserved by the flat plateau of the reentrant gradient (shown as squares). Phase 1 represents the initial slower decompression that allows for a reentrant to preserve a starting solubility condition that is lower than the melt inclusion. Phase 2 then involves the timescale associated with creating the gradient that is then measured in the reentrant.

The use of a two-stage decompression model was similarly required to model the H_2O, CO_2 and S profiles measured from four mafic REs in olivine from the October 17th, 1974, steady eruption of Volcan de Fuego, Guatemala (Lloyd et al., 2014). Although

good fits could be achieved for their H_2O and S profiles using a constant decompression model starting from the MI storage region, to also accurately model the CO_2 profiles, an initial slower decompression period between MI storage and a shallower depth was found to be necessary.

Table 3.2. Description of the 31 reentrants analyzed in this study, including information on sampling location and stratigraphy, reentrant length, and interior reentrant volatile concentrations.

Reentrant Name	Eruption	Sample Locality	Fall Layer^	Temp	Length of Reentrant	FTIR Inner H_2O (wt.%)	FTIR Inner CO_2 (ppm)	Interior Pressure* (MPa)	Rim Pressure* (MPa)
BT F2-5 RE #3	Bishop	Locality 25	F2	740	220	3.5	0	73	26
BT F2-5 RE #1	Bishop	Locality 25	F2	740	240	3.75	0	82	31
BT F4-5 RE #10	Bishop	Locality 25	F4	740	90	3.78	0	84	54
BT F4-5 RE #4	Bishop	Locality 25	F4	740	180	3	0	55	17
BTF7-1 RE #4	Bishop	Locality 25	F7	740	110	3.36	0	68	53
BTF7-1 RE #2	Bishop	Locality 22	F7	740	260	3.7	0	80	32
BTF8-2 RE #1	Bishop	Locality 876	F8	740	120	4.9	0	133	78
BTF8-2 RE #2	Bishop	Locality 876	F8	740	400	4.1	0	97	36
BTF9-2 RE #2	Bishop	Locality 876	F9	740	330	4.2	281	148	51
BTF9_138 RE #2	Bishop	Locality 876	F9	740	170	4.5	218	150	34
BTF9_141 RE #1	Bishop	Locality 764	F9	740	240	4.3	0	103	73
BTF9_141 RE #2	Bishop	Locality 764	F9	740	300	3.9	240	130	46
BTF9-2 RE #1	Bishop	Locality 764	F9	740	120	5.42	60	172	55
P1963-6 RE #1	Oruanui	Locality 2288	F1	780	220	1.86	91	38	13
P1968 BB2 RE #1	Oruanui	Locality 2288	F1	780	450	2.9	0	62	11
P1968-1 RE #5	Oruanui	Locality 2288	F1	780	240	3.4	90	90	32
P1970-A RE #6	Oruanui	Locality 2751	F2	780	160	3.5	99	90	53
P1971-3 RE #1	Oruanui	Locality 2751	F2	780	220	2.2	0	35	16
P1971-3 RE #2	Oruanui	Locality 2751	F2	780	140	2.5	25	45	25
P2305-D RE #1	Oruanui	Locality 1086	F3	780	270	3.9	0	95	50
P2305-E RE #1	Oruanui	Locality 1086	F3	780	310	4	0	96	49
P2305-F RE #1	Oruanui	Locality 1086	F3	780	310	3.3	0	73	51
MM11 RE #14	HRT	Mt. Everts	lower	800	110	2.1	200	67	22
MM10 RE #18	HRT	Mt. Everts	lower	800	170	3.3	235	110	33
MM10 RE #21	HRT	Mt. Everts	lower	800	150	3.4	50	100	30
MM7 RE #10	HRT	Mt. Everts	middle	800	120	2.63	180	75	53
MM7 RE #13	HRT	Mt. Everts	middle	800	230	2.07	205	63	36
MM5 RE #2	HRT	Mt. Everts	middle	800	140	3.15	450	150	71
MM4 RE #6	HRT	Mt. Everts	middle	800	225	2.05	420	100	54
MM4 RE #12	HRT	Mt. Everts	middle	800	195	2.05	408	94	47
MM4 RE #13	HRT	Mt. Everts	middle	800	180	2.88	300	106	73

*Calculated using H_2O and CO_2 solubility relationships from volatilecalc (Newman and Lowenstern 2002).
^Here we adapt the fall layers and sample localities for the Bishop from Wilson and Hildreth (1997), and for the Oruanui from Wilson (2001).

5.3 Timescales of Initial Decompression

We can estimate the amount of time associated with the initial, slower decompression by modeling the time it would take for the melt in an RE to reequilibrate from starting values that are similar to MI concentrations to final H_2O and CO_2 concentrations that match the innermost part of each RE (Fig. 3.8, Table 3.2). Two approaches were used to evaluate this time. In the first, we assumed an instantaneous decompression step followed by a sustained reequilibration period at constant pressure. In this scenario, the RE starts with uniform concentrations of H_2O and CO_2 that are the same as co-erupted MI concentrations. The exterior boundary condition, following the instantaneous decompression, is fixed to the H_2O and CO_2 concentrations associated with the interior of each individual RE. We consider the RE to have reequilibrated with the external melt when flat plateaus have developed in the interior of the RE, that is, where profiles have concentrations of H_2O within 0.1 wt% and CO_2 within 10 ppm of reequilibration, well within the error of measurement. This method provides a minimum estimate for the time required for reequilibration. On this basis, reequilibration times for Bishop REs are <1 to 13 hours, for Oruanui REs, 4 hours to 3 days, and for Huckleberry Ridge REs, 1.5 to 30 hours (Fig. 3.9). For comparison, diffusive loss of H from enclosed MIs from Huckleberry Ridge material requires <12 hours to 5 days (Myers et al., 2016), which overlaps with but extends to longer times than the estimate for the REs. However, as noted above, the timescales calculated using this step-function approach are minimum values.

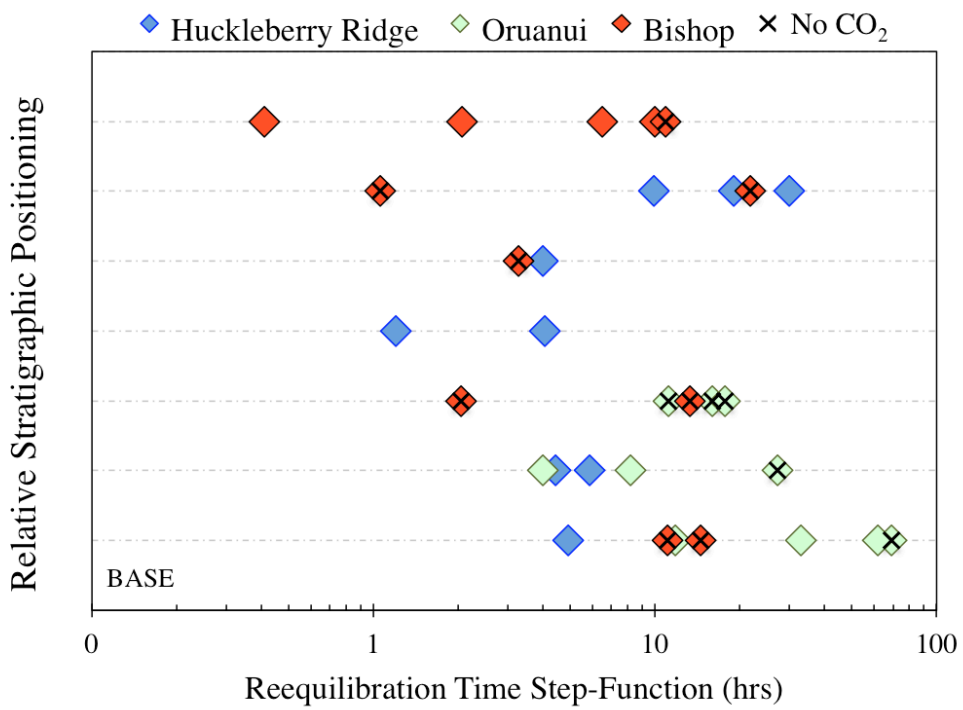

Figure 3.9. Time taken for each RE to reequilibrate from the starting MI concentrations to those measured within the interior, assuming an instantaneous pressure change (step-function).

The second approach used to estimate the timescale of the initial decompression experienced by REs is to assume constant slow decompression from their pre-eruptive storage region to the same shallower depth, beyond which the decompression rate rapidly increases, producing the modeled reentrant gradient. In this second approach, we applied our constant decompression model to all REs, use the same starting and ending H_2O and CO_2 conditions and criterion for when reequilibration has been achieved, as outlined above for the instantaneous decompression case. For Bishop REs, the initial slower decompression rates range from $5.0 \times 10^{-3} - 4.5 \times 10^{-4}$ MPa/s, implying 3 hours to 4.5 days of slower ascent. For Oruanui, the slower decompression rates ($1.0 \times 10^{-3} - 2 \times 10^{-4}$ MPa/s) require reequilibration times as long as 1-7 days. And lastly, the Huckleberry REs require decompression rates of $5.0 \times 10^{-3} - 2 \times 10^{-3}$ MPa/s, equating to times of 5 hours to

1 day, similar to the range preserved using the step function. However, these continuous decompression timescales for the Huckleberry REs could not be calculated with any certainty as no plausible degassing path exists from their 'starting MI' region and their preserved interior H_2O and CO_2 conditions (Fig. 3.3). This could be due to significant reorganization of the eruptible melt bodies surrounding the quartz host prior to eruption (Myers et al., 2016), meaning that an accurate estimate for their starting melt composition is not well constrained.

The Bishop and Oruanui REs that require the longest reequilibration time tend to have H_2O and CO_2 concentrations in their interiors that record the shallowest depths and, at least in the Bishop fall deposit, generally lack CO_2 (Fig. 3.7, Fig. 3.10). This last observation confirms the requirement for an initially sluggish stage of magma ascent, because CO_2 takes longer to reequilibrate than H_2O. For the Bishop Tuff, the H_2O and CO_2 concentrations measured in the interiors of REs, which we interpret to reflect reequilibration or partial reequilibration during an initial slow phase of ascent, appear to trend towards deeper pressures in samples from higher in the stratigraphy (Figs. 3.3, 3.6). A few RE interior concentrations from the upper fall layers (F8 and F9) in the Bishop even overlap with the starting MI range (Fig. 3.6). This observation represents the transition between a scenario where there is the need for a two-stage model to reproduce the RE profiles, to the situation where modeling of the measured profiles can use the MI starting conditions. This changeover is reflected in the diminishing 'misfit' associated with using RE interior volatile concentrations compared to using the volatile concentrations of co-erupted MIs as starting conditions (Table 3.3). This observation

Table 3.3. Starting conditions for each ascent model, where two options are presented: (1) H_2O and CO_2 values are based on concentrations measured from the interior of the reentrants, verses (2) based on co-erupted melt inclusion concentrations. The chi-squared misfit between the modeled slope and measured data are given for each reentrant, for both sets of starting conditions. Error in volatile analysis are as follows: Bishop [H_2O=0.2 wt.%, CO_2=20 ppm], Oruanui Phase 1 & 2 [H_2O=0.2 wt.%, CO_2=30 ppm], Oruanui Phase 3 [H_2O=0.3 wt.%, CO_2=20 ppm] and Huckleberry [H_2O=0.3 wt.%, CO_2=30 ppm].

	Starting MIs		Starting REs			Ascent based on Reentrants							Ascent based on Melt Inclusions						
Reentrant Name	Starting Pressure (MPa)*	MI H2O Start (wt.%)	FTIR Inner H_2O (wt.%)	FTIR Inner CO_2 (ppm)	Starting Pressure (MPa)*	Ascent Rate 1D Code MPa/s	dP/dt Error Bar	Bubble Radius	Ascent Time (hr)	Ascent Rate	MI Chi^2	Ascent Rate 1D Code MPa/s	dP/dt Error Bar	Bubble Radius	Ascent Time (hr)	Ascent Rate	MI Chi^2
BT F2-5 RE #3	175	5.4	3.5	0	73	0.02	0.01	0	0.88	0.78	0.8	0.01	0.001	0	4.58	0.39	1.2
BT F2-5 RE #1	175	5.4	3.75	0	82	0.041	0.01	0	0.49	1.61	0.3	0.013	0.002	0	3.53	0.51	2.4
BT F4-5 RE #10	175	5.4	3.78	0	84	0.24	0.05	0	0.09	9.41	0.4	0.074	0.001	0	0.62	2.90	4.9
BT F4-5 RE #4	175	5.4	3	0	55	0.02	0.005	0	0.63	0.78	0.4	0.0084	0.003	0	5.46	0.33	0.8
BTF7-1 RE #4	175	5.4	3.36	0	68	0.17	0.07	0	0.09	6.67	0.2	0.044	0.01	0	1.04	1.73	2.0
BTF7-1 RE #2	175	5.4	3.7	0	80	0.02	0.005	0	0.97	0.78	0.1	0.006	0.0002	0	7.64	0.24	1.2
BTF8-2 RE #1	175	5.4	4.9	0	133	0.42	0.12	0	0.08	16.47	0.8	0.14	0.03	0	0.33	5.49	8.2
BTF8-2 RE #2	175	5.4	4.1	0	97	0.018	0.005	0	1.34	0.71	0.8	0.006	0.001	0	7.64	0.24	4.1
BTF9-2 RE #2	220	5.4	4.2	281	148	0.026	0.004	0	1.47	1.02	0.9	0.016	0.003	100	3.65	0.63	1.4
BTF9_138 RE #2	220	5.4	4.5	218	150	0.062	0.01	80	0.63	2.43	1.0	0.042	0.004	20	1.39	1.65	0.9
BTF9_141 RE #1	175	5.4	4.3	0	103	0.027	0.005	0	0.96	1.06	0.7	0.015	0.001	0	3.06	0.59	2.9
BTF9_141 RE #2	220	5.4	3.9	240	130	0.021	0.002	0	1.59	0.82	0.9	0.012	0.002	100	4.86	0.47	1.1
BTF9-2 RE #1	175	5.4	5.42	60	172	0.22	0.03	0	0.20	8.63	1.0	0.22	0.02	0	0.21	8.63	1.7
P1963-6 RE #1	190	5	1.86	91	38	0.0034	0.001	20	2.29	0.13	1.0	0.0028	0.001	120	17.86	0.11	4.6
P1968 BB2 RE #1	190	5	2.9	0	62	0.0072	0.001	0	2.01	0.28	1.0	0.0026	0.001	0	19.23	0.10	3.8
P1968-1 RE #5	190	5	3.4	90	90	0.054	0.003	20	0.41	2.12	0.6	0.028	0.004	0	1.79	1.10	0.7
P1970-A RE #6	190	5	3.5	99	90	0.11	0.01	0	0.20	4.31	1.0	0.034	0.007	0	1.47	1.33	1.2
P1971-3 RE #1	190	5	2.2	0	35	0.0052	0.002	0	1.34	0.20	0.1	0.003	0.002	0	16.67	0.12	0.1
P1971-3 RE #2	190	5	2.5	25	45	0.022	0.004	0	0.44	0.86	0.9	0.012	0.002	0	4.17	0.47	1.2
P2305-D RE #1	170	5	3.9	0	95	0.076	0.03	0	0.31	2.98	1.0	0.012	0.002	0	3.70	0.47	6.0
P2305-E RE #1	170	5	4	0	96	0.044	0.05	0	0.54	1.73	0.6	0.016	0.003	0	2.78	0.63	2.9
P2305-F RE #1	170	5	3.3	0	73	0.09	0.002	0	0.19	3.53	1.0	0.015	0.002	0	2.96	0.59	3.3
MM11 RE #14	200	4.7	2.1	200	67	0.014	0.002	10	1.13	0.55	0.6	0.012	0.001	40	4.40	0.47	0.5
MM10 RE #18	200	4.7	3.3	235	110	0.044	0.006	70	0.63	1.73	0.9	0.03	0.004	100	1.76	1.18	0.8
MM10 RE #21	200	4.7	3.4	50	100	0.054	0.003	80	0.46	2.12	0.5	0.026	0.006	100	2.03	1.02	1.2
MM7 RE #10	150	4.1	2.63	180	75	0.072	0.015	0	0.25	2.82	0.2	0.028	0.004	40	1.39	1.10	0.4
MM7 RE #13	150	4.1	2.07	205	63	0.033	0.01	40	0.45	1.29	0.2	0.0086	0.002	200	4.52	0.34	2.7
MM5 RE #2	210	3.9	3.15	450	150	0.059	0.02	0	0.66	2.31	0.4	0.064	0.01	0	0.87	2.51	1.3
MM4 RE #6	210	3.9	2.05	420	100	0.013	0.002	0	1.92	0.51	0.6	0.011	0.002	80	5.05	0.43	2.1
MM4 RE #12	210	3.9	2.05	408	94	0.009	0.002	0	2.59	0.35	0.3	0.007	0.002	120	7.94	0.27	0.6
MM4 RE #13	210	3.9	2.88	300	106	0.12	0.02	100	0.22	4.70	0.8	0.016	0.001	20	3.47	0.63	5.8

*Calculated using H_2O and CO_2 solubility relationships from volatilecalc (Newman and Lowenstern, 2002). Fragmentation pressure =10 Mpa for all analyses.

initial slow period of magma ascent results from a less interconnected conduit system that supports a model by which these faster ascent rates are recording the maturing of the conduit system, where the evolves over the course of the eruption such that later erupted magma experiences little to no initial slow stage of decompression. This hypothesis finds support in a qualitative model by Scandone et al. (2007), who argued that the development phase leading up to a large explosive eruptions require a full interconnectivity between the storage region and the eruptive system.

5.4 Comparison of MI and RE Reequilibration Times

As previously mentioned, scatter in measured H_2O concentrations from fully enclosed MIs in the Huckleberry Ridge Tuff is interpreted to reflect the diffusion of H through the quartz lattice during extended periods of time in lower pressure (and H_2O) conditions (Myers et al. 2016). Variations in H_2O values of enclosed MIs can therefore be modeled to provide additional diffusive loss timescale information. The time it takes for diffusive loss to achieve the measured H_2O concentration can be determined using the following parameters: estimates for initial MI H_2O values at the time of trapping, or following extended storage time at high temperature, (2) estimates of external H_2O concentrations, pre-eruptive temperature, and (3) the size of each inclusion and distance to rim (see Myers et al., 2016 and Chapter IV for full details on methods and assumptions used). For the Huckleberry Ridge, 78% (n=93) of MIs require <12 hours to 5 days of residence in a partially degassed melt to recreate their measured H_2O concentrations, with the lowest measured H_2O values requiring up to ~10 days (Myers et al., 2016). Applying the same model to reproduce the H_2O ranges measured from the Bishop MIs sampled

from the first fall layer, 78% of inclusions (n=23) have experienced no apparent diffusive loss, equating to <22 hours (based on temperature and error bar, see Chapter 4) in the conduit. Five Bishop MIs require 1-6 days of lower pressure diffusive loss. However, in the first and third fall layers of the Oruanui, there is a wide range of H_2O (~3.5-5.6 wt%) contents in MIs for restricted ranges in CO_2 (Fig. 3.3). These Oruanui MIs (48% of 107) are inferred to have experienced >15 hours in a lower pressure melt, where 63% of these require 1 to 5 days of diffusive loss, and 20% require 5-15 days (Fig. 3.10).

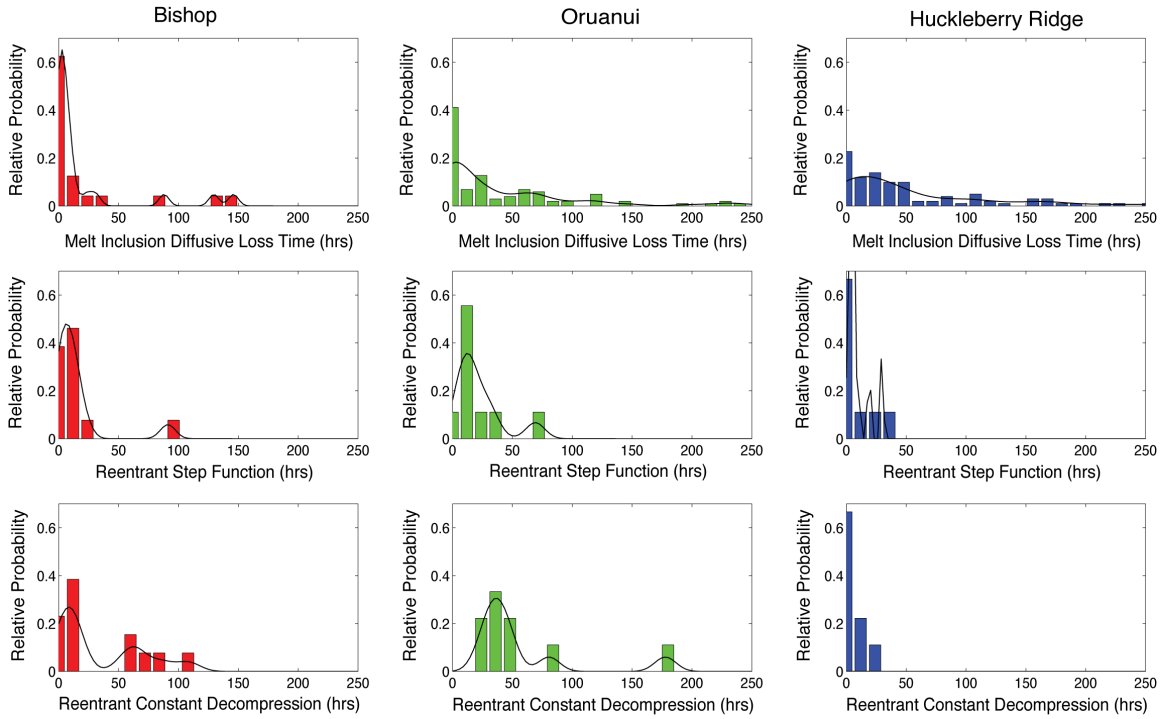

Figure 3.10. Relative probability distributions for the initial slow decompression based off of diffusive loss times from: (top) H diffusion through quartz from enclosed melt inclusions (Myers et al., 2016; Chapter IV); (2) reentrant reequilibration assuming a step function and (3) reentrant reequilibration through a constant decompression model.

Comparing these MI based diffusive loss timescales with the reequilibration times calculated for REs allows us to better constrain the opening behavior for these three supereruptions, assuming they are responding to a similar decompression history (Fig. 3.10). The minimum conduit timescales come from the RE step-function reequilibration

model, whereas in the Bishop and Oruanui, the constant decompression model either overlaps with or exceeds the diffusive loss timescales estimated from the H_2O values in MIs (Fig. 3.10). This suggests, particularly for the Bishop and Oruanui eruptions, that the two reequilibration approaches (step vs. continuous decompression) for modeling the initial slow phase with REs likely bracket the true history. It is thus likely that the transition between the slower first phase and the faster final ascent occurred prior to complete reequilibration to the interior RE concentrations. Overall agreement in the extent of diffusive loss time preserved by MIs and REs is relatively good (Fig. 3.10). As an accurate reequilibration time for Huckleberry REs using the constant decompression model could not be achieved, there is still a longer time associated with H_2O scatter in these MIs that cannot be reconstructed from their REs. There are two likely explanations for this: (1) the starting H_2O and CO_2 conditions for these MIs are less well constrained, as trace element chemistry suggests significant reorganization of the quartz hosts between MI entrapment and storage conditions prior to eruptions (Myers et al., 2016), or (2) REs that preserve a longer conduit history were not measured and modeled in this study.

6. Implications for using reentrants to determine ascent rates

This dataset represents the first comprehensive study to exploit reentrants in rhyolitic systems to understand the evolution of a large, explosive volcanic eruption. Our results, and comparison with decompression rates estimated from diffusive loss of H from MIs, confirm the benefit of modeling gradients in reentrants to estimate ascent rate from erupted volcanic products. The majority of reentrants require ascent rates between 0.7 and 10 m/s, equating to ascent times in the conduit of tens of minutes up to a few

hours. Reentrant reequilibration to lower H_2O and CO_2 conditions compared to their co-erupted melt inclusions suggests that the majority of REs experienced an initially slower ascent period, on the order of 12 hours to several days, prior to final ascent. This slow-moving beginning perhaps represents the initial development of the conduit system, and is supported by scatter in measured H_2O concentrations from enclosed MIs. This suggests that ascent times estimated using the measured volatile gradients preserved in the REs are minimum values and can miss the hours to days of slower initial ascent conditions.

By collecting samples from stratigraphically controlled levels in the deposits we were able to compare these modeled ascent rates with field constrained interpretations of the progress of each eruption, in order to provide context for our results. Using this approach, we observed that in the Oruanui samples there is a noted increase in ascent rate associated with the deposits inferred to be associated with increased flux rates (Phase 3). Faster ascent rates in all three eruptions are also associated with deeper interior and mouth pressures (recorded by reentrants and higher H_2O and CO_2 concentrations), and increase with higher stratigraphic height in all three deposits (particularly the Bishop Tuff). We interpret these REs to represent the 'maturing' of the conduit system and the overcoming of any initially sluggish ascent behavior.

7. Bridge

In Chapter III, I modeled profiles to fit measured H_2O and CO_2 profiles from quartz-hosted reentrants to calculate ascent rates through the opening stratigraphy for both the Bishop and Oruanui eruptions. From this I show that most reentrants from these

systems have experienced an initial slow ascent phase prior to the faster final ascent conditions. However, in the upper portions of the Bishop eruption, the initial slow phase is absent, suggesting that reentrants can record 'maturing' of the conduit system. Finally, through integrating these ascent rates with field based stratigraphy and inferences on mass discharge rates and caldera-formation, ascent rates are shown to correlate positively with higher discharge rates, and larger vent geometries. These ascent timescales are then compared to those calculated from melt inclusions (Chapter IV). In Chapter IV, I calculate diffusive loss timescales based on H_2O concentrations measured in melt inclusions from the very initial deposits of the Oruanui and Bishop fall deposits. Using the inference that longer residence periods within the conduit system equates to the degree of overpressure in the underlying magma system, we use the degree of diffusive loss to say something about what triggered these two eruptions.

CHAPTER IV

INFERRING MAGMA ASCENT TIMES AND CONDUIT PROCESSES IN RHYOLITIC EXPLOSIVE ERUPTIONS USING DIFFUSIVE LOSSES OF HYDROGEN FROM MELT INCLUSIONS

This chapter includes material co-authored with Paul Wallace (University of Oregon) and Colin Wilson (Victoria University of Wellington). I was lead author on the paper, which involved sample preparation, analysis, synthesis of all data, modeling and writing the manuscript. Paul Wallace and Colin Wilson served as co-advisors, aiding with field sampling, data interpretation and feedback on manuscript drafts.

1. Timescales of Rhyolitic Magma Development and Eruption

The processes involved in the formation and eruption of voluminous silicic magma bodies occur over a wide spectrum of timescales. At one end there are the longer-scale histories of magma generation and crystallization, where dating of mineral phases such as sanidine and zircon can illuminate the timing of accumulation and longevity of these voluminous systems (e.g. Vazquez and Reid, 2002; Charlier et al., 2008; Reid et al., 2011; Chamberlain et al., 2014a; Wotzlaw et al., 2014; Matthews et al., 2015). At the other extreme, high-resolution diffusion modeling of transects from individual crystals has afforded quantification of the later-stage processes of magma accumulation and mixing prior to eruption (e.g. Druitt et al., 2012; Allan et al., 2013; Chamberlain et al., 2014b; Till et al. 2015). However, few geochemical tools exist to help inform on the timing of eruption progression at the very initiation of voluminous caldera-forming events. Clues to what triggers these events require the ability quantify and integrate

information on the pre-eruptive state of the magmatic system with the timing of initial magma movement to the surface.

The importance of developing new tools to interrogate the initiation of large silicic explosive eruptions stems from the uncertainty surrounding what provokes the parental magma systems into mobilization and eruption. Many researchers have proposed that overpressure due to buoyancy, magma recharge, or volatile exsolution can trigger large explosive eruptions (Malfait et al., 2014; Carrichi et al., 2014; Stock et al., 2016). However, there remains controversy about how much overpressure can develop near the roof of larger magmatic bodies (see Gregg et al., 2015). Alternative triggering mechanisms involve forces or processes external to the magma body, such as roof destabilization or tectonic rifting (Gregg et al., 2012; Allan et al., 2012; de Silva and Gregg, 2014; Gregg et al., 2015; Myers et al., 2016). Discriminating between these mechanisms may be possible if the state and behavior of magma at eruption onset could be assessed (e.g. Allan et al., 2012, Myers et al., 2016). In particular, because magma ascent rates generally reflect the overpressure in the underlying magma body for a given vent geometry (Jaupart and Allegre, 1991; Woods and Koyaguchi, 1994; Melnik and Sparks, 1999), determining ascent rates for the earliest erupted materials can indicate whether or not internal triggering by overpressure in the source magma body was important. As of now, some of the most-developed tools for recording the decompression timescales prior to and during explosive eruptions come from evaluations of pumice vesicularity and bubble number densities (Toramaru, 2006, Shea et al., 2011; Rotella et al., 2014; Simmons et al., 2017). However, decompression estimates from pumices tend to be excessively high, likely affected by supersaturation and rapid nucleation at levels

close to the fragmentation depth (Toramaru, 2006). Thus, these ascent rates do not reflect an integration of the whole ascent process, but rather are weighted towards a snapshot of rapid nucleation occurring closer to the fragmentation depth.

Records of magma chamber perturbations and conduit processes during the opening stages of eruption can also be gained by studying volatile species, which react quickly to depressurization events. Although gradients of H_2O and CO_2 preserved in reentrants (crystal-hosted open melt pockets) can be used to assess final ascent timescales, their ability to record decompression events lasting for longer than several hours is inhibited by their tendency to rapidly reequilibrate (Liu et al., 2007; Chapter III). Melt inclusions, however, lose their original H_2O concentration under gradually reducing pressure conditions through diffusive losses of H through the host lattice (provided that rupture does not occur). This process is more sensitive to changing external conditions on timescales of the order of days (Severs et al., 2007; Myers et al., 2016). For example, the majority of melt inclusions sampled from individual layers in the initial fall deposit of the Huckleberry Ridge tuff, Yellowstone, were found to undergone changes for 5 days or more at pressures lower than those of original entrapment, with the extreme examples reflecting up to two weeks of diffusive losses at magmatic temperatures (Myers et al., 2016).

Here we present measurements of volatile contents from melt inclusions sampled in the very initial deposits of two supereruptions that preserve end-member onset characteristics: the start-stop opening behavior of the Oruanui eruption (Taupo, New Zealand) contrasted against the continuous eruption of the Bishop Tuff (California, USA). We then apply a diffusion model to calculate the amount of time each melt inclusion and

host crystal spent in the conduit system. For both eruptions the pre-eruptive conditions of the magma reservoirs are well characterized, as are the chronologies of opening behavior, inferred from field deposits (Oruanui: Wilson, 2001, Allan et al., 2012, 2017; Bishop: Wilson and Hildreth, 1997). With these constraints we are able to assess the processes responsible for eruption initiation, through the incorporation of timescales of initial magma movement given by the extent of melt inclusions from initial fall material that have experienced extensive H loss during ascent.

2. Geological Setting

2.1 Bishop Tuff, Long Valley, California

Eruption of the >600 km^3 (magma) Bishop Tuff at 0.767 Ma led to the formation of Long Valley caldera, a 27 by 15 km depression located in eastern California (Hildreth, 1979, 2004; Wilson and Hildreth, 1997, Hildreth and Wilson, 2007; Chamberlain et al., 2014b). Deposits of the Bishop eruption are a sequence of plinian pumice fall deposits, pre-dating and coeval with several large, partly welded ignimbrite packages (Wilson and Hildreth, 1997). The fall layers are divided into nine units (F1-F9) based on clast size variations and depositional bedding characteristics, and are preserved east of the caldera (Fig. 4.1; Wilson and Hildreth, 1997). Importantly, there are no significant (more than a few hours) depositional breaks inferred from any of the Bishop Tuff deposits, where early fallout graded directly into climactic eruption (Wilson and Hildreth, 1997).

The pre-eruptive configuration of the Bishop Tuff magma body has been studied in great detail through the use of Fe-oxide thermometry, compositional data (e.g. whole pumices, glass shards, melt inclusions, phenocryst chemistry and zonation), and through

oxygen isotopes, all pointing to a thermally and compositionally stratified magma chamber prior to eruption (Hildreth, 1979, Wallace et al., 1999, Bindeman and Valley, 2002, Hildreth and Wilson, 2007, Ghiorso and Evans, 2008, Roberge et al., 2013, Chamberlain et al. 2015, Evans et al. 2016). Here, however, we are only concerned with the fact that the majority of the earlier erupted eastern ignimbrite units, and their associated fall deposits, are interpreted to have erupted from the relatively non-zoned upper portion of the pre-eruptive magmatic body (Hildreth, 1979; Chamberlain et al., 2015).

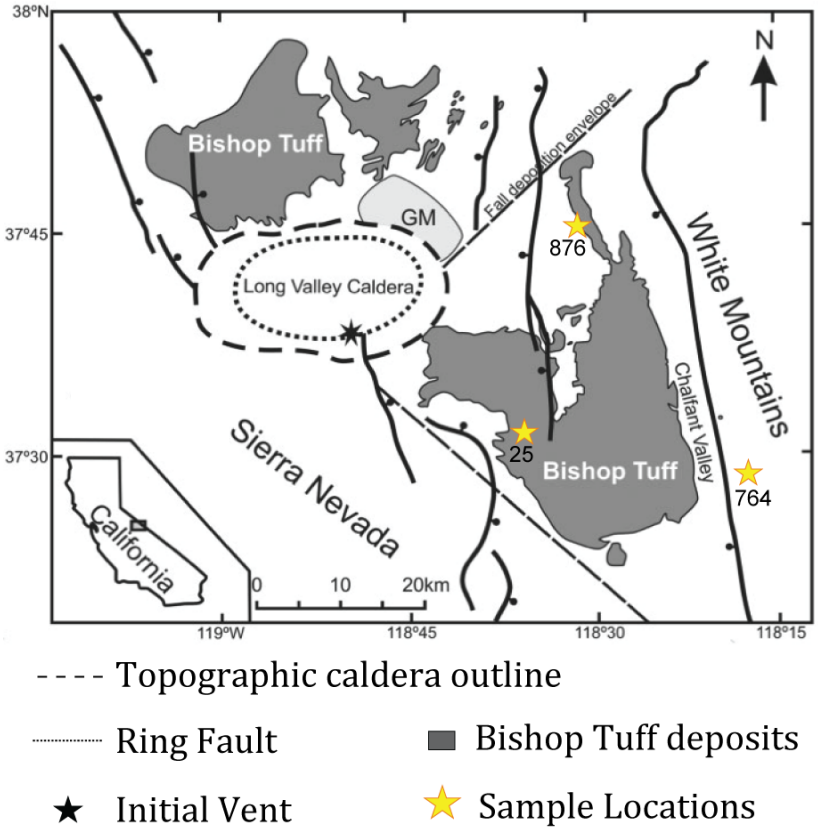

Figure 4.1. Simplified map of the Long Valley caldera area, including major structural faults (thick lines, ball on downthrown side) and outcrop areas of the Bishop Tuff ignimbrite (gray shaded areas), modified from Chamberlain et al. (2014a,b). Stars denote sample locations used in this study, all within the fall depositional envelope, with locality numbers from Wilson and Hildreth (unpublished data).

2.2 Oruanui, Taupo, New Zealand

The 25.4 ka Oruanui eruption is the largest event associated with Taupo volcano, NZ, with a magma volume of 530 km^3. Taupo volcano is at the southern end of the central segment of the Taupo Volcanic Zone (TVZ), one of the most productive and active regions of rhyolitic magma generation in the world (Sutton et al., 1995, Wilson et al., 2009). The Oruanui eruption is divided into ten phases, based on bedding in the fall deposits, but consists of several eruptive hiatuses (Wilson 2001). Ignimbrite was generated coevally with all phases of the eruption. The eruption is inferred to have stopped after phase one, equating to withdrawal of <0.1% of the total magma volume (Wilson, 2001; Allan et al., 2012). After several months of inactivity, the eruption began again, albeit incorporating several shorter time breaks on the order of hours to days (Wilson, 2001). The first two phases of this eruption are marked by the presence of a laterally injected, 'foreign' biotite-bearing magma, movement of which from an adjacent independent magmatic system 15 km away was driven through rifting processes (Allan et al., 2012). With the initiation of phase 3 came the transition from a single vent on the northern edge of what was to become the caldera margin, to an elongated vent geometry on the eastern margin (Fig. 4.2; Wilson, 2001). Phase 3 is about an order of magnitude more voluminous than the earlier phases, and is also associated with a spike in abundance of juvenile mafic material, collectively representing a shift to higher magma fluxes and perhaps associated with the onset of significant collapse into what eventually because the Oruanui caldera (Wilson, 2001).

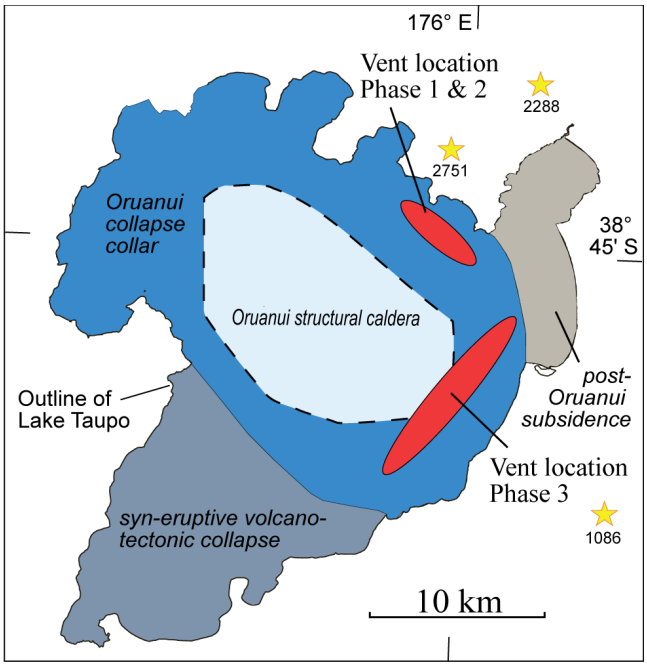

Figure 4.2. Map of Taupo volcano from Wilson (2001), showing the major components of the Oruanui caldera (terminology from Lipman, 1997). Vent regions for the first three phases of the Oruanui eruption are shown as ovals, and stars depict sampling locations. Sample locality numbers are based upon descriptions from Wilson (2001 and unpublished data).

Zircon dating using U-Th techniques, coupled with geochemical data from the products of earlier activity, indicate that the Oruanui magma system was active for about 40,000 years pre-eruption (Sutton et al., 1995), but that assembly of the melt-dominant body that was erupted was accomplished in a few centuries (Wilson and Charlier, 2009; Allan et al., 2013, 2017). Mineral-specific studies have shown that its geochemical evolution involved an open system, with significant contributions from greywacke country rock and partly-melted intermediate and felsic intrusions incorporated until the time of eruption (Liu et al., 2006; Charlier et al., 2008; Allan et al., 2013, 2017). Although there is compositional diversity in the erupted rhyolite, there is no systematic compositional zonation in the eruptive products, and there is only minor diversity in the

range of physical properties (e.g. crystal content, density) in the felsic pumices (cf. Bishop Tuff: Wilson et al., 2006; Hildreth and Wilson, 2007).

3. Methods

The aim of this study is to reconstruct the magma decompression history for the opening stages of the Bishop and Oruanui supereruptions. For the Bishop, we focused our sampling on a detailed examination of the first fall layer (F1 of Wilson and Hildreth, 1997), collecting material at six distinct levels from three localities (Fig. 4.1; Table 4.1). In the area shown in Fig. 1, F1 is up to 17 cm thick, with two coarser, crystal-rich zones used as distinct markers. All Bishop F1 material is fine-grained (medium lapilli or smaller), meaning that single pumices could not be utilized for study. Instead bulk material was collected, and the thickness of each F1 section and sample position in the fall deposit was recorded (Table 4.1). Sampling for the Oruanui eruption focused on individual pumice clasts sampled from deposits of the first three eruptive phases. The fall deposits from phases 1 and 2, where preserved at the most proximal localities (Fig. 4.2), have larger clasts when compared to fall deposits from the rest of the eruption, which are unusually fine-grained because of magma-water interaction (Self and Sparks, 1978). Some material used in this study from phases 1 and 2 were collected and reported on previously for glass and whole rock major and trace element chemistry by Allan et al. (2013, 2017). Two (of four) of the layers used from Phase 1 (P1963 and P1968), and all layers from phases 2 and 3 involved crushing and picking quartz from single pumices (n=20). Sample layers P1958 and P1962 involved a bulk crushing and picking of multiple pumices. Density information was collected for select pumices from these layers (Table

4.1). Additional biotite-bearing pumices intermixed at the stratigraphic level sampled as P1968 (Allan et al., 2013) were also sampled as single clasts.

Table 4.1. Sample locality information for all samples used in this study. For select samples where whole pumices could be used, density information was also recorded from Allan et al. (2013).

Eruption	Sample Locality	Samples Collected	Thickness of Sample (cm)	Distance from Base of F1(cm)	Layer Description		Outcrop Description
Bishop	Locality 25	BTMMF1-8	4	8	First coarse crystal rich zone in F1		West side of Owens Gorge near Upper Power House penstocks. Thick section of F1 and F2, with the fall continuing to F6. Capped by ignimbrite.
Bishop	Locality 25	BTMMF1-9	2	15	15-17 cm from base of F1		
Bishop	Locality 22	BTMMF1-2	3.25	0.75	Basal portion		Chalk Bluffs. Full stratigraphy present from F1-F9, with thick ignimbrite on top.
Bishop	Locality 495	BTMMF1-4	3	19	In the second coarse zone of F1		Lower south wall of Owens Gorge. Fall deposit stratigraphy present from F1-2, overlain by 80-m thick Ig1Ea ignimbrite.
Bishop	Locality 495	BTMMF1-5	4	7	In the lower coarse zone of F1		
Bishop	Locality 495	BTMMF1-6a	1	0	In tact first section of F1		
Bishop	Locality 495	BTMMF1-6b	1	1	In tact first section of F1		
Eruption	Sample Locality	Samples Collected	Thickness of Sample (cm)	Distance from Base of Phase 1 (cm)	Density	# of pumices analyzed	Outcrop Description
Oruanui	Locality 2288	P1958	8	0	Unknown	Bulk	Punatekahi scoria quarry. Fall Phases 1-3 are found interbedded with phase flows F4 and capped by Phase 7 flows
Oruanui	Locality 2288	P1962	10	22	0.6-0.8	Bulk	
Oruanui	Locality 2288	P1963	6	45	P1963-3= 0.66g/cm^3, P1963-5= 0.77g/cm^3,	4	
Oruanui	Locality 2288	P1968-Biotite Bearing	Intermixed		P1968-BB1= 0.9g/cm^3	2	
Oruanui	Locality 2288	P1968	6	200	P1968-2= 1.3g/cm^3, P1968-3= 0.65g/cm^3,	4	
Oruanui	Locality 2751	Additional sampling of P1970			P1970-1= 0.62g/cm^3, P1970-2= 0.91g/cm^3,	3	Phases 1 and 2 present, with a thin ignimbrite interbedded with phase 2.
Oruanui	Locality 2751	Additional sampling of P1971			Unknown	4	Phases 1 and 2 present, with a thin ignimbrite interbedded with phase 2.
Oruanui	Locality 1086	P2305			P2305-E= 0.94g/cm^3	3	Phase 3 present in a 100 cm thick exposed zone

All pumice clasts sampled from the Oruanui eruption were washed in deionized water to remove adhering matrix ash and dried at 110 ºC for 24 hours prior to crushing. Whole quartz crystals from materials collected from both eruptions were then separated and viewed in isopropyl alcohol to pick those preserving adhering matrix glass and containing one or more fully enclosed, glassy melt inclusions (MI). After the first side of

each inclusion had been intersected by lapping and polishing, descriptions of its size, the presence or absence of a vapor bubble, and distance from the inclusion to the closest crystal rim were recorded. The crystal was then flipped and the melt inclusion doubly intersected (Fig. 4.3).

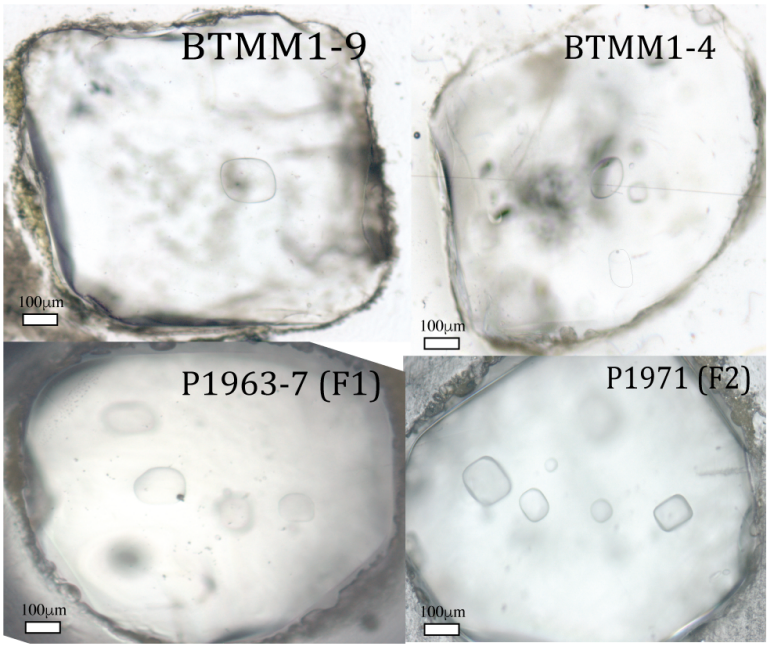

Figure 4.3. Photomicrographs of select quartz-hosted melt inclusions used in this study from both the Bishop and Oruanui deposits. The melt inclusion from sample P1963-7 contains a small vapor bubble.

All doubly intersected glasses were measured for H_2O and CO_2 absorbances using a Thermo Nicolet Nexus 670 Fourier transform infrared (FTIR) spectrometer interfaced with a Continuum IR microscope at the University of Oregon. Measured absorbances were converted to H_2O and CO_2 concentrations using Beer-Lambert law ($c_i = M_i \cdot A/\rho \cdot d \cdot \varepsilon$), where c_i is the concentration of the absorbing species, M_i is the molecular weight of the species (g/mol), A is the absorbance (height) of the relevant vibration band, ρ is the glass density (g/L), d is the thickness of the wafer analyzed (cm) and ε is the molar absorption coefficient (L/mol·cm). In rhyolitic compositions, ρ and ε strongly depend on total H_2O

concentration. This requires the use of an iterative process to converge on appropriate values [Eq. 1 (Skirius, 1990) and Eq. 2 (Leschik et al. 2004)]:

$$\rho = 2350 - 12.6\ C_{H2O} \quad \text{Eq. 1}$$

$$\varepsilon = 80 - 1.36\ C_{H2O} \quad \text{Eq. 2,}$$

where C_{H2O} is the concentration of total dissolved H_2O in wt.%. In order to use the 3550 cm^{-1} peak for total H_2O and minimize fringing in backgrounds, the thickness for all doubly-polished quartz wafers had to be between 25 and 45 μm. The absorption coefficient (ε) for molecular CO_2 (2350 cm^{-1}) in rhyolitic glass is 1214 L/mol·cm (Behrens et al., 2004). Peak heights were calculated using a straight-line background correction (Dixon et al., 1995). Thicknesses were averaged between those measured using a digital micrometer (±2 μm) and the thickness measured using the reflectance interference fringe method (Wysoczanski and Tani, 2006); agreement between the two methods is within ±4 μm. Average errors for H_2O and CO_2 concentrations for all inclusions are ±0.3 wt.% and ±10 ppm, respectively.

After FTIR analysis, the quartz wafers were set in a 1-inch epoxy mount for analysis of major elements using a Cameca SX-100 electron microprobe (EPMA) at the University of Oregon. Operating conditions were 15 kV and 10 nA sample current for Si, Ca, Na, Fe, Al, and K, and 50 nA current for Cl, F, Mg and Ti. A beam size of 5-10 μm was used for all analyses. Sodium, K, Si, and Al were measured first, and their concentrations were calculated using a time-dependent intensity correction in Probe for Windows (Donovan et al., 2007**)**. Glasses were then analyzed for trace elements by Laser-Ablation Inductively Coupled Plasma Mass Spectrometry (LA-ICP-MS) at Oregon State University using a 50-μm spot size, with four glasses (GSD-1G, BHVO, ANTO,

and BCR) for secondary standards, ^{29}Si as an internal standard, and glass standard GSE-1G for calibration. Major, trace, and volatile element concentrations for all MIs, along with their associated errors, can be found in online Supplement Chapter IV Table 1 and 2, with average concentrations for each layer found in Table 4.2.

4. Results

4.1 Major and Trace Elements: Bishop

All Bishop quartz-hosted MIs (n=23) from the six F1 layers sampled are high-silica rhyolite (SiO_2 = 76-77.5 wt.%, volatile-free). Major element data show a negative correlation between SiO_2 and Al_2O_3, consistent with compositional control dominated by feldspar crystallization (Fig. 4.4a), further supported by low concentrations of feldspar-compatible trace elements (Ba <7 ppm, Sr <5 ppm, Eu <DL, Table 4.2). Although concentrations of Cl and Li appear more scattered (Fig 4.4b, e), concentrations of U (4-9 ppm), Nb (20-30 ppm) and H_2O (4.2-5.8 wt.%) produce continuous arrays when plotted against Rb (120-190 ppm). These trace elements are expected to be moderately to highly incompatible for the Bishop mineral assemble during crystallization (Hildreth, 1979; Wallace et al., 1999; Roberge et al., 2013; Fig. 4.4c-e). Matrix glass compositions taken from Chamberlain et al. (2015) for fall layers F1, F2 and F7 overlap with the majority of F1 quartz-hosted inclusions measured here, but there are two less evolved inclusions (Rb=120-140 ppm, Nb=20 ppm) that overlap with F9 matrix glass. Using appropriate partition coefficients (see Fig. 4.4 caption) and an equilibrium crystallization model, the range of compositions is consistent with ~35-50% crystallization of the least-evolved MI compositions (which overlaps with middle-erupted Bishop Tuff compositions) to yield

Table 4.2. Averaged major, trace element and volatile compositions for melt inclusions from the Oruanui and Bishop initial fall layers. The full melt inclusion compositional dataset can be found in online Supplement Chapter IV, Tables 1 and 2.

Eruption	**ORUANUI** *PHASE 1*	**ORUANUI** *BB PHASE 1*	**ORUANUI** *PHASE 2*	**ORUANUI** *PHASE 3*	**BISHOP** *F1*
	n=47	*n=12*	*n=21*	*n=19*	*n=24*
SiO_2	77.25	77.00	76.91	77.04	76.61
Al_2O_3	12.37	12.30	12.57	12.31	12.45
FeO	1.11	0.98	1.12	1.09	0.65
MgO	0.13	0.10	0.13	0.13	0.04
CaO	1.06	0.77	1.05	1.07	0.47
K_2O	3.27	4.28	3.38	3.29	4.95
Na_2O	4.70	4.45	4.72	4.95	4.77
TiO_2	0.12	0.10	0.12	0.12	0.07
Anhydrous Total	93.28	92.82	92.45	93.93	98.36
EPMA Concentrations (ppm)					
Cl	2001	2427	1955	2039	803
F	495	535	432	494	568
FTIR Measured Concentrations					
H_2O (wt.%)	4.69	4.52	4.84	4.53	5.26
Error	0.33	0.20	0.41	0.18	0.16
CO_2 (ppm)	101	38	91	18	61
Error	10	7	10	5	3
Pressure (Mpa)	172	163	170	160	170
Trace Elements LA-ICP-MS (ppm)					
Li	53	64	59	43	69
B	21	22	23	20	52
P	84	82	75	89	61
Ti	780	710	737	792	394
Rb	124	143	126	120	175
Sr	59	36	52	57	1
Y	18	22	17	19	20
Zr	103	96	91	101	75
Nb	6	8	6	6	24
Sn	2	2	2	2	3
Ba	533	630	511	508	2
La	18	22	17	18	15
Ce	40	46	38	39	36
Pr	4	5	4	4	4
Nd	15	17	13	15	13
Sm	3	3	2	3	3
Eu	0.4	0.3	0.4	0.4	BDL
Gd	2.7	2.9	2.4	2.7	3.0
Dy	3.0	3.3	2.6	2.9	3.2
Er	2.0	2.3	1.5	1.9	2.1
Yb	2.0	2.4	1.7	1.9	2.1
Hf	3.2	3.1	2.8	3.1	3.2
Ta	0.5	0.7	0.5	0.5	2.2
Pb	16	18	16	15	32
Th	11	13	10	11	18
U	3	3	3	3	8

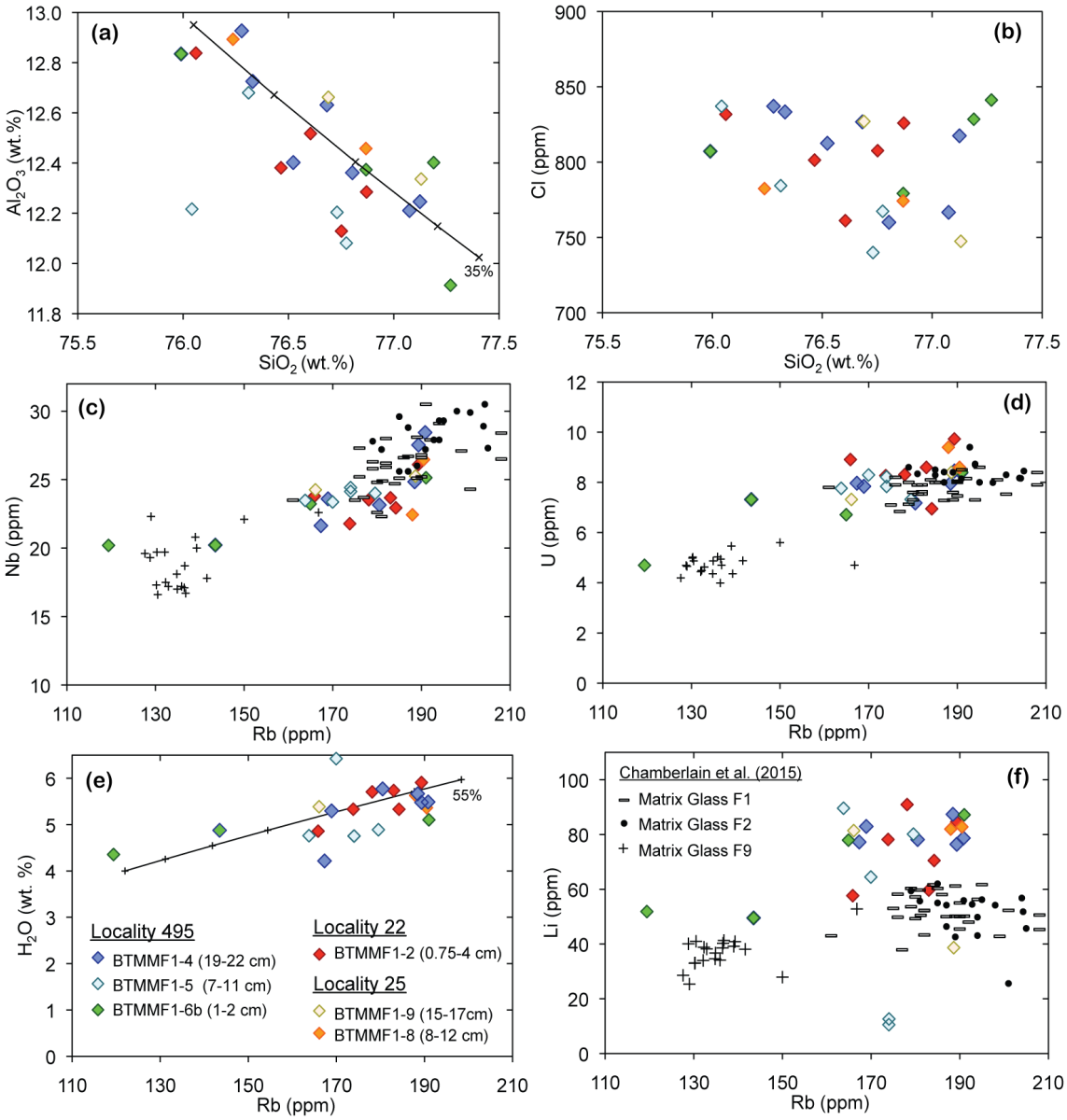

Figure 4.4. Major, trace and volatile elements plotted vs. SiO_2 (a,b) and Rb (b-f) for MIs from the six F1 layers sampled from the Bishop fall deposit. Legend, including sampling level, is shown in the lower left panel. Matrix glass data for select fall layers from Chamberlain et al. (2015) are shown for trace element plots (c,d,f). Black curves show equilibrium crystallization (in wt.%) calculated using bulk partition coefficients as follows: D = 0 for Cl and Li, D = 0.3 for Rb, and D = 0.2 for U (Roberge et al., 2013), appropriate for a high-silica rhyolite crystallizing quartz and two feldspars, with biotite and amphibole absent. For H_2O, D = 0.4 was used to simulate crystallization of vapor-saturated rhyolitic melt (see discussion in text).

the most-evolved MI compositions. Overall, MIs from any single sampled layer in unit F1 tend to fall along fractional crystallization arrays rather than in tight clusters (e.g. BTMMF1-4; see Fig. 4.4).

4.2 Major and Trace Elements: Oruanui

Quartz-hosted melt inclusions from Phase 1 (n= 47), Phase 2 (n= 21), and Phase 3 (n=19), plus the 'foreign' biotite-bearing rhyolite from Phase 1 (n=12), are all high-silica rhyolite (SiO_2 = 76.3-77.7 wt.%, volatile-free). The dominance of plagioclase on the crystallizing assemblage is again indicated by the negative correlation between Al_2O_3 and SiO_2, requiring 40% equilibrium crystallization to produce the entire range (Fig 4.5a). Concentrations of Nb (5-8.5 ppm), Li (20-70 ppm), and Cl (1800-2200 ppm) all produce shallow positive slopes when plotted against Rb (Fig. 4.5b,c,f), which is highly incompatible (D_{Rb}=0.07: Liu et al., 2006) in the Oruanui crystallizing assemblage (plagioclase, orthopyroxene, hornblende, quartz, Fe-Ti oxides). The fractionation relationship observed between Rb and U (2.4-4.0 ppm) requires 40% crystallization to produce the entire array (Fig. 4.5d). Although Rb concentrations in Phases 1 and 2 range from 100-160 ppm, there is a dominant cluster that falls between 110-130 ppm Rb. This cluster also contains the majority of Phase 3 MIs and Oruanui high-silica rhyolite matrix glass analyzed by Allan et al., (2017). Although MIs from the biotite-bearing rhyolite plot on a similar evolutionary trend, they fall to the higher end of trace element arrays (e.g. Rb 135-155 ppm) and are easily distinguished by their higher Cl (2200-2600 ppm). A few Phase 1 MIs also plot in this higher Cl field (Fig. 4.5b).

Table 4.3. Averaged major, trace element and volatile compositions for reentrants from the Oruanui and Bishop fall layers. The full reentrant dataset can be found in online Supplement Chapter III, Table 2.

Eruption	BISHOP	BISHOP	ORUANUI	ORUANUI	ORUANUI	ORUANUI
SAMPLE	***Average F2***	***Average F4***	***Average P1***	***Average BB***	***Average P2***	***Average P3***
SiO_2	76.59	76.82	76.98	76.52	76.98	77.10
Al_2O_3	12.50	12.40	12.55	12.95	12.59	12.38
FeO	0.65	0.66	1.18	0.93	1.05	1.14
MgO	0.03	0.04	0.14	0.10	0.12	0.12
CaO	0.46	0.46	1.17	0.71	0.90	1.04
Na_2O	4.13	4.40	4.74	4.38	4.61	4.76
K_2O	5.58	5.17	3.11	4.31	3.64	3.34
TiO_2	0.07	0.06	0.14	0.10	0.12	0.11
Anhydrous Total	98.02	98.03	96.70	95.80	96.93	97.04
EPMA Concentrations (ppm)						
Cl (ppm)	813	886	1851	2343	2084	1999
F (ppm)	301	451	346	203	223	277
FTIR Measured Concentrations						
H_2O	3.60	3.14	2.77	2.95	2.59	3.73
CO_2	0	50	45	0	31	0
Trace Element LA-ICP-MS Concentrations (ppm)						
Li	24	45	56	65	55	21
B	49	60	18	20	23	19
P	53	53	83	76	75	68
Ti	360	414	848	648	730	774
Rb	160	191	116	148	127	116
Sr	1	1	66	30	46	59
Y	19	22	20	22	20	21
Zr	67	73	116	85	95	106
Nb	23	26	7	8	7	7
Sn	2.6	2.7	1.5	1.8	2.0	1.5
Ba	2	2	519	600	508	516
La	13	14	18	21	20	18
Ce	31	34	41	48	43	40
Pr	3	4	4	5	4	4
Nd	12	13	15	16	15	16
Sm	2.5	2.9	3.3	3.0	2.5	2.9
Eu	BDL	BDL	0.5	0.2	0.4	0.5
Gd	3.3	2.6	2.7	3.2	2.7	3.4
Dy	3.2	3.3	3.8	3.1	3.1	3.6
Er	1.9	1.8	2.2	2.6	1.9	2.2
Yb	2.1	2.4	2.0	2.3	2.2	2.2
Hf	3.4	3.4	3.6	2.6	3.3	3.3
Ta	2.5	2.1	0.6	0.7	0.7	0.6
Pb	27	33	15	18	17	14
Th	18	19	10	14	12	11
U	7	9	3	3	3	3

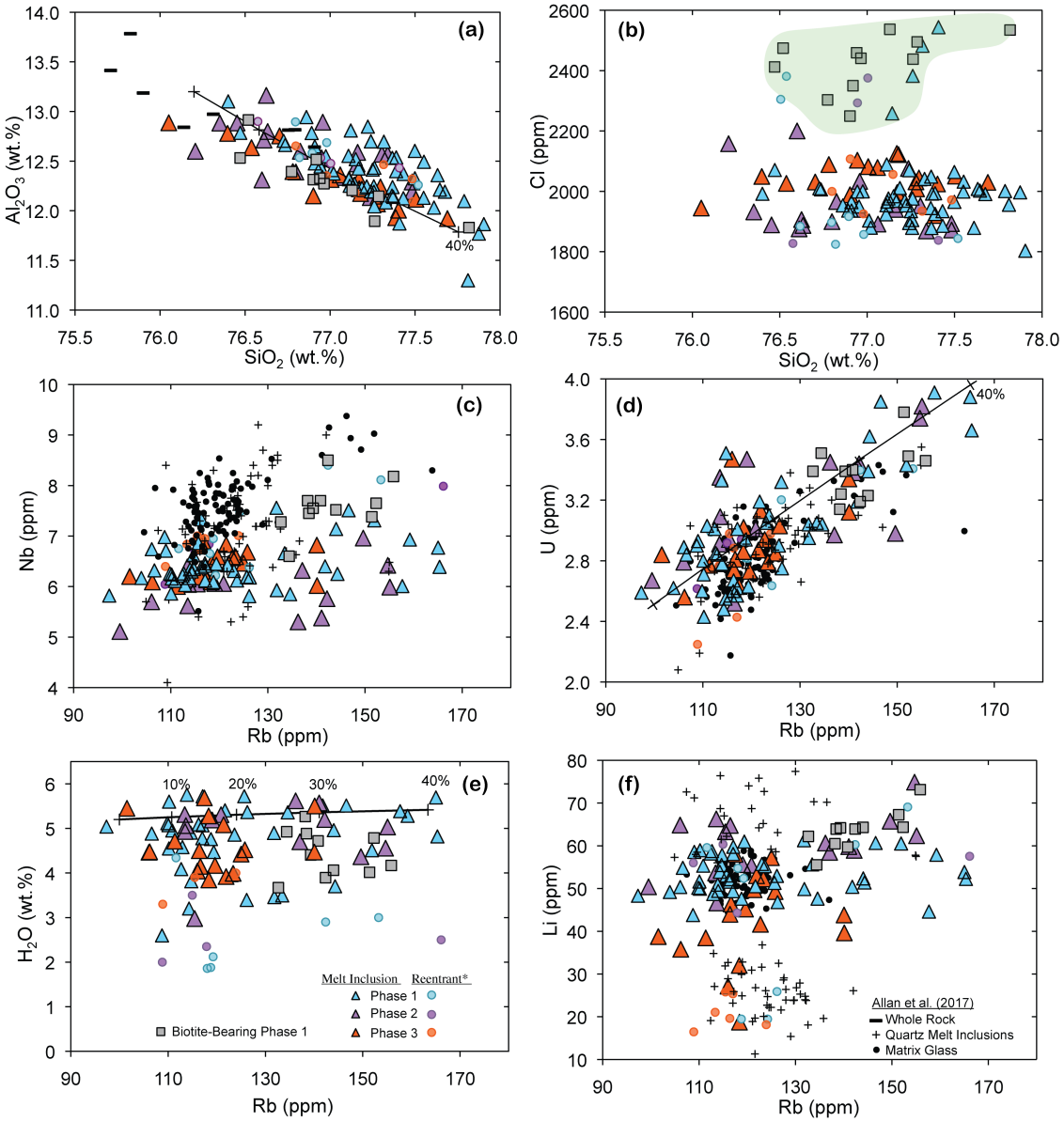

Figure 4.5. Major, trace and volatile elements plotted vs. SiO_2 (a,b) and Rb (b-f) for melt inclusions and reentrants from pumices in the first three phases of the Oruanui eruption. Legend for all samples measured in this study is shown in the lower left panel. The legend for whole rock, matrix glass data, and quartz-hosted MIs (from Phase 10), all previously measured by Allan et al. (2017) is shown in the lower right panel, with whole rock in plot (a), and trace element data appearing in plots (c,d,f). Partition coefficients used were Rb (0.07, Liu et al., 2006) and U (0.2, Roberge et al., 2013).

From each phase we also analyzed several open melt pockets, referred to hereafter as reentrants. These reentrants are open to the surrounding melt, meaning they can diffusively reequilibrate with changing external conditions. Although in the case of Nb

and U vs. Rb their concentrations overlap with the majority of the MIs, the volatile elements appear more scattered (e.g. H_2O, Li, Cl; Fig. 4.5). For example, a few reentrants from Phase 1 and Phase 2 have Cl concentrations similar to the biotite-bearing magma (Fig. 4.5b), and preserve lower H_2O concentrations compared to all MIs analyzed (Fig. 4.5e). These relationships probably reflect some exchange of crystals between the main Oruanui magma and the 'foreign' biotite-bearing magma in the conduit prior to fragmentation (Allan et al., 2012). Additionally, reentrants from Phase 1 and 3 have low Li concentrations compared to the main MI trend (Fig. 4.5f). Average reentrant major, trace and volatile concentrations, taken from Chapter III, can be found in Table 4.3.

4.3 H_2O and CO_2 Concentrations: Bishop and Oruanui

Water and CO_2 concentrations were measured in MIs from both the Bishop and Oruanui deposits. In all MIs measured from the Bishop and Oruanui eruptions, no relationship was observed between the H_2O concentration and the size of inclusion, or distance to rim (e.g. Lloyd et al. 2013; Appendix C, Fig 1C). For Bishop, concentrations of H_2O range from 4.0-6.0 wt.%, with >80% of inclusions falling between 4.75 and 5.77 wt.% (error ±0.3 wt.%). The majority of CO_2 concentrations for the F1 inclusions <60 ppm, in agreement with previous measurements on early Bishop MIs (Roberge et al., 2013). In general, the H_2O and CO_2 concentrations of F1 MIs overlap with MIs analyzed for the other 8 fall layers. However, one inclusion from the upper portion of F1 contains 225 ppm CO_2, a concentration similar to F9 reentrants (see Chapter III, Fig. 6a) and middle Bishop compositions (Wallace et al., 1999).

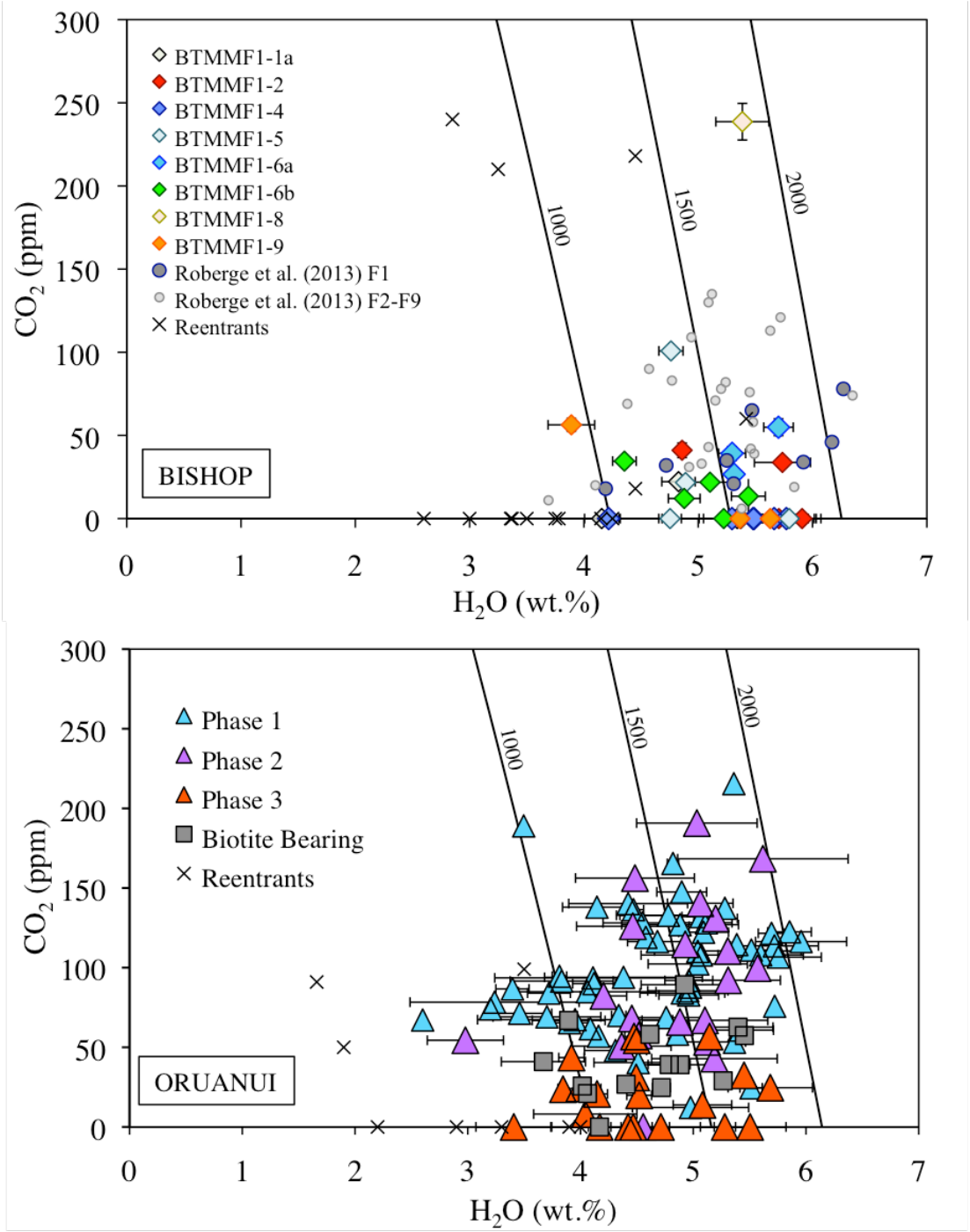

Figure 4.6. Water vs. CO_2 for MIs from the Bishop (top) and Oruanui (bottom) fall deposits. Curves show vapor saturation isobars calculated using VolatileCalc (Newman and Lowenstern, 2002) at 740°C for the Bishop (Evans et al. 2016), and 780°C for the Ouranui (Allan et al., 2017). Concentrations of H_2O vs. CO_2 are also displayed (as an x) for co-erupted reentrants (Chapter III).

In contrast to the narrow H_2O range preserved by Bishop F1 MIs, the first three phases of the Oruanui eruption have varied MI H_2O concentrations ranging from 3.0-6.0 wt.%, particularly characteristic of phases 1 and 3 (Fig. 4.6b). If the one MI from Phase 2 that contains lower H_2O (3.0 wt%) is excluded, the remaining 20 Phase 2 inclusions contain 4.1-5.6 wt.% H_2O. This narrower range is similar to the 3.75-5.4 wt.% H_2O range measured from the intermixed Phase 1 biotite-bearing pumices. Concentrations of CO_2 are more varied between the three phases: Phase 1 and 2 MIs contain up to 200 ppm CO_2, whereas all MIs from Phase 3 pumices contain <60 ppm CO_2. No correlation was found between those inclusions that contained vapor bubbles and the concentration of H_2O or CO_2 (Appendix C, Fig. 2C). For those places where individual layers contained pumices that were large enough for density analyses, no relationship was observed between density and H_2O or CO_2 concentration (Appendix C, Fig. 2C).

Discussion

5.1. H_2O concentrations from quartz-hosted MIs

Melt inclusions from the first fall layer (F1) of the Bishop Tuff show minimal scatter in their measured H_2O concentrations (>80%: 4.75-5.77 wt.%), and the trace element data generally fall along a fractionation trend (Fig. 4.4e). This is in contrast to the wide range of H_2O concentrations and more limited variation in Rb measured in MIs from the first three phases of the Oruanui eruption (Fig. 4.5e). This scatter in Oruanui H_2O concentrations is further pronounced by the more linear arrays observed for other major and trace elements (e.g. Al_2O_3, U and Cl vs. Rb; Fig. 4.5). We interpret this H_2O

variability in Oruanui MIs to be caused by diffusive loss of H species from MIs through the quartz host crystal during ascent (see Myers et al., 2016; Chapter II).

Although the diffusion of most elements through the quartz lattice occurs at much slower rates, H diffusion can occur on the timescales of hours to days at magmatic temperatures (Severs et al., 2007). This was previously demonstrated for the Huckleberry Ridge supereruption (2.08 Ma, 2,500 km^3), where each fall horizon has a wide range of H_2O contents (~1.0 to 4.5 wt.%) in sealed MIs (Myers et al., 2016; Chapter II). In this interpretation, the MIs with the highest H_2O values reflect magmatic concentrations at the storage depth prior to eruption, and any lower values reflect variable diffusive losses to a degassing external melt. The extent of H_2O loss for any individual inclusion can then be used to calculate a decompression timescale for each MI and host crystal through the use of a diffusion model, if the initial and external melt concentrations of H_2O can be constrained (see Section 5.3).

5.2. Temperature estimates

Because the diffusivity of H-species in minerals is strongly temperature dependent (e.g., Johnson and Rossman, 2013), accurate estimates for the pre-eruptive magma temperature are crucial for determining timescales of diffusive loss. For the first fall layers from the Bishop tuff we adopt a pre-eruptive temperature of 740ºC (Hildreth 1979, Bindeman and Valley, 2002; Hildreth and Wilson, 2007; Evans et al., 2016). Although in the later stages of the Bishop eruption there is evidence for an increase in magmatic temperature associated with the contribution of a less-evolved magma (Wark et al., 2007; Chamberlain et al., 2015), oxide pairs from the upper fall layers 7-9 provide

confirmation of the 740ºC temperature (Hildreth and Wilson, 2007). The temperature evolution of the pre-eruptive Oruanui magma body has been studied in great detail (Allan et al., 2013, 2017), constrained by amphibole rim thermometry and orthopyroxene zonation. This pre-eruptive temperature was confirmed through the use of five different thermometers, including oxide pairs, amphibole thermometry, and orthopyroxene-melt equilibrium, providing a pre-eruptive estimate of 780±20ºC (Allan et al., 2017). All temperature estimates used here are assumed to be constant through magmatic ascent.

5.3. Modeling diffusive loss of H through quartz

As was previously discussed in Myers et al. (2016), to calculate the amount of time associated with the diffusive H loss from each MI through the quartz host, we need to constrain: (1) the diffusion coefficient of H in quartz, (2) the H_2O partition coefficient between quartz and the melt (0.0001: Qin et al., 1992), (3) the initial MI H_2O concentration, and (4) the external H_2O concentration. As previously established in Myers et al. (2016), we estimate a diffusion coefficient of 10^{-11} m^2/s, using the diffusion model of Cottrell et al. (2002), by fitting the H loss experimental data of Severs et al. (2007). In Severs et al. (2007) heating of quartz-hosted Bishop MIs at 800 ºC and 1 atmosphere for set periods of time caused significant loss of H_2O in MIs (within days; Fig. 4.7c,d). Both the partition coefficient for H_2O in quartz and the diffusivity affect the timescale of diffusive loss of H_2O from an MI. Because of this, different values for the partition coefficient will result in differences in diffusivity calculated from the Severs et al. (2007) data. However, any set of values for partition coefficient and diffusivity that successfully reproduce the Severs et al. (2007) results will yield the same diffusive loss

time when applied to an unknown melt inclusion. In order to convert the value of the diffusion coefficient at 800°C calculated using Severs et al. (2007) to temperatures of relevance for the Oruanui (780ºC) and Bishop (740ºC) tuffs, we used the Arrhenius relation $D = D_0\exp(-E/RT)$, where the activation energy E was taken from Kasper (1975). This gives a diffusion coefficient of 3.1x 10^{-12} m^2/s for the Bishop, and 6.9 x 10^{-12} m^2/s for the Oruanui.

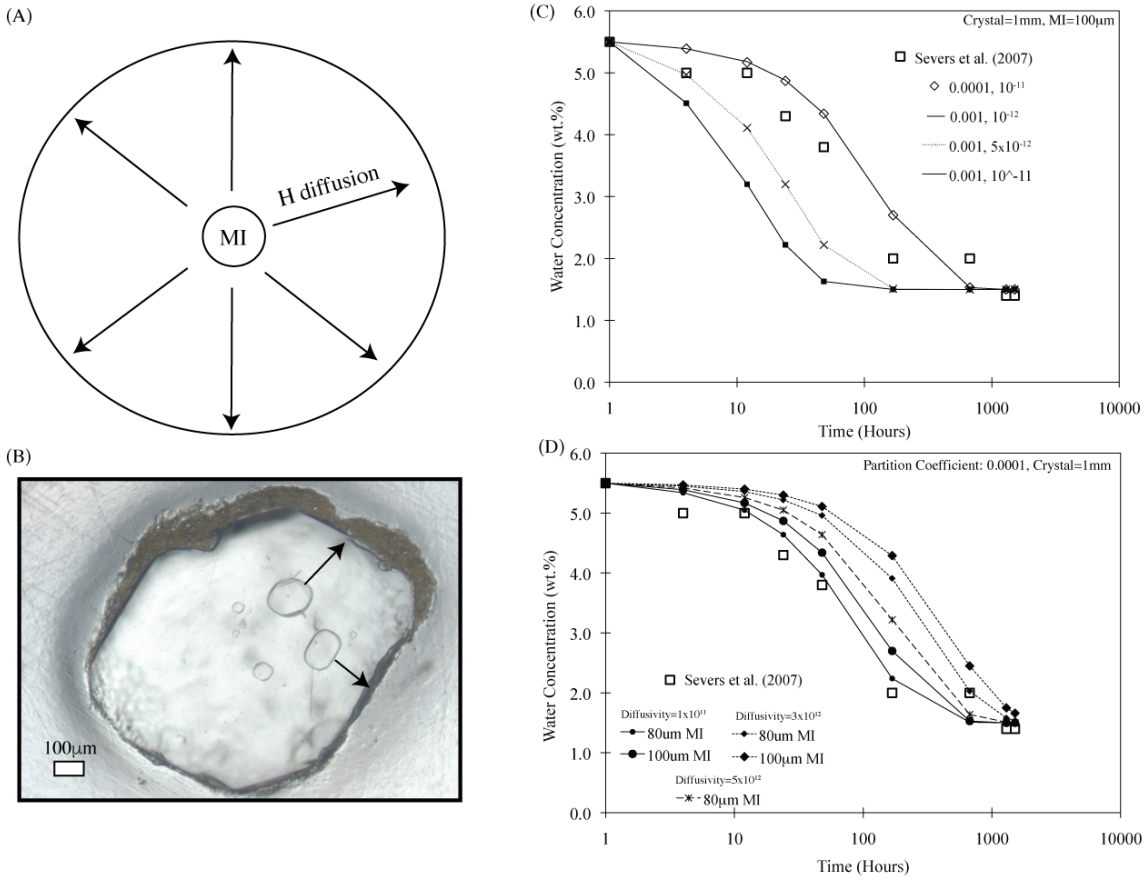

Figure 4.7. (A) Schematic model of the simplified crystal geometry used in modeling diffusive loss of H through the quartz lattice using the numerical model by Cottrell et al. (2002). The melt inclusion is assumed to be perfectly spherical and in the center of a spherical quartz grain (B) Photomicrograph of a quartz grain, where the closest edge distance plus the radius of the average melt inclusion diameter is taken as the radius of the crystal. (C) Testing the relationship between partition coefficient and diffusivity to fit the Severs et al. (2007) dataset. (D) Effect of melt inclusion size on calculated diffusivity to fit the Severs et al. (2007) dataset, assuming a partition coefficient of 0.0001 (Qin et al., 1992).

To approximate the initial H_2O contents (before diffusive loss) we assumed that H_2O behaved moderately incompatibly through partial loss to a vapor phase during vapor-saturated crystallization (Roberge et al., 2013; Fig. 4.4e). During crystallization, the higher solubility of H_2O compared to CO_2 causes dissolved H_2O to increase in the melt, but to a lesser extent than it would if the system were not vapor saturated. For the Bishop MIs, a vapor–melt partition coefficient for H_2O of 0.4 can explain the compositional variations observed for Rb and H_2O and incorporates, within error (±0.3 wt.%), all of the least-degassed (highest) H_2O melt inclusions from all samples (Fig. 4.8a).

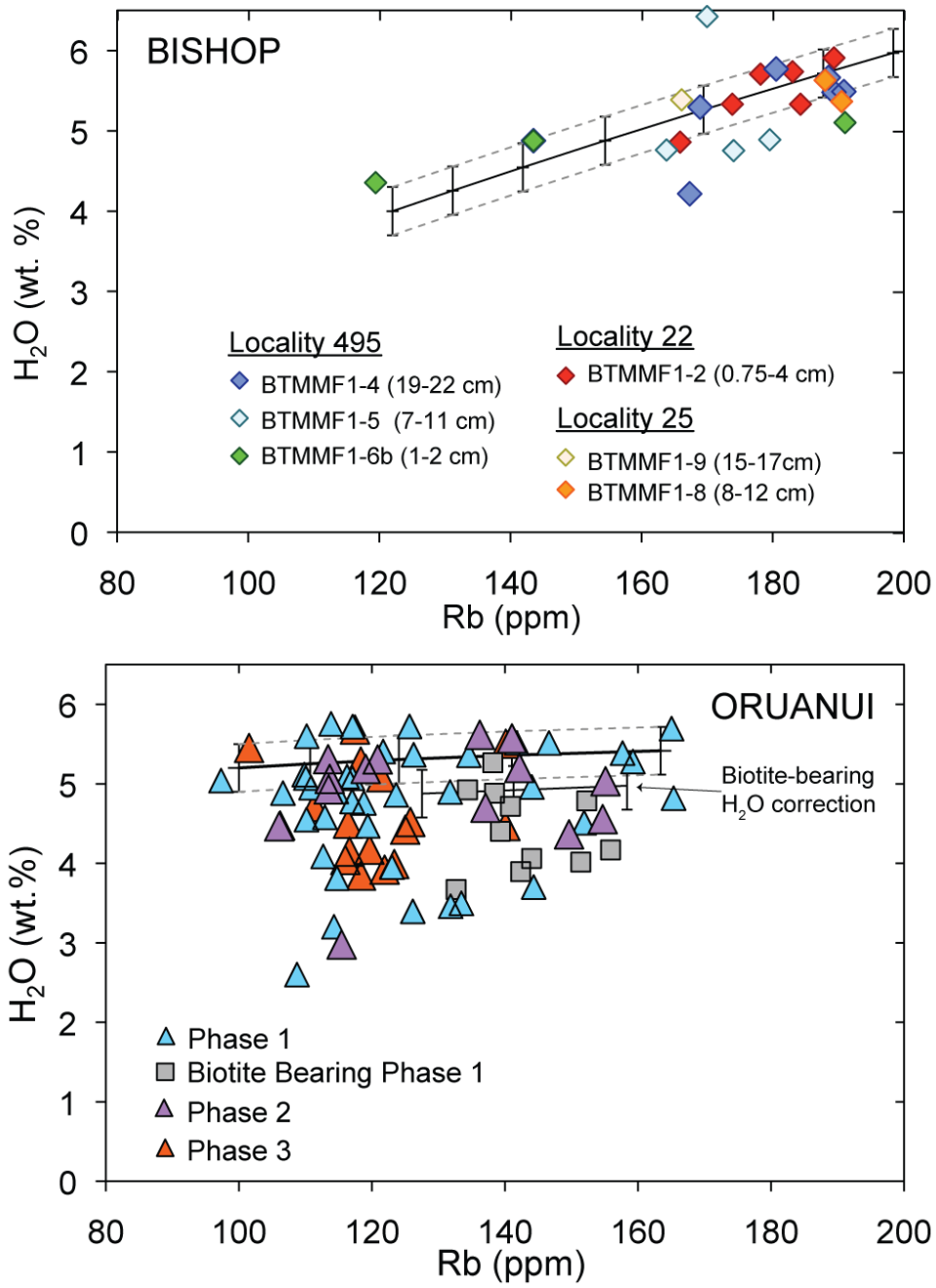

Figure 4.8. Rb vs. H_2O for melt inclusions from the Bishop (top) and Oruanui (bottom) early fall deposits. Inclusions that fall within error of the fractionation line represent those inclusions that have experienced no diffusive loss and are inferred to represent their storage concentration.

In the case of the Oruanui, the upper limit of all measured H_2O concentrations falls along a similar level regardless of Rb concentration (Fig. 4.8b). If we applied a fractionation slope of D_{H2O}=0.4 it would create an incorrect scenario where many

inclusions at lower Rb concentrations were being corrected to lower H_2O values. This requires an alternative approach to restoring each MIs original (storage) H_2O concentration. The model we use is based on an assumption that the MIs were trapped with variable Rb and H_2O and then held in a magma chamber such that all MIs re-equilibrated to the surrounding H_2O concentration. In this scenario, the highest H_2O concentration (within the 0.3 wt.% error range) would best estimate the initial H_2O concentration (Fig. 4.8b). As the biotite-bearing inclusions are not associated with the compositional evolution represented by Oruanui magma body or their pre-eruptive storage conditions (see Allan et al., 2012), an independent Rb vs. H_2O fractionation line was created to constrain the highest H_2O value inclusions (within error) as representing the 'storage' magma concentrations for these inclusions (Fig. 4.8b). We note that the differences in how we estimated the initial H_2O contents for the Bishop and Oruanui MI data have only a minimal effect on the final estimated timescale of diffusive loss.

The external melt H_2O concentration was estimated specifically for each layer using the average H_2O value measured from the interior end of co-erupted reentrants (Fig. 4.6; Table 4.3). We use reentrants to estimate the surrounding magma concentration because they re-equilibrate with the depressurizing melt within hours (Liu et al., 2007, Chapter III). For the Oruanui, exterior concentrations thus estimated were: Phase 1 = 2.15 wt.%, Phase 2 = 2.85 wt.%, Phase 3 = 3.73 wt.% (Table 4.3). For the Bishop, F1 reentrants were not measured; however, reentrants from F2 and F4 were. On the basis of the compositional similarities of F2 matrix glass with F1 melt inclusions (Fig. 4.4), we use the average H_2O concentration measured from these reentrants (H_2O=3.4 wt.%) as our best estimate for the exterior boundary condition. It should be noted here that the

choice of exterior H_2O concentration has a strong influence on the diffusive loss times calculated, as each MI was modeled for diffusive loss time assuming an instantaneous pressure drop (step function). A more realistic scenario would be that each MI responded to a constantly decreasing external H_2O concentration throughout its ascent until it reached the depth at which the interiors of REs last equilibrated. This approach, however, would yield longer timescales and requires a greater number of model assumptions that are not easily constrained, so we have adopted the first, simpler approach.

The diffusion model used (Qin et al., 1992; Cottrell et al., 2002) assumes (for mathematical convenience) a spherical MI in the center of a spherical phenocryst (Fig. 4.8a). The timescales calculated for H_2O loss from each MI are also strongly dependent on the inclusion size and distance from crystal rim as input conditions (Lloyd et al., 2013). Here we use the average inclusion diameter and the minimum distance to rim (measured in 2D section) as model parameters, providing again a minimum timescale estimate.

5.4. Diffusive Loss Timescales and Ascent Rates

The majority of F1 Bishop MIs (~78%, n = 18) have experienced no discernable diffusive loss between their measured and restored H_2O concentrations, within the analytical error of H_2O ±0.3 wt.% (Fig. 4.8a). In order to record a >0.3 wt.% loss, a quartz-hosted MI at temperatures similar to the early Bishop Tuff (740°C) would have to sit in the conduit at shallower depths than its long-term storage conditions for 22 hours. This inference means that the majority of F1 Bishop MIs spent less than 1 day ascending to the surface. The remaining five inclusions yield scattered degrees of loss, with one requiring 24 hours, three requiring 4-6 days, and the longest belonging to a large MI (165

μm) in a large crystal (600 μm), with an H_2O concentration of 4.75 wt.%, implying a time gap between initial upward transport and final ascent of as long as 13 days.

In contrast to the dominantly short timescales for the Bishop MIs, 48% (n=52) of Oruanui MIs have experienced >15 hours (based on Oruanui temperatures of 780°C) in the melt at lower pressures than those of long-term storage. Of these 52 inclusions, 63% of these indicate 1 to 5 days of diffusive loss, and 20% indicate 5-15 days (Fig. 4.9). The extent of this diffusive loss in the Oruanui is clast specific, and MIs measured from individual pumices sampled from the same phase have anywhere between 30 and 100% of their MIs having lost some amount of H_2O to a degassed, exterior melt (Table 4.4). Although the percentage of inclusions that have experience diffusive loss is variable between clasts, patterns do emerge from individual phases. Specifically, in Phase 1 clasts, those inclusions that have experienced loss dominantly preserve diffusive loss times between <24 hours and 5 days, with few inclusions preserving times greater than 5 days.

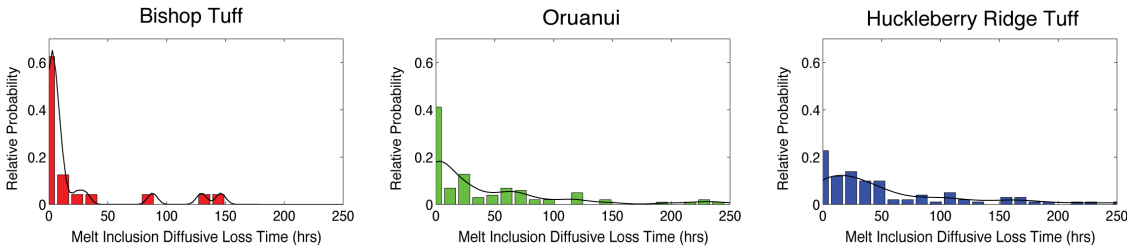

Figure 4.9: Relative probability distributions for the extent of diffusive loss time preserved by the early F1 Bishop and Oruanui (Phases 1-3) melt inclusions. These distributions are compared with the Huckleberry Ridge Tuff data from Myers et al. (2016).

Phase 3 pumices, however, have the largest number of inclusions from any Oruanui phase requiring more than five days in the conduit system (Table 4.4, Fig. 4.9). However, there are still equal number of inclusions preserving 1-5 days of diffusive loss

time, and MIs recording <1 day. This suggests that movement of magma towards the surface for the onset of Phase 3 activity was influenced by the earlier movement and release of material from Phase 2, but ascent was slowed or stalled within the conduit system prior to its eventual eruption. Additional information taken from reentrants (Chapter III) could be used to discern between these two ideas (slow ascent vs. stalling) for Phase 3 MIs. As reentrants are open to the exterior melt, during ascent H_2O and CO_2 compositional gradients form in response to the decompressing external melt (see Chapter III). Ascent rates calculated from Phase 3 reentrants preserve consistently faster final ascent conditions and deeper starting depths than Phase 1 and 2 reentrants. This suggests that the variable H_2O concentrations preserved in Phase 3 melt inclusions are recording a deeper-seated stalling event rather than slow continuous ascent towards the surface.

To translate these diffusive loss times into ascent rates, an initial storage depth before diffusive loss began is required. To do this we first estimate the starting pressure (Table 4.4) for each MI using the restored H_2O and measured CO_2 concentrations, which have pressure dependent solubilities. These pressures, which represent the crystallization pressures of the quartz hosts, are converted into depths using a crustal density of 2600 kg/m^3 (Table 4.4). The fastest ascent rate that can be detected with the H loss method for the Bishop is 0.078 m/s and for the Oruanui is 0.12 m/s. These rates are restricted because faster ascent than those rates would not cause detectable H_2O loss from enclosed inclusions, for their respective temperatures. The slowest ascent rates for the Bishop (average of 3 inclusions > 4 days) is 0.01 ± 0.004 m/s, where for the Oruanui (average of

17 inclusions > 4 days) this rate is 0.011 ± 0.004 m/s. This suggests that, within error, both systems appear to start their initial ascent at similar rates.

Table 4.4. Breakdown of the number of melt inclusions from each layer sampled in the Bishop and Oruanui eruptions that have experienced diffusive loss to an exterior melt. A melt inclusion is defined as having experienced diffusive loss if its measured H_2O concentration is lower (outside of error) than the 'restored' H_2O concentration (Fig. 4.8).

		Number MIs lower than 0.3 wt.%	Total Number of MIs	Percentage experience loss	Average Time Diffusive Loss Time (hr)	Median Time Diffusive Loss Time (hr)	< 1 day	#1-5 days	# >5 days	Pressure of Origin* (MPa)	Depth of Origin (km)
P1958	F1	11	17	65	38	16	11	5	1	171	6.7
P1962	F1	9	12	75	53	22	7	4	1	171	6.7
P1963	F1	6	15	40	42	15	11	4	1	171	6.7
P1968	F1	6	14	43	43	15	10	3	1	171	6.7
BB1 P1968	F1	5	8	63	71	35	3	3	2	145	5.7
BB2 P1968	F1	1	4	25	24	15	3	1	0	145	5.7
P1971	F2	5	12	42	35	18	9	3	0	172	6.7
P1970	F2	3	7	43	29	18	5	2	0	172	6.7
P2305-D	F3	8	8	100	122	117	0	5	3	159	6.2
P2305-E	F3	3	5	60	123	90	2	2	1	159	6.2
P2305-F	F3	2	6	33	149	149	4	0	2	159	6.2
Bishop	F1	5	23	22	49	22	18	4	1	158	6.19

*Pressure of origin is based off of the averaged restored H_2O and CO_2 solubility concentrations. These pressure were translated into depths using a crustal density of 2,600 kg/m^3.

5.5 Implications for the Triggering of Voluminous Caldera-Forming Eruptions

In the Huckleberry Ridge Tuff, MI evidence for ascent times of hours to weeks for co-erupted crystals in single layers requires that magma rose and was released episodically over periods of up to two weeks, during generation of the fall deposits studied (Myers et al. 2016). Additionally, single fall layers contain crystals from both faster ascending magma (<12 hours) and magma that had decompressed to varying degrees for varying times within the conduit system (days to weeks). This diversity in calculated ascent rates within single layers is interpreted to result from mixing in the conduit of slowly ascending magma with more rapidly ascending magma (Myers et al. 2016; Chapter II). In the case of the Bishop, this model may be less applicable, as the majority of melt inclusions have spent less than 24 hours within the conduit. However, it could explain the presence of those inclusions that represent 1-6 days within the conduit

system, that they represented parcels of magma that had begun ascent earlier and were overtaken by the dominant volumes of faster-ascending magma.

Looking at the Oruanui, the variability in extent of diffusive loss preserved in single clasts, and between each phase, provides strong evidence that these quartz-hosted MIs are recording a range of decompression rates and times within the conduit system. In Phases 1 and 2, the bulk of MIs record timescales on the order of 1 day, with a secondary population in most single clasts recording timescales on the order of 1-5 days (Table 4.4, Fig. 4.9). In Phase 3 the longer ascent times preserved by a number of MIs (> 5 days, n=6 of 19; 1-5 days n=7 of 19) suggest that these inclusions spent a more extensive period of time at lower pressures, equating to average ascent rates of 0.009 m/s. However coupling this diffusive loss information with reentrants from Phase 3, which preserve final ascent timescales on the order of 2-5 m/s, thereby requires a model where material was slowly ascending to the surface (or stalled), and then incorporated in the faster ascending final eruption, much like what was proposed for the Huckleberry Ridge Tuff (Myers et al. 2016; Chapter II).

We next compare the extent of diffusive loss of each MI, taken as the difference between restored original H_2O concentration and measured H_2O concentration, versus the calculated diffusive loss times (Fig. 4.10). The percentage of inclusions that have undergone diffusive loss between the three systems is extremely variable. The estimates from the Huckleberry Ridge are the most extreme (for 88% of inclusions the difference is greater than the error in H_2O) compared to what are observed for the Oruanui (46%) and Bishop (22%) systems. Given the sensitivity of these diffusive loss processes to temperature, it is logical that the hotter Huckleberry Ridge system (T=800°C) generated

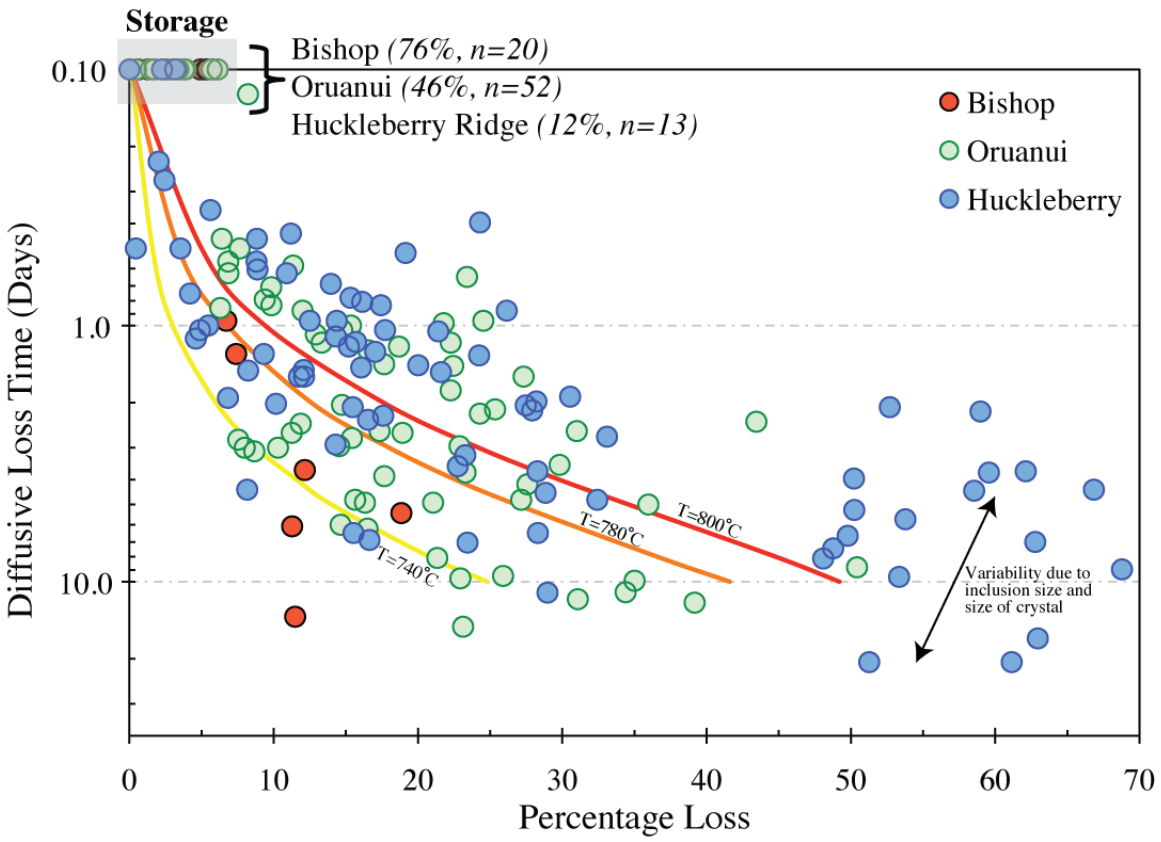

Figure 4.10. Diffusive loss times based on the output from the Cottrell et al. (2002) model (see discussion for details). Percentage loss is the difference between the measured MI H_2O concentration and the restored H_2O concentration (based on reconstruction to a Rb-controlled fractionation trend: Fig. 4.9). Solid lines represent the model outputs (temperature dependent) for a 100-micrometer diameter inclusion in a 500-micrometer diameter crystal sitting in a 2 wt.% melt.

the largest number of MIs that experienced diffusive loss as magma ascended towards the surface. However, the number of inclusions that have experienced significant loss and record longer diffusive loss times is substantially higher in the Huckleberry and Oruanui systems when compared to the Bishop (Fig 4.9, Fig. 4.10).

Similarities between the Huckleberry Ridge and Oruanui system case studies include: (1) field evidence for time breaks (i.e. pauses in deposition) between eruptive episodes, (2) co-erupted material experiencing different ascent histories and (3) significant variability in the H_2O contents in co-erupted MIs, equating to days, and in

some layers weeks, in the conduit system. In the Huckleberry Ridge, these observations combined with geochemical evidence for tapping of several distinct magma bodies, was used to argue that external triggering was important at the onset of eruption (Myers et al. 2016; Chapter II). Through the inference that the rate at which magma ascends reflects the extent of overpressure in the underlying magma body (Jaupart and Allegre, 1991; Woods and Koyaguchi, 1994; Melnik and Sparks, 1999), the H_2O scatter in the early-erupted materials for the Oruanui, particularly in Phase 3, could also imply that chamber overpressure was not the dominant control in triggering initial movement of magma towards the surface. This inference is consistent with that previously proposed by Allan et al. (2012) that external modulation (rifting) was a controlling factor in initiating and modulating this eruption. In contrast, we infer that the overwhelming number of MIs that preserve ascent times of <1 day in the earliest Bishop Tuff fall layer suggests that this eruption was primarily triggered through overpressure within the magma body.

6. Conclusions

Here we assess the timescales of rhyolitic magma ascent at the opening of three supervolcanic eruptions, based on diffusive loss of H from sealed, quartz-hosted, rhyolitic melt inclusions. Using pre-existing constraints on eruption timings from fall deposit stratigraphy, we contrast the Oruanui eruption, where initial activity was episodic and modulated by external rifting, against the rapid and continuous opening of the Bishop Tuff. Both of these eruptions were then compared and contrasted against previously published data by Myers et al. (2016) for the Huckleberry Ridge Tuff. New data from quartz-hosted MIs from the Oruanui and Bishop deposits have major and trace element

concentrations (e.g. Nb, U) that form continuous arrays against SiO_2 or Rb, indicative of chemical differentiation being controlled through crystallization. However, in the first and third fall layers of the Oruanui, there is a wide range of H_2O (~3.5-5.6 wt%) in MIs for restricted ranges in CO_2, similar (albeit still more modest) to what was observed for the Huckleberry Ridge Tuff (1.0-4.7 wt.%; Myers et al., 2016). This is in contrast to the first fall layer in the Bishop Tuff, which preserves a limited H_2O range (~4.8-5.6 wt%). Diffusive loss modeling of Bishop MIs indicates that 78% of inclusions (n=23) have experienced no observable diffusive loss, equating to <22 hours (based on temperature and error of H_2O measurement) in the conduit, whereas five other Bishop MIs indicate 1-12 days of lower pressure diffusive loss. Conversely, in the Oruanui, 48% of 107 MIs have experienced >15 hours in a lower pressure melt, where 63% of these require 1 to 5 days of diffusive loss, and 20% require 5-15 days. These Oruanui percentages are closer to, albeit still less than, those calculated from the Huckleberry Ridge Tuff, where 88% of all inclusions have experienced some amount of diffusive loss.

We propose that these differences can be linked to differences in eruptive behavior. For instance, in the Bishop Tuff, fall deposition graded continuously into escalating flow activity (Wilson and Hildreth, 1997). This is consistent with our modeling results where the majority of inclusions are inferred to have spent little time in the conduit system. In contrast, the Oruanui eruption contains several lines of evidence from field observations that the Oruanui eruption started and stopped several times (Wilson, 2001) and that rifting modulated initial activity (Allan et al., 2012). These inferences are supported by the higher degrees of diffusive water loss preserved in MIs and the variable ascent rates in co-erupted clasts. In the Huckleberry, slow ascent from three distinct

magma bodies allowed for diffusive loss to have occurred from the majority of inclusions, which were erupted episodically and sequentially during eruption onset, most likely from separate vents. The slow ascent rates suggests that the magma bodies were not strongly overpressured at eruption onset. We thus find that careful evaluation of H_2O concentrations in MIs and reentrants in co-erupted quartz crystals can help to reconstruct the nature of initial magma ascent and in evaluating possible controls on eruption onset.

7. Bridge

In Chapter IV, I calculate diffusive loss timescales based on H_2O concentrations measured in melt inclusions from the initial deposits of the Oruanui and Bishop fall deposits. Using the inference that longer residence periods within the conduit system relates to the degree of overpressure in the underlying magma system, we use the degree of diffusive loss, paired with field evidence, to say something about what triggered these two eruptions, and then compared to these results to Chapter II. Chapter V discusses the petrologic history of the Cebolla Creek Tuff. Combining melt inclusion volatile concentrations with phenocryst zoning, we investigate the pre-eruptive state of a homogenous crystal-rich mush, which typically are thought to require late-stage heating to erupt.

CHAPTER V

PRE-ERUPTIVE VOLATILE CONCENTRATIONS AND STORAGE CONDITIONS ASSOCIATED WITH THE CRYSTAL-RICH CEBOLLA CREEK TUFF, SOUTHERN ROCKY MOUNTAIN VOLCANIC FIELD

This chapter includes co-authored material with Chloe Elliot, Mike Dungan, Amy Krauss and Paul Wallace (all University of Oregon), and in preparation for submission to *Lithos*, discusses the petrologic and volatile pre-eruptive history of the Cebolla Creek Tuff. I was lead author on the paper, which involved sample preparation, analysis, synthesis of all data, and writing the manuscript. Chloe Elliot and Amy Krauss helped with geochemical analyses. Mike Dungan (University of Oregon) served as the main advisor, aiding in field sampling, data interpretation and manuscript editing. Paul Wallace (University of Oregon) helped with field sampling and provided feedback on manuscript drafts.

1. Introduction

The Cebolla Creek Tuff is a non-zoned crystal-rich (35-40%) ignimbrite (250 km^3) erupted from the San Juan focus of the Southern Rocky Mountain volcanic field (SRMVF) in SW Colorado (Lipman, 2007). The eruption of such voluminous and homogeneous, crystal-rich dacitic magmas, widely referred to as a 'monotonous-intermediates' (Hildreth, 1981), have stirred interest and debate with respect to the processes responsible for the mobilization, as well as the extraordinary homogeneity on the hand-sample scale, of such viscous magmas (Bachmann et al., 2002; Dufek and Bachmann, 2010; Huber et al., 2012). Another example from this region is the enormous

crystal-rich (40-50%) Fish Canyon Tuff (FCT, 28.02 Ma), postulated to represent a remobilized, near-solidus granodioritic pluton (Bachmann et al., 2002). This assertion is supported by petrological evidence (e.g. resorption textures; see Bachmann et al., 2002), isotopic characteristics (Charlier et al., 2007), and age-calibrated trace element systematics (Wotzlaw et al., 2013), requiring a model to explain the mobilization of the previously crystal-locked mush. Most numerical models propose that the mobilization of these crystal-rich magma bodies requires significant influx of heat and volatiles from an underplating magma (Bachmann et al., 2002; Bachmann and Bergantz, 2003, 2006; Huber et al., 2010; Burgisser and Bergantz, 2011). However, of the 10 monotonous intermediate ignimbrites from the San Juan field, only one other unit besides the FCT has been documented through petrographic study (the Masonic Creek Tuff: Sliwinski et al., 2017). The remaining examples lack detailed studies that could be used to assess the applicability of the FCT rejuvenation model to other crystal-rich eruption units. Furthermore, although these models require the addition of volatiles into the system, as of yet, no study from the region has directly measured and quantified the volatile concentrations associated with a monotonous intermediate pre-eruptive magma.

The Cebolla Creek Tuff provides an distinctive opportunity to investigate another monotonous intermediate in the San Juan region, as it is the only unit that has been found to contain rapidly quenched, glassy melt inclusions. Melt inclusions are advantageous for assessing the pre-eruptive volatile concentrations (H_2O, CO_2, Cl, F and S) of the melt, because host crystals largely protect against the effects of degassing that occur during ascent (e.g. Lowenstern, 1995; Wallace, 2005; Kent, 2008, and references within). Here the evolution of the Cebolla Creek Tuff magma is evaluated using the volatile

concentrations, major and trace element compositions of plagioclase-hosted melt inclusions, as well as the petrologic growth history of plagioclase and amphibole phenocrysts.

2. Geological Background

The San Juan focus of the SRMVF consists of thirty voluminous, mid-Tertiary ignimbrites and their associated calderas (Fig. 5.1a), twenty of which were erupted from 26.9-29.4 Ma (Lipman, 2007, Lipman and McIntosh, 2008). This heightened volcanic activity is part of an ignimbrite "flare-up" event of widespread caldera-forming eruptions across much of the western United States (Humphreys, 1995). The increased activity is attributed to a regional transition from a low- to high-angle of plate convergence, creating an increasingly extensional regime (Lipman, 2007). Slab-rollback (Humphreys, 1995) promoted rapid upwelling of hot asthenospheric mantle to a hydrated upper-mantle lithosphere, the latter being associated with a long period of 'refrigeration' (Dumitru, 1991; Farmer et al., 2008). The rapid heating of lithospheric mantle allowed for production of large volumes of melt on geologically short timescales.

Initial volcanism (36-30 Ma) in the Southern Rocky Mountain volcanic field was dominated by andesitic-dacitic lava eruptions, forming a stratovolcanic field. Starting at 29 Ma, eruption frequencies and volumes rapidly increased, with the volcanism shifting to more silicic, caldera-forming ignimbrite events (Lipman, 2007). These ignimbrites tend to be either crystal-poor rhyolites or crystal-rich dacites, but with several units preserving a zonation between the two end members. Peak volcanic discharge rates in the field are associated with the nine ignimbrites that make up the products of central San

Juan caldera complex (26.9-28.8 Ma), including the voluminous 28.02 Ma Fish Canyon Tuff, the eruption of which formed the 35x75 km La Garita Caldera (Lipman, 2007).

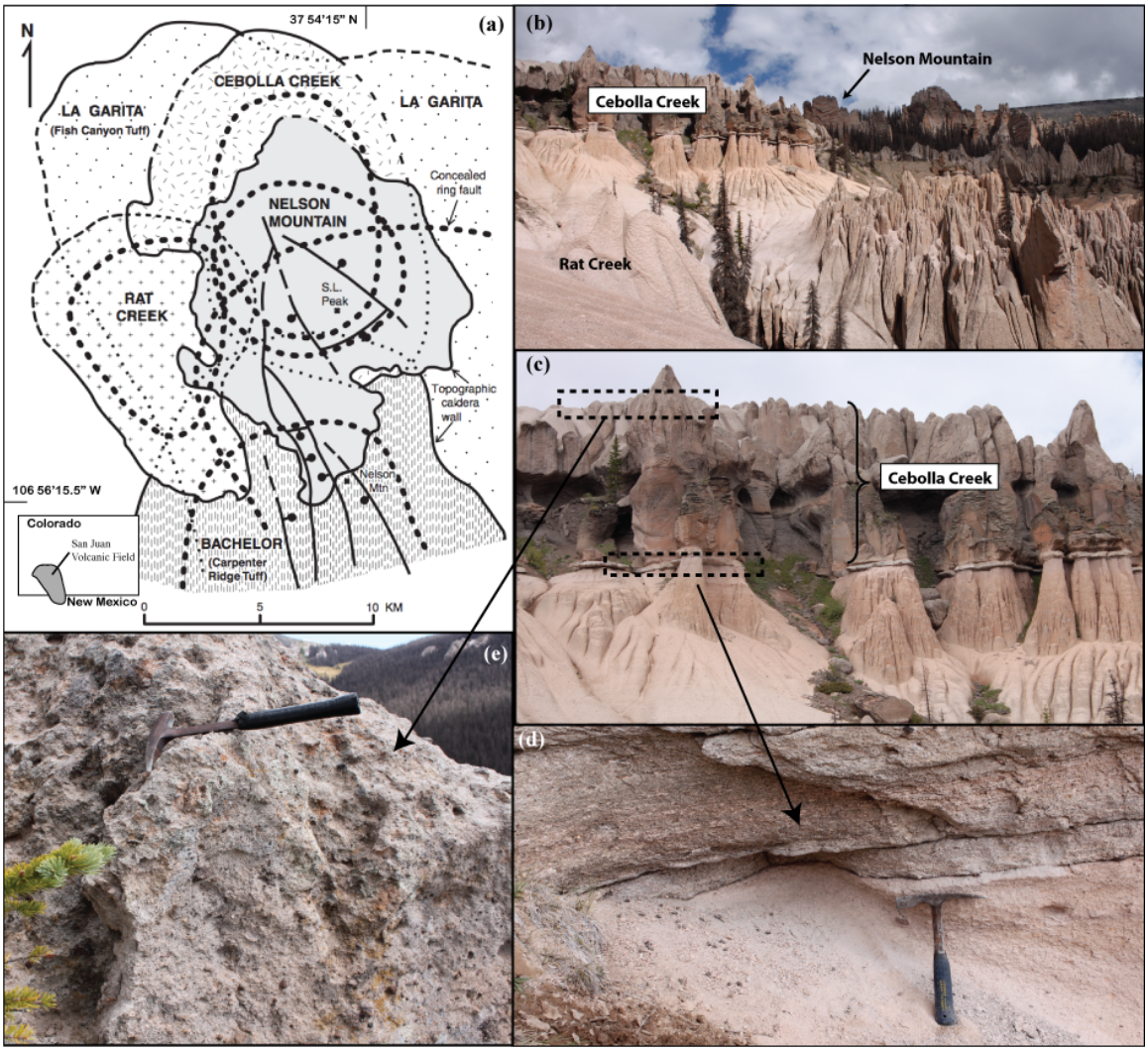

Figure 5.1. clockwise from upper left (a) Simplified geological map outlining the extent of selected ignimbrite tuffs associated with the San Juan region, with the bottom left insert outlining the location of the volcanic field (modified from Lipman and McIntosh, 2008). One of the main sampling areas in this study, the Wheeler Geologic Monument is located 15 km ESE of Nelson Mountain. (b) Photograph of the Wheeler Geologic Monument where all three ignimbrites of the San Luis complex are exposed. The Rat Creek Tuff makes up the lower portion of the Wheeler Geologic Monument, with the thin layer (0.5 m) halfway up marking the transition into the Cebolla Creek Tuff. Nelson Mountain is the very cap. (c) Close up of the Cebolla member exposed at the Wheeler Geologic monument, where ticked boxes encompass the sampled areas. Arrows point to close-up of sample locations at the base (d) and upper portion (e) of the Cebolla Creek Tuff.

The Cebolla Creek Tuff (~250 km^3) is the middle unit of three compositionally distinct ignimbrites that were erupted in a short period of time from the San Luis caldera complex. These three tuffs are among the last (of 10) that were erupted from the central San Juan caldera complex (Lipman, 2007). The San Luis complex is located along the northwestern margin of the La Garita Caldera, and the three tuffs are partly ponded within the La Garita depression (Fig. 5.1a). The Cebolla Creek Tuff is the least evolved, least heterogeneous, and most crystal-rich (35-40 vol%) of the three units. The underlying Rat Creek Tuff (150 km^3) and overlying Nelson Mountain Tuff (500 km^3) are compositionally zoned from basal, crystal-poor rhyolite to upper, crystal-rich dacite (Fig. 5.1; Lipman, 2007). Bracketing age constraints come from argon ages on sanidine from the older Rat Creek (26.92 ± 0.05 Ma) and younger Nelson Mountain (26.91±0.03 Ma) tuffs (Lipman and McIntosh, 2008). These dates render these three units indistinguishable in age, and imply a recurrence rate of <50,000 years (Lipman and McIntosh, 2008).

3. Analytical Methods

Seven poorly to moderately-welded Cebolla Creek bulk-rock samples were collected within the central caldera cluster of the San Juan Volcanic Field (Table 5.1). The majority of samples were collected from distinct stratigraphic levels from the excellent exposure in the Wheeler Geologic Area (Fig. 5.1). Whole-rock compositions of three of the more welded samples were analyzed by X-ray fluorescence for major and trace elements at the Geoanalytical Lab at Washington State University, using the methods of Johnson et al. (1999). These three samples include the basal (BOTOF) and upper ignimbrite (TopCeb1) from the Wheeler Geologic Area (Fig. 5.1) and one

Table 5.1. Whole rock major and trace element data for three Cebolla Creek whole rock samples, including sampling locations.

	TopCeb 1^	BOTOF	15L-123
Normalized Major Elements (Weight %):			
SiO_2	61.32	60.69	62.94
TiO_2	0.774	0.776	0.709
Al_2O_3	17.70	17.93	17.06
FeO*	5.96	6.04	5.29
MnO	0.129	0.140	0.126
MgO	2.45	2.42	1.62
CaO	4.98	5.13	4.35
Na_2O	3.44	3.48	4.00
K_2O	2.94	3.08	3.58
P_2O_5	0.315	0.309	0.315
Total	95.05	95.98	98.63
**Major elements are normalized on a volatile-free basis, with total Fe expressed as FeO.*			
Trace elements (in ppm)			
La	41.86	38.62	43.72
Ce	83.92	78.58	86.17
Pr	10.19	9.63	10.46
Nd	39.19	37.61	39.98
Sm	7.68	7.54	7.81
Eu	1.92	1.86	1.82
Gd	6.22	6.08	6.21
Tb	0.90	0.91	0.92
Dy	5.18	5.21	5.20
Ho	1.01	1.02	1.02
Er	2.68	2.71	2.73
Tm	0.38	0.38	0.40
Yb	2.45	2.44	2.52
Lu	0.39	0.37	0.39
Ba	970	823	1088
Th	7.78	6.75	8.35
Nb	13.44	13.34	14.15
Y	26.56	27.21	27.51
Hf	5.84	4.98	5.80
Ta	0.81	0.77	0.88
U	2.42	2.32	3.00
Pb	14.71	13.70	15.45
Rb	86.7	103.9	100.9
Cs	2.36	4.30	2.54
Sr	734	754	675
Sc	10.9	11.4	10.3
Zr	230	197	232
Nonwelded Cebolla A: 38° 05.900', 106° 59.308’ ^Wheeler TopCeb : 37.8840° N, 106.7840° W ^Basal Wheeler BOTOF: 37.8840° N, 106.7840° W Mid Wheeler (CCT-WFM): 37.8840° N, 106.7840° W ^Basal Vitrophere 15L-123: 38° 05.900', 106° 59.308’			

vitrophyre sample 15L-123, taken from Los Pinos Pass (Table 1). The two more welded samples, TopCeb1 and 15L-123, where made into thin sections for textural evaluation.

Samples were hand crushed and picked for amphibole, biotite, and plagioclase phenocrysts. Mineral separates were mounted individually in order to ensure lengthwise orientation for core/rim comparison. Although typically devitrified in most of the bulk rock material sampled, glassy melt inclusions (MIs) hosted in plagioclase phenocrysts were found in one sample (Ceb A). Most of these glassy plagioclase-hosted inclusions contain vapor bubbles, and the glass coloration ranged from clear to brown, where brown inclusions tend to be located in the interior of grains. All grains were individually polished to a ¼-μm finish, and then those that contained a glassy MI were doubly intersected for analysis of H_2O and CO_2 measurement by Fourier-transform infrared spectroscopy (FTIR) at the University of Oregon. Some doubly-polished grains exposed multiple melt inclusions which allowed for additional compositional analysis in single grains.

For all FTIR analyses, the main infrared spectra peaks of interest for this study were the total water peak at 3550 cm^{-1} and the 2350 cm^{-1} CO_2 peak, common in more evolved compositions. Absorbance was converted into water concentration using the Beer-Lambert law: $c_i = M_i \cdot A/\rho \cdot d \cdot \varepsilon$, where c_i is the concentration of the species (in wt.%), M_i is the molecular weight of the species (g/mol), A is the absorbance (height) of the relevant vibration band, ρ is the sample density (g/L), d is the thickness of the area analyzed (cm) and $\underline{\varepsilon}$ is the molar absorbance (L/mol·cm). An iterative procedure was used to converge on appropriate values of ρ and ε [Eq. 1 (Skirius, 1990) and Eq. 2 (Leschik et al., 2004)].

$$\rho = 2350 - 12.6 \times H_2O \text{ concentration (wt.\%)} \quad \text{Eq. 1}$$

$$\varepsilon = 80 - 1.36 \times H_2O \text{ concentration (wt.\%)} \quad \text{Eq. 2}$$

Final glass densities range from 2290-2340 kg/m^3. The thickness of each inclusion was measured using both a digital micrometer (±2 μm) and the reflectance interference fringe method of Wysoczanski and Tani (2006), and the average result from the two methods was used in the final concentration calculation. Based on uncertainties in all variables entered into Beer-Lambert Law, average 1 SE uncertainty for H_2O is ± 0.16 wt.% and for CO_2 ± 10 ppm.

Following FTIR measurements, all polished doubly intersected melt inclusions and mineral separates were embedded in a 1-inch epoxy mount. Melt inclusions, and amphibole and biotite phenocrysts were analyzed for major elements, plus Cl and F using a Cameca SX-100 electron microprobe at the University of Oregon. Operating conditions for all glasses were 15 kV and 10 nA sample current for Si, Ca, Na, Fe, Al, Mg, and K, and 50 nA current for Cl, F, S, P and Ti, with a beam size of 10 μm. Amphibole and biotite major element analyses were run using 15 kV, a current of 30 nA, and a focused 1 μm beam. For all analyses Na, K, Si, and Al were measured first, and their concentrations were calculated using a time-dependent intensity correction using Probe for Windows (Donovan et al. 2007**)**. To account for compositional dependence of these corrections on H_2O concentration, FTIR measured H_2O concentrations were added to each individual melt inclusion analysis, and estimated structural water concentrations considered for amphibole (2.0 wt.%) and biotite (5.0 wt.%). Plagioclase phenocrysts were imaged and measured for major elements using a JEOL JXA 8230 electron probe microanalysis

(EPMA) system at Victoria University of Wellington. Operating conditions for all feldspar analyses were 15 kV and 12 nA for Si, Ca, Na, Fe, Al, and K, with a focused beam size of 1 μm. Prior to analysis, back-scattered electron (BSE) images were taken to identify zoning patterns, which were then used to determine analytical spots. Host plagioclase spot analyses were also taken next to each melt inclusion analyzed for H_2O and CO_2.

Amphibole and glasses were subsequently analyzed for trace elements using Laser-Ablation Inductively Coupled Plasma Mass Spectrometry (LA-ICP-MS) at Oregon State University using a 30-μm spot size for glasses and 50-μm for amphibole, with five glass standards (GSD-1G, BHVO, ANTO, NIST-612, and BCR) for calibration, ^{29}Si as an internal standard, and GSD-1G as a check standard throughout the run. Additional trace element measurements on amphibole phenocrysts were obtained at the Earth Observatory of Singapore, using the same operating conditions, and GSD-1G, BCR and HVO-2G as standards.

4. Results

4.1 Whole-rock chemistry and petrologic overview

The SiO_2 range for the three whole-rock analyses (60.7-62.9 wt.%) is in good agreement with the 61-64 wt.% range previously reported for the Cebolla Creek Tuff (Lipman, 2007; Lipman and McIntosh, 2008). Modal phenocryst abundances, in rank order, are: plagioclase, amphibole, biotite, magnetite, with minor amounts of apatite, and traces of olivine (xenocrystic?), quartz, and sanidine (Fig. 5.2). Some of the phenocrysts

appear fractured, perhaps due to fragmentation during eruption, a process that has a more pronounced effect on crystal-rich magmas (e.g. Best and Christiansen, 1997). The matrix

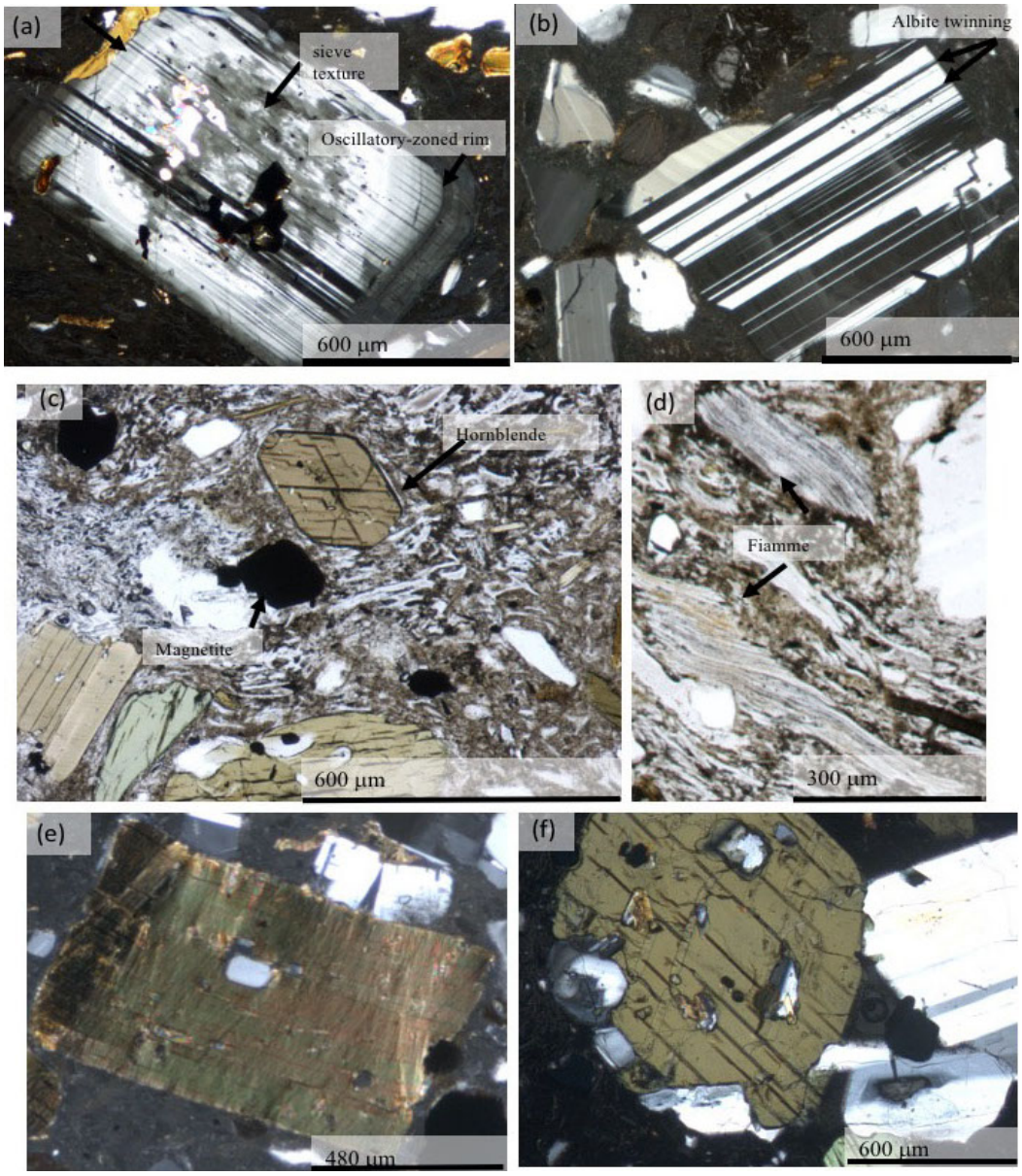

Figure 5.2. Photomicrographs of phenocrysts and matrix textures that typify the Cebolla Creek Tuff. Scale bars for each image are shown as black lines. (a) Euhedral plagioclase phenocryst with oscillatory-zoned rim and sieved texture core. (b) Subhedral plagioclase with albite twinning. (c) Matrix with non-welded texture containing euhedral hornblende phenocrysts, hornblende fragments, magnetite and subhedral biotite phenocrysts. (d) Example of the moderately-welded, fiamme texture most pronounced in sample TopCeb1. (e) Euhedral biotite phenocrysts in these samples often exhibit signs of stress in the form of wavy extinction, and contain inclusions of magnetite and feldspar. (f) Larger hornblende phenocrysts containing complex intergrowth of plagioclase.

is moderately welded, characterized by thin-walled vesicles and compaction textures, including fiamme. The degree of welding is not uniform, as some thin sections preserve more defined textures (e.g. better developed fiamme) than others (Fig. 5.2c,d).

4.2 Plagioclase compositions

Plagioclase is the volumetrically dominant phenocryst phase (60-70%), with two textural types present: (1) the more dominant, larger, and euhedral (1-2 mm), oscillatory-zoned phenocrysts, many of which display partly-dissolved cores, versus (2) weakly zoned (An_{33-45}) fragmented phenocrysts (<1 mm), some of which preserve albite twining. Oscillatory plagioclase is normally zoned on a first-order basis. Core concentrations range from An_{51-79}, and rims (within 10 μm of matrix glass) converge on An_{39-44} (Table 5.2). Some grains include one high-An zone between the inner core and several hundred micrometers from the rim, often following a dissolution zone (Fig. 5.3). Point analyses of the weakly to non- zoned plagioclase phenocrysts, the prevailing hosts for the melt inclusions analyzed here, range from An_{35-43}, thereby overlapping with the rim compositions of oscillatory-zoned plagioclase.

Table 5.2. Plagioclase major element concentrations (EPMA, in wt.%) with average 1 SE. Plagioclases analyses are taken from three samples: 15L-123, Top Ceb and Ceb A, with sample locations found in Table 5.1. All samples with an 'L' label are associated with a spot location from an oscillatory zone (see Fig. 5.2).

Sample Name	An	SiO_2	TiO_2	Al_2O_3	CaO	Na_2O	K_2O	Total
	AVRG. 1 SE	*0.07*	*0.01*	*0.07*	*0.06*	*0.03*	*0.01*	
15L-123 Plag_2 L1	71	50.61	0.07	31.62	14.34	3.09	0.17	99.90
15L-123 Plag_2 L2	71	50.50	0.04	31.69	14.30	3.15	0.18	99.86
15L-123 Plag_2 L3	78	48.63	0.04	33.12	15.70	2.33	0.11	99.92
15L-123 Plag_2 L4	54	55.04	0.02	28.87	10.70	4.86	0.41	99.90
15L-123 Plag_2 L5	41	58.42	0.00	26.61	8.19	6.03	0.68	99.92
15L-123 Plag_1 L1	79	48.15	0.02	33.38	15.96	2.25	0.11	99.88
15L-123 Plag_1 L2	54	55.19	0.05	28.77	10.67	4.85	0.39	99.92
15L-123 Plag_1 L3	44	57.72	0.04	27.10	8.76	5.69	0.58	99.89
15L-123 Plag_1 L4	41	58.37	0.00	26.57	8.24	6.07	0.64	99.89
15L-123 Plag_1 L5	42	58.33	0.00	26.67	8.35	5.99	0.64	99.98
15L-123 Plag_1 L6	42	58.27	0.00	26.71	8.38	5.99	0.54	99.89
15L-123 Plag_3 L1	55	54.73	0.01	29.01	11.10	4.68	0.43	99.95
15L-123 Plag_3 L2	54	54.90	0.03	28.71	11.06	4.82	0.44	99.97
15L-123 Plag_3 L3	73	49.97	0.00	32.02	14.83	2.88	0.19	99.90
15L-123 Plag_3 L4	74	49.73	0.00	32.32	14.99	2.77	0.15	99.95
15L-123 Plag_3 L6	69	51.16	0.05	31.37	13.75	3.36	0.20	99.89
15L-123 Plag_3 L7	60	53.47	0.05	29.72	12.09	4.28	0.30	99.90
15L-123 Plag_3 L8	41	58.44	0.00	26.77	8.12	5.99	0.64	99.96
15L-123 Plag_4 L1	34	60.58	0.00	25.36	6.56	6.56	0.90	99.96
15L-123 Plag_4 L2	35	60.13	0.01	25.56	6.86	6.55	0.84	99.96
15L-123 Plag_4 L3	42	58.47	0.02	26.58	8.29	5.91	0.66	99.94
15L-123 Plag_4 L4	42	58.49	0.00	26.62	8.23	6.00	0.62	99.96
15L-123 Plag_5 RIM	45	58.61	0.01	26.91	8.41	5.35	0.63	99.92
15L-123 Plag_6 RIM	43	58.55	0.01	26.89	8.30	5.61	0.58	99.93
15L-123 Plag_7 RIM	45	57.54	0.04	27.22	8.92	5.61	0.58	99.91

Sample Name	An	SiO_2	TiO_2	Al_2O_3	CaO	Na_2O	K_2O	Total
	AVRG. 1 SE	*0.07*	*0.01*	*0.07*	*0.06*	*0.03*	*0.01*	
TopCeb1 Plag_1 L1	73	50.14	0.05	32.09	14.67	2.83	0.19	99.98
TopCeb1 Plag_1 L2	76	49.39	0.02	32.50	15.28	2.58	0.15	99.93
TopCeb1 Plag_1 L3	81	47.80	0.05	33.53	16.37	2.03	0.10	99.88
TopCeb1 Plag_1 L4	76	49.31	0.02	32.48	15.28	2.57	0.14	99.82
TopCeb1 Plag_1 L5	74	50.29	0.02	31.92	14.76	2.66	0.26	99.90
TopCeb1 Plag_1 L7	68	51.41	0.03	31.05	13.72	3.45	0.22	99.88
TopCeb1 Plag_1 L8	53	55.06	0.01	28.79	10.73	4.93	0.38	99.91
TopCeb1 Plag_3 L1	65	51.91	0.02	30.74	13.25	3.77	0.25	99.93
TopCeb1 Plag_3 L2	68	51.69	0.04	31.05	13.51	3.35	0.23	99.87
TopCeb1 Plag_3 L3	57	54.28	0.03	29.29	11.36	4.58	0.38	99.91
TopCeb1 Plag_3 L4	62	52.75	0.05	30.20	12.57	4.02	0.29	99.89
TopCeb1 Plag_3 L5	53	55.33	0.03	28.64	10.55	4.96	0.41	99.91
TopCeb1 Plag_3 L6	43	57.81	0.01	27.00	8.66	5.88	0.56	99.92
TopCeb1 Plag_5 L2	51	55.72	0.00	28.38	10.23	5.16	0.43	99.92
TopCeb1 Plag_5 L3	43	57.88	0.03	26.99	8.60	5.86	0.55	99.91
TopCeb1 Plag_5 L4	49	56.29	0.02	28.00	9.85	5.28	0.44	99.88
TopCeb1 Plag_5 L5	43	57.60	0.00	27.19	8.54	5.99	0.59	99.91
TopCeb1 Plag_2 RIM	44	58.75	0.00	26.65	8.37	5.50	0.65	99.92
TopCeb1 Plag_4 RIM	44	58.47	0.04	26.86	8.41	5.56	0.63	99.96
TopCeb1 Plag_6 RIM	43	58.58	0.01	26.84	8.33	5.60	0.61	99.96
TopCeb1 Plag_7 RIM	39	59.01	0.03	26.16	7.72	6.27	0.75	99.94
TopCeb1 Plag_8 RIM	39	59.61	0.02	26.11	7.51	5.91	0.76	99.92

Table 5.2. *(continued)* Plagioclase major element data are all from sample 'Ceb A' and are a spot analysis near a measured melt inclusion.

Sample Name	An	SiO_2	TiO_2	Al_2O_3	CaO	Na_2O	K_2O	Total
AVRG. 1 SE		*0.07*	*0.01*	*0.07*	*0.06*	*0.03*	*0.01*	
Cebolla1 #1 feld_1	43	56.92	0.03	28.34	8.53	5.93	0.60	100.70
Cebolla1 #1 feld_1_2	37	56.82	0.02	26.53	7.41	6.51	0.76	98.33
Cebolla1 #3 feld_1	35	60.38	0.00	26.45	7.11	6.64	0.82	101.71
Cebolla1 #3 feld_2	37	56.23	0.02	26.57	7.41	6.39	0.73	97.68
Cebolla1 #3 feld_3	35	58.35	0.01	26.33	7.04	6.80	0.85	99.74
Cebolla1 #9 feld_1	39	60.19	0.06	27.25	7.58	6.12	0.67	102.24
Cebolla1 #12 feld_1	43	57.74	0.00	27.48	8.37	5.82	0.62	100.38
Cebolla1 #14 feld_1	43	56.56	0.01	27.86	8.42	5.84	0.63	99.68
Cebolla1 #14 feld_2	39	58.11	0.00	27.16	7.71	6.28	0.73	100.36
Cebolla1 #15 feld_1	41	57.02	0.02	27.66	8.20	5.99	0.66	99.92
Cebolla1 #18 feld_1	43	56.69	0.00	27.22	8.59	5.95	0.60	99.41
Cebolla1 #18 feld_2	46	56.05	0.02	27.84	9.24	5.61	0.53	99.59
Cebolla1 #21 feld_1	39	57.31	0.00	27.30	7.85	6.30	0.71	99.86
Cebolla1 #21 feld_2	41	57.22	0.01	27.77	8.23	6.06	0.65	100.33
Cebolla1 #23 feld_1	40	56.60	0.03	27.62	7.83	6.05	0.68	99.13
Cebolla1 #26 feld_1	41	58.21	0.02	27.70	8.10	6.13	0.67	101.20
Cebolla1 #28 feld_1	38	57.18	0.02	27.08	7.67	6.34	0.73	99.36
Cebolla1 #30 feld_1	41	56.57	0.03	27.60	8.07	5.88	0.63	99.06
Cebolla1 #30 feld_1_ 2	41	56.07	0.00	27.33	8.26	6.15	0.66	98.78
Cebolla1 #31 feld_1	34	58.27	0.03	26.02	6.77	6.77	0.91	99.15
Cebolla1 #32 feld_1_2	41	55.85	0.00	27.07	8.06	5.95	0.66	97.94
Cebolla1 #35 feld_1	38	57.97	0.03	26.82	7.54	6.40	0.75	99.86
Cebolla1 #35 feld_2	49	53.67	0.03	28.39	9.58	5.27	0.47	97.79
Cebolla1 #40 feld_1	41	57.51	0.01	27.71	8.20	6.17	0.67	100.61
Cebolla1 #40 feld_1_2	41	58.72	0.00	27.93	8.12	6.13	0.69	101.96

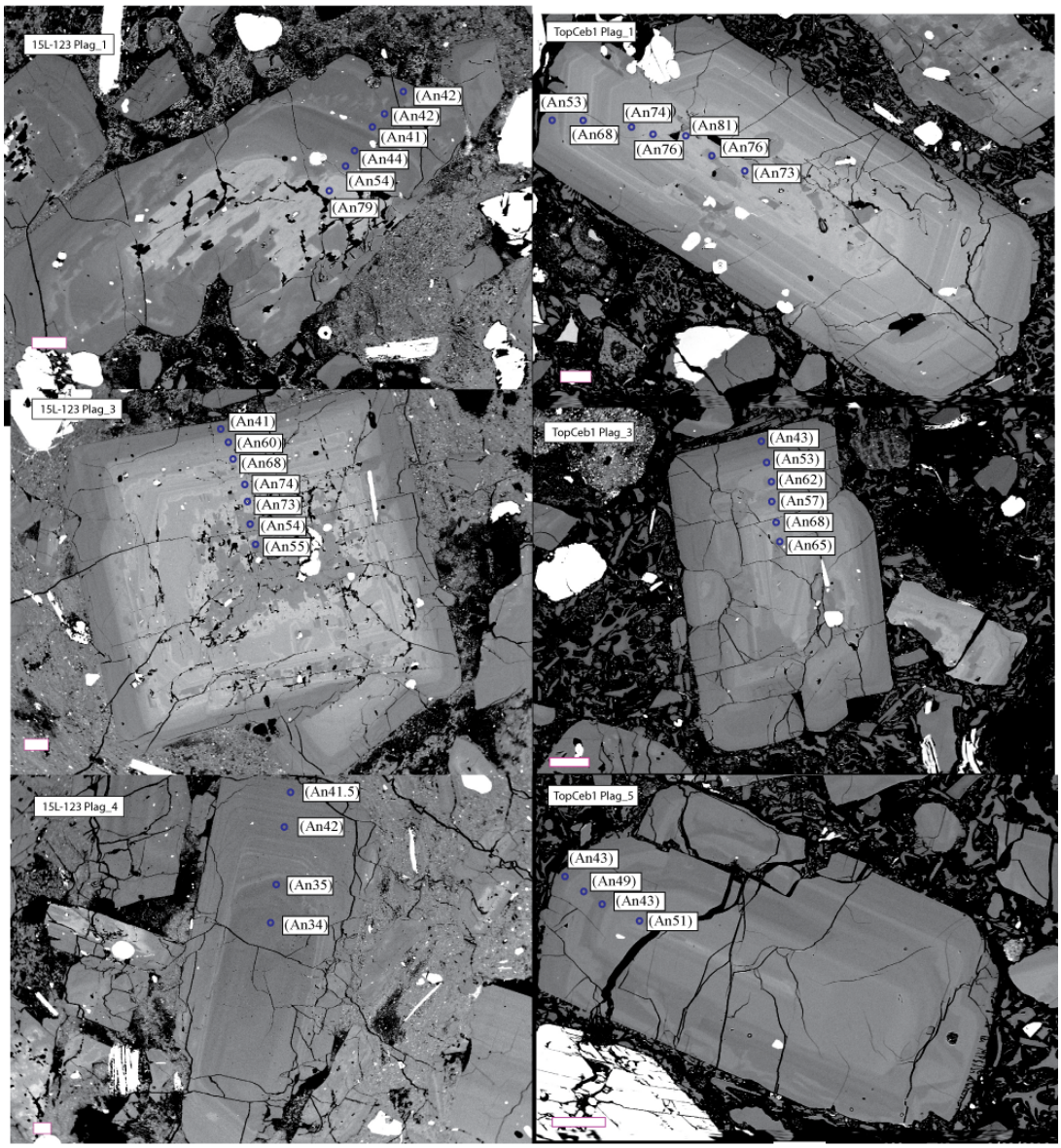

Figure 5.3. BSE images of oscillatory zoned plagioclase phenocrysts, where blue circles mark analytical spot. Anorthite (An) concentration is shown next to each point. Plagioclase grains were imaged from two separate samples, 15L-123 and TopCeb1. White box in lower left corner of each photo represents 100 μm.

4.3 Amphibole major and trace element chemistry

Amphibole (hornblende) phenocrysts are largely euhedral to subhedral and contain abundant oxides, apatite, and melt inclusions (Fig. 5.3a). The amphiboles exhibit relatively homogeneous Al_2O_3 concentrations (8.3-9.8 wt.%) and Mg# values (63-68;

where Mg# is defined as 100*Mg/Mg+Fe*) between rim and core analyses, where EPMA rims were measured near the LA-ICP-MS pit, typically falling within 50 mm of the edge (Fig. 5.4; Table 5.3). A few core analyses reach 10.3-12.1 wt.% Al_2O_3, but some entire phenocrysts are comparably aluminous (Table 5.3). There are no zoning trends for F and Cl in amphiboles (Fig. 5.4c, Table 5.3), and biotites are similarly homogeneous for halogen concentrations. The latter are not significant findings however, as EPMA totals biotite are consistently too low (~92%), perhaps due to post-emplacement degradation.

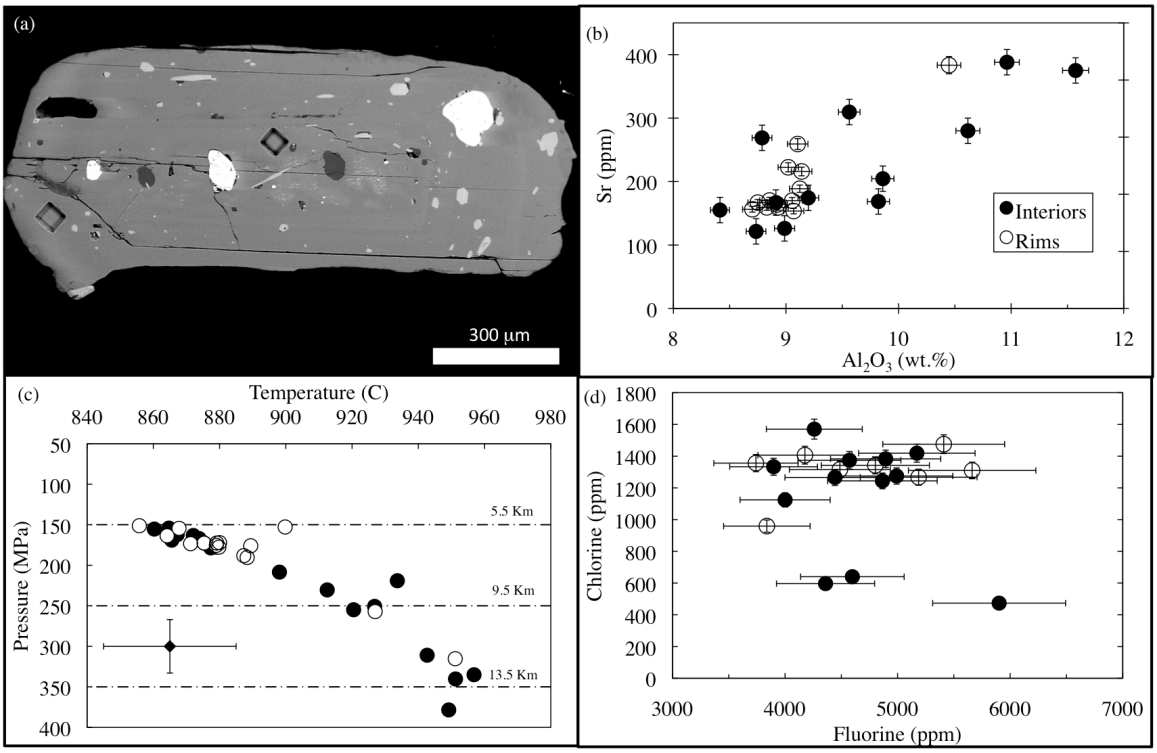

Figure 5.4. (a) BSE image of an amphibole phenocryst from BOTOF Amph-12. Square boxes represents LA-ICP-MS laser pits. (b) Sr (ppm) measured for amphiboles from BOTOF, TopCeb and CebA using LA-ICP-MS verses Al_2O_3 (wt.%) for core (black circles) and rim (white circles) analyses (c) Pressure (MPa) vs. temperature (°C) for all interior and rim using the Ridolfi et al. (2010) thermobarometer. Dashed lines represent depth conversion using a crustal density of 2600 kg/m^3 (d) Cl vs. F concentrations in ppm measured using EPMA.

Table 5.3. Amphibole major and trace element concentrations (EMPA, wt.%) from three different samples, two taken from the Wheeler Geologic Area (TopCeb 1, CebBOTOF) and the third CebA is the sample where glassy melt inclusions were found and analyzed. Totals are displayed anhydrous (see Methods). Concentrations of F and Cl were converted into ppm.

	Position	Mg #	SiO_2	TiO_2	Al_2O_3	FeO	MnO	MgO	CaO	Na_2O	K_2O	Total	F (ppm)	Cl (ppm)	Temp	Pressure	H_2O
	Avrg. 1 SD		*0.11*	*0.42*	*0.05*	*0.32*	*0.03*	*0.05*	*0.14*	*0.06*	*0.04*				*Using Ridolfi et al. 2010*		
CebAAmph-1	Inner		-	-	-	-	-	-	-	-	-	-	-	-	-	-	-
CebAAmph-1	Rim	67	44.25	2.08	8.64	12.01	0.60	13.40	11.10	1.96	0.87	94.9	-	650	871	173	4.3
CebAAmph-10	Inner	66	44.98	2.21	8.45	12.24	0.53	13.41	11.47	1.97	0.90	96.2	-	690	867	162	4.1
CebAAmph-10	Rim	-	-	-	-	-	-	-	-	-	-	-	-	-	-	-	-
CebAAmph-11	Inner	66	44.55	2.17	8.57	12.58	0.49	13.45	11.49	1.92	0.93	96.1	-	880	874	167	4.0
CebAAmph-11	Rim	67	45.52	2.14	8.48	12.45	0.52	14.00	11.40	2.01	0.89	97.4	-	780	868	154	3.7
CebAAmph-6	Rim	66	45.05	2.19	8.78	12.32	0.55	13.64	11.52	1.98	0.95	97.0	-	660	875	172	4.1
CebAAmph-9	Inner	67	45.39	2.17	8.67	11.91	0.46	13.56	11.43	1.93	0.92	96.4	-	990	866	169	4.4
CebAAmph-9	Rim	66	45.81	2.13	8.67	12.80	0.48	13.75	11.44	1.95	0.91	97.9	-	820	900	153	4.3
CebAAmph-15	Inner	65	42.04	2.81	11.51	12.83	0.39	13.35	11.41	2.29	0.90	97.5	4360	597	957	335	5.0
CebAAmph-15	Rim	67	45.17	2.05	8.99	12.66	0.50	14.25	11.36	1.99	0.96	97.9	4487	1315	879	175	3.8
CebAAmph-14	Inner	66	44.74	2.33	8.98	12.64	0.50	13.86	11.19	1.83	0.92	97.0	4894	1383	877	179	4.1
CebAAmph-14	Rim	66	45.64	1.98	8.29	12.65	0.56	13.76	11.36	1.87	0.92	97.0	3742	1356	856	151	4.0
CebAAmph-16	Inner	65	45.28	1.96	8.44	13.24	0.58	14.10	11.32	1.84	0.95	97.7	4865	1244	865	154	3.6
CebAAmph-16	Rim	68	43.62	2.24	8.81	11.90	0.56	14.02	11.27	1.80	0.90	95.1	5035	1063	-		
TopCeb1 amp-26	Inner	68	44.64	2.32	8.83	11.70	0.49	13.72	11.31	2.00	0.95	96.0	-	920	879	178	4.0
TopCeb1 amp-26	Rim	-	-	-	-	-	-	-	-	-	-	-	-	-	-	-	-
TopCeb1 amp-24	Inner	66	43.40	2.60	10.35	12.69	0.38	13.61	11.62	2.25	0.98	97.9	4001	1124	927	251	4.2
TopCeb1 amp-24	Rim	-	-	-	-	-	-	-	-	-	-	-	-	-	-	-	-
TopCeb1 amp-25	Inner	67	45.39	2.05	8.73	12.89	0.50	14.43	11.37	1.87	0.88	98.1	4260	1570	872	163	3.8
TopCeb1 amp-25	Rim	67	45.98	1.89	8.75	12.40	0.58	14.37	11.39	1.83	0.89	98.1	4177	1406	864	164	4.2
TopCeb1 amp-14	Inner	62	42.74	2.53	9.82	14.75	0.47	13.38	11.32	2.03	1.02	98.1	4572	1374	934	219	3.9
TopCeb1 amp-14	Rim	65	44.92	2.23	8.83	12.95	0.49	13.61	11.36	2.05	0.90	97.3	0	770	875	173	4.0
TopCeb1 amp-12	Inner	67	45.60	2.07	8.41	12.22	0.57	14.03	11.38	1.77	0.88	96.9	4444	1266	860	155	4.1
TopCeb1 amp-12	Rim	66	44.54	2.06	8.92	12.61	0.61	13.89	11.33	1.83	0.92	96.7	9070	1270	880	178	4.1
TopCeb1 amp-15	Inner	64	42.17	3.37	12.13	13.02	0.42	13.04	10.37	2.22	1.01	97.8	5902	474	949	378	5.2
TopCeb1 amp-15	Rim	63	41.70	3.10	11.04	12.99	0.41	12.53	11.51	2.21	1.05	96.5	-	330	951	315	4.7
CebBOTOFamp-10	Inner	64	41.79	2.89	10.96	12.81	0.44	12.60	11.35	2.05	0.97	96.5	4991	1275	943	311	5.1
CebBOTOFamp-10	Rim-1	67	44.23	2.11	8.93	12.59	0.58	14.40	11.33	1.94	0.89	97.7	5662	1310	889	176	3.6
CebBOTOFamp-10	Rim-2	66	43.89	2.18	9.12	12.54	0.46	13.72	11.30	1.81	0.95	96.7	5410	1475	888	190	4.1
CebBOTOFamp-12	Inner	67	42.89	2.27	9.86	12.30	0.51	13.76	11.24	1.82	0.98	96.3	5171	1419	912	230	4.3
CebBOTOFamp-12	Rim	65	44.21	2.24	8.68	12.82	0.58	13.36	11.43	1.98	0.97	96.3	-	850	880	172	3.8
CebBOTOFamp-1	Inner	66	42.37	2.15	11.57	12.36	0.33	13.74	11.39	2.19	1.07	97.7	4598	640	951	340	4.8
CebBOTOFamp-1	Rim	63	42.94	2.65	10.45	13.86	0.48	13.07	11.40	2.24	1.11	98.7	3839	959	927	257	4.0
CebBOTOFamp-3	Inner	65	43.50	2.72	10.35	12.67	0.45	13.08	11.52	2.17	1.06	97.5	-	-	920	255	4.5
CebBOTOFamp-3	Rim	67	44.36	2.08	9.14	12.33	0.51	13.96	11.35	1.95	0.92	97.2	5187	1267	887	188	4.1
CebBOTOFamp-4	Inner	66	44.10	2.49	9.56	12.42	0.48	13.63	11.38	1.93	1.00	97.5	3899	1333	898	208	4.2
CebBOTOFamp-4	Rim	67	44.54	2.00	8.83	12.56	0.59	14.18	11.28	1.84	0.90	97.3	4802	1342	879	173	3.9

Table 5.3. *(continued)* Amphibole trace element concentrations (LA-ICP-MS) with averaged SE. CaO was used an internal standard.

	Position	Li	Sc	Co	Ni	Cu	Zn	Ga	Rb	Sr	Y	Zr	Nb	Sn	Ba	La	Ce	Pr	Nd	Sm	Eu	Gd	Dy	Er	Yb	Pb
	Avrg. 1 SD	*0.9*	*6.3*	*3.1*	*1.5*	*0.2*	*10.1*	*4.5*	*0.1*	*10.4*	*12.6*	*8.0*	*3.1*	*0.8*	*8.5*	*2.1*	*7.0*	*1.3*	*5.2*	*1.9*	*0.4*	*1.5*	*1.3*	*0.9*	*0.5*	*0.1*
CebAAmph-1	Inner	6.1	81	49	20	0.8	187	37	3.0	419	77	99	15	2.1	381	16	64	12	67	19	4.6	17	13	8	6	1.1
CebAAmph-1	Rim	6.9	112	45	14	0.8	224	33	2.8	238	130	108	30	4.0	292	37	151	24	133	35	6.6	31	28	16	13	1.8
CebAAmph-10	Inner	5.8	155	48	15	0.7	203	23	2.2	269	212	100	35	4.5	162	69	237	38	190	51	7.7	50	41	23	17	1.5
CebAAmph-10	Rim	5.5	130	41	15	0.6	214	24	2.3	135	197	106	38	4.6	171	55	203	36	180	50	7.3	51	37	20	17	1.4
CebAAmph-11	Inner	5.4	133	48	14	0.8	210	27	2.6	167	162	102	34	4.6	201	41	180	31	155	39	6.4	39	34	18	16	1.8
CebAAmph-11	Rim	6.4	103	43	15	0.9	224	25	2.4	124	150	86	34	4.6	165	55	197	35	176	43	5.8	42	32	18	12	1.5
CebAAmph-6	Rim	6.4	116	47	13	1.1	240	28	2.2	139	168	102	36	5.2	185	58	227	35	183	45	6.8	40	31	19	15	1.5
CebAAmph-9	Inner	5.7	125	46	15	0.6	220	23	2.0	126	173	98	35	4.2	148	43	175	31	155	46	6.4	41	31	19	15	1.3
CebAAmph-9	Rim	5.9	141	86	28	1.4	518	40	2.2	139	198	108	41	7.0	167	46	196	33	173	48	7.8	51	38	23	19	1.5
CebAAmph-15	Inner	-	-	-	-	-	-	-	-	-	-	-	-	-	-	-	-	-	-	-	-	-	-	-	-	-
CebAAmph-15	Rim	-	-	-	-	-	-	-	-	-	-	-	-	-	-	-	-	-	-	-	-	-	-	-	-	-
CebAAmph-14	Inner	-	-	-	-	-	-	-	-	-	-	-	-	-	-	-	-	-	-	-	-	-	-	-	-	-
CebAAmph-14	Rim	-	-	-	-	-	-	-	-	-	-	-	-	-	-	-	-	-	-	-	-	-	-	-	-	-
CebAAmph-16	Inner	-	-	-	-	-	-	-	-	-	-	-	-	-	-	-	-	-	-	-	-	-	-	-	-	-
CebAAmph-16	Rim	-	-	-	-	-	-	-	-	-	-	-	-	-	-	-	-	-	-	-	-	-	-	-	-	-
TopCeb1 amp-26	Inner	6.7	93	42	14	-	186	-	2.6	174	188	112	39	-	202	61	213	38	189	49	7.9	43	38	19	15	1.7
TopCeb1 amp-26	Rim	8.8	95	45	14	-	183	-	3.1	205	155	102	35	-	226	38	147	27	139	37	6.3	34	30	16	14	1.7
TopCeb1 amp-24	Inner	-	-	-	-	-	-	-	-	-	-	-	-	-	-	-	-	-	-	-	-	-	-	-	-	-
TopCeb1 amp-24	Rim	5.8	84	42	12	-	173	-	3.5	156	165	118	39	-	182	41	163	30	154	40	6.7	38	33	17	14	1.6
TopCeb1 amp-25	Inner	5.0	95	42	14	-	178	-	2.4	122	185	89	40	-	144	43	168	31	163	44	6.9	42	37	19	15	1.5
TopCeb1 amp-25	Rim	4.6	87	43	13	-	181	-	2.5	135	167	101	41	-	161	43	168	30	154	41	6.4	38	33	17	14	1.6
TopCeb1 amp-14	Inner	6.5	104	44	14	-	179	-	2.9	169	176	117	37	-	199	44	169	31	162	43	7.6	40	35	17	15	1.7
TopCeb1 amp-14	Rim	9.4	90	42	12	-	197	-	2.5	121	165	94	41	-	151	41	161	30	151	41	6.3	36	33	16	14	1.6
TopCeb1 amp-12	Inner	8.4	105	41	10	-	193	-	2.8	155	170	103	41	-	201	43	170	32	160	44	6.7	38	34	18	14	1.7
TopCeb1 amp-12	Rim	6.7	114	43	12	-	204	-	2.6	132	193	107	48	-	184	49	198	37	185	50	7.8	43	39	20	16	1.7
TopCeb1 amp-15	Inner	-	-	-	-	-	-	-	-	-	-	-	-	-	-	-	-	-	-	-	-	-	-	-	-	-
TopCeb1 amp-15	Rim	-	-	-	-	-	-	-	-	-	-	-	-	-	-	-	-	-	-	-	-	-	-	-	-	-
CebBOTOFamp-10	Inner	6.2	102	51	21	-	167	-	6.2	388	73	91	13	-	401	22	73	12	59	17	5.0	16	14	8	7	2.8
CebBOTOFamp-10	Rim-1	5.8	96	43	13	-	182	-	2.6	127	182	100	43	-	168	46	177	33	166	44	6.7	39	35	18	15	1.6
CebBOTOFamp-10	Rim-2	5.7	101	45	15	-	162	-	3.3	160	186	108	39	-	205	46	177	33	171	46	7.3	41	36	19	16	1.7
CebBOTOFamp-12	Inner	5.8	75	46	16	-	173	-	3.1	205	145	115	34	-	243	38	145	26	135	36	6.5	32	27	15	13	1.8
CebBOTOFamp-12	Rim	5.5	84	46	15	-	175	-	3.1	197	145	112	36	-	212	37	143	26	137	36	6.4	32	28	15	13	1.7
CebBOTOFamp-1	Inner	6.2	70	40	7	-	132	-	5.2	375	93	157	17	-	370	34	109	19	99	24	6.4	23	18	9	8	4.0
CebBOTOFamp-1	Rim	6.3	97	45	15	-	158	-	4.5	376	109	128	25	-	509	25	96	19	100	27	6.2	26	22	11	9	1.8
CebBOTOFamp-3	Inner	5.7	80	42	8	-	186	-	3.5	280	118	118	29	-	287	34	127	22	115	30	6.0	26	23	12	11	2.2
CebBOTOFamp-3	Rim	6.3	85	40	11	-	187	-	3.2	190	155	147	36	-	241	40	152	28	145	38	6.9	34	29	16	13	1.7
CebBOTOFamp-4	Inner	5.4	80	42	17	-	158	-	2.9	310	98	99	22	-	219	32	117	21	103	26	5.3	23	19	10	8	2.5
CebBOTOFamp-4	Rim	5.6	84	42	13	-	188	-	2.6	127	163	99	41	-	173	42	164	30	153	38	5.9	35	31	17	14	1.4

4.4 Melt inclusion major, trace, and volatile chemistry

All analyzed feldspar-hosted melt inclusions (MIs) are rhyolitic (average SiO_2 = 74.2 ±0.46 wt.%), with low MgO (BDL, <0.01 wt.%), FeO (average 1.0 ± 0.12 wt.%), TiO_2 (average 1.0 ± 0.07 wt.%), and CaO (average 1.0 ± 0.08 wt.%) concentrations (Fig. 5.5). Matrix glass analyses overlap with MIs in their SiO_2 (74.2-74.6 wt.%) and Al_2O_3 (0.2-0.3 wt.%) concentrations, but fall to higher values of K_2O and lower concentrations of FeO (Fig. 5.5), CaO (0.6 wt.%) and TiO_2 (0.2 wt.%). The tight clustering of MI and matrix glass into a narrow SiO_2 range, and to more evolved compositions compared to the whole rock (60.7-62.9 wt.%), suggests that entrapment occurred during a similar window of melt evolution near the end of the crystallization history of the Cebolla Creek magma. This is supported by the relatively restricted An values (An_{38}-An_{43}, Table 5.4) of all MI feldspar hosts compared to the large An diversity preserved by the oscillatory zoned plagioclases (An_{41-79}). Due to the small size of MIs (~50x50 μm) and the large diameter of the LA-ICP-MS spot (30 μm), several trace element analyses were affected by contributions from the host feldspar; *i.e.,* increased levels of CaO and Sr, and depletions in elements such as Ti that are incompatible in feldspar. These trace element concentrations were not included in any plots or calculations, and are displayed in italics in Table 5.4.

Volatile analyses on plagioclase-hosted inclusions (n = 21) represent the first *in-situ* measurements for San Juan focus eruptive products. Water concentrations are from 2.0-4.7 wt.%, with an average of 3.2 wt.% (Fig. 5.6). In phenocrysts with more than one inclusion measured, H_2O and CO_2 inclusions plot closely together, roughly along isobars

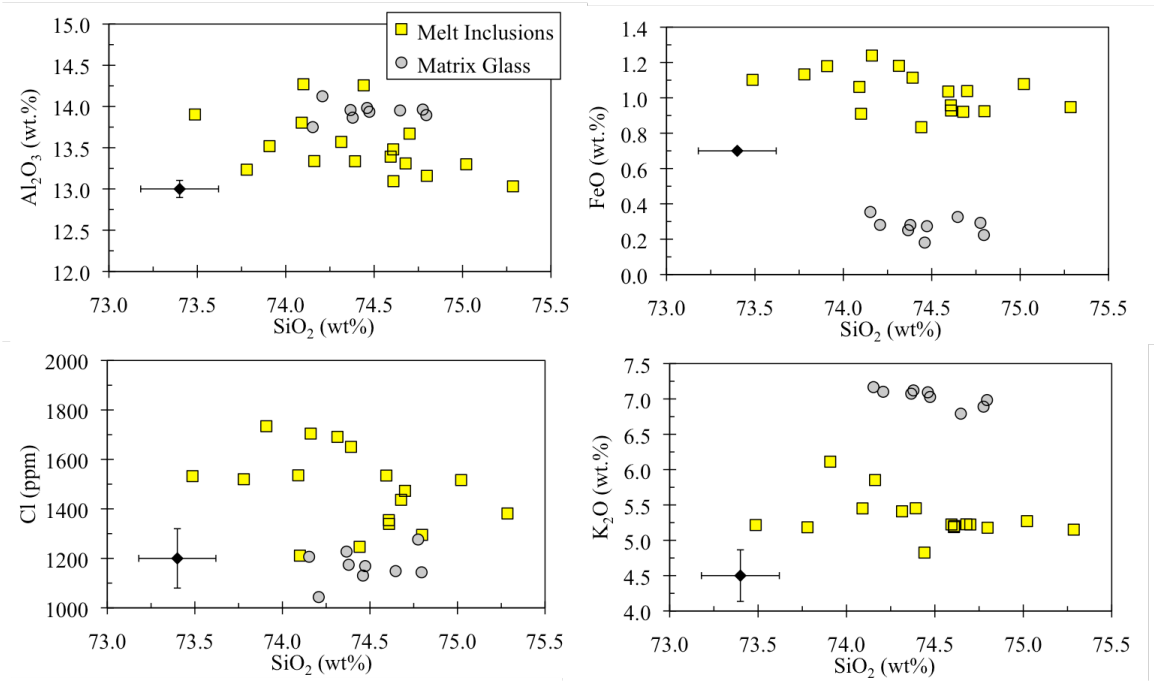

Figure 5.5. Concentrations of Al_2O_3, FeO, K_2O and SiO_2 (all in wt.%) and Cl (ppm) for Cebolla Creek Tuff matrix glass (grey circles) and plagioclase-hosted melt inclusions (yellow squares) from sample Ceb A (Table 5.4), measured using EPMA. 1SE bars are calculated off of repeat analysis of glass standard NBS K-411 and are listed in Table 5.4.

(Fig. 5.6). The highest measured CO_2 concentration contains 350 ppm, but the majority of values (67%) are between 20-140 ppm. Most inclusions fall along a closed degassing pathway (using 0.0-1.0 wt.% exsolved gas), assuming a starting concentration in the region of the highest H_2O value. However, a group of inclusions (H_2O = 2.2-2.7 wt.%) fall to the left of likely degassing trends (Fig. 5.6). Concentrations of Cl range from 1300-1700 ppm, S between 80-140 ppm and F, although more scattered, falls between the detection limit (~700 ppm) and 3500 ppm (Fig. 5.5). Average matrix glass concentrations of Cl (1170 ppm), F (800 ppm), and S (BDL, <40 ppm) are lower than values obtained from melt inclusions (Table 5.4; Fig. 5.5).

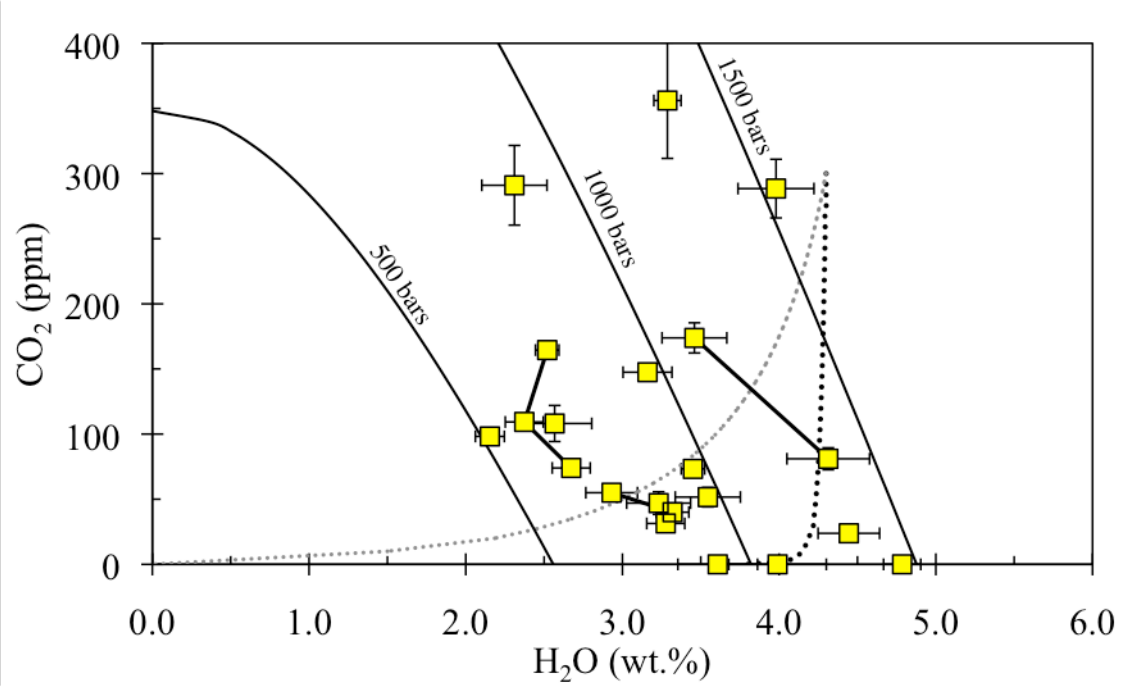

Figure 5.6. Measured H_2O (wt.%) and CO_2 (ppm) concentrations with their associated errors for plagioclase enclosed melt inclusions, shown as squares. Tie lines connect melt inclusions that are hosted in the same phenocryst. Solid lines represent bars of constant pressure (Newman and Lowenstern, 2002) using a temperature of 870°C based on MELTs modeling and amphibole thermometry (see discussion). The black dotted line represents open system degassing and the grey dashed line represents the closed-system degassing path assumed an exterior vapor concentration of 1 wt.%.

Some feldspars contain multiple inclusions that were simultaneously intersected and analyzed to evaluate: (1) magma evolution during growth, (2) compositional differences between brown and clear inclusions, and (3) whether the presence of a vapor bubble(s) correlated with H_2O and/or CO_2 variations (Fig. 5.7). Major and trace elements measured in interior MIs and those closer to the rim show little consistent variability that persists between grains. The only compositional differences noted between brown and clear inclusions in the same host were that the former contain higher Cl and Na_2O concentrations, but this is not an indicative characteristic compared to the overall variability observed in clear inclusions (Table 5.4). Inclusions that contain vapor bubbles

Table 5.4. Melt inclusion major (EPMA, in wt.%, Cl, F, S and P2O5 in ppm) and volatile (H_2O in wt.% and CO_2 in ppm, measured by FTIR) concentrations. All major element concentrations are normalized volatile free. Errors are shown as 1SE concentrations based off of repeat analysis of NBS-K-411 glass. Dashes represent samples where totals were poor or data was absent.

				Anhydrous Normalized Major Elements wt.% (EPMA)									Volatiles (microprobe)				FTIR				
Name	Type	Color	An Host	SiO_2	TiO_2	Al_2O_3	FeO	MgO	CaO	Na_2O	K_2O	Anhydrous Total	P_2O_5 (ppm)	F (ppm)	S (ppm)	Cl (ppm)	Measured Water (wt.%)	1SE	Measured CO_2 (ppm)	1SE	Pressure (bars)*
	Avg. 1 SE			0.28	0.03	0.01	0.08	0.06	0.89	0.04	0.01		33	230	20	14					
Ceb A #1	MI	Brown	43	-	-	-	-	-	-	-	-	-	-	-	-	-	2.57	0.24	108	14	672
Ceb A #3	MI 1	Clear	37	75.3	0.18	13.03	0.95	0.18	0.88	4.11	5.15	93.79	104	714	116	1381	-	-	-	-	-
Ceb A #3	MI 3	Clear	35	74.7	0.20	13.31	0.92	0.17	0.98	4.13	5.23	94.30	-	2359	78	1437	3.46	0.21	174	12	1127
Ceb A #3	MI 2	Clear	37	74.8	0.21	13.16	0.92	0.18	0.94	3.83	5.18	94.54	-	-	127	1295	4.31	0.26	81	8	1359
Ceb A #6	MI	Clear	-	74.3	0.26	13.57	1.18	0.23	0.79	3.95	5.41	95.15	64	1161	84	1691	4.79	0.12	-	-	1457
Ceb A #9	MI 1	Brown	39	73.5	0.23	13.90	1.10	0.19	0.90	4.27	5.22	95.34	-	-	139	1532	2.93	0.16	55	2	721
Ceb A #9	MI 3	Brown	32	74.7	0.22	13.67	1.04	0.18	0.82	3.99	5.22	94.74	54	15	135	1473	3.32	0.10	40	1	851
Ceb A #9	MI 2	Clear	39	75.0	0.22	13.30	1.08	0.20	0.75	3.84	5.27	95.50	6	1565	87	1517	3.23	0.20	47	9	826
Ceb A #10	MI	Clear	Qtz	-	-	-	-	-	-	-	-	-	-	-	-	-	3.99	0.31	-	-	1076
Ceb A #12	MI	Clear	43	74.2	0.28	13.34	1.24	0.24	0.83	3.72	5.85	94.19	-	1767	77	1704	2.31	0.21	291	31	866
Ceb A #13	MI	Clear	44	-	-	-	-	-	-	-	-	-	-	-	-	-	3.29	0.09	356	44	1347
Ceb A #15	MI	Brown	41	-	-	-	-	-	-	-	-	-	-	-	-	-	3.55	0.21	52	8	967
Ceb A #18	MI	Clear	43	73.9	0.32	13.52	1.18	0.23	0.88	3.51	6.11	95.22	0	1669	140	1734	4.44	0.20	24	1	1326
Ceb A #21	MI 4	Clear	39	74.4	0.15	14.26	0.83	0.19	0.98	4.13	4.83	93.56	-	394	100	1247	2.67	0.12	74	4	654
Ceb A #21	MI 1	Clear	41	74.6	0.16	13.09	0.93	0.19	0.82	3.99	5.20	94.40	-	-	107	1339	2.37	0.12	109	4	604
Ceb A #21	MI 2	Clear	41	74.1	0.01	14.27	0.91	0.18	0.98	4.13	4.83	93.56	-	2266	0	1211	2.52	0.08	165	3	743
Ceb A #26	MI	Clear	41	74.1	0.20	13.80	1.06	0.20	0.93	3.60	5.45	95.03	-	-	113	1536	3.61	0.25	-	-	908
Ceb A #28	MI 1	Clear	38	74.6	0.22	13.39	1.04	0.20	0.94	3.87	5.22	95.35	101	3512	95	1535	3.28	0.12	31	2	820
Ceb A #30	MI	Clear	41	74.4	0.28	13.34	1.11	0.22	0.84	4.01	5.45	95.18	43	1762	109	1651	2.15	0.09	98	2	516
Ceb A #32	MI	Brown	41	74.6	0.13	13.48	0.96	0.19	0.84	3.90	5.19	95.16	-	-	74	1355	3.16	0.16	148	6	960
Ceb A #35	MI	Clear	38	-	-	-	-	-	-	-	-	-	-	-	-	-	3.98	0.24	289	23	1544
Ceb A #40	MI	Clear	41	73.8	0.24	13.23	1.13	0.21	0.71	3.92	5.18	95.42	88	-	83	1520	3.45	0.08	73	2	959

*A temperature of 870°C was used to calculate saturation pressure in VolatileCalc (Newman and Lowenstern 2002).

Table 5.4. *(continued)* Melt inclusion trace element (LA-ICP-MS, in ppm) data with average 1SE, where trace element concentrations were calculated using an average SiO_2 concentration of 74.4 wt.%.

			Conc. (ug/g)																												
Name	Type	Color	Li	B	P	Ti	Rb	Sr	Y	Zr	Nb	Sn	Ba	La	Ce	Pr	Nd	Sm	Eu	Gd	Dy	Er	Yb	Hf	Ta	Pb	Th	U
	Avg. 1 SE		*3.7*	*6.0*	*26.9*	*118*	*5.3*	*15.3*	*1.2*	*13.3*	*1.6*	*0.2*	*30.4*	*1.5*	*2.6*	*0.3*	*1.4*	*0.4*	*0.1*	*0.4*	*0.3*	*0.2*	*0.2*	*0.5*	*0.1*	*1.1*	*0.8*	*0.5*
Ceb A #1	MI	Brown	49	18	88	1452	135	244	13	179	14	0.8	594	36	65	6.6	20	1.3	0.4	3.4	3.0	1.4	1.7	3.6	0.8	21	12	5.2
Ceb A #3	MI 1	Clear	36	22	80	1176	149	136	15	181	16	1.2	587	37	69	7.2	22	2.9	0.6	3.5	2.0	1.7	1.3	6.6	0.8	26	14	5.2
Ceb A #3	MI 3	Clear	-	-	-	-	-	-	-	-	-	-	-	-	-	-	-	-	-	-	-	-	-	-	-	-	-	-
Ceb A #3	MI 2	Clear	-	-	-	-	-	-	-	-	-	-	-	-	-	-	-	-	-	-	-	-	-	-	-	-	-	-
Ceb A #6	MI	Clear	-	-	-	-	-	-	-	-	-	-	-	-	-	-	-	-	-	-	-	-	-	-	-	-	-	-
Ceb A #9	MI 1	Brown	37	15	159	1416	150	223	15	194	19	1.2	807	37	75	7.1	27	3.4	0.6	1.2	2.7	2.1	1.4	5.5	1.4	26	13	5.8
Ceb A #9	MI 3	Brown	18	9	58	952	97	73	12	147	14	0.9	575	27	49	5.1	18	1.9	0.2	2.6	1.5	1.1	0.8	4.0	1.0	13	10	3.2
Ceb A #9	MI 2	Clear	*19*	*12*	*74*	*595*	*61*	*544*	*8*	*85*	*7*	*0.4*	*547*	*23*	*35*	*4.1*	*12*	*2.3*	*0.7*	*1.4*	*1.8*	*0.6*	*0.7*	*3.4*	*0.4*	*12*	*6*	*2.5*
Ceb A #10	MI	Clear	-	-	-	-	-	-	-	-	-	-	-	-	-	-	-	-	-	-	-	-	-	-	-	-	-	-
Ceb A #12	MI	Clear	-	-	-	-	-	-	-	-	-	-	-	-	-	-	-	-	-	-	-	-	-	-	-	-	-	-
Ceb A #13	MI	Clear	36	16	85	1669	160	101	15	287	20	1.3	731	37	76	6.9	23	4.5	0.5	3.2	3.1	1.7	1.7	6.1	1.1	24	11	5.8
Ceb A #15	MI	Brown	27	18	87	1544	177	143	15	223	21	1.0	788	35	75	6.6	23	3.0	0.3	3.4	2.2	2.1	1.3	6.2	1.5	28	13	6.3
Ceb A #18	MI	Clear	6	21	60	1277	103	86	14	180	16	1.1	548	28	55	6.1	24	3.3	0.6	2.5	2.1	1.6	2.2	4.7	1.3	14	14	4.8
Ceb A #21	MI 4	Clear	37	18	93	1383	152	110	15	157	15	1.3	587	39	74	6.2	27	4.3	0.8	4.1	2.0	1.8	1.8	3.7	1.2	27	13	7.0
Ceb A #21	MI 1	Clear	-	-	-	-	-	-	-	-	-	-	-	-	-	-	-	-	-	-	-	-	-	-	-	-	-	-
Ceb A #21	MI 2	Clear	*28*	*14*	*66*	*716*	*94*	*606*	*11*	*76*	*10*	*0.7*	*535*	*27*	*57*	*4.8*	*16*	*2.2*	*1.0*	*2.1*	*1.2*	*0.9*	*1.3*	*1.9*	*0.6*	*16*	*9*	*3.6*
Ceb A #26	MI	Clear	-	-	-	-	-	-	-	-	-	-	-	-	-	-	-	-	-	-	-	-	-	-	-	-	-	-
Ceb A #28	MI 1	Clear	-	-	-	-	-	-	-	-	-	-	-	-	-	-	-	-	-	-	-	-	-	-	-	-	-	-
Ceb A #30	MI	Clear	24	16	60	1270	104	100	16	158	18	1.1	569	29	57	6.1	23	3.5	0.6	3.2	2.5	1.5	1.8	4.8	1.2	19	16	5.1
Ceb A #32	MI	Brown	*28*	*10*	*118*	*475*	*82*	*892*	*6*	*45*	*5*	*0.6*	*607*	*28*	*45*	*3.9*	*16*	*1.8*	*1.1*	*1.3*	*0.7*	*0.6*	*0.7*	*0.9*	*0.2*	*19*	*5*	*1.8*
Ceb A #35	MI	Clear	-	-	-	-	-	-	-	-	-	-	-	-	-	-	-	-	-	-	-	-	-	-	-	-	-	-
Ceb A #40	MI	Clear	*18*	*14*	*97*	*930*	*113*	*627*	*12*	*128*	*12*	*1.4*	*688*	*31*	*58*	*5.4*	*21*	*1.6*	*0.8*	*1.8*	*1.2*	*1.1*	*1.3*	*2.9*	*0.6*	*21*	*10*	*3.5*

*Raised concentrations of Sr and Ca from LA-ICP-MS measurement suggest that part of the plagioclase host was abalated with the melt inclusion. For these samples we have excluded those suspect concentrations plagioclase compatible concentrations from plots and italicized them here .

have equivalent concentrations of H_2O as other inclusions within the same phenocryst, whereas CO_2 concentrations tend to be lower in those inclusions with vapor bubbles (Fig. 5.7).

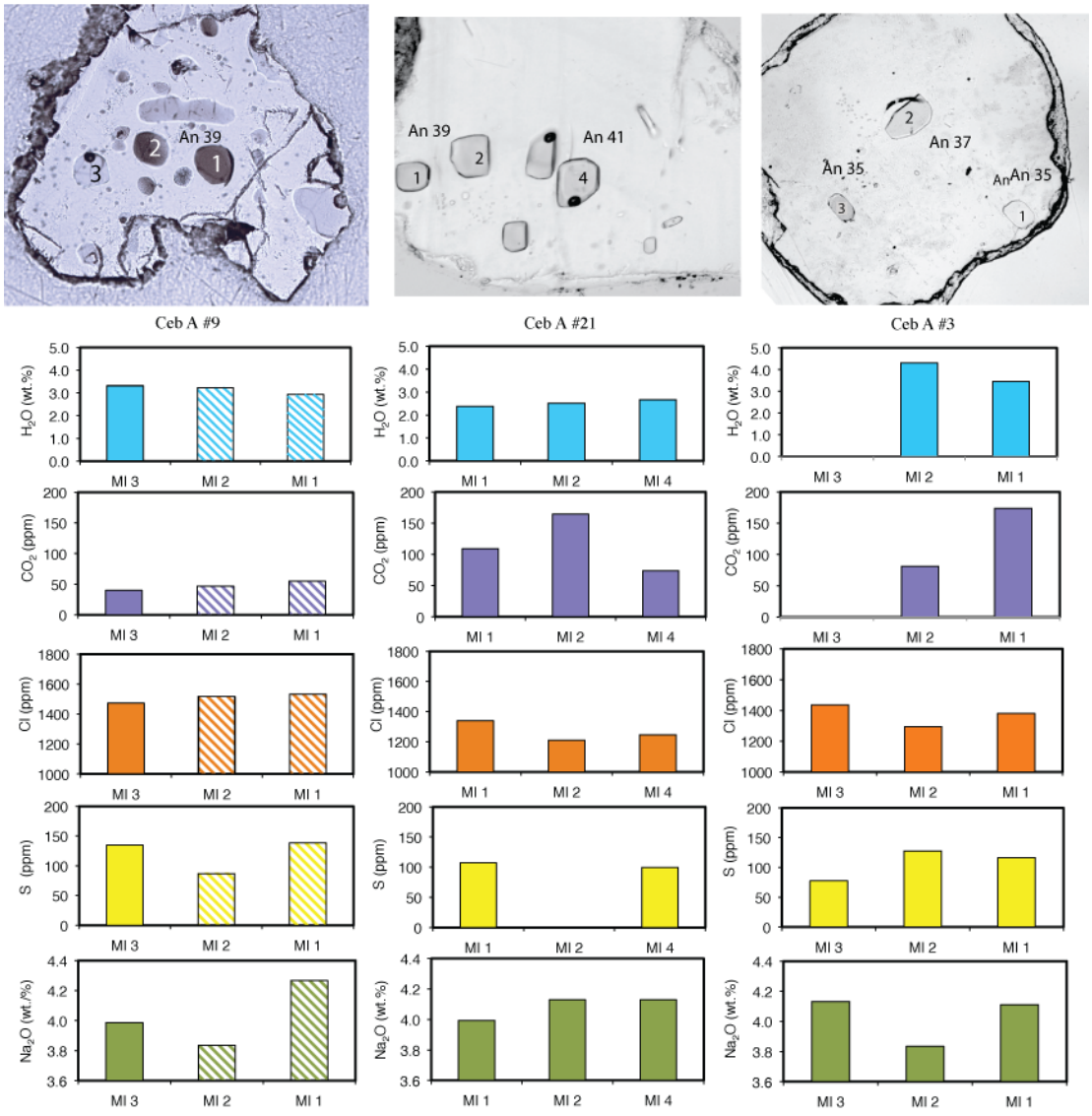

Figure 5.7. Three feldspar grains are shown, all of which contain multiple melt inclusions (MIs). All labeled inclusions were analyzed for major elements (Cl and S shown here, analyzed by EPMA), and volatile concentrations (FTIR), with some inclusions having trace element data (Table 5.4). Species concentrations (H_2O, CO_2, Cl, S, Na_2O) are shown for each labeled MI beneath the pairing photo, where brown inclusions in Ceb A #9 are shown with dashes.

5. Discussion

5.1 Reconstructing storage conditions

We applied the amphibole thermobarometer to core and rim analyses from three samples (Ceb A: inclusion bearing; TopCebA: top of the unit at Wheeler Monument; CebBOTOF: bottom of the unit at Wheeler Monument) to constrain amphibole crystallization temperatures and pressures (Ridolfi et al., 2010). In this thermobarometer, more alumunious compositions correspond to deeper, higher pressure crystallization (e.g. Allan et al., 2013). For core analyses (n = 17), T_{aver}= 912±36°C (1 s.d.), whereas rims, excluding four high Al_2O_3 outliers (Fig. 5.4d), yielded $T_{aver.}$= 872±11°C. This decrease in temperature between amphibole cores and rims is correlated with decreasing Sr concentration (Fig. 5.4), indicative a system experiencing cooling during crystallization of the main crystal assemblage. Because of the uncertainty associated with the amphibole thermometer (±20 °C), it is necessary to apply other techniques to confirm these cooler rim-temperature estimates. However, the lack of two-feldspar or oxide pairs means we have to rely on alternative approaches. The second approach we use is to back-calculate the temperature required for our plagioclase concentrations (An_{35-43}, Table 5.4) to be in equilibrium with the measured H_2O concentrations from their hosted melt inclusions, using the updated hygrometer of Waters and Lange (2015). Although this hygrometer is dependent on the input of temperature and pressure, the pressure effect is negligible (±1000 bars per ±0.1 wt.% H_2O). The average melt inclusion H_2O-concentration (3.2 wt.%) yields an equilibrium temperature of 885°C, whereas the higher end of the range (~4.5 wt.%), leads to a lower temperature (830°C). The third approach is to use the updated Rhyolite MELTS, which includes

solubility relationships, to determine what temperature our mineral assemblage (excluding amphibole; see below) becomes stable (Ghiorso and Gualda, 2015). The input conditions for this calculation were: (1) the most dominant rim compositions of plagioclase An_{40-44}, (2) equilibrium (i.e. precipitation) with biotite, and (3) 3.2 wt.% H_2O. The result, 880-890°C (An_{41}, biotite in), is in good agreement with the other methods presented. We stress that all these approaches are associated with significant uncertainties, but suggest that an average temperature ~870±20°C is a useful approximation of the pre-eruptive magma body.

Solubility relations of melt-inclusion H_2O and CO_2 constrain entrapment pressures and provide our most robust method for restoring the pre-eruptive storage depth. Several inclusions contain lower concentrations of H_2O and CO_2 relative to the highest values measured, but this is most likely due to post-entrapment diffusive loss, leakage along cleavage planes (e.g. Rutherford and Devine, 1996), or loss of CO_2 into vapor bubbles (Moore et al. 2015). Using VolatileCalc (Newman and Lowenstern, 2002), the highest measured H_2O concentrations (4.0-4.5 wt.%) and CO_2 concentrations (300-350 ppm) from plagioclase-hosted inclusions provide minimum pressures of entrapment around 150 MPa, corresponding to 5.5 km depth (using a crustal density of 2600 kg/m^3). These values are minima because any loss of H_2O will lower pressure estimates. Pressure estimates based on H_2O-CO_2 for individual melt inclusions are in Table 5.4. These pressures correspond, within error, to the pressures estimated from the amphibole rim compositions using the Ridolfi et al. (2010) barometer ($P_{avrg.}$=184±30 MPa), whereas amphibole cores reach pressures up to ~350 MPa. Taken together, the pre-eruptive Cebolla Creek magmatic system is inferred to have resided at pressures of ~150-200 MPa

(5.5-7.0 km depths), and at a temperature of ~870°C (average of estimates from three methods) prior to evacuation.

5.2 Evolution of the San Juan volcanic field

The Cebolla Creek Tuff is unusual with respect to other ignimbrite units in the SRMVF, as its homogeneous dacitic whole-rock composition (SiO_2 61-64 wt.%) makes it the least evolved (out of 30 ignimbrites; Lipman, 2007). Additionally, its crystal rich (35-40%) nature, and specific mineralogy (plagioclase, amphibole, and biotite, lacking pyroxene, sanidine and quartz) are unusual among the other ignimbrites in the San Juan volcanic focus. To constrain the degree of fractional crystallization required to create the plagioclase-hosted melt inclusion compositions from the whole rock we used rhyolite MELTs (Ghiorso and Gualda, 2015). Whole rock vitrophyre sample 15L-123 was used as the starting composition, chosen because of its lower degree of post-depositional alteration (i.e. higher total, Table 5.1). Estimates for oxygen fugacity come from Fe–Ti oxide oxybarometry on the Fish Canyon tuff, which gives NNO +1.3-2.4 (Whitney and Stormer, 1985). Here we adopted NNO+2. Melt inclusions helped constrain estimates for starting pressure conditions (150-200 MPa) and volatile concentrations (H_2O_{start} = 3.5 wt.%, CO_{2start} = 300 ppm). The outputs from this run produced fairly good replication of melt inclusion data for FeO, Na_2O, TiO_2 and Al_2O_3 after 30-40% crystallization, however MgO and CaO data are less well constrained (Fig. 5.8). These offsets could be the result of the inability of MELTs to precipitate amphibole in the crystallization assemblage, due to the lack of thermodynamic data. As the crystallinity of the Cebolla Creek Tuff is around 35-40%, the MELTs estimate of 30-40% fractional crystallization to recreate the

compositional gap represented by the whole rock and melt inclusion compositions suggests the Cebolla Creek experienced a largely closed-system history, with little melt-crystal separation.

We next evaluate the Cebolla Creek Tuffs whole rock, melt inclusion and matrix glass in the context of the most compositional similar units from the SRMVF. The closest comparison in terms of mineralogy are the amphibole-bearing andesitic fiamme that occur in upper vitrophyres in some San Juan ignimbrites, specifically in the older tuffs in the Platora caldera complex (Dungan, unpublished data). These fiamme are thought to represent snapshots of the more mafic underplating magma. Although these fiamme include pyroxene (augite) phenocrysts, which are absent in the Cebolla Creek Tuff, the plagioclase, biotite and amphibole mineralogy, and lack of quartz and sanidine, is the same. Whole-rock chemistry from these fiamme fall on a trajectory in between Cebolla whole rock and matrix glass compositions, with one sample overlapping with Cebolla Creek whole rock (Fig. 5.8). Because of the more mafic and hydrous nature of the Cebolla Creek Tuff, we also compare it to the Huerto Andesite, inferred to represent the magma that ponded and differentiated within the crust below the Fish Canyon magma body (Bachmann et al., 2002; Parat et al., 2005). Although this hornblende-bearing calc-alkaline andesite has a different mineralogy (+two pyroxene, lacks biotite), its whole rock compositions also overlap with those from Cebolla Creek Tuff (Fig. 5.8).

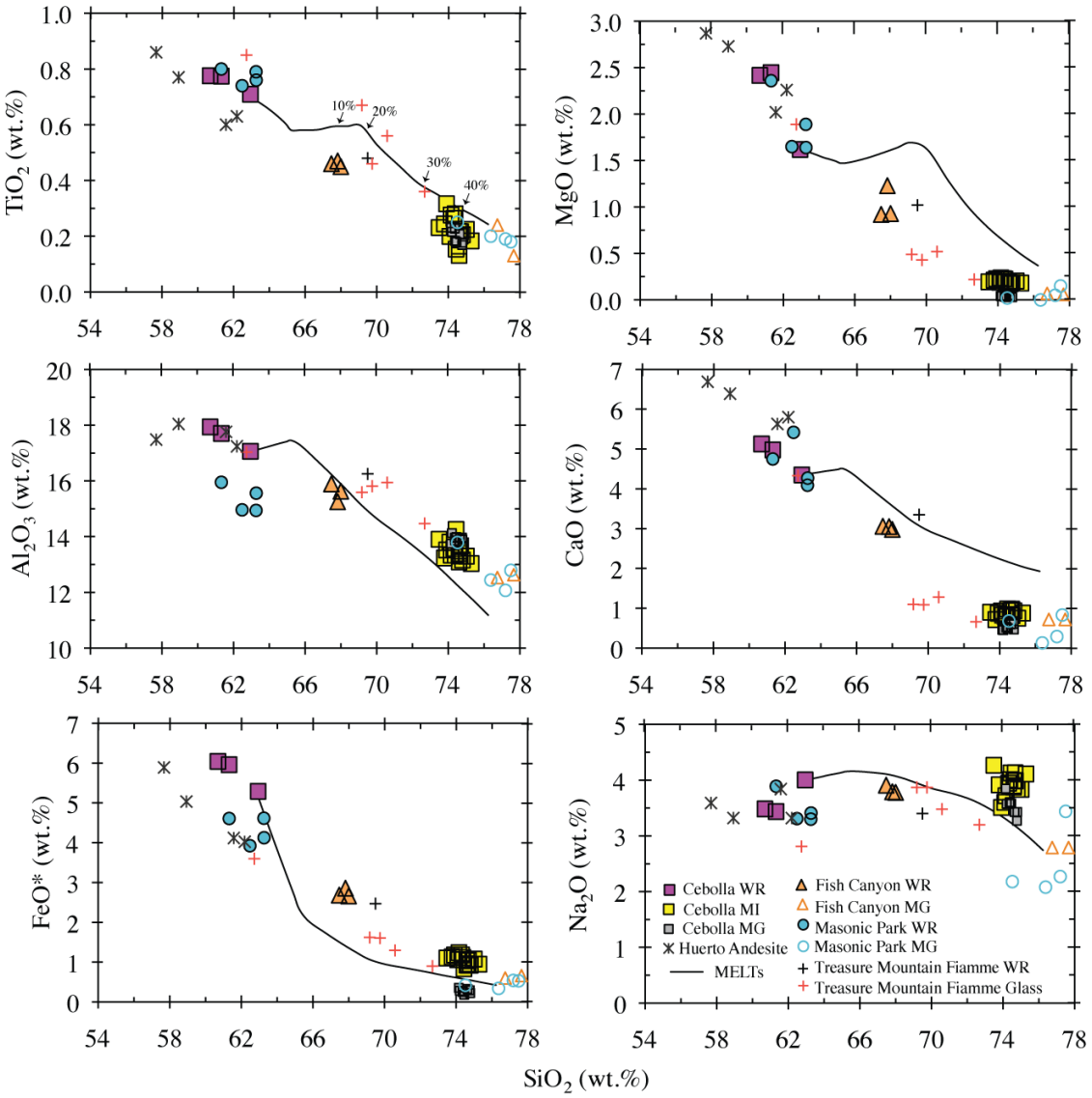

Figure 5.8. Major element data for Cebolla Creek Tuff whole rock and melt inclusion samples (shown as purple and yellow filled squares, respectively) compared with other whole rock and glass analyses from samples in the San Juan Volcanic Field (plus symbols: Andesitic fiamme associated the Treasure Mountain tuff; triangles: Fish Canyon; stars: Huerto Andesite). Black lines represent the predicted evolution of the whole rock sample 15L-123 using MELTs (see discussion). All major elements display a coherent crystallization trend, with the exception of FeO. Fractional crystallization percentages are shown on TiO_2 vs. SiO_2.

Finally, the most applicable comparison is to evaluate the whole rock and matrix glass of the two other monotonous intermediates that have been studied in the region: the

Fish Canyon (40-50 vol% crystals of plag + san + qtz + amph + biot; Bachmann et al., 2002, 2005) and Masonic Park (45 vol% crystals of plag + biot + cpx; Sliwinski et al., 2017) tuffs. Both of these ignimbrites preserve a large separation between their whole rock (largely homogenous) and matrix glasses, with the Masonic Park range corresponding perfectly with the range preserved by the Cebolla Creek Tuff. Overall, this combined dataset produces coherent evolutionary trends, suggesting that although different pressure, compositional, and/or temperature histories may account for each ignimbrites varied mineralogy, a broadly similar evolution trend is preserved from major tuffs in the region.

5.3 Comparison with other Monotonous Intermediates

There are two (of 5) other monotonous intermediate tuffs associated with the central San Juan region that have been previously investigated, the Fish Canyon (Bachmann et al., 2002, 2005) and Masonic Park (Sliwinski et al., 2017) tuffs. As discussed above, the whole rock and matrix glasses generally agree with the compositional range observed in the Cebolla Creek Tuff (Fig. 5.8). However, in both of these ignimbrites, strong An-rich enrichments are observed at the rims of plagioclase phenocrysts, as well as a reverse zonation preserved in clinopyroxene (Masonic Park) and amphibole (Fish Canyon). These phenocrysts are interpreted to record a late-stage reheating event shortly prior to eruption. Elemental concentrations measured in core-to-rim transects across Fish Canyon Tuff amphiboles also record increased temperatures in their rim analyses (higher Al_2O_3 concentrations), as well as enrichments in Sr and Ba. These have been interpreted as the result of late-stage, thermally-induced dissolution of

feldspar (Bachmann et al., 2005). Similar enrichments in Sr and Ba are observed in plagioclase microlites and phenocrysts rims in Masonic Park samples (Sliwinski et al., 2017). This evidence led the respective authors to propose that magma recharge was an important factor in remelting of near solidus plutons prior to the eruption of these crystal-rich silicic magmas.

Cebolla Creek Tuff amphiboles are characterized by opposite trends; Sr and Ba concentrations are higher and more variable in amphibole cores, and converge towards lower, and much less variable values at rims (Table 5.4, Fig. 5.4b). This trend is more indicative of plagioclase crystallization, and is supported by the preservation of late-stage growth (100-200 μm) rather than dissolution textures in the majority of phenocrysts (Fig. 5.3; Table 5.2). Halogen (F and Cl) concentrations also appear not to vary between amphibole cores and rims (Fig. 5.4d). Major element zonation in amphiboles is relatively minor and, where zoning is observed, Al_2O_3 concentrations decrease towards the rim (i.e., normal zoning; Table 5.4b), corresponding to lower crystallization temperatures and pressures (Fig. 5.4c). These observations point to a system where plagioclase and amphibole phenocrysts were assembled into their final pre-eruptive magmatic body from a larger, warmer and deeper crystallization region to explain the high An sieve-textured cores, with partial dissolution zones prior to a significant amounts of normal zoned growth, and the deeper core pressures associated with amphibole cores (Figs. 5.3 and 5.4d).

6. Conclusion

Petrologic evidence from amphibole and plagioclase phenocrysts from the Cebolla Creek Tuff indicates a cooling and crystallizing magmatic body prior to eruption. Plagioclase-hosted melt inclusion compositions are consistent with ~ 40% crystallization of the whole-rock magma composition, indicating a largely closed-system history with little melt-crystal separation. Melt inclusions are hosted in the most evolved plagioclase compositions (An_{36-44}) and are compositionally similar to the matrix glass, suggesting that they record conditions just prior to the onset of eruption. Volatile analyses for these melt inclusions present the first *in situ* estimates for the SRMVF, with average concentrations (±1s.d.) as follows: H_2O=3.2±0.95 wt.%, CO_2=90±87 ppm, Cl=1480±160 ppm, S=100±33 ppm, and F=1560±950 ppm. The highest measured H_2O (~ 4.0-4.5 wt.%) and CO_2 concentrations (300-350 ppm) provide minimum pressures of entrapment around 150 MPa, corresponding to depths around 5.5 km depth. Amphibole thermometry in conjunction with MELTs modeling provides a pre-eruptive temperature estimate of ~870±20 ºC. Cores and rims analyzed from subhedral amphibole phenocrysts provide no evidence for late-stage volatile (e.g., Cl or F) enrichments or depletions and preserve lower temperatures, pressures and concentrations of feldspar-compatible trace elements, indicative of a cooling and crystallizing magma body. This is supported by the lack of late-stage reverse zonation or strong dissolution textures on the rims of plagioclase phenocrysts, which all converge to similar ~An_{40} concentrations. Taken together, the mineral assemblage from the Cebolla Creek Tuff precludes a late-stage heating, volatile fluxing or mafic recharge event, making it unique compared to others in the region (e.g. Fish Canyon and Masonic Park tuffs).

CHAPTER VI

DISSERTATION SUMMARY

My dissertation research investigated four voluminous caldera-forming eruptions. By reconstructing their storage dynamic and evolution (including pressure, temperature and geochemical evolution), with the rates at which magma ascended to the surface, I ultimately interpreted what triggered these systems into mobilization. The results from this work have been to establish the usefulness of two, volatile diffusion models to calculate ascent rates of rhyolitic magma at the onset of caldera-forming eruptions.

The first volatile-based technique involves modeling H diffusion through a host mineral from an enclosed melt inclusion that originally preserves pre-eruptive storage H_2O concentrations. During slow magma ascent, H will be lost from the external melt into a vapor phase, driving diffusion from the sealed melt inclusion through the crystal lattice and into the lower-H_2O melt. Using this method, I have demonstrated that eruptions containing evidence for stop/start deposition have greater degrees of H_2O scatter preserved in their enclosed melt inclusions, indicative of sluggish (days to weeks) and variable decompression prior to each explosive event (e.g. Huckleberry Ridge, Oruanui, Chapters II and IV). This observation strongly suggests that these systems are beginning under low degrees of overpressure, meaning magma mobilization is initiated and modulated by external factors (e.g. tectonics, roof destabilization) rather than by strong internally-driven volatile over-pressurization.

The second method directly quantifies the timescale (hours) of final decompression immediately prior to the explosive event using melt-filled channels in minerals that are not fully sealed off from the external melt (Chapter III). During rapid

ascent, gradients in H_2O and CO_2 concentrations form in these channels as they diffusively react to a degassing external melt. Importantly, these H_2O and CO_2 gradients reequilibrate on timescales <1 day, meaning that they only preserve information on final ascent and do not record initial sluggish ascent from a deep storage zone. By numerically modeling the decompression rate that recreates the measured H_2O and CO_2 gradients, an estimate of the final ascent conditions can be reconstructed. I applied this method to samples throughout the stratigraphy of all three caldera-forming eruptions to understand how these systems were evolving over time.

APPENDIX A

CHAPTER II SUPPLEMENTARY FIGURES

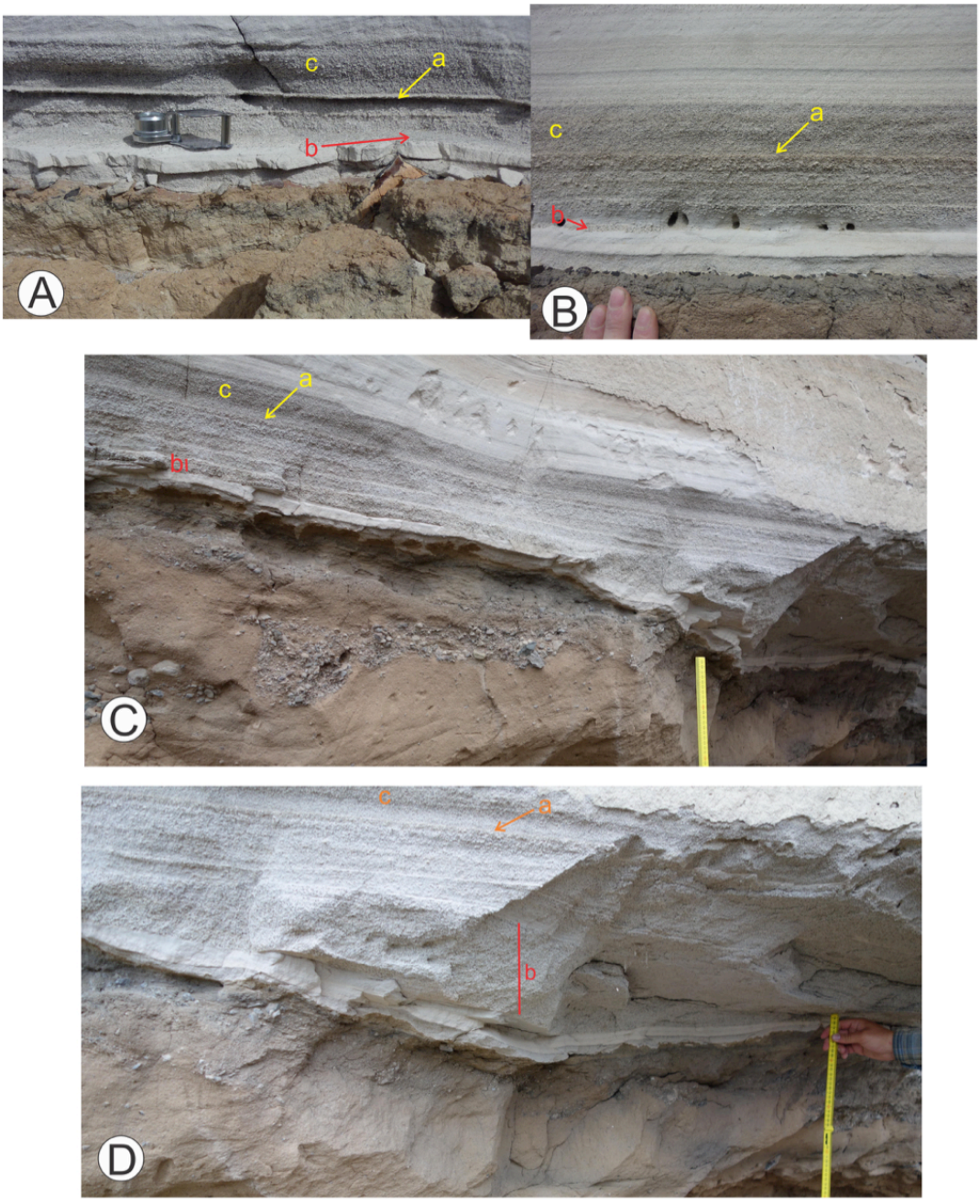

Chapter II, Figure A1: (continued: see page 142 for explanation)

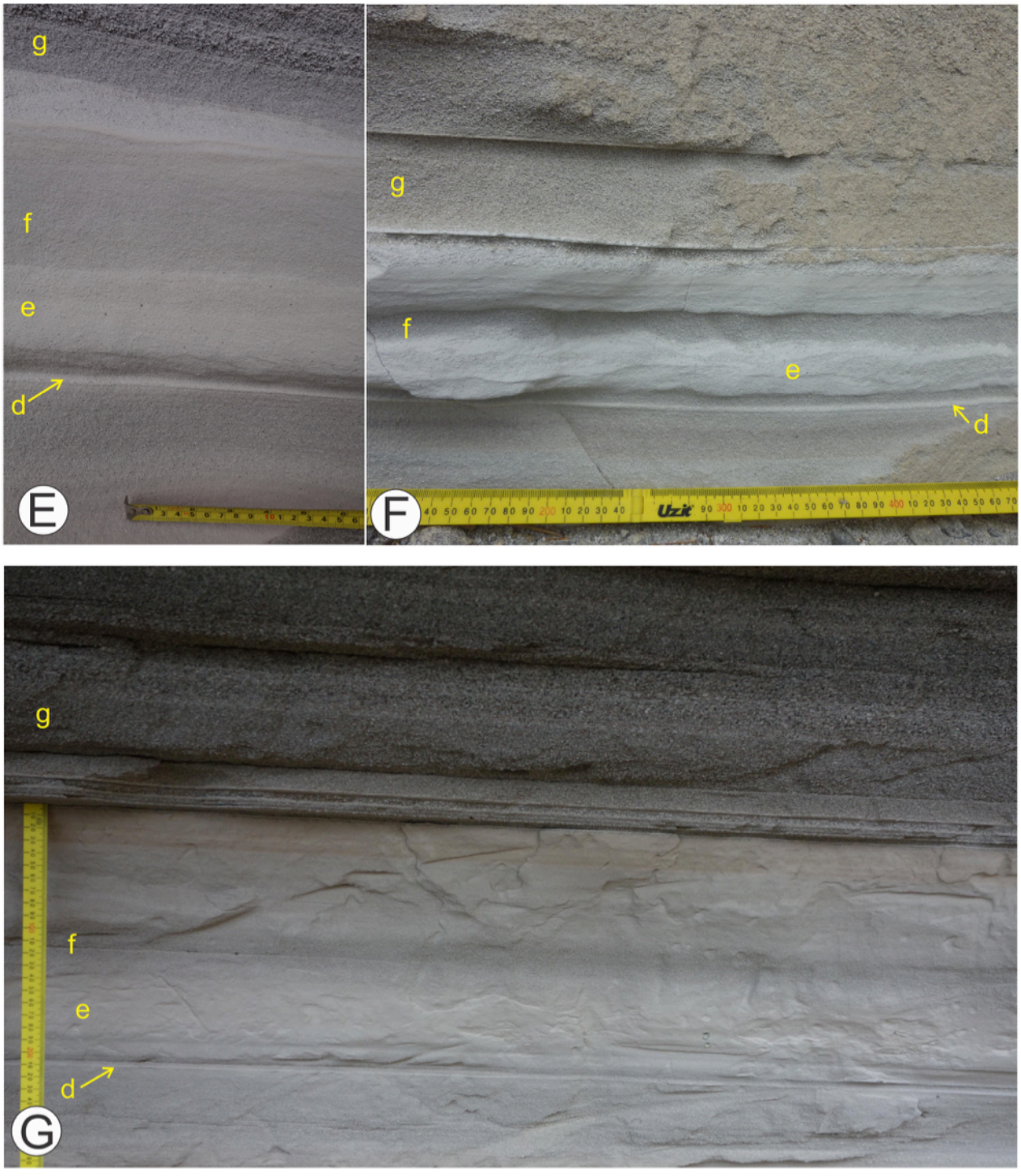

Chapter II, Figure A1: (continued: see page 142 for explanation)

Chapter II, Figure A1: (continued: see page 142 for explanation)

Chapter II Figure 1A: Evidence for depositional hiatuses and reworking in the initial HRT fall deposits. Images are from two sites 1.7 km apart along the western rim of Mount Everts (red star in Fig. 1); at UTM references 0526522 m E; 4979967 m N (panels A, E and F) and 0526792 m E, 4978329 m N (panels B, C, D, G and H), and a third site at the southwestern limits of the HRT ignimbrite in Swan Valley (orange star in Fig. 1) at 0440934 m E, 4824718 m N (Panel I).

(A) to (D): Basal part of the fall deposits. Marker horizon 'a' and the laminated fall deposits (e.g. layer 'c') above can be correlated to mm-scale precision between the two sites. Horizon 'b' is generally thin (<1-2 cm) and discontinuous where shown in panels A and B, but then thickens to ~13 cm in a shallow swale (panels C and D). The massive nature of the overthickened material, its friable, vesicular nature and its confinement to a swale are interpreted to indicate reworking by water as a small-scale mass flow at this level.

(E) to (G): Contrasts in the bedding structures occur at the transition (about 65 cm above the basal contact; see Fig. 1) between the fine-ash dominated basal parts, and the coarse ash to fine lapilli-dominated middle parts of the fall deposits. Where most clearly preserved and little affected by reworking, two normally graded beds mark the transition and imply that development of the later, stronger plume was initially episodic, with settling out of thin layers of fine ash (Panel G). Correlated horizons are labeled 'd' through 'g'. In Panel F, note the ripple bedforms in layer 'e'. In Panel E, note that the reworking has blurred the interval between horizons 'f' and 'g'. The thin parallel-bedded layers below layer 'g' are intact in Panel G, but reworked into a single layer in Panel F, and reworked and removed in Panel E.

(H) View of the lower, fine-ash-dominated portion of the HRT fall deposits. Note the two zones of inferred wind reworking within the fine ash deposits, and the sharp break (horizon 'h': see Panel G for detail) into the coarser ash to fine lapilli middle parts of the fall deposits (at about 65 cm above base in the Fig. 1 log).

(I) Image of part of the fall deposits covering the same horizon 'h' as in Panel H. This locality (orange star in Fig. 1) is about 180 km SSW of the Mount Everts locations (red star in Fig. 1). Note the alternations of more massive and micro-rippled ash, the latter inferred to represent periods of reworking that are contemporaneous with those seen at the Mount Everts localities.

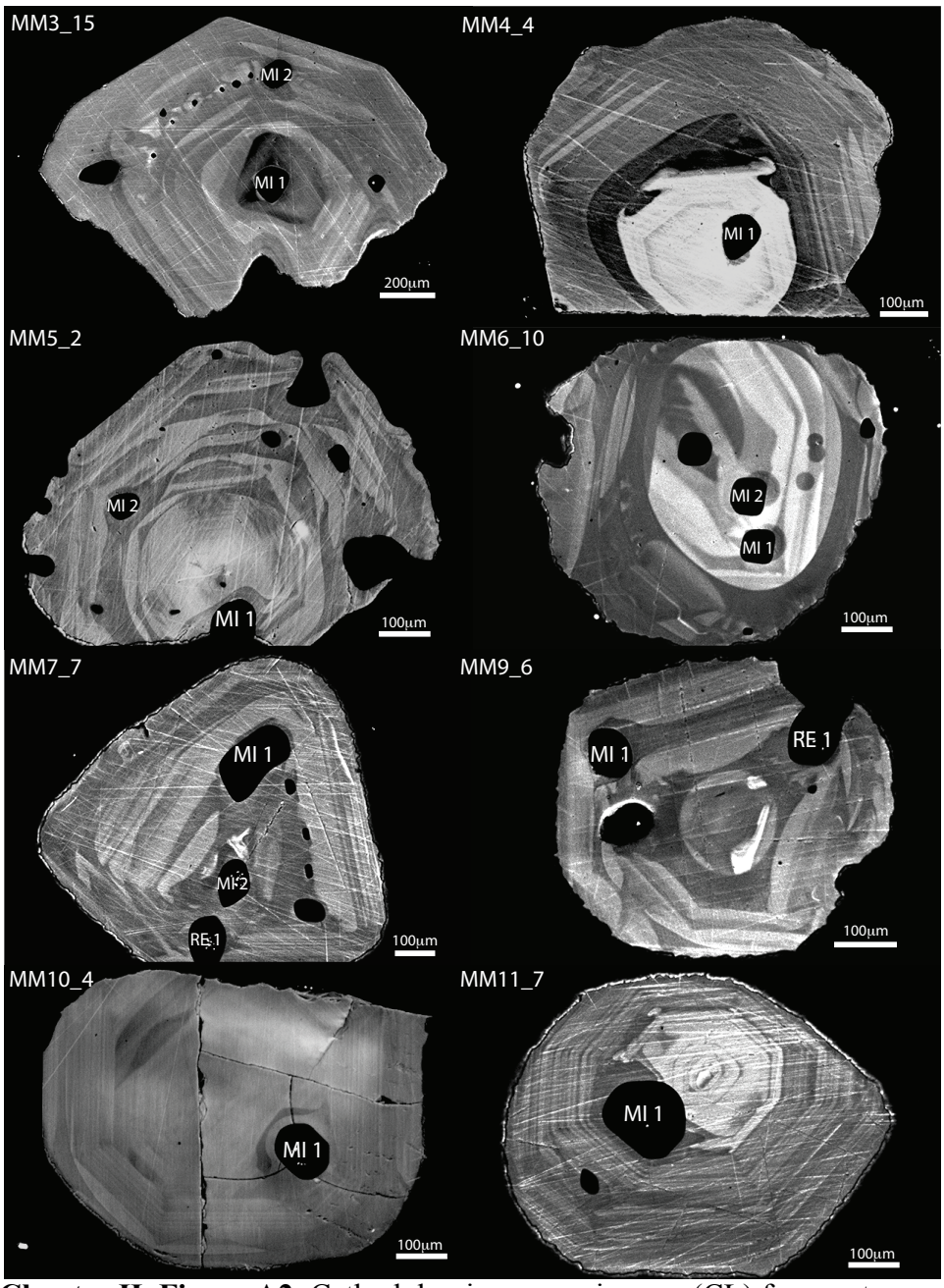

Chapter II, Figure A2: Cathodoluminescence images (CL) for quartz crystals hosting melt inclusions and reentrants. Images were taken at Victoria University, New Zealand, using JEOL 6610L Scanning Electron Microscope fitted with a Robinson CL detector. Images were obtained using a large aperture (3) and an accelerating voltage of 20 kV. One representative quartz crystal from each sampled layer is shown to display the diversity in textures preserved. All melt inclusions and reentrants that were analyzed for major and trace elements (including volatiles) are labeled. Most quartz crystals contain internal cores with oscillatory zoned overgrowths, indicating at least one dissolution event. Interestingly, although the CL images highlight a complex growth history, MI and REs from quartz in any sampled layer show a large degree of overlap in composition (see Fig. 3A).

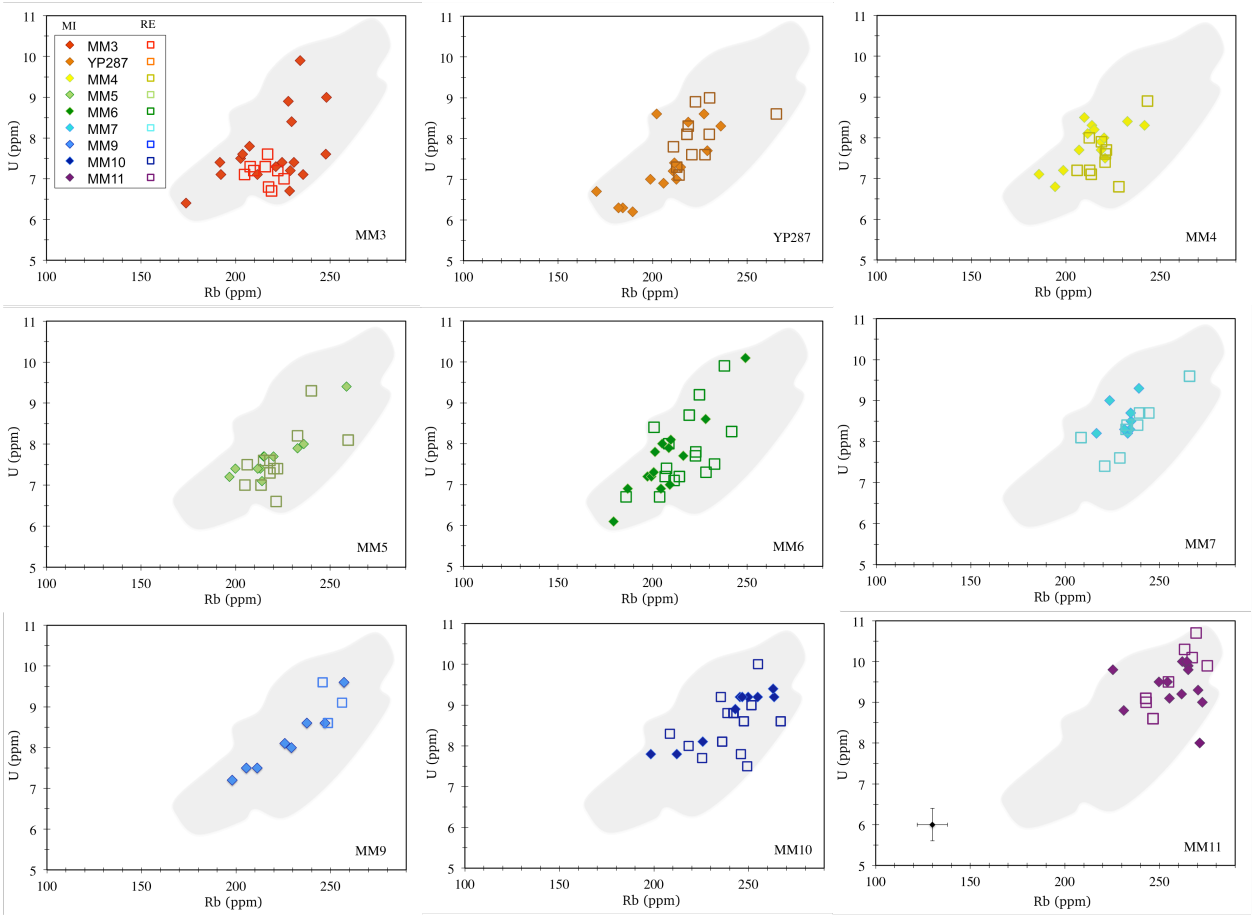

Chapter II, Figure 3A: U vs. Rb for MIs (filled diamonds) and REs (squares) from the nine layers sampled; each panel shows data for an individual layer. The gray shading denotes the range represented by all analyzed MIs and REs. In any individual panel, RE concentrations largely overlap with MI compositions. Error bars shown in the bottom right panel show the average ±1 SE analytical uncertainty. Analytical uncertainties for all analyzed MI and RE are in Myers et al., (2016).

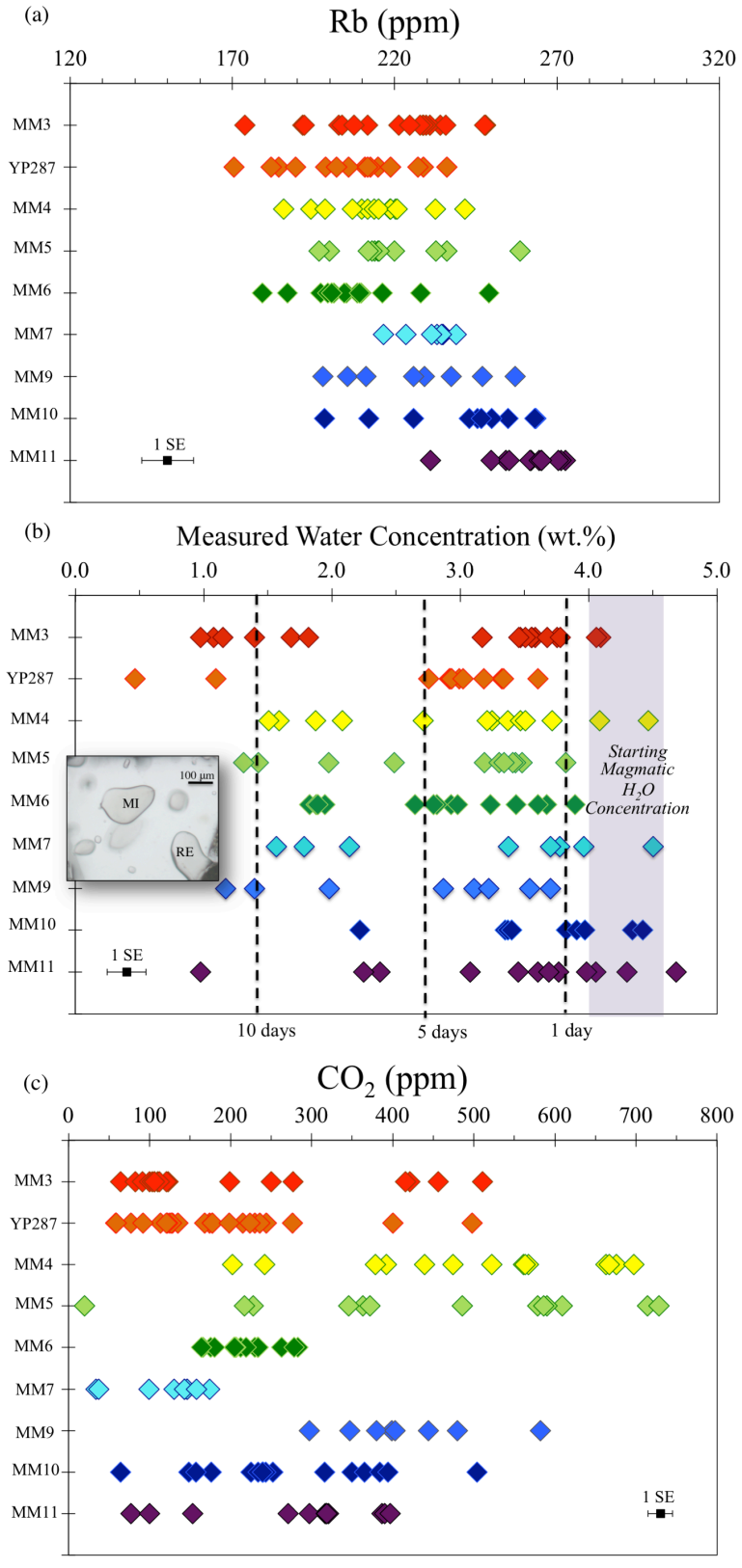

Chapter II, Figure 4A: (see next page for explanation)

Chapter II, Figure 4A: (a) Rb concentrations in MIs as a function of stratigraphic height. The maximum range of variability for MIs from a single sample is a factor of 1.4. Similar ranges of variability are found for all incompatible trace elements that are unable to diffuse on short time scales through the host quartz crystal.

(b) H_2O concentrations of MIs as a function of stratigraphic height. The large ranges in H_2O values for each unit are interpreted to result from variable diffusive loss from the MIs during ascent implying that many inclusions spent significant time at lower pressures, surrounded by variably degassed melt. The dashed lines represent the concentration of H_2O for an inclusion of 100 mm diameter after a specified time of diffusive loss in degassed melt (with 1 wt.% H_2O), assuming an initial concentration in the MI that is within the shaded field (~4.5 wt.%). Diffusive loss was modeled as described in the text using Cottrell et al., (2002) and a diffusivity calculated from experimental results of Severs et al., (2007). MIs with H_2O concentrations close to the shaded region require ascent timescales of <12 hours and thus most closely represent pre-ascent storage conditions. In contrast, MIs with ~1.5 wt.% H_2O require diffusive loss to the external melt at lower pressures for 10 days or more.

(c) CO_2 concentrations of MIs as a function of stratigraphic height. Dissolved CO_2 in MIs is sensitive to trapping pressure. All MIs analyzed in this study are bubble free, so the measured CO_2 concentration should reflect the value from the time of inclusion trapping. Estimated trapping pressures for the MIs are shown in Fig. 4.

Error bars on all panels show the average ±1 SE analytical uncertainty. Analytical uncertainties for all analyzed MI and RE are in Myers et al., 2016.

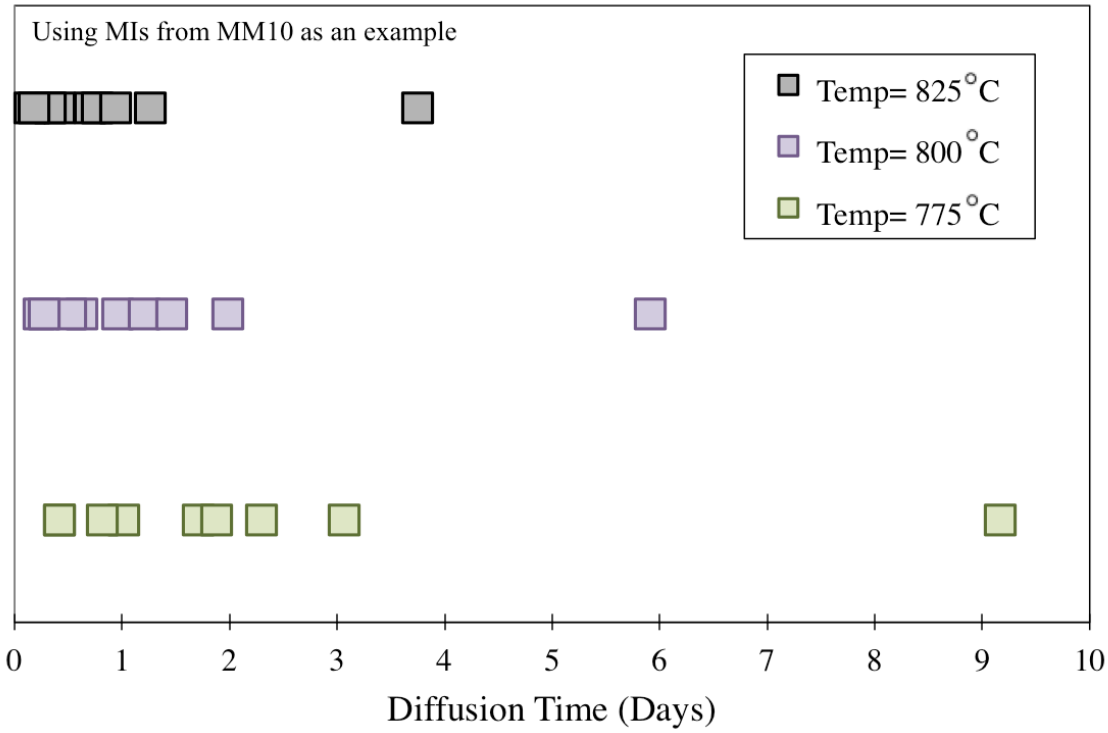

Chapter II Figure 5A: Effect of temperature variation on calculated diffusive loss timescales. Diffusive loss times for MIs from unit MM10 were calculated at temperatures of 825 °C, 800 °C and 775 °C using the Cottrell et al. (2002) model (as described in the text). The results suggest a factor of 3 or less uncertainty in our estimated timescales resulting from uncertainties in our temperature estimates (see text for discussion).

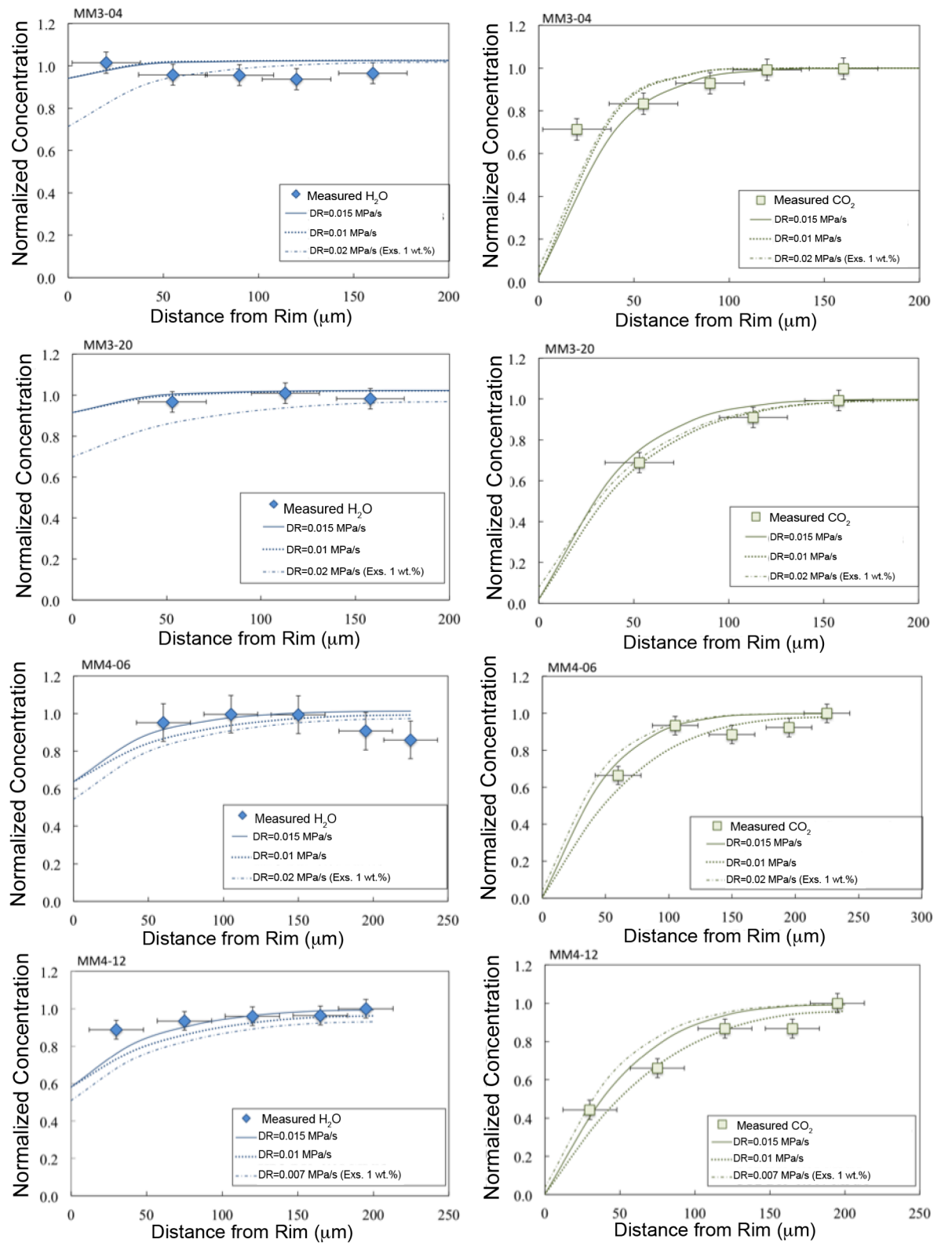

Chapter II Figure 6A: (See page 150 for explanation)

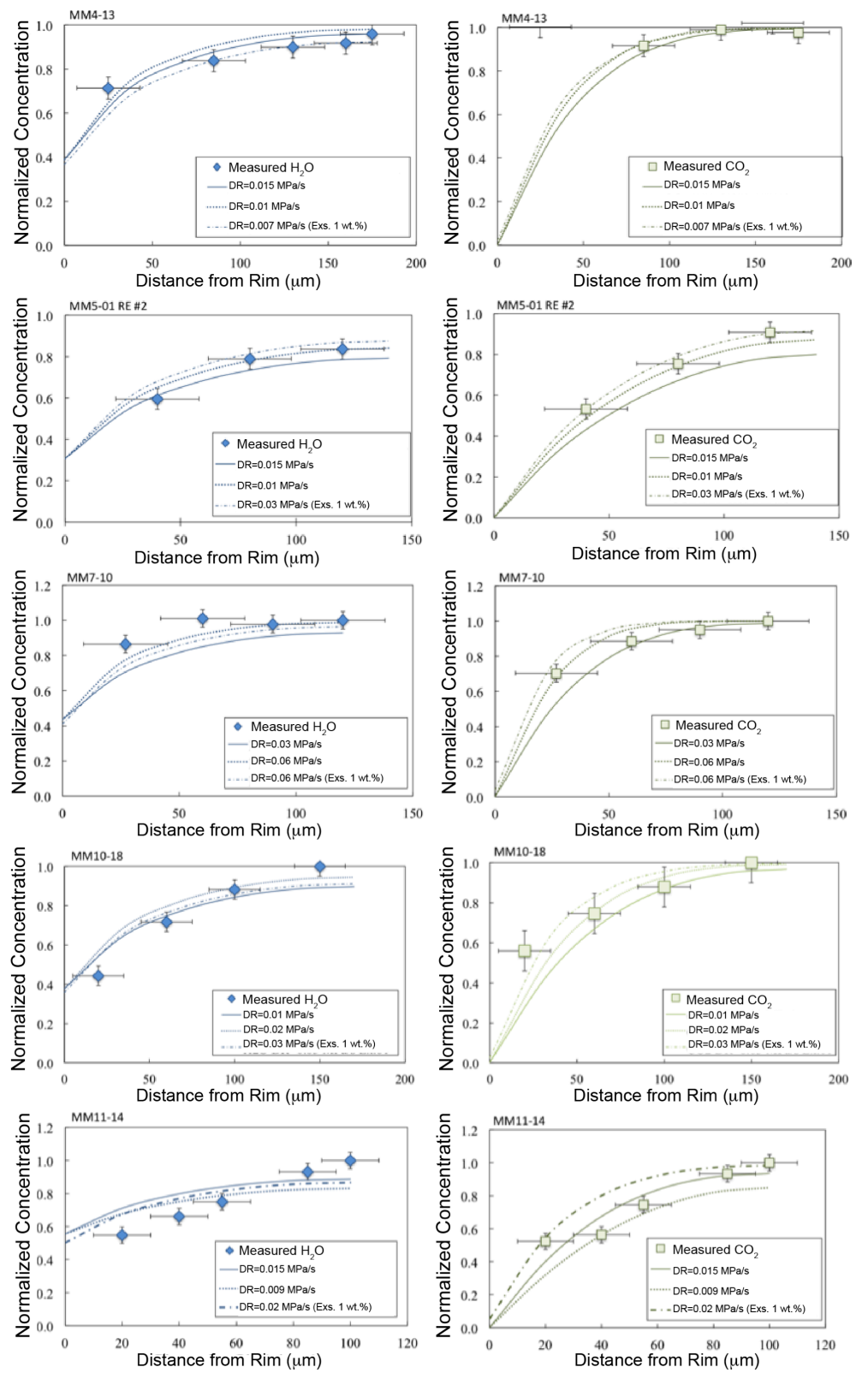

Chapter II Figure 6A: (See page 150 for explanation)

Chapter II Figure 6A: Normalized H_2O and CO_2 concentrations in REs compared to modeled concentration profiles for different decompression rates. In total, ten REs were analyzed from six of the nine sampled layers in the initial fall deposit. Modeled concentration profiles were calculated using the code of Liu et al., (2007) as discussed in the text. The best fitting profiles for nine REs are shown, and the tenth is shown in Fig. 5. The results suggest a range in decompression rates of 0.007-0.03 MPa/s. The first two curves in each best-fit model (solid and dotted lines) are for open-system degassing, whereas the third curve (dashed line) represents a closed-system model with 1 wt.% exsolved gas (Liu et al., 2007).

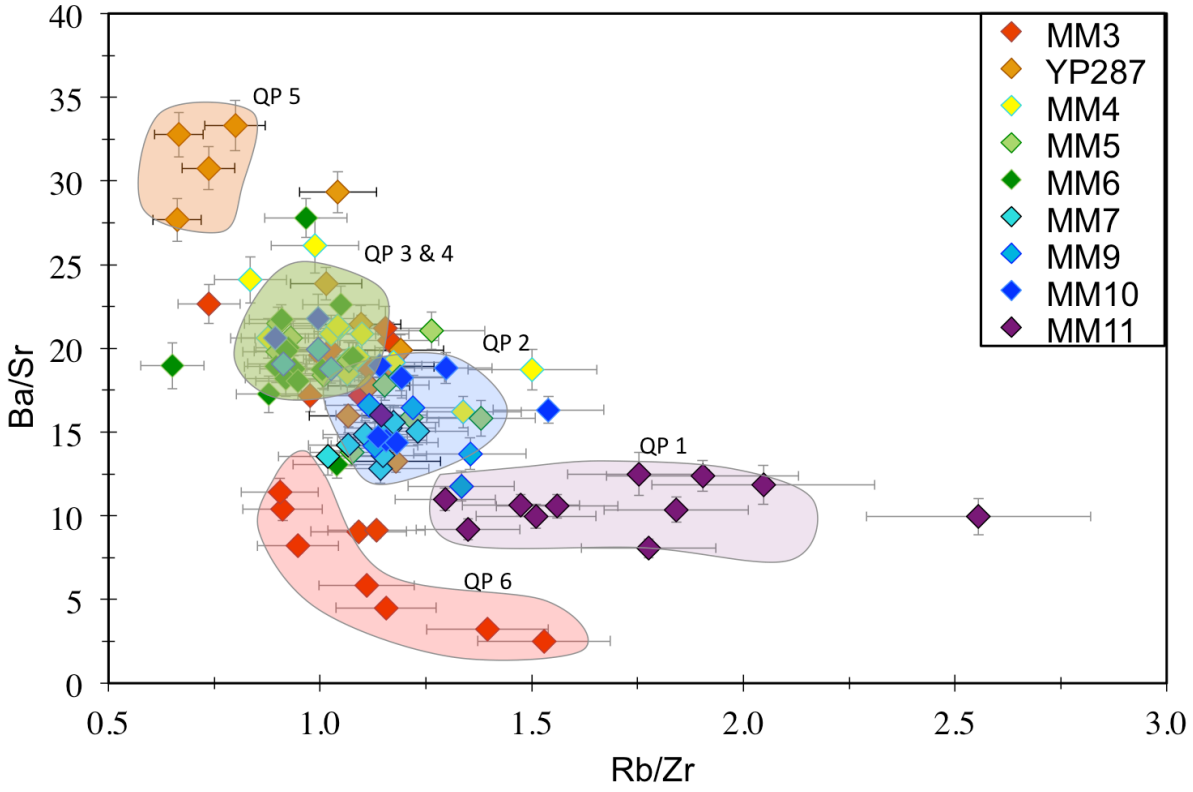

Chapter II Figure 7A: Ba/Sr vs. Rb/Zr ratios for all MIs. MIs from samples MM3, YP287, and MM11 represent distinct compositional end members. The Rb/Zr ratio should increase during crystallization differentiation, whereas the Ba/Sr ratio is sensitive to the proportions of plagioclase vs. sanidine. The observed variations thus suggest two evolutionary trends. Cluster analysis using MI compositions, as described in the text, provides support for distinct compositional clusters (shown as colored fields, labeled as quartz populations QP1-6 (see Fig. 7, Chapter II)). Although QPs 3 and 4 have similar Ba/Sr and Rb/Zr ratios in this figure, they are distinguished on the basis of their CO_2 concentrations (Figs. 4; Appendix A Fig. 4c). Error bars show average ±1 SE analytical uncertainties.

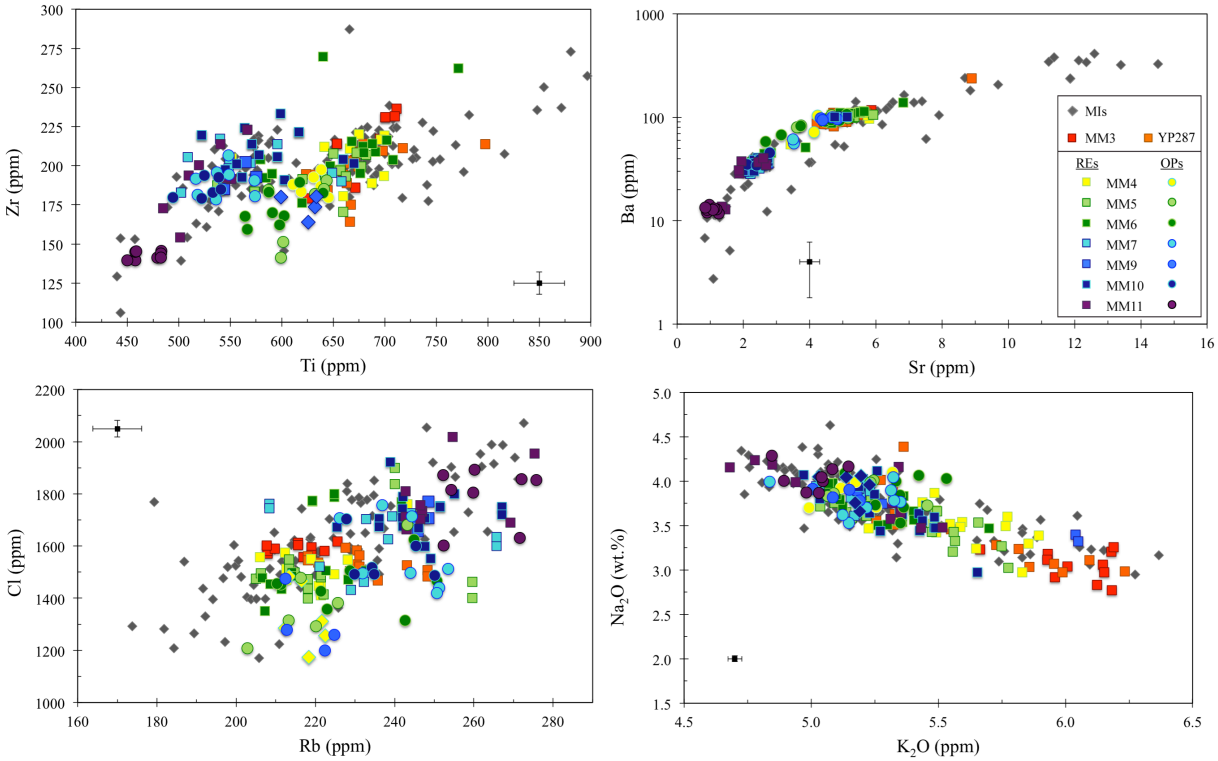

Chapter II Figure 8A: Volatiles and trace elements for MIs, REs, and obsidian pyroclasts from all nine levels sampled in the initial HRT fall deposits. Zr, Ti, Ba, Sr, and Rb were analyzed by LA-ICP-MS and Na_2O, K_2O, and Cl by electron microprobe. MIs are shown as gray diamonds, whereas REs (squares) and obsidian pyroclasts (circles) are colored according to their corresponding MM sample number. Error bars show the average ±1 SE analytical uncertainty. Analytical uncertainties for all MIs, REs and obsidian pyroclasts are in Myers et al. 2016.

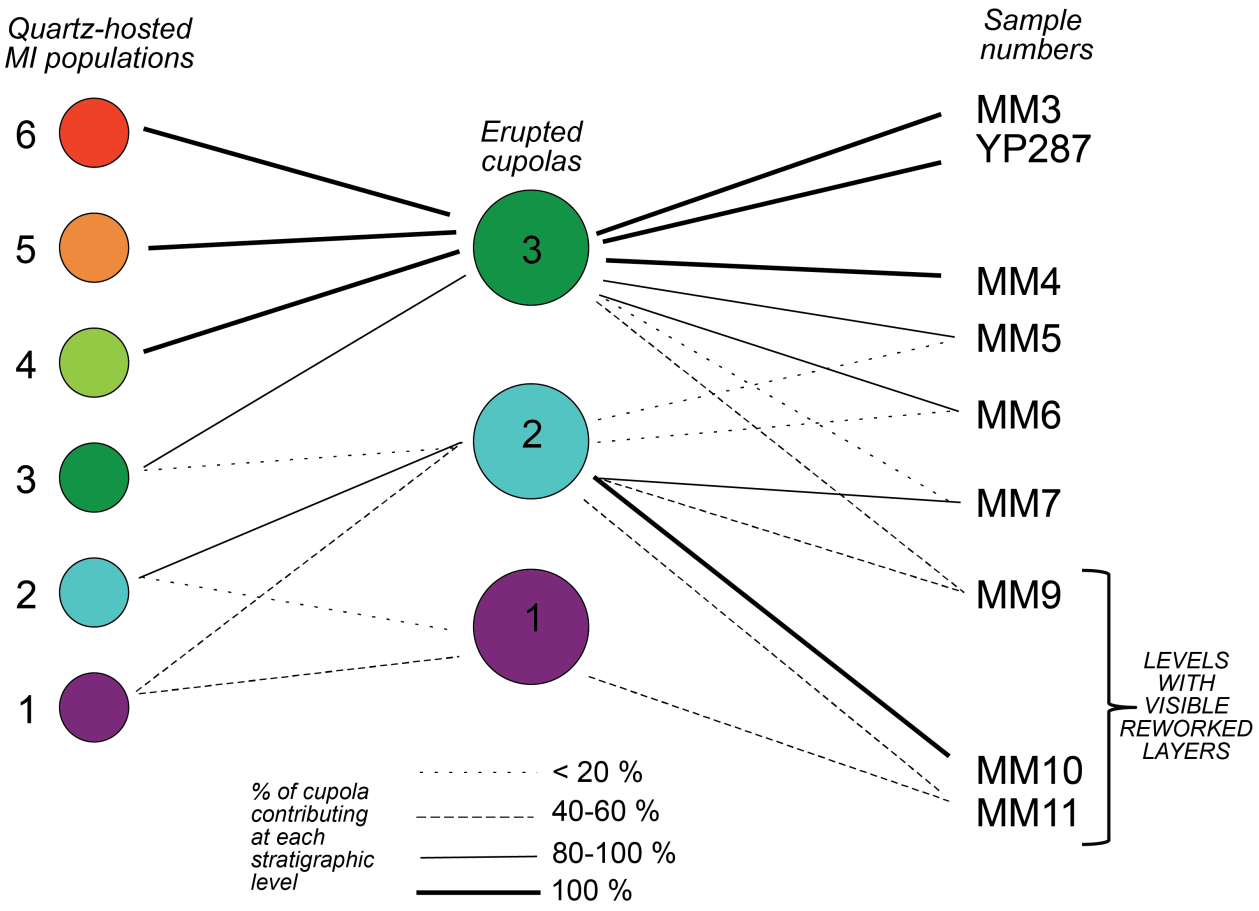

Chapter II Figure 9A: Simplified schematic showing the distribution and proportions of the different quartz populations (based on MI compositions) in each of the erupted cupolas (left side) and the distribution and proportions of magma from the three cupolas (based on RE and obsidian pyroclast compositions) in each of the sampled layers (right side; see Fig. 1 for sample stratigraphy). Line thickness and style depict proportions: lines converging on each cupola from the left sum to 100%; lines converging on each sample from the left also sum to 100%. Importantly, this diagram shows the systematic shifts over time (stratigraphic height) in the source cupolas; lower units were sourced from cupolas 1 and 2, whereas the majority of material upwards from sample layer MM6 was sourced from cupola 3.

APPENDIX B

CHAPTER III SUPPLEMENTARY FIGURES

Temperature Estimate

We the pre-erupted magma temperature associated with the fall material for all three systems, where temperature is assumed to be constant through magmatic ascent. For all fall samples from the Bishop tuff we adopt a constant temperature of 740ºC (Hildreth and Wilson, 2007; Evans et al., 2016). Although in the later portions of the eruption there is evidence for an increase in magmatic temperature associated with the contribution of a less-evolved magma (Wark et al., 2007; Chamberlain et al., 2014), oxide pairs from the upper fall layers 7-9 provide confirmation of the 740ºC temperature (Hildreth and Wilson, 2007). The temperature evolution of the pre-erupted Oruanui magma body has been studied in great detail (Allan et al., 2013, 2017), with significant cooling (~50ºC), constrained by orthopyroxene zonation occurring prior to eruption. This was confirmed with oxide pairs (Allan et al. in review), providing a pre-eruptive estimate of 780ºC. Temperature estimates for the Huckleberry Ridge fall deposit have been constrained to 800ºC using Zr in melt inclusions, two feldspar thermometry and through comparison with phase equilibrium (Myers et al., 2016; Swallow et al., 2017, in review).

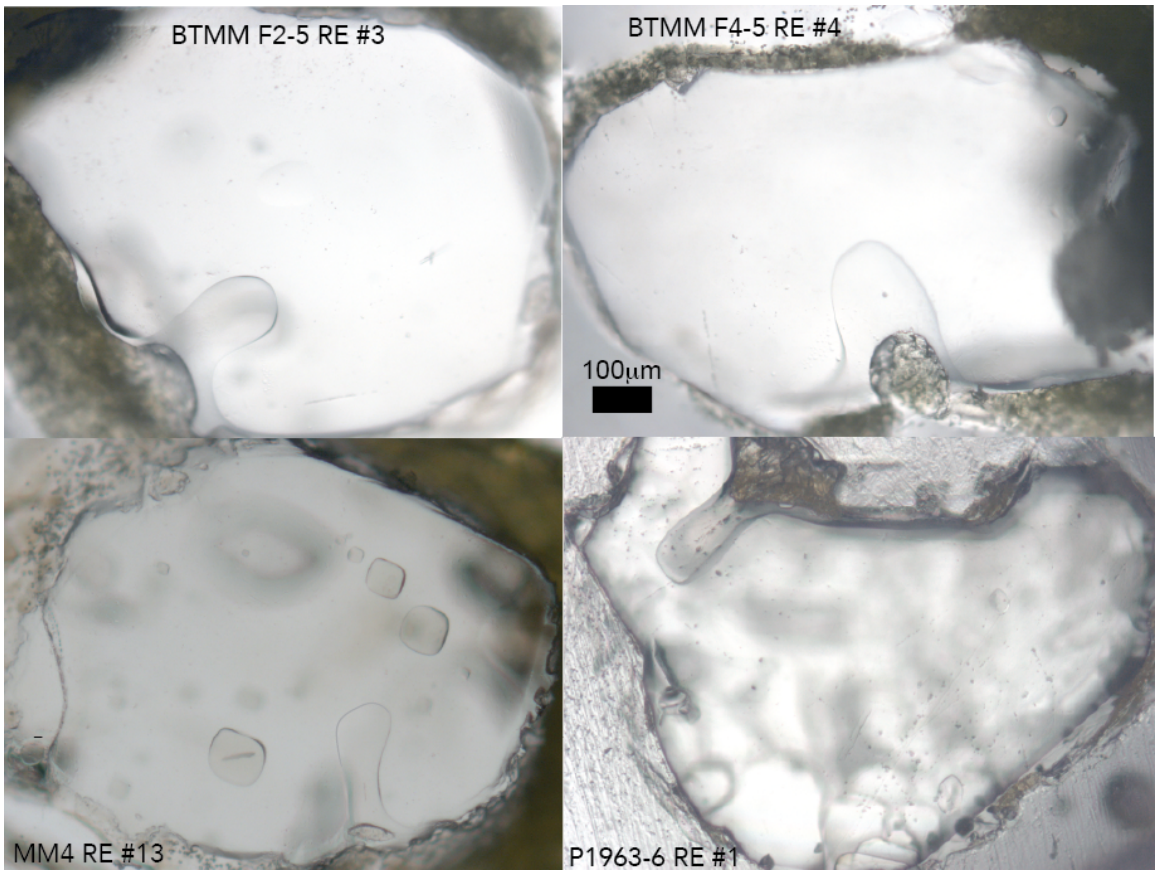

Chapter III Figure 1B: Photomicrographs of select reentrants that preserve well-formed bubbles at their mouths. Details on each reentrant can be found in Chapter III, Table 2.

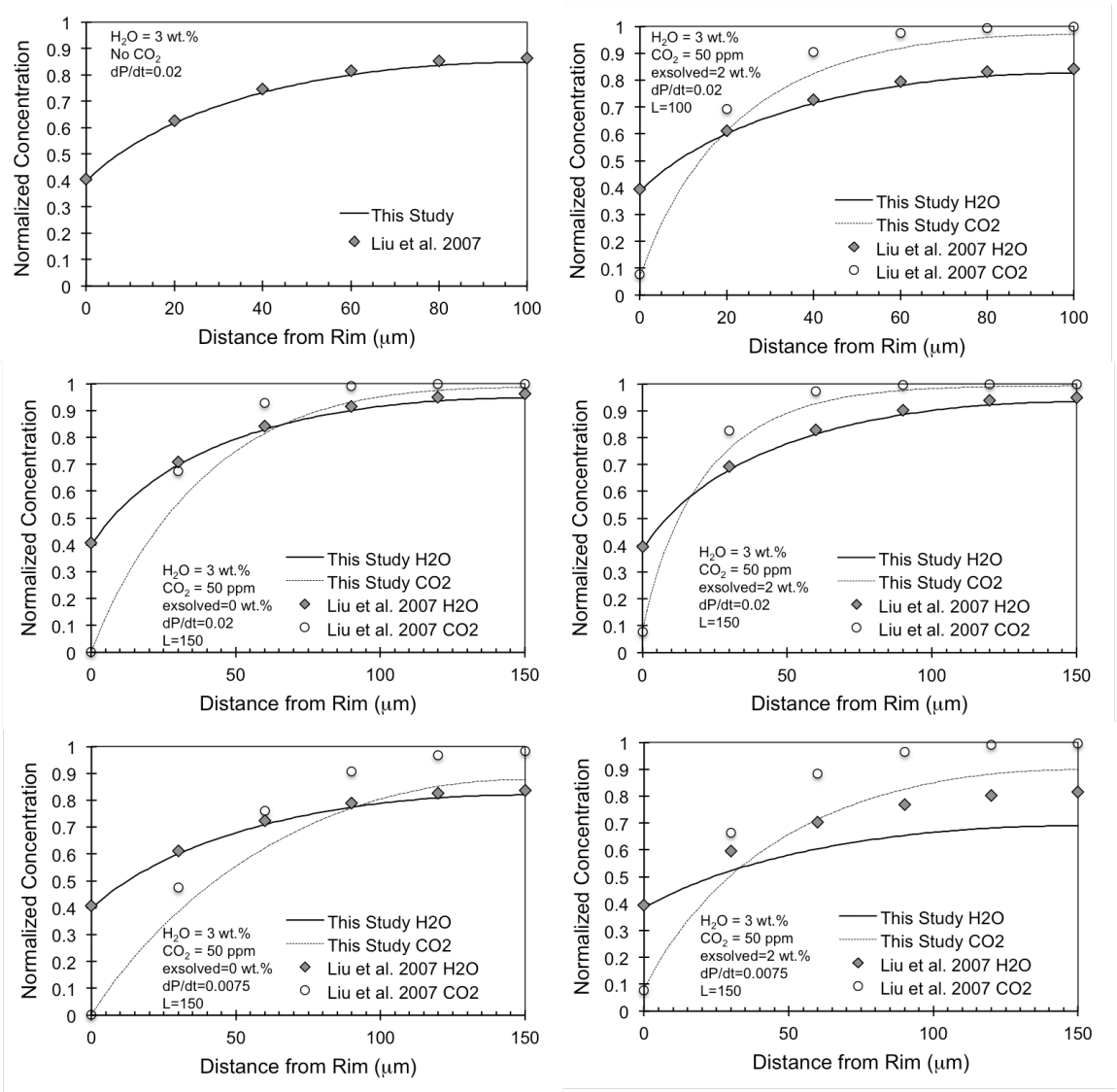

Chapter III Figure 2B: Comparison between modeled results from our code with that of Liu et al. (2007). Important parameters that were tested included: length of reentrant, presence of a vapor bubble (most important when CO_2 is in the system) and decompression rate.

Agreement between the original 1-D Fortran code of Liu et al. (2007) and the one presented here is excellent, with the greatest offsets being in the interior CO_2 profiles for shorter REs and slower ascent times, due to implementation of the updated CO_2 diffusivity (Supplementary Fig. 1B). Due to the updated faster diffusivity of CO_2 (Zhang et al. 2007), shorter reentrants and those that experienced slower decompression have larger offsets in their interior concentrations than those produced by the Liu et al. (2007) code (Appendix B Fig. 1B). In order to evaluate the effect these updated diffusivities would have on the best-fit decompression rate, we input a series of Liu et al. (2007) profiles with a known decompression rate, exsolve gas, starting conditions and reentrant length, into our updated code. Overall, the best-fit decompression rate found to reproduce the Liu et al. (2007) code is equal to or slightly faster (up to a factor of 1.2) using our updated code (Appendix B Table 1B).

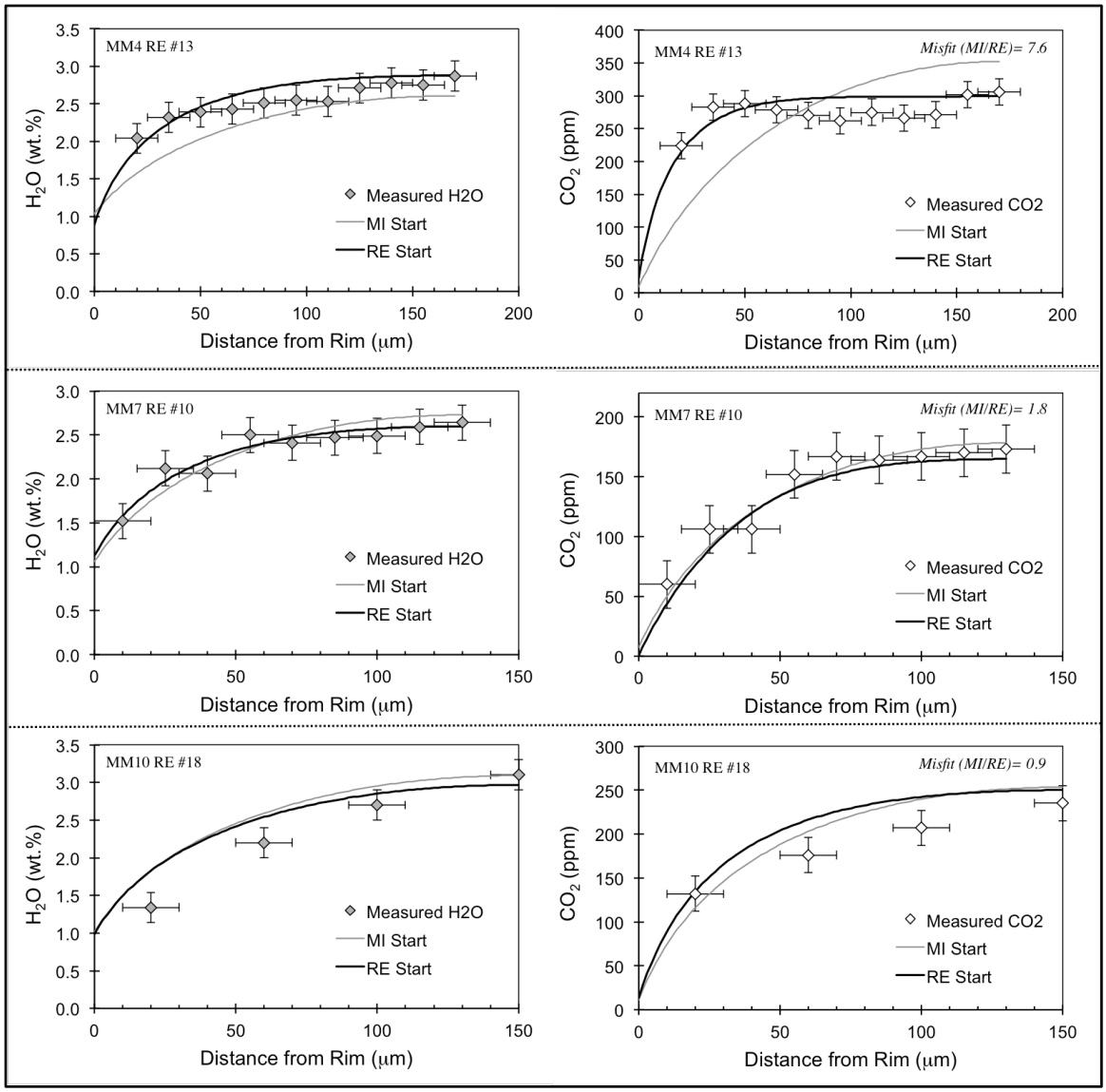

Chapter III Figure 3B: H_2O and CO_2 profiles for three separate reentrants from the Huckleberry Ridge tuff where diamonds represent FTIR measured spots. All black solid lines represent the best fit profile using the interior reentrant concentrations as starting conditions, whereas grey lines represent using the concentrations from a co-erupted melt inclusion. The misfit ratio between using the melt inclusion vs. reentrant as starting conditions is written on all CO_2 profiles, where ratios range between ~1 (similar results) to 8 (reentrant starting conditions are far better).

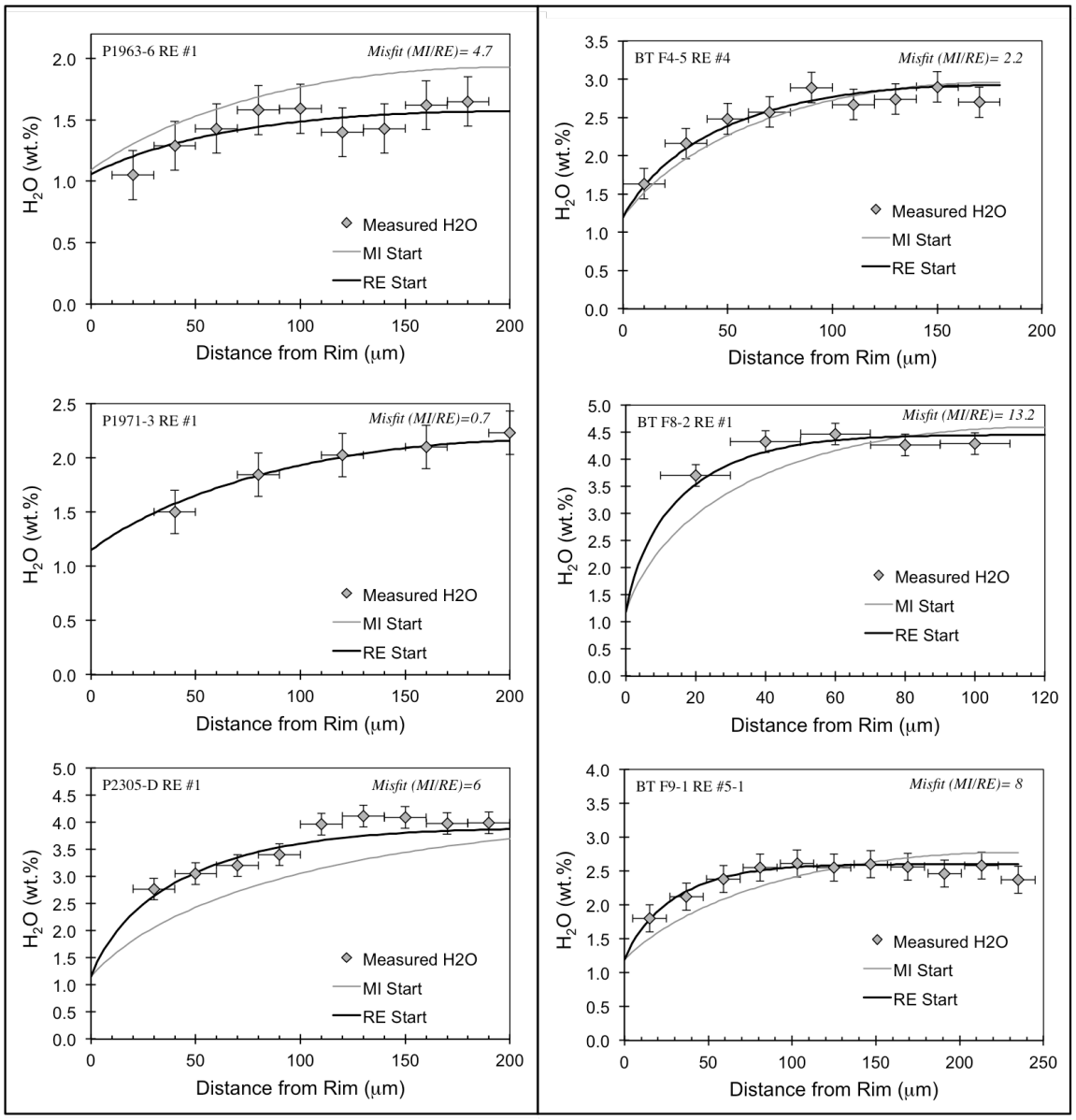

Chapter III Figure 3B (continued): H_2O profiles for three separate reentrants from both the Oruanui (left column) and Bishop (right column) tuffs, where diamonds represent FTIR measured spots. All black solid lines represent the best fit profile using the interior reentrant concentrations as starting conditions, whereas grey lines represent using the concentrations from a co-erupted melt inclusion. The misfit ratio between using the melt inclusion vs. reentrant as starting conditions is written on all profiles, where ratios range between ~1 (similar results) to 13 (reentrant starting conditions are far better).

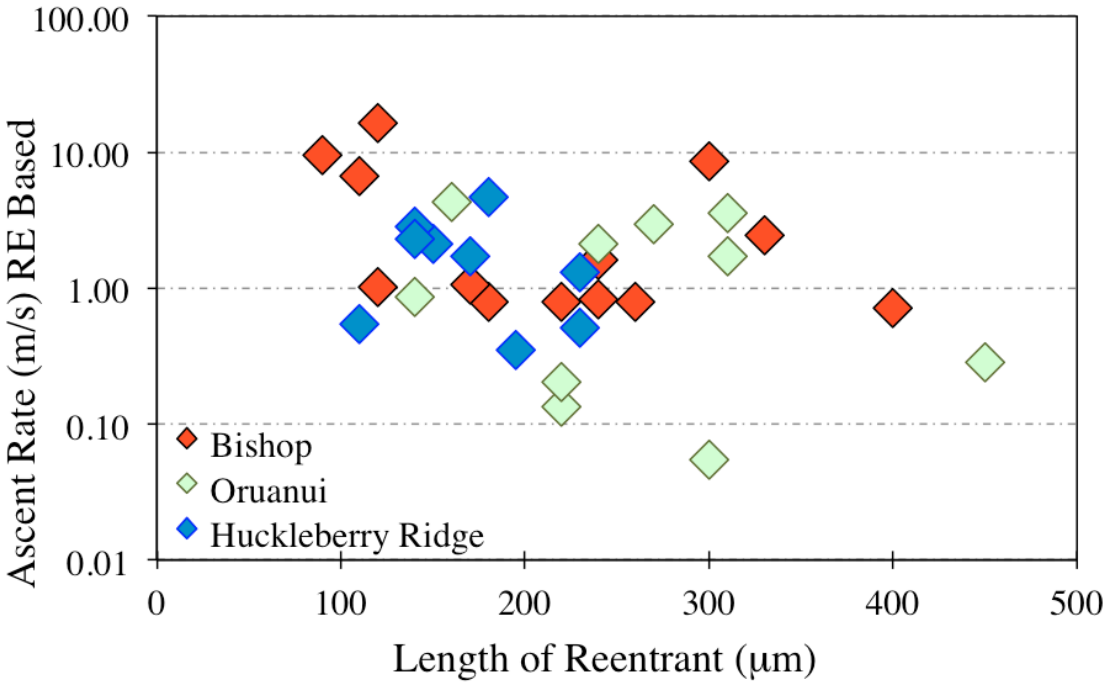

Chapter III Figure 4B: Ascent rate in m/s plotted against the length of reentrant, in mm, for reentrants from all three eruptions. Although the fastest ascent rates are associated with the shortest reentrants, there is little correlation between ascent rate and length of reentrant.

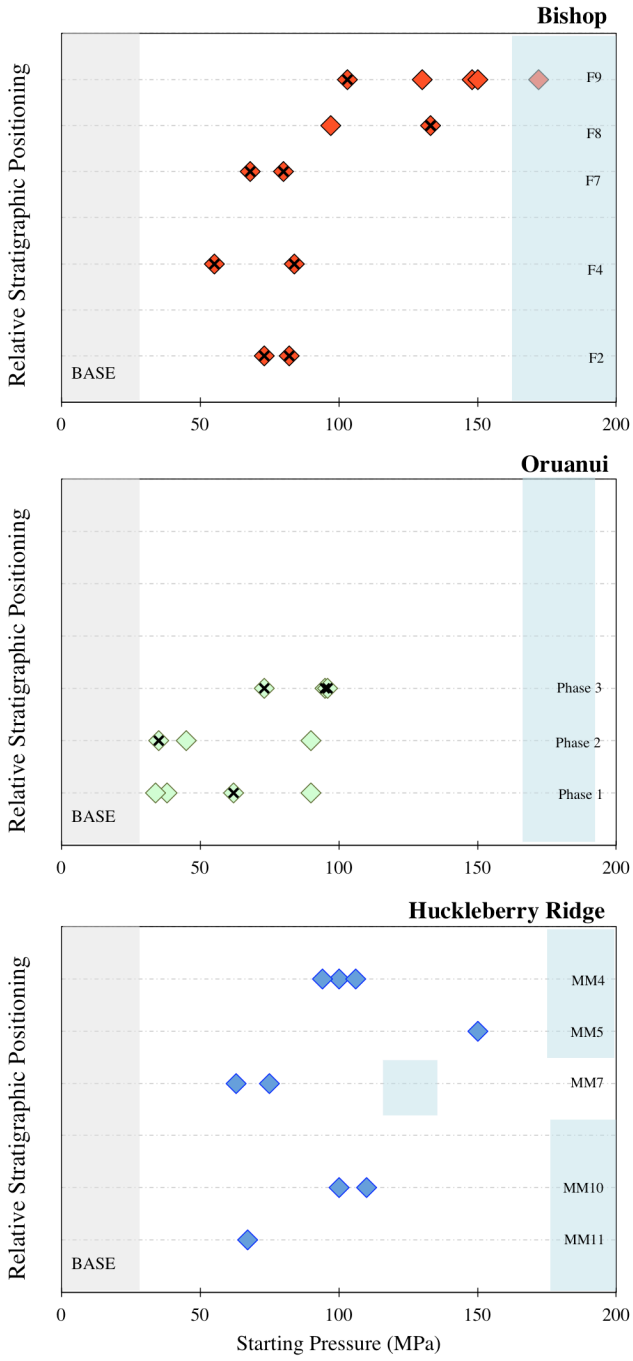

Figure 5B: Each reentrant is shown as a diamond, where those containing X's contained no measureable CO_2. Starting pressure for each reentrant is based on the solubility pressure associated with the innermost H_2O and CO_2 concentrations (converted to pressure using a crustal density of 2600 kg/m^3). The grey field represents the fragmentation region used in this study. The blue region represents the range of pressure associated with the starting depths from co-erupted melt inclusions (Wallace et al., 1999; Roberge et al., 2013; Liu et al., 2006; Myers et al., 2016; Chapter 4).

APPENDIX C

CHAPTER IV SUPPLEMENTARY FIGURES

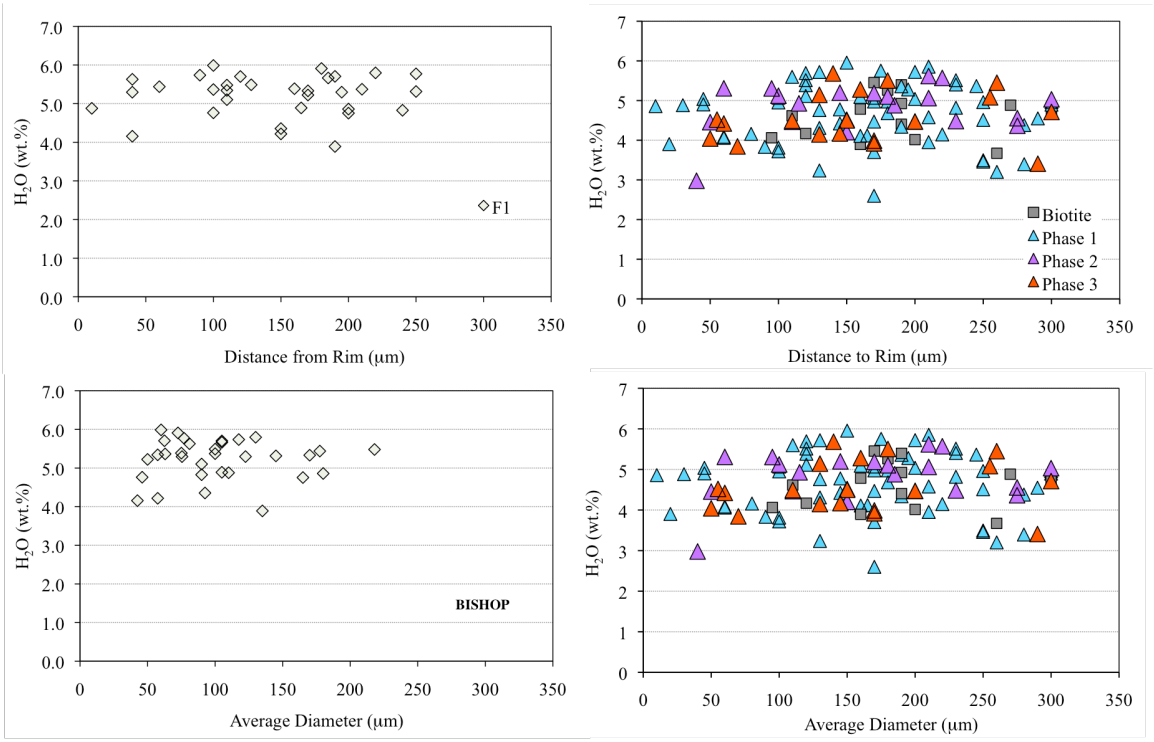

Appendix C Figure 1C: Water concentration verses distance to the nearest quartz rim and the averaged diameter for individual quartz-hosted melt inclusions for the first fall layer of the Bishop and the first three phases of the Oruanui eruption.

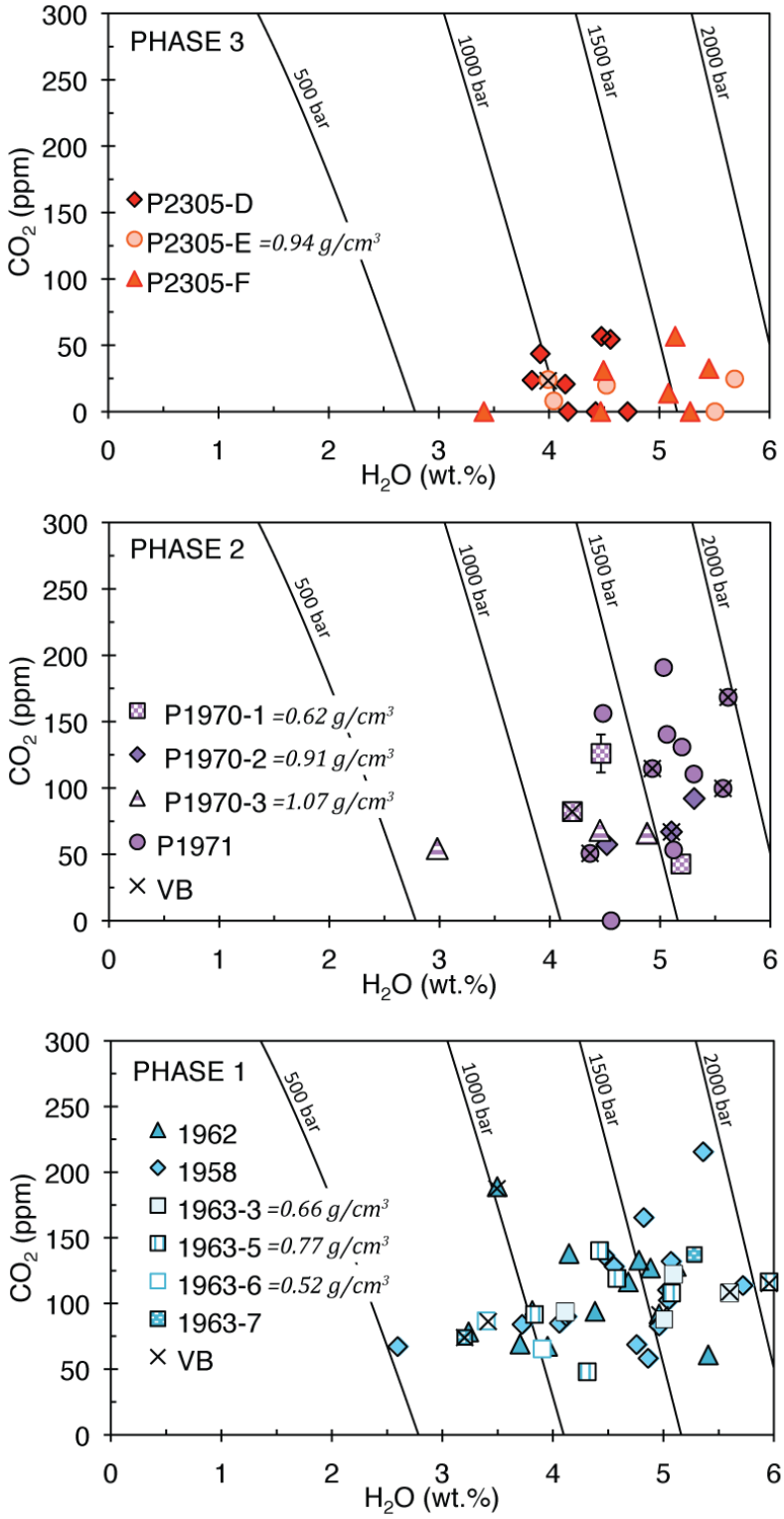

Appendix C Figure 2C: Water vs. CO_2 concentrations for MIs from individual clasts for the first three phases of the Oruanui eruption, from which density information was also collected (Allan et al., 2013).

REFERENCES CITED

Allan, A.S., Wilson, C.J.N., Millet, M.-A., Wysoczanski, R.J. (2012). The invisible hand: Tectonic triggering and modulation of a rhyolitic supereruption. Geology, 40, 563-566.

Allan, A.S.R., Morgan, D.J., Wilson, C.J.N. Millet, M.-A. (2013). From mush to eruption in centuries: assembly of the super-sized Oruanui magma body. Contributions to Mineralogy and Petrology, 166, 143-164.

Allan, A.S.R., Barker, S.J., Millet, M.-A., Morgan, D.J., Rooyakkers, S.J., Schipper, C.I., Wilson, C.J.N. (2017). A cascade of magmatic events during the assembly and eruption of a super-sized magma body. Contributions to Mineralogy and Petrology in press, doi: 10.1007/s00410-017-1367-8

Almeev, R.R., Bolte, T., Nash, B.P., Holtz, F., Erdmann, M., Cathey, H.E. (2012). High-temperature, low-H_2O silicic magmas of the Yellowstone hotspot: an experimental study of rhyolite from the Bruneau–Jarbidge eruptive center, Central Snake River Plain, USA. Journal of Petrology, 53, 1837-1866.

Bachmann, O., Dungan, M.A., Lipman, P.W. (2002). The Fish Canyon magma body, San Juan volcanic field, Colorado: rejuvenation and eruption of an upper-crustal batholith. Journal of Petrology, 43, 1469-1503.

Bachmann, O., Bergantz, G.W. (2003). Rejuvenation of the Fish Canyon magma body: A window into the evolution of large-volume silicic magma systems. Geology, 31, 789-792.

Bachmann O., Dungan, M.A., Bussy, F. (2005). Insights into shallow magmatic processes in large silicic magma bodies: the trace element record in the Fish Canyon magma body, Colorado. Contributions to Mineralogy and Petrology, 149, 338-349.

Bachmann, O., Bergantz, G.W. (2006). Gas percolation in upper-crustal silicic crystal mushes as a mechanism for upward heat advection and rejuvenation of near-solidus magma bodies. Journal of Volcanology and Geothermal Research, 149, 85-102.

Baker, D.R., Lang, P., Robert, G., Bergevin, J.F., Allard, E., Bai, L. (2006). Bubble growth in slightly supersaturated albite melt at constant pressure. Geochimica et Cosmochimica Acta, 70, 1821-1838.

Barker, S.J., Wilson, C.J.N., Smith, E.G.C., Charlier, B.L.A., Wooden, J.L., Hiess, J., Ireland, T.R. (2014). Post-supereruption magmatic reconstruction of Taupo

volcano (New Zealand), as reflected in zircon ages and trace elements. Journal of Petrology, 55, 1511-1533.

Behrens, H., Tamic, N., Holtz, F. (2004). Determination of the molar absorption coefficient for the infrared absorption band of CO_2 in rhyolitic glasses. American Mineralogist, 89, 301-306.

Best, M.G., Christiansen E.H. (1997). Origin of broken phenocrysts in ash-flow tuffs. Geology Society American Bulletin, 109, 63-73.

Bindeman, I.N., Valley, J.W. (2002). Oxygen isotope study of the Long Valley magma system, California: isotope thermometry and convection in large silicic magma bodies. Contributions to Mineralogy and Petrology, 144, 185-205.

Blundy, J., Cashman, K.V., Rust, A., Witham, F., (2010). A case for CO_2-rich arc magmas. Earth and Planetary Sciences, 290, 289-301.

Boehnke, P., Watson, E.B., Trail, D., Harrison, T.M., Schmitt, A.K. (2013). Zircon saturation re-revisited. Chemical Geology, 351, 324-334.

Burgisser A., Bergantz G.W. (2011). A rapid mechanism to remobilize and homogenize highly crystalline magma bodies. Nature, 471, 212-215.

Bursik, M., Renshaw, C., McCalpin, J. Berry, M. (2003). A volcanotectonic cascade: Activation of range front faulting and eruptions by dike intrusion, Mono Basin-Long Valley Caldera, California. Journal of Volcanology and Geothermal Research, 108, 2393.

Caricchi, L., Annen, C., Blundy, J., Simpson, G., Pinel, V., (2014). Frequency and magnitude of volcanic eruptions controlled by magma injection and buoyancy. Nature Geoscience, 7, 126-130.

Cashman, K.V. (2004). Volatile controls on magma ascent and eruption. The State of the Planet: Frontiers and Challenges in Geophysics, 109-124.

Cashman, K.V., McConnell, S.M. (2005). Multiple levels of magma storage during the 1980 summer eruptions of Mount St. Helens, WA. Bulletin of Volcanology, 68, 57-75.

Cashman, K.V., Giordano, G. (2014). Calderas and magma reservoirs. Journal of Volcanology and Geothermal Research, 288, 28-45.

Castro, J. M., Gardner, J.E. (2008). Did magma ascent rate control the explosive-effusive transition at the Inyo volcanic chain, California?. Geology, 36(4), 279-282.

Castro, J.M., Dingwell, D.B. (2009). Rapid ascent of rhyolitic magma at Chaitén volcano, Chile. Nature, 461, 780-783.

Chamberlain, K.J., Wilson, C.J.N., Wooden, J.L., Charlier, B.L.A., Ireland, T.R. (2014a). New perspectives on the Bishop Tuff from zircon textures, ages and trace elements. Journal of Petrology, 55, 395-426.

Chamberlain, K. J., Morgan, D. J., Wilson, C.J.N., (2014b). Timescales of mixing and mobilisation in the Bishop Tuff magma body: perspectives from diffusion chronometry. Contributions to Mineralogy and Petrology, 168, 1-24.

Chamberlain, K.J., Wilson, C.J.N., Wallace, P. J., Millet, M. A. (2015). Micro-analytical perspectives on the Bishop Tuff and its magma chamber. Journal of Petrology, 56 (3), 605-640.

Charlier, B.L.A., Bachmann, O., Davidson, J.P., Dungan, M.A, Morgan, D.J. (2007). The upper crustal evolution of a large silicic magma body: evidence from crystal-scale Rb-Sr isotopic heterogeneities in the Fish Canyon magmatic system, Colorado. Journal of Petrology, 48, 1875-1894.

Charlier, B.L.A., Wilson, C.J.N., Davidson, J. P. (2008). Rapid open-system assembly of a large silicic magma body: time-resolved evidence from cored plagioclase crystals in the Oruanui eruption deposits, New Zealand. Contributions to Mineralogy and Petrology, 156, 799-813.

Charlier, B.L.A., Morgan, D.J., Wilson, C.J.N., Wooden, J.L., Allan, A.S.R., Baker, J.A., (2012). Lithium concentration gradients in feldspar and quartz record the final minutes of magma ascent in an explosive supereruption. Earth and Planetary Science Letters, 319-320, 218-227.

Christiansen, R.L. (2001). The Quaternary and Pliocene Yellowstone Plateau volcanic field of Wyoming, Idaho, and Montana. U.S. Geological Survey Professional Papers 729-G, G1-G143.

Cottrell, E., Spiegelman, M., Langmuir, C.H., (2002). Consequences of diffusive reequilibration for the interpretation of melt inclusions. Geochemistry, Geophysics, Geosystems, 3, 1026.

de Silva, S.L., Gregg, P.M. (2014). Thermomechanical feedbacks in magmatic systems: implications for growth, longevity, and evolution of large caldera-forming magma reservoirs and their supereruptions. Journal of Volcanology and Geothermal Research, 282, 77-91.

Dingwell, D.B., (1996). Volcanic dilemma: flow or blow?. Science, 273, 1054.

Dixon, J.E., Stolper, E.M., Holloway, J.R. (1995). An experimental study of water and carbon dioxide solubilities in mid-ocean ridge basaltic liquids. Part I: calibration and solubility models. Journal of Petrology, 36, 1607-1631.

Donovan, J.J., Kremser, D., Fournelle, J.H. (2007). Probe for Windows User's Guide and Reference, Enterprise Edition. Probe Software, Inc., Eugene, OR.

Druitt, T. H., Costa, F., Deloule, E., Dungan, M., Scaillet, B. (2012). Decadal to monthly timescales of magma transfer and reservoir growth at a caldera volcano. Nature, 482(7383), 77-80.

Dufek, J., Bergantz, G.W. (2005). Transient two-dimensional dynamics in the upper conduit of a rhyolitic eruption: A comparison of closure models for the granular stress. Journal of Volcanology and Geothermal Research, 143, 113-131.

Dufek, J., Bachmann, O. (2010). Quantum magmatism: magmatic compositional gaps generated by melt-crystal dynamics. Geology. 38, 687-690.

Dumitru, T.A. (1991). Effects of subduction parameters on geothermal gradients in forearcs, with an application to Franciscan subduction in California. Journal of Geophysical Research, 96, 621-641.

Eichelberger, J.C., Carrigan, C.R., Westrich, H.R. and Price, R.H. (1986). Non-explosive silicic volcanism. Nature, 313, 598-602.

Evans, B. W., Hildreth, W., Bachmann, O., Scaillet, B. (2016). In defense of magnetite-ilmenite thermometry in the Bishop Tuff and its implication for gradients in silicic magma reservoirs. American Mineralogist, 101, 407-414.

Farmer, G.L., Bailley, T., Elkins-Tanton L.T. (2008). Mantle source volumes and the origin of the mid-Tertiary ignimbrite flare-up in the southern Rocky Mountains, western US. Lithos, 102, 279-294.

Ferguson, D.J., Gonnermann, H.M., Ruprecht, P., Plank, T., Hauri, E.H., Houghton, B.F., Swanson, D.A. (2016). Magma decompression rates during explosive eruptions of Kīlauea volcano, Hawaii, recorded by melt embayments. Bulletin of Volcanology, 78, 71.

Gardner, J.E. (2007). Heterogeneous bubble nucleation in highly viscous silicate melts during instantaneous decompression from high pressure. Chemical Geology, 236, 1-12.

Gardner, J.E., Thomas, R.M., Jaupart, C., Tait, S. (1996). Fragmentation of magma during Plinian volcanic eruptions. Bulletin of Volcanology, 58, 144-162.

Ghiorso, M.S., Evans, B.W. (2008). Thermodynamics of rhombohedral oxide solid solutions and a revision of the Fe-Ti two-oxide geothermometer and oxygen-barometer. American Journal of Science, 308, 957-1039.

Ghiorso M.S., Gualda, G.A.R. (2015). An H_2O–CO_2 mixed fluid saturation model compatible with rhyolite-MELTS. Contributions to Mineralogy and Petrology, 169, 53.

Gonnermann, H.M., Manga, M. (2013). Dynamics of magma ascent in the volcanic conduit. Modeling volcanic processes: The physics and mathematics of volcanism, 55-84.

Gregg, P.M., de Silva, S.L., Grosfils, E.B., Parmigiani, J.P. (2012). Catastrophic caldera-forming eruptions: thermomechanics and implications for eruption triggering and maximum caldera dimensions on Earth. Journal of Volcanology and Geothermal Research, 241-242, 1-12.

Gregg, P.M., Grosfils, E.B., de Silva, S.L. (2015). Catastrophic caldera-forming eruptions II: the subordinate role of magma buoyancy as an eruption trigger. Journal of Volcanology and Geothermal Research, 305, 100-113.

Hampel, A., Hetzel, R. (2008). Slip reversals on active normal faults related to the inflation and deflation of magma chambers: numerical modeling with application to the Yellowstone-Teton region. Geophysical Research Lettetters, 35, L07301.

Hildreth, W. (1979). The Bishop Tuff: evidence for the origin of compositional zonation in silicic magma chambers. Geological Society of America Special Papers, 180, 43-76.

Hildreth, W. (1981). Gradients in silicic magma chambers: implications for lithospheric magmatism. Journal of Geophysical Research, 86, 10153-10192

Hildreth, W. (2004). Volcanological perspectives on Long Valley, Mammoth Mountain, and Mono Craters: several contiguous but discrete systems. Journal of Volcanology and Geothermal Research, 136(3), 169-198.

Hildreth, W., Mahood, G.A. (1986). Ring-fracture eruption of the Bishop Tuff. Geological Society of America Bulletin, 97, 396-403.

Hildreth, W., Wilson, C.J.N. (2007). Compositional zoning of the Bishop Tuff. Journal of Petrology, 48, 951-999.

Huber, C., Bachmann, O., Manga, M. (2010). Two competing effects of volatiles on heat transfer in crystal-rich magmas: thermal insulation vs. defrosting. Journal of Petrology, 51, 847-867.

Huber, C., Bachmann, O., Dufek, J. (2012). Crystal-poor versus crystal-rich ignimbrites: A competition between stirring and reactivation. Geology, 40, 115-118.

Humphreys, E.D. (1995). Post-Laramide removal of the Farallon slab, western United States. Geology, 23, 987-990.

Humphreys, M., Menand, T., Blundy, J.D., Klimm, K. (2008). Magma ascent rates in explosive eruptions: constraints from H_2O diffusion in melt inclusions. Earth and Planetary Science Letters, 270(1), 25-40.

Jaupart, C. (1996). Physical models of volcanic eruptions. Chemical Geology, 128, 217-227.

Jaupart, C., Allègre, C.J. (1991). Gas content, eruption rate and instabilities of eruption regime in silicic volcanoes. Earth and Planetary Science Letters, 102, 413-429.

Jellinek, A.M., DePaolo, D.J. (2003). A model for the origin of silicic magma chambers: precursors of caldera-forming eruptions. Bulletin of Volcanology, 65, 363-381.

Johnson, E.A., Rossman, G.R. (2013). The diffusion behavior of hydrogen in plagioclase feldspar at 800–1000 ºC: Implications for re-equilibration of hydroxyl in volcanic phenocrysts. American Mineralogist, 98, 1779-1787.

Johnson, D. M., Hooper, P. R., Conrey, R. M. (1999). XRF analysis of rocks and minerals for major and trace elements on a single low dilution Li-tetraborate fused bead. Advances in X-ray Analysis, 41, 843–867 Le Bas, MJ.

Kasper, R.B. (1975). Cation and oxygen diffusion in albite. Ph.D. dissertation, Brown University, Providence, Rhode Island

Kent, A. J. (2008). Melt inclusions in basaltic and related volcanic rocks. Reviews in Mineralogy and Geochemistry, 69, 273-331.

Klug, C., Cashman, K.V. (1996). Permeability development in vesiculating magmas: implications for fragmentation. Bulletin of Volcanology, 58, 87-100.

Leschik, M., Heide, G., Frischat, G.H., Behrens, H., Wiedenbeck, M., Wagner, N., Heide, K., Geißler, H., and Reinholz, U. (2004). Determination of H_2O and D_2O contents in rhyolitic glasses. Physics and Chemistry of Glasses, 45, 238-251.

Lipman, P.W. (1997). Subsidence of ash-flow calderas: relation to caldera size and magma-chamber geometry. Bulletin of Volcanology 59, 198-218.

Lipman, P.W. (2007). Incremental assembly and prolonged consolidation of Cordilleran magma chambers: Evidence from the Southern Rocky Mountain volcanic field. Geosphere, 3, 42-70.

Lipman, P.W., McIntosh, W.C. (2008). Eruptive and noneruptive calderas, northeastern San Juan Mountains, Colorado: Where did the ignimbrites come from?. Geological Society American Bulletin, 120(7-8), 771-795.

Liu, Y., Zhang, Y., Behrens, H. (2005). Solubility of H_2O in rhyolitic melts at low pressures and a new empirical model for mixed H_2O–CO_2 solubility in rhyolitic melts. Journal of Volcanology and Geothermal Research, 143, 219-235.

Liu, Y., Anderson, A. T., Wilson, C. J. N., Davis, A. M., Steele, I. M. (2006). Mixing and differentiation in the Oruanui rhyolitic magma, Taupo, New Zealand: evidence from volatiles and trace elements in melt inclusions. Contributions to Mineralogy and Petrology, 151(1), 71-87.

Liu, Y., Anderson, A.T., Wilson, C.J.N. (2007). Melt pockets in phenocrysts and decompression rates of silicic magmas before fragmentation. Journal of Geophysical Research: Solid Earth, 112(B6), B6204.

Lloyd, A.S., Plank, T., Ruprecht, P., Hauri, E.H., Rose, W. (2013). Volatile loss from melt inclusions in pyroclasts of differing sizes. Contributions to Mineralogy and Petrology, 165, 129-153.

Lloyd, A.S., Ruprecht, P., Hauri, E.H., Rose, W., Gonnermann, H.M., Plank, T. (2014). NanoSIMS results from olivine-hosted melt embayments: magma ascent rate during explosive basaltic eruptions. Journal of Volcanology and Geothermal Research, 283, 1-18.

Loewen, M.W., Bindeman, I.N. (2015). Oxygen isotope and trace element evidence for three stage petrogenesis of the youngest episode (260–79 ka) of Yellowstone rhyolitic volcanism. Contributions to Mineralogy and Petrology, 170, 39.

Lowenstern, J. B. (1995). Applications of silicate-melt inclusions to the study of magmatic volatiles. Magmas, fluids, and ore deposits, 23, 71-99.

Malfait, W.J., Seifert, R., Petitgirard, S., Perrillat, J.P., Mezouar, M., Ota, T., Nakamura, E., Lerch, P., Sanchez-Valle, C. (2014). Supervolcano eruptions driven by melt buoyancy in large silicic magma chambers. Nature Geoscience, 7, 122-125.

Mangan, M., Sisson, T. (2000). Delayed, disequilibrium degassing in rhyolite magma: decompression experiments and implications for explosive volcanism. Earth and Planetary Science Letters, 183, 441-455.

Mason, B. G., Pyle, D. M., Oppenheimer, C. (2004). The size and frequency of the largest explosive eruptions on Earth. Bulletin of Volcanology, 66, 735-748.

Mastin, L.G. (2002). Insights into volcanic conduit flow from an open‐source numerical model. Geochemistry, Geophysics, Geosystems, 3, 1-18.

Mastin, L.G. (2005). The controlling effect of viscous dissipation on magma flow in silicic conduits. Journal of Volcanology and Geothermal Research, 143, 17-28.

Matthews, N.E., Vazquez, J.A., Calvert, A.T. (2015). Age of the Lava Creek supereruption and magma chamber assembly at Yellowstone based on $^{40}Ar/^{39}Ar$ and U‐Pb dating of sanidine and zircon crystals. Geochemistry, Geophysics, Geosystems, 16, 2508-2528.

Melnik, O., Sparks, R.S.J. (1999). Nonlinear dynamics of lava dome extrusion. Nature, 402, 37-41.

Melnik, O., Sparks, R.S.J. (2002). Modelling of conduit flow dynamics during explosive activity at Soufrière Hills Volcano, Montserrat. Geological Society, London, Memoirs, 21, 307-317.

Moore L.R., Gazel E, Tuohy, R., Lloyd, A.S., Esposito, R., Steele-MacInnis, M., Hauri, E.H., Wallace, P.J., Plank, T., Bodnar, R.J. (2015). Bubbles matter: an assessment of the contribution of vapor bubbles to melt inclusion volatile budgets. American Mineralogist, 100, 806-823.

Myers, M.L., Wallace, P.J., Wilson, C.J.N, Morter, B.J., Swallow, E.J. (2016). Prolonged ascent and episodic venting of discrete magma batches at the onset of the Huckleberry Ridge supereruption, Yellowstone. Earth and Planetary Science Letters, 451, 285-297.

Newman, S., Lowenstern, J.B. (2002). VolatileCalc: a silicate melt–H_2O–CO_2 solution model written in Visual Basic for Excel. Computers and Geosciences, 28, 597-604.

Papale, P., Neri, A., Macedonio, G. (1998). The role of magma composition and water content in explosive eruptions: 1. Conduit ascent dynamics. Journal of Volcanology and Geothermal Research, 87(1), 75-93.

Parat, F., Dungan, M.A., Lipman, P.W. (2005). Contemporaneous trachyandesitic and calc-alkaline volcanism of the Huerto Andesite, San Juan volcanic field, Colorado, USA. Journal of Petrology, 46(5),859-891.

Peppard, B.T., Steele, I.M., Davis, A.M., Wallace, P.J., Anderson, A.T. (2001). Zoned quartz phenocrysts from the rhyolitic Bishop Tuff. American Mineralogist, 86, 1034-1052.

Qin, Z., Lu, F. Anderson, A.T., (1992). Diffuse reequilibration of melt and fluid inclusions. American Mineralogist, 77(5-6), 565-576.

Reid, M.R., Vazquez, J.A., Schmitt, A.K. (2011). Zircon-scale insights into the history of a Supervolcano, Bishop Tuff, Long Valley, California, with implications for the

Ti-in-zircon geothermometer. Contributions to Mineralogy and Petrology, 161, 293-311.

Ridolfi, F., Renzulli, A., Puerini, M. (2010). Stability and chemical equilibrium of amphibole in calc-alkaline magmas: an overview, new thermobarometric formulations and application to subduction-related volcanoes. Contributions to Mineralogy and Petrology, 160, 45-66.

Riker, J.M., Cashman, K.V., Rust, A.C., Blundy, J.D. (2015). Experimental constraints on plagioclase crystallization during H_2O-and H_2O–CO_2-saturated magma decompression. Journal of Petrology, 56, 1967-1998.

Roberge, J., Wallace, P.J., Kent, A.J.R. (2013). Magmatic processes in the Bishop Tuff rhyolitic magma based on trace elements in melt inclusions and pumice matrix glass. Contributions to Mineralogy and Petrology, 165, 237-257.

Roche, O., Druitt, T.H. (2001). Onset of caldera collapse during ignimbrite eruptions. Earth and Planetary Science Letters, 191, 191-202.

Rotella, M.D., Wilson, C.J.N., Barker, S.J., Cashman, K.V., Houghton, B.F., Wright, I.C. (2014). Bubble development in explosive silicic eruptions: insights from pyroclast vesicularity textures from Raoul volcano (Kermadec arc). Bulletin of Volcanology, 76, 862.

Rutherford, M.J., Hill, P.M. (1993). Magma ascent rates from amphibole breakdown: an experimental study applied to the 1980–1986 Mount St. Helens eruptions. Journal of Geophysical Research, 98, 19667-19685.

Rutherford, M.J., Devine, J.D. (1996). Preeruption pressure-temperature conditions and volatiles in the 1991 dacitic magma of Mount Pinatubo. In: Fire and Mud: eruptions and lahars of Mount Pinatubo, Philippines 751-766.

Rutherford, M.J. (2008). Magma ascent rates. Reviews in Mineralogy and Geochemistry 69, 241-271.

Scandone, R., Cashman, K.V., and Malone, S.D. (2007). Magma supply, magma ascent and the style of volcanic eruptions. Earth and Planetary Science Letters, 253, 513-529.

Self, S. (2006). The effects and consequences of very large explosive volcanic eruptions. Philosophical Transactions of the Royal Society of London A: Mathematical, Physical and Engineering Sciences, 364, 2073-2097.

Self, S., Sparks, R.S.J. (1978). Characteristics of widespread pyroclastic deposits formed by the interaction of silicic magma and water. Bulletin of Volcanology, 41, 196-212.

Severs, M.J., Azbej, T., Thomas, J.B., Mandeville, C.W., Bodnar, R.J. (2007). Experimental determination of H_2O loss from melt inclusions during laboratory heating: evidence from Raman spectroscopy. Chemical Geology, 237, 358-371.

Shea, T., Gurioli, L., Houghton, B.F., Cioni, R., Cashman, K. V. (2011). Column collapse and generation of pyroclastic density currents during the AD 79 eruption of Vesuvius: the role of pyroclast density. Geology, 39, 695-698.

Simakin, A.G., Ghassemi, A. (2010). The role of magma chamber-fault interaction in caldera forming eruptions. Bulletin of Volcanology, 72, 85-101.

Simmons, J.M., Carey, R.J., Cas, R.A.F., Druitt, T.H. (2017). High magma decompression rates at the peak of a violent caldera-forming eruption (Lower Pumice 1 eruption, Santorini, Greece). Bulletin of Volcanology, 79, 42.

Skirius, C.M., 1990. Pre-eruptive H_2O and CO_2 content of Plinian and ash-flow Bishop Tuff magma. University of Chicago Ph.D. Dissertation.

Sliwinski, J.T., Bachmann, O., Dungan, M.A., Huber, C., Deering, C.D., Lipman, P.W., Martin, L.H.J., Liebske C. (2017). Rapid pre-eruptive thermal rejuvenation in a large silicic magma body: the case of the Masonic Park Tuff, Southern Rocky Mountain volcanic field, CO, USA. Contributions to Mineralogy and Petrology, 172, 30.

Sparks, R.S.J. (1978). The dynamics of bubble formation and growth in magmas: a review and analysis. Journal of Volcanology and Geothermal Research, 3, 1-37.

Stock, M.J., Humphreys, M.C., Smith, V.C., Isaia, R., Pyle, D. M. (2016). Late-stage volatile saturation as a potential trigger for explosive volcanic eruptions. Nature Geoscience, 9, 249-254.

Sutton, A. N., Blake, S., Wilson, C. J. (1995). An outline geochemistry of rhyolite eruptives from Taupo volcanic centre, New Zealand. Journal of Volcanology and Geothermal Research, 68(1-3), 153-175.

Swallow, E.J., Wilson, C.J.N, Myers, M.L., Wallace, P.J., Collins, K.S., Smith, E.G.C. (in review). Evacuation of multiple magma bodies and the onset of caldera collapse in a supereruption, captured in glass and mineral chemistries. Earth and Planetary Science Letters.

Thomas, N., Jaupart, C., Vergniolle, S. (1994). On the vesicularity of pumice. Journal of Geophysical Research, 99, 15-633.

Till, C.B., Vazquez, J.A., Boyce, J.W. (2015). Months between rejuvenation and volcanic eruption at Yellowstone caldera, Wyoming. Geology, 43, 695-698.

Toramaru, A. (2006). BND (bubble number density) decompression rate meter for explosive volcanic eruptions. Journal of Volcanology and Geothermal Research, 154, 303-316.

Vazquez, J.A., Reid, M.R. (2002). Time scales of magma storage and differentiation of voluminous high-silica rhyolites at Yellowstone caldera, Wyoming. Contributions to Mineralogy and Petrology, 144, 274-285.

Wallace, P.J., Anderson, A.T., Davis, A.M. (1999). Gradients in H_2O, CO_2, and exsolved gas in a large-volume silicic magma system: Interpreting the record preserved in melt inclusions from the Bishop Tuff. Journal of Geophysical Research: Solid Earth, 104, 20097-20122.

Wallace, P.J., Dufek, J., Anderson, A. T., Zhang, Y. (2003). Cooling rates of Plinian-fall and pyroclastic-flow deposits in the Bishop Tuff: inferences from water speciation in quartz-hosted glass inclusions. Bulletin of Volcanology, 65, 105-123.

Wallace, P.J. (2005). Volatiles in subduction zone magmas: concentrations and fluxes based on melt inclusion and volcanic gas data. Journal of Volcanology and Geothermal Research, 140, 217-240.

Wark, D.A., Hildreth, W., Spear, F.S., Cherniak, D.J. and Watson, E.B. (2007). Pre-eruption recharge of the Bishop magma system. Geology, 35, 235-238.

Waters, L.E., Lange, R.A. (2015). An updated calibration of the plagioclase-liquid hygrometer-thermometer applicable to basalts through rhyolites. American Mineralogist, 100, 2172-2184.

Watson, E.B., Harrison, T.M. (1983). Zircon saturation revisited: temperature and composition effects in a variety of crustal magma types. Earth and Planetary Science Letters, 64, 295-304.

Whitney, J.A., Stormer, J.C., (1985). Mineralogy, petrology, and magmatic conditions from the Fish Canyon Tuff, central San Juan volcanic field, Colorado. Journal of Petrology 26(3), 726-762.

Wilson, C.J.N. (2001). The 26.5 ka Oruanui eruption, New Zealand: an introduction and overview. Journal of Volcanology and Geothermal Research, 112, 133-174.

Wilson, C.J.N., Hildreth, W. (1997). The Bishop Tuff: new insights from eruptive stratigraphy. Journal of Geology, 105, 407-439.

Wilson, C J.N., Blake, S., Charlier, B.L.A., Sutton, A.N. (2006). The 26·5 ka Oruanui eruption, Taupo volcano, New Zealand: development, characteristics and evacuation of a large rhyolitic magma body. Journal of Petrology, 47, 35-69.

Wilson, C.J.N., Charlier, B.L.A. (2009). Rapid rates of magma generation at contemporaneous magma systems, Taupo volcano, New Zealand: insights from U-Th model-age spectra in zircons. Journal of Petrology, 50, 875-907.

Wilson, C.J.N., Gravley, D.M., Leonard, G.S., Rowland, J.V. (2009). Volcanism in the central Taupo Volcanic Zone, New Zealand: tempo, styles and controls. In: T. Thordarson, Self, S., Larsen, G., Rowland, S.K., Hoskuldsson, A. (Editor), Studies in Volcanology: The Legacy of George Walker. Special Publications of IAVCEI 2, 225-247.

Woods, A.W., Koyaguchi, T. (1994). Transitions between explosive and effusive eruptions of silicic magma, Nature, 370, 641–644.

Wotzlaw, J.F., Schaltegger, U., Frick, D.A., Dungan, M.A., Gerdes, A., Günther, D. (2013). Tracking the evolution of large-volume silicic magma reservoirs from assembly to supereruption. Geology, 41, 867-870.

Wotzlaw, J. F., Bindeman, I. N., Watts, K. E., Schmitt, A. K., Caricchi, L., Schaltegger, U. (2014). Linking rapid magma reservoir assembly and eruption trigger mechanisms at evolved Yellowstone-type supervolcanoes. Geology, 42, 807-810.

Wysoczanski, R., Tani, K. (2006). Spectroscopic FTIR imaging of water species in silicic volcanic glasses and melt inclusions: an example from the Izu-Bonin arc. Journal of Volcanology and Geothermal Research, 156, 302-314.

Zhang, Y., Jenkins, J., Xu, Z. (1997). Kinetics of the reaction $H_2O + O \rightarrow 2OH$ in rhyolitic glasses upon cooling: geospeedometry and comparison with glass transition. Geochimica et Cosmochimica Acta, 61(11), 2167-2173.

Zhang, Y., Xu, Z., Zhu, M., Wang, H. (2007). Silicate melt properties and volcanic eruptions. Reviews of Geophysics, 45.